

ON THE INTEGRATION OF COMPUTATIONAL FLUID DYNAMICS (CFD)
SIMULATIONS WITH MONTE CARLO (MC) RADIATION TRANSPORT
ANALYSIS

by

Fawaz Ali

A THESIS SUBMITTED IN PARTIAL FULFILLMENT
OF THE REQUIREMENTS FOR THE DEGREE OF

Master of Science

in

The Faculty of Science

Modelling and Computational Science

Supervisor: Dr. Ed Waller, Faculty of Energy Systems and Nuclear Science

Examining Board: Dr. Anthony Waker, Faculty of Energy Systems and Nuclear
Science

Dr. Lixuan Lu, Faculty of Energy Systems and Nuclear Science

External Examiner: Dr. Glenn Harvel, Faculty of Energy Systems and Nuclear
Science

UNIVERSITY OF ONTARIO INSTITUTE OF TECHNOLOGY

December 2009

© Fawaz Ali, 2009

ABSTRACT

Numerous scenarios exist whereby radioactive particulates are transported between spatially separated points of interest. An example of this phenomenon is, in the aftermath of a Radiological Dispersal Device (RDD) detonation, the resuspension of radioactive particulates from the resultant fallout field. Quantifying the spatial distribution of radioactive particulates allow for the calculation of potential radiation doses that can be incurred from exposure to such particulates. Presently, there are no simulation techniques that link radioactive particulate transport with subsequent radiation field determination and so this thesis develops a coupled Computational Fluid Dynamics (CFD) and Monte Carlo (MC) Radiation Transport approach to this problem. Via particulate injections, the CFD simulation defines the spatial distribution of radioactive particulates and this distribution is then employed by the MC Radiation Transport simulation to characterize the resultant radiation field. GAMBIT/FLUENT are employed for the CFD simulations while MCNPX is used for the MC Radiation Transport simulations.

Keywords: Computational Fluid Dynamics, CFD, Monte Carlo Radiation Transport, Code Coupling, Resuspension, Radioactive Particulate, Radiological Dispersal Device (RDD), GAMBIT, FLUENT, MCNPX, Bluff Body

DEDICATION

To my late grandmother, who instilled the importance of education in me, and to my parents and siblings.

ACKNOWLEDGEMENTS

First and foremost, I would like to express my sincere gratitude to my thesis supervisor, Dr. Ed Waller for his guidance throughout my undergraduate and graduate experience at UOIT and to thank him for all the opportunities that he has afforded me.

I would like to say thank you to Amin Patel and to my fellow graduate students in the Modelling and Computational Science program for their support and friendship.

My heartfelt thanks go out to Sharman Perera and Khalid Rizk for their help in acquiring and installing the computational infrastructure and software required for this thesis and the tremendous support they provided me in learning the fundamentals of Computational Fluid Dynamics simulations. I am truly grateful to Sharman and Khalid for their assistance during my time in graduate school.

Special thanks to Defence Research and Development Canada's CBRNE Research and Technology Initiative for their generous funding in support of this thesis.

Last, but certainly not least, I would like to thank my parents and siblings for without whose love and support, this thesis would not have been possible.

TABLE OF CONTENTS

ABSTRACT	ii
DEDICATION	iii
ACKNOWLEDGEMENTS	iv
LIST OF TABLES	viii
LIST OF FIGURES	x
LIST OF APPENDICES	xiii
LIST OF ACRONYMS	xiv
NOMENCLATURE	xv
CHAPTER 1: INTRODUCTION	1
1.1 Background	5
1.1.1 Examples of Resuspension Events	5
1.1.2 Advances in Computational Techniques for Particulate Resuspension Modelling.....	8
1.1.3 Hybrid Techniques for Modelling Phenomena in Nuclear Engineering	10
1.2 Motivation of Research	14
1.3 Objective of Research	19
1.4 Applicability of Research.....	21
CHAPTER 2: THEORETICAL BACKGROUND	25
2.1 Fluid Dynamics Theory.....	25
2.1.1 Shear Stress.....	26
2.1.2 Reynolds Number	27
2.1.3 Boundary Layer	29
2.1.4 Computational Fluid Dynamics.....	30
2.1.5 Turbulence Modelling	33
2.2 Particulate Resuspension Theory	34
2.2.1 Forces Acting on a Particulate.....	34
2.2.1.1 Removal Forces	35
2.2.1.1.1 Influence of Reynolds Number	38
2.2.1.1.2 Influence of Rock ‘n’ Roll Motion.....	42

2.2.1.1.3 Influence of Shear Stress.....	46
2.2.1.2 Adhesion Forces.....	48
2.2.1.2.1 Electrostatic Force.....	48
2.2.1.2.2 van der Waals Force.....	50
2.2.1.2.3 Capillary Force.....	51
2.2.2 Effect of Particulate Size on Resuspension.....	53
2.2.3 Time-Dependence of Particulate Resuspension.....	59
2.2.4 Parameters Affecting Particulate Resuspension.....	64
2.3 Radiation Transport Theory.....	67
2.3.1 Description of Radiation Types.....	67
2.3.2 Monte Carlo Radiation Transport.....	69
2.4 Integration of Fluid Dynamics and Monte Carlo Radiation Transport.....	71
2.5 Summary.....	73
CHAPTER 3: EXPERIMENTAL SETUP AND MODELLING METHODOLOGY.....	74
3.1 Description of the WIS Wind Tunnel.....	74
3.1.1 Physical Configuration of the WIS Wind Tunnel.....	74
3.1.2 Radionuclide Properties of Resuspension Particulate.....	80
3.2 Modelling Methodology.....	81
3.2.1 Computational Fluid Dynamics Modelling.....	83
3.2.1.1 GAMBIT Setup.....	83
3.2.1.2 FLUENT Setup.....	87
3.2.2 Black Box Data Processing.....	99
3.2.2.1 Black Box 1 Development.....	101
3.2.2.1.1 Selection of Time Steps.....	101
3.2.2.1.2 Spatial Partitioning and Particulate Airborne Activity Calculations	105
3.2.2.2 Black Box 2 Development.....	116
3.2.3 Monte Carlo Radiation Transport Modelling.....	118
3.2.4 Dose Calculations.....	124
3.2.4.1 Dose Rate Calculations.....	125
3.2.4.2 Time-Integrated Dose Calculations.....	129
3.2.4.3 Surface Activity-to-Dose Conversion Factor Calculations.....	130

3.3 Summary	133
CHAPTER 4: RESULTS AND DISCUSSION.....	135
4.1 CFD Simulation Results.....	136
4.2 Black Box Data	144
4.3 MC Radiation Transport Results.....	150
4.4 Dose Calculation Results	152
4.4.1 Assessment of Reasonableness.....	154
4.4.1.1 Submersion Dose Technique	155
4.4.1.2 Point Source Technique	162
4.4.2 Comparison of Dose Calculation Techniques	170
4.5 Summary	172
CHAPTER 5: CONCLUSIONS AND RECOMMENDATIONS.....	173
5.1 Conclusions	173
5.2 Recommendations	175
APPENDIX A: WIS WIND TUNNEL DATA	178
APPENDIX B: RADIATION DATA FOR WIS WIND TUNNEL MATERIALS.....	187
APPENDIX C: SPATIAL BOUNDS FOR WIS WIND TUNNEL PARTITIONS.....	190
APPENDIX D: CONSTRUCTION OF WIS WIND TUNNEL GEOMETRY IN MCNPX	193
APPENDIX E: DESCRIPTION OF TURBULENCE MODELS	201
APPENDIX F: DESCRIPTION OF METHODS FOR PARTICULATE TRANSPORT	204
APPENDIX G: CONVERSION OF PARTICULATE SPATIAL DISTRIBUTION TO ACTIVITY	216
APPENDIX H: DESCRIPTION OF MONTE CARLO APPROXIMATIONS TO RADIATION TRANSPORT EQUATIONS	220
APPENDIX I: VOLUMETRIC ACTIVITY AND BIAS PARTITION DATA	228
APPENDIX J: SUBMERSION DOSE AND POINT SOURCE TECHNIQUE DATA	233
APPENDIX K: COMPUTER CODES WRITTEN FOR THESIS.....	237
REFERENCES	281

LIST OF TABLES

1.1	Difference between Coupling Approaches for Reactor Safety Analysis and Radioactive Particulate Resuspension.....	13
1.2	Description of the Basic Steps of Resuspension in Urban Environments....	18
2.1	Description of the Resuspension Process for Low Reynolds Number Flow	38
2.2	Description of the Resuspension Process for High Reynolds Number Flow.....	42
2.3	Description of the Influence of Shear Stress on Particulate Resuspension...	47
2.4	Description of the Formation of the Electrostatic Force.....	49
2.5	Description of the Formation of the van der Waals Force.....	50
2.6	Description of the Formation of the Capillary Force.....	52
2.7	Effect of Particulate Size on Its Resuspension Potential.....	56
2.8	Relationship between Particulate Diameter and Particulate Motion.....	58
2.9	Relationship between the Amount of Resuspension and the Transient Nature of the Fan Air Intake Velocity.....	61
2.10	Description of Parameters Directly Affecting Particulate Resuspension....	65
2.11	Attributes of Different Radiation Types.....	68
2.12	Description of the Basic Steps of a MC Radiation Transport Simulation....	69
2.13	Basic Steps of the CFD-MC Radiation Transport Coupling Procedure.....	72
3.1	Description of the Materials Used in the WIS Wind Tunnel.....	80
3.2	Identification of Codes Selected.....	81
3.3	Boundary Types Employed in the GAMBIT Model.....	86
3.4	Description of Boundary Conditions Employed by the Wind Tunnel Geometry in GAMBIT.....	88
3.5	Description of Input Required to Characterize the Flow Conditions.....	89
3.6	Inputs Required by Particulate Trajectory-based Time Step Calculations...	94
3.7	Description of Rakes Employed for Particulate Injections.....	97
3.8	Description of MATLAB Codes Created for Black Box Development.....	100
3.9	Properties of Spatial Partitions.....	111
3.10	Description of Particulate Spatial Distribution to Airborne Particulate	

Activity Conversion Algorithm	111
3.11 Regions to Be Defined in MCNPX.....	120
3.12 Description of Data Card Contents in MCNPX Input File.....	121
3.13 Internal Dose Rate Equations.....	125
3.14 Internal Dose Rate Calculation Assumptions.....	125
3.15 External Dose Rate Equations.....	127
4.1 Time Step Iterations Where the Radiation Field is Characterized.....	144
4.2 Particulate Accounting Data for Each Time Step Iteration.....	145
4.3 Normalized External Dose Rate Data for Detector Location 1.....	150
4.4 Normalized External Dose Rate Data for Detector Location 2.....	151
4.5 Total Internal and External Dose Delivered at Each Detector Location.....	153
4.6 Internal and External Dose Conversion Factors at Each Detector Location..	153
4.7 Submersion Dose Rate Equations.....	159
4.8 Normalized Submersion Dose Rate Data.....	161
4.9 Time-Integrated Submersion Dose Data.....	161
4.10 Point Source to Detector Distance Equations.....	165
4.11 Point Source Dose Rate Equations.....	167
4.12 Time-Integrated Point Source Dose Data.....	169
4.13 Time-Integrated Point Source Dose Data (Scaled Up to the Number of Spatial Partitions).....	169

LIST OF FIGURES

1.1	Description of Parameters Directly Affecting the Radiological Impact of a Resuspension Event.....	3
1.2	Impact of Urban Topographies on Radioactive Particulate Resuspension	18
1.3	Illustration of the Research Blueprint.....	20
2.1	Illustration of Boundary Layer Location and Variation of Fluid Velocity Within this Region.....	29
2.2	Finite Control Volume.....	31
2.3	Description of the Forces Acting on a Particulate.....	34
2.4	Illustration of Boundary Layer Vortex.....	36
2.5	Effect of Low Reynolds Number Flow on Particulate Resuspension.....	40
2.6	Effect of High Reynolds Number Flow on Particulate Resuspension.....	41
2.7	Rock ‘n’ Roll Motion of a Particulate Exposed to Boundary Layer Flow	43
2.8	Effect of Shear Stress on Particulate Motion in the Boundary Layer.....	46
2.9	Formation of the Electrostatic Force.....	49
2.10	Formation of the van der Waals Force.....	50
2.11	Formation of the Capillary Force.....	52
2.12	Effect of Particulate Size on Resuspension.....	55
2.13	Qualitative Description of the Variation of the Cumulative Fraction of Particulates Resuspended with Time.....	60
2.14	Parameters Affecting Particulate Resuspension.....	64
2.15	Illustration of the Basic Steps of a MC Radiation Transport Simulation	69
2.16	Description of CFD-MC Radiation Transport Coupling.....	72
3.1	Exterior View of WIS Wind Tunnel.....	75
3.2	Interior View of WIS Wind Tunnel (Downstream View).....	76
3.3	Interior View of WIS Wind Tunnel (Downstream View Without Bluff Body).....	78
3.4	Three-Dimensional Rendering of the WIS Wind Tunnel.....	79
3.5	Decay Chain for Lanthanum-140.....	80
3.6	Three-Dimensional View of Wind Tunnel Geometry in GAMBIT.....	84

3.7	Two-Dimensional View of Wind Tunnel Geometry in GAMBIT (Looking Downstream from Inlet).....	85
3.8	View of Full Wind Tunnel Geometry in FLUENT.....	88
3.9	Screenshot of Particulate Data File Exported by FLUENT.....	99
3.10	Identification of Wind Tunnel Region to be Partitioned.....	106
3.11	Partitioning of Wind Tunnel Geometry.....	108
3.12a	Spatial Partitions about the Symmetry Plane.....	109
3.12b	Spatial Partitions to the Left of the Plate and Bluff Body.....	109
3.12c	Spatial Partitions to the Right of the Plate and Bluff Body.....	110
3.13	Hypothetical Dose Rate Distribution Over Time.....	129
3.14	High-Level Overview of the CFD-MC Radiation Transport Coupling Methodology.....	134
4.1	Plot of Flow Quantity Scaled Residuals Versus Elapsed Number of Iterations.....	137
4.2	Total Pressure Distribution along the +x/-z Plane.....	138
4.3	Vortices Present Behind the Bluff Body along the +x/-z Plane.....	139
4.4	Total Pressure Distribution along the +y/-z Plane.....	139
4.5	Vortices Present Atop the Bluff Body along the +y/-z Plane.....	140
4.6	Vortices Present Behind the Bluff Body along the +y/-z Plane.....	140
4.7	Illustration of Particulates' Trajectories in the Wind Tunnel Domain.....	142
4.8	Comparison of Velocity Probe Data with FLUENT Calculations.....	143
4.9	Temporal Variation of Volumetric Activity for Partitions Centred About the Symmetry Plane	147
4.10	Temporal Variation of Volumetric Activity for Partitions to the Left of the Plate and Bluff Body.....	147
4.11	Temporal Variation of Volumetric Activity for Partitions to the Right of the Plate and Bluff Body.....	148
4.12	Depiction of Single Radiation Source.....	156
4.13	Illustration of Source Locations.....	157
4.14	Illustration of a Point Source.....	162
4.15	Hypothetical Configuration of the Single Representative Partition at the	

i^{th} Time Step Iteration.....	167
--	-----

LIST OF APPENDICES

A	WIS WIND TUNNEL DATA.....	178
B	RADIATION DATA FOR WIS WIND TUNNEL MATERIALS.....	187
C	SPATIAL BOUNDS FOR WIS WIND TUNNEL PARTITIONS.....	190
D	CONSTRUCTION OF WIS WIND TUNNEL GEOMETRY IN MCNPX.....	193
E	DESCRIPTION OF TURBULENCE MODELS.....	201
F	DESCRIPTION OF METHODS FOR PARTICULATE TRANSPORT....	204
G	CONVERSION OF PARTICULATE SPATIAL DISTRIBUTION TO ACTIVITY.....	216
H	DESCRIPTION OF MONTE CARLO APPROXIMATIONS TO RADIATION TRANSPORT EQUATIONS.....	220
I	VOLUMETRIC ACTIVITY AND BIAS PARTITION DATA.....	228
J	SUBMERSION DOSE AND POINT SOURCE TECHNIQUE DATA.....	233
K	COMPUTER CODES WRITTEN FOR THESIS.....	237

LIST OF ACRONYMS

MATLAB	MATrix LABoratory
RDD	Radiological Dispersal Device
CFD	Computational Fluid Dynamics
MC	Monte Carlo
CBRN	Chemical, Biological, Radiological, Nuclear

NOMENCLATURE

Computational Fluid Dynamics Quantities	
τ	Shear stress in the boundary layer, Pa
μ	Dynamic viscosity of fluid, Pa·s
ρ	Density of fluid, kg·m ⁻³
u	Fluid velocity, m·s ⁻¹
$u_{\text{flow stream}}$	Velocity of main flow stream, m·s ⁻¹
$\frac{\partial u}{\partial y}$	“Strain Rate”/velocity gradient in the boundary layer, s ⁻¹
Re	Reynolds Number
L	Characteristic length of fluid domain feature, m
ξ	Flow conservation variable
Γ_p	Moment of particulate about asperity P, N·m
r	Radius of particulate, m
a	Distance between asperities P and Q, m
F_D	Drag force, N
F_L	Lift force, N
Δt	Time step for particulate transport, s
Length	Length scale for particulate transport, m
u_p	Particulate velocity, m·s ⁻¹
i	Time step iteration for particulate transport
t_{elapsed}	Elapsed time for which a particulate is transported in wind tunnel, s
\bar{t}_{elapsed}	Average elapsed time for which particulates in the wind tunnel are being transported, s, hrs
k	Turbulent kinetic energy, m ² ·s ⁻²
ε	Turbulent dissipation rate, m ² ·s ⁻³

		Radiation Transport Quantities	
ω	Specific dissipation rate, s^{-1}		
β^{-}	Beta radiation		
γ	Gamma radiation		
λ	Decay constant of radioisotope, s^{-1}		
A	Activity of radioisotope, Bq		
ϕ_R	Flux of radioactive particles of type R, particles·cm ⁻² ·s ⁻¹		
$T_{\frac{1}{2}}(^{140}\text{La})$	Half-life of Lanthanum-140, hrs	40.22	[36]
N_A	Avogadro's Constant, nuclei·mol ⁻¹	6.02×10^{23}	
$\rho_{^{140}\text{La}}$	Density of Lanthanum-140, g·cm ⁻³	6.19	[47]
$M_M^{^{140}\text{La}}$	Molar mass of Lanthanum-140, g·mol ⁻¹	138.91	[36]
D	Diameter of particulate, cm		
\forall	Volume of spatial partition, m ³		
A_{\forall}	Volumetric activity in spatial partition, Bq·m ⁻³		
Bias	Bias of an active partition		
$\dot{D}_{\text{internal},1}$	Internal dose rate at detector 1, Sv·hr ⁻¹		
$\dot{D}_{\text{internal},2}$	Internal dose rate at detector 2, Sv·hr ⁻¹		
$\dot{D}_{\text{external},1}$	External dose rate at detector 1, Sv·hr ⁻¹		
$\dot{D}_{\text{external},2}$	External dose rate at detector 2, Sv·hr ⁻¹		
$\dot{D}_{\text{submersion},1}$	Submersion dose rate at the detector 1, Sv·hr ⁻¹		
$\dot{D}_{\text{submersion},2}$	Submersion dose rate at the detector 2, Sv·hr ⁻¹		
$\dot{D}_{\gamma,1}$	Point source dose rate at detector 1, Sv·s ⁻¹		

$\dot{D}_{\gamma,2}$	Point source dose rate at detector 2, $\text{Sv}\cdot\text{s}^{-1}$		
BR	Breathing rate, $\text{m}^3\cdot\text{hr}^{-1}$	1.2	[34]
DCF	Dose conversion factor, $\text{Sv}\cdot\text{Bq}^{-1}$	1.10×10^{-9}	[44]
$DF_{\text{MCNPX},1}$	MCNPX normalized external dose rate at detector 1, $\text{Sv}\cdot\text{hr}^{-1}\cdot\gamma_{\text{S}}^{-1}$		
$DF_{\text{MCNPX},2}$	MCNPX normalized external dose rate at detector 2, $\text{Sv}\cdot\text{hr}^{-1}\cdot\gamma_{\text{S}}^{-1}$		
$Y_{^{140}\text{La}}$	Gamma Yield for Lanthanum-140	2.17	[36]
η	Surface activity-to-dose conversion factor, $\text{Sv}\cdot\text{Bq}^{-1}\cdot\text{m}^2$		
$A_{\text{S}}^{\text{plate}}$	Plate surface activity, $\text{Bq}\cdot\text{m}^{-2}$		
\bar{A}_{V}	Spatially averaged volumetric activity, $\text{Bq}\cdot\text{m}^{-3}$		
$K(t)$	Resuspension factor at time t, m^{-1}		
\bar{V}	Volume of point source, m^3		
\bar{d}_1	Distance between detector 1 and point source, cm		
\bar{d}_2	Distance between detector 2 and point source, cm		
CF	Flux-to-dose rate conversion factor, $\text{Sv}\cdot\text{cm}^2\cdot\gamma^{-1}$	5.20×10^{-12}	[46]

Independent Quantities		
------------------------	--	--

g	Acceleration due to gravity, $\text{m}\cdot\text{s}^{-2}$	-9.81
t	Time, s, hrs	

CHAPTER 1

INTRODUCTION

A Chemical, Biological, Radiological, Nuclear (CBRN) event will cause hazardous particulates to be released and eventually settle to the ground. First responders or military forces will be required to operate on or in the vicinity of the contaminated area. As such, the movement of personnel and vehicles and/or the presence of wind in the contaminated zone can transport these hazardous particulates from the ground and into the breathing space (this phenomenon is termed *resuspension*). These particulates, if radioactive, can deliver a significant dose commitment to those present in and around the contamination premises.

Presently, there is a lack of quantitative understanding of resuspension that can support risk assessments made by military field commanders. Thus, an international collaboration, led by Canada with participation from Germany and the UK, has been initiated to develop experimental and theoretical expertise to assist decision makers during a radiological dispersal device (RDD) event [1]. This collaboration consists of researchers performing experimental and modelling studies on resuspension. The purpose of the former is to conduct resuspension experiments in laboratory and field environments such that measured data can be made readily available. The purpose of the modelling studies are to (a) provide an alternative to expensive and time consuming field-scale experiments, (b) examine the dependence of resuspension on a single parameter while holding all others constant, and (c) validating with experimental results. The mandate of this thesis serves to further the modelling capabilities of this international collaboration.

Particulates can incorporate chemical and/or biological agents; however radioactive particulate is of interest to this work. With this being said, it is important that the following distinction be made:

The term *particulate* refers to the small, solid pieces of matter that are released from an RDD and a collection of particulate (i.e., the pluralized form of particulate) is termed particulates. These particulates which are composed of radioactive material emit *radioactive particles*. Thus, in this thesis, the term *particulate/particulates* refer to the solid pieces of matter released from an RDD while *radioactive particles* refer to the radiation emitted from a particulate.

The analysis of particulate resuspension is an important field of research in the nuclear industry. Of primary concern are the potential radiation doses one can receive from the inhalation of resuspended radioactive material and the external doses from re-deposited fields or cloud submersion. Two of the foremost scenarios that are considered when investigating particulate resuspension in nuclear environments are:

- (1) *The hazardous release of radioactive material from an RDD in urban, densely populated areas.* Shortly after the detonation of the RDD, the radioactive material, in the form of particulate, will settle on the ground only to be later resuspended by external forces¹⁾.
- (2) *Release of radioactive material (particularly fission products) from a nuclear reactor after a severe accident* whereby deposited material can be resuspended thereby increasing the eventual release of radioactive material into the environment.

Regardless of the scenario considered, the literature review performed by Nicholson [2] found that the inhalation of resuspended particulates in the first few weeks following a contamination event is as important as inhalation immediately following the event.

¹⁾ The term *external forces*, also referred to as *resuspension agents*, constitute forces produced by disturbances such as wind, vehicle movement, human activities such as walking and running, amongst others.

When modelling a resuspension scenario, the ultimate aim is to assess the radiological impact. To achieve this aim, the following must be obtained:

- (1) the particulate spatial distribution (i.e. the locations in space where the particulates have been displaced to), and
- (2) conversion of the particulate spatial distribution to a radiation dose

In order to develop this model, several parameters must be modelled and are outlined in Figure 1.1.

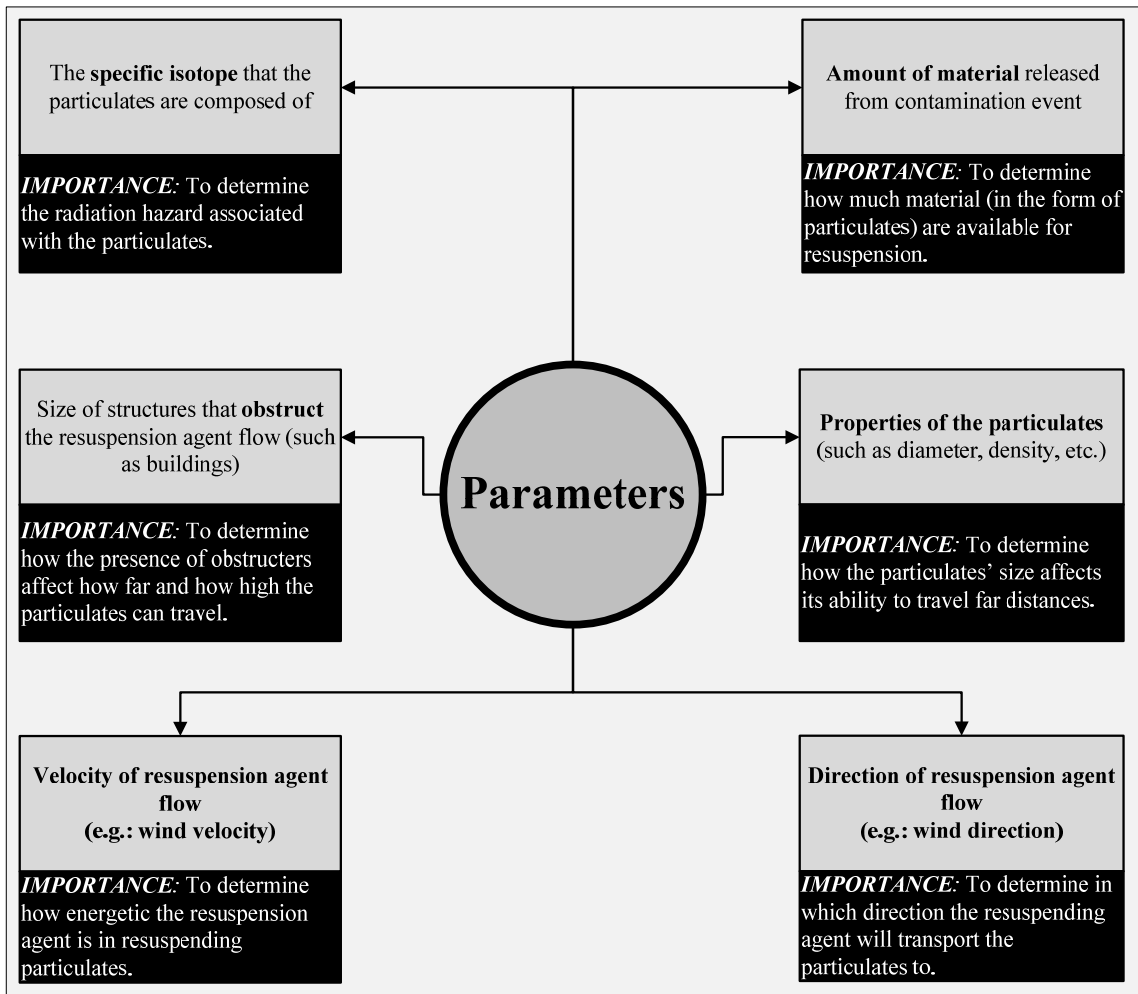


Figure 1.1 – Description of Parameters Directly Affecting the Radiological Impact of a Resuspension Event [3]

It is evident from Figure 1.1 that a multi-disciplinary/hybrid approach should be taken in order to achieve the above stated aim, which will involve the following fields of study:

(1) *Computational Fluid Dynamics (CFD)*

The international collaboration described at the beginning of this chapter has chosen CFD to model both the fluid flow and the displacement (i.e. resuspension) of particulates via the fluid flow in complex scenarios and geometries.

(2) *Radiation Transport*

Radiation transport techniques are required to convert the particulate spatial distribution produced by the CFD calculations to radiation dose.

The objective of this thesis is the development of a methodology to couple the above two disciplines in order to assess the radiological hazard from a resuspension event and the use of CFD and radiation transport techniques in concert to achieve this objective are further discussed in Section 1.3.

In order to place the use of CFD and radiation transport techniques to assess the radiological hazard from a resuspension event into context, a review of the research conducted in the following categories is provided:

- (a) examples of resuspension events
- (b) the use of CFD calculations to model particulate resuspension, and
- (c) hybrid techniques used to model phenomena in nuclear engineering

The results of this review are discussed in the following section.

1.1 Background

A review of the literature pertinent to the abovementioned categories has yielded no evidence that CFD has been used in conjunction with radiation transport techniques to analyze radioactive particulate resuspension. However, the literature review, as documented below, has allowed for (a) an understanding of how the research conducted for this thesis relates to modern computational research performed for radioactive particulate resuspension and (b) the review of literature that have a direct impact on the CFD model developed in Section 3.2.1.

The results of the literature review in each of the abovementioned categories will be discussed in their respective sub-sections.

1.1.1 Examples of Resuspension Events

The purpose of this section is to illustrate the importance of the resuspension of radioactive particulates. The research examined focussed on the resuspension of radioactive particulates – particulates which were formed from man-made sources, particularly those from nuclear weapons fallout and contamination events such as the Chernobyl accident. The summaries below describe resuspension studies conducted at contaminated sites:

- Shinn, Homan et al. [4] examined the resuspension of alpha-emitting plutonium aerosols at the Nevada Test Site. Resuspension studies were conducted at four locations on the site, namely at *Area 5* (non-nuclear tests here distributed plutonium oxide particulates), *Area 11* (better known as Plutonium Valley; non-nuclear tests conducted here), *Area 19* (site of Little Feller 2 nuclear test), and *Area 20* (site of Palanquin nuclear test). It was found that Areas 5 and 11 (non-nuclear test sites) had higher plutonium aerosol concentrations than those at Areas 19 and 20 (nuclear test sites) where the plutonium contamination were enclosed in small amorphous glass beads, rendering most of them un-resuspendable. As such,

it was found that the non-nuclear test sites had higher resuspension factors²⁾ and airborne plutonium activity³⁾ than those of the nuclear test sites. The effects of disturbances, both natural and man-made, on the resuspension were also noted at the respective locations. The most important finding is the effect of seasonal variation on plutonium aerosol resuspension. Here, it was found that the maximum plutonium specific activity⁴⁾ occurred during the months of March and April. This was attributed to the fact that the onset of above-freezing temperatures begins during this time of year. However, at Area 20, it was found that the specific activity remained constant throughout the year. Moreover, the effect of wildfires and raking activities at Areas 20 and 19, respectively, was examined and it was found that these disturbances drastically increased both the plutonium airborne activity and specific activity.

- Shinn [5] studied the resuspension of plutonium aerosols at the Maralinga cleanup site in South Australia. Being a former nuclear test site, a soil cleanup initiative began in October 1996 to eliminate the potential for public exposure to the residual plutonium. To quantify the effect of the cleanup, resuspension measurements were made, namely those of resuspension factor and plutonium airborne concentration. Once the soil surfaces had been cleaned and subjected to a few years of natural weathering, it was found that the plutonium airborne concentrations were noticeably reduced with respect to measurements made immediately after the cleanup. Based on plutonium airborne concentrations at a particular vicinity on the site, it is anticipated that the overall site concentration will become equivalent to the cited global background of 0.1 $\mu\text{Bq}/\text{m}^3$.

²⁾ The *resuspension factor* is defined as the airborne particulate concentration (in $\mu\text{g}/\text{m}^3$ or Bq/m^3) divided by the ground/surface particulate concentration (in $\mu\text{g}/\text{m}^2$ or Bq/m^2) prior to the introduction of a resuspension agent [3].

³⁾ The *airborne plutonium activity* is the total activity of the plutonium aerosols contained in a volume of air divided by the volume of air sampled.

⁴⁾ The *plutonium specific activity* is the total activity of the plutonium aerosols sampled divided by the cumulative mass of the plutonium aerosols sampled.

- Langer [6] examined the resuspension of soil particulates from soil contaminated with plutonium in an area known as the “903 Field” in Colorado, USA. The field was adjacent to a former outdoor drum storage area. These drums contained waste oil, consisting of plutonium, from machining operations and the contamination of the 903 Field is attributed to leakage from these drums. The effect of surface type on the resuspension of plutonium aerosols were investigated and it was found that resuspension over soil surfaces were less effective than resuspension over grass surfaces. Moreover, to assess the radiological hazard from the contaminated field, measurements were made on and in the vicinity of the field. It was stated that the airborne plutonium concentration did not exceed the cited United States Department of Energy (USDOE) limit of 20 fCi/m³ ⁵⁾.
- Wagenpfeil et al. [7] studied the resuspension of coarse particulates (i.e. particulate whose aerodynamic diameters⁶⁾ are greater than 10 µm) in the Chernobyl region, composed of the beta and gamma-emitting Cesium-137 radionuclide. Resuspension was studied from wind flow and agricultural activities and it was found that the resuspension factor measured from agricultural activities was 1000 times greater than that due to wind flow. Notably, during the wind-driven resuspension activities, it was found that at higher wind speeds, more coarse particulates were resuspended and transported to higher elevations. Moreover, the analysis of the data acquired from the agricultural activities allowed the authors to examine the dependence of activity on particulate size and it was found that the highest activity occurred for coarse particulates.

The research described above exemplifies the complex nature of resuspension as shown by the effect that natural and human activities, surface type, and particulate size have on the amount of resuspension that occurs and the resultant radiation dose.

⁵⁾ 1 f = 10⁻¹⁵

⁶⁾ For an irregularly shaped particulate, its actual geometric diameter is difficult to measure. With the use of a shape factor, an *aerodynamic diameter* is calculated instead. The movement of this irregularly shaped particulate is then modelled as a sphere with a unit density and whose geometric diameter is equal to the aerodynamic diameter [8].

However, the measurement of resuspension-related quantities such as those of resuspension factor, airborne activity, and specific activity provide an avenue by which the scale of contamination and the effectiveness of cleanup initiatives (such as those outlined by Shinn [5]) can be quantified. Moreover, these quantities are also used to determine whether the contamination possesses radiation levels that are above the limits set out by the nuclear regulatory body of the host country (for example, see Langer [6]). As stated previously, the dose delivered by the resuspended radioactive particulates are of interest and the measurements of resuspension-related quantities (such as those just described) are pivotal in performing a dose estimate.

Of course, the research outlined in this section is based on experimental work. Experimentation affords the researcher an opportunity to not only characterize the radiological hazard posed by a contaminated site, but also to explore the fundamental processes governing the resuspension of particulates. However, modelling/computational techniques allow for an understanding of how specific parameters impact particulate resuspension. The research summarized in the following sub-section document the advances made in computational techniques used to model particulate resuspension.

1.1.2 Advances in Computational Techniques for Particulate Resuspension Modelling

With the advent of ever increasing computing power, CFD calculations employing advanced numerical algorithms have been applied to model the flow in large and complex geometries. Of particular interest to this thesis is the modelling of flow and particulate resuspension in the vicinity of flow obstructers. An example of flow obstructers⁷⁾ are buildings and thus, CFD can be used to analyze the fluid flow and particulate resuspension in urban geometries. However, CFD codes cannot simulate the radioactive properties of the particulates and hence, cannot predict the radiation field produced from the resuspension. Herein demonstrates the need to couple CFD and radiation transport techniques.

⁷⁾ *Flow obstructers* are also termed *bluff bodies*.

The summaries below describe research pertinent to the abovementioned advances in particulate resuspension modelling:

- Nigro et al. [9] and Krajnović et al. [10] modelled the flow over and around a cube with a Reynolds Number of 40,000. Using the Large Eddy Simulation (LES) turbulence model, flow structures in the vicinity of the cube have been revealed. On a general basis, the flow structures described in [9] and [10] are in agreement with both each other and the cited experimental results. The most important flow structures revealed are those directly behind the cube (note that the flow has been modelled to approach the front of the cube). Here, twin vortices circulating in opposite directions, are present. As will be shown in Section 4.1, these vortices will play a pivotal role in the resuspension and deposition of particulates.
- Harwell [11] conducted a CFD simulation in support of resuspension trials conducted inside a resuspension wind tunnel. The wind tunnel consisted of a plate that held the radioactive particulates and fans (for injecting air into the wind tunnel) located nearby the plate. The intent of the CFD simulation was to find the spatial location where particulates were resuspended to. The importance of this work lay in the boundary conditions used, and its applicability to the work performed in this thesis will be discussed further in Section 3.2.1.
- Hill, Flemming et al. [12] also conducted CFD simulations in support of evaluating the extent to which military vehicles are contaminated when responding to a CBRN event. The CFD simulation consisted of the following steps: (1) calculate the flow field around the military vehicle, (b) place particulates on points around the wheel, and (C) observe the displacement of particulates from the calculated flow field. The CFD results, in the form of particulate deposition on the surface of the wheel, were compared to experimental data and the comparison showed that the CFD simulation produced results reasonably close to the experimental results. However, Hill, Flemming et al. [12]

state that on a general basis where experimental data is not available, validating the results of the CFD simulation can be problematic.

Based on the research outlined above, it is clear that steps have been taken to employ CFD as a tool to model the resuspension of particulates. However, the need to couple CFD with radiation transport techniques to assess the radiological hazard from a resuspension event must be fulfilled. Recently, the coupling of disparate disciplines has emerged as an approach to formulate solutions to problems pertinent to nuclear engineering. Such approaches are documented in the following sub-section.

1.1.3 Hybrid Techniques for Modelling Phenomena in Nuclear Engineering

The presence of physics codes to model phenomena in diverse fields such as heat transfer, structural mechanics, chemical engineering, and radiation transport has provided the framework by which different disciplines can overlap and exchange information with each other. The coupling of disciplines has gained prominence in many fields, particularly the nuclear engineering field. This field is of particular interest since the integration of different disciplines is required to perform key analysis of nuclear systems. For example, a safety analysis of a nuclear reactor will require calculations in the fields of nuclear reactor physics, thermodynamics, fluid dynamics, and heat transfer, just to name a few.

Luxat [13] provided a comprehensive overview on the need for and challenges of coupling physics-based software for analyses pertinent to the nuclear industry. Here, it is stated that to model complex realistic problems, programming scripts such as MATLAB (MATrix LABoratory) have to be employed to act as an interface between the codes. Anticipating that the coupling of physics codes represent the direction in which nuclear engineering-based simulations are heading, Luxat continues to state that coupling nuclear reactor physics and thermalhydraulics calculations have been undertaken. Notably, Luxat [13] maintains that the results produced by coupled models cannot be easily verified and

that such results cannot be directly compared to physical measurements – rather, the acceptance of the results are based on its “reasonableness”.

Examples of the coupling of codes performed for nuclear reactor safety analysis are outlined below:

- Fehri et al. [14] described how the thermalhydraulics code ARTHUR (Advanced Routines of Thermal-Hydraulics for Unsteady-states Reactors) and the reactor physics code DONJON-3 have been coupled for the purposes of nuclear reactor safety analysis. To perform the coupling, the reactor power distribution is calculated from DONJON-3 which then serves as input into ARTHUR. ARTHUR then calculates, among others, fuel temperature, coolant density, and coolant temperature.
- Szymandera et al. [15] described the development and use of the PhysicsShell software. PhysicsShell is a software tool that provides a generic framework that couples physics codes used for nuclear reactor safety analyses. The algorithm used by PhysicsShell commences with the user input. Here, the user defines the codes that are to be coupled, the initial values of variables pertinent to the first code in the coupling sequence, and the variables that are to be updated (if a time-dependent or iterative calculation is performed). An input file is then created for the second code in the coupling sequence and this code is then executed. This process is repeated, provided that a time-dependent or iterative calculation is performed, for the number of time steps/iterations requested.
- Popescu et al. [16] described the coupling of the thermalhydraulic code TUF and ELOCA (which models the response of CANDU nuclear fuel under specified flow conditions). The purpose of this coupling is to ensure proper feedback between flow conditions and the resultant fuel response. The TUF code, which is the first code in the coupling sequence, passes coolant conditions (such as average

coolant temperature and coolant pressure) to ELOCA which then calculates the fuel temperature and heat transfer rates from the fuel to the coolant.

- Hu et al. [17] identified the use of CFD in conjunction with Monte Carlo radiation transport methods as increasingly attractive tools for nuclear reactor modelling. Upon identifying FLUENT to perform thermalhydraulics calculations and MCNP to perform reactor physics calculations, a unit reactor core cell consisting of a single nuclear fuel rod surrounded by coolant has been modelled in order to illustrate how the coupling between these codes is performed. To initiate the coupling, an MCNP simulation was performed whereby the reactor power density distribution is obtained and then exported to FLUENT which uses this distribution as a heat source. FLUENT uses this heat source to calculate heat transfer and fluid transport within the cell and then the resultant cell temperature and density are used to update the neutron cross sections in the cross section generation code NJOY. Another MCNP run then commences with the updated cross section and density and the resultant reactor power density distribution is then exported to FLUENT as a heat source. This process is then repeated until the results are converged. Hu et al. [17] note that the results are in agreement with “intuitive expectations”.
- Seker et al. [18] performed a similar coupling exercise as that outlined in [17]; however, STAR-CD has been used for the thermalhydraulic calculations. To illustrate how the coupling between STAR-CD and MCNP is done, a 3x3 PWR (Pressurized Water Reactor) cell was modelled. The coupling between these codes is facilitated by the McSTAR computer program which is written in the FORTRAN90 programming language. The basic methodology for the coupling is identical to that employed in [17]. To assess the quality of the results produced by the coupling between STAR-CD and MCNP, STAR-CD has also been coupled with the deterministic radiation transport code DeCART. When comparing the results produced by the two coupled systems, namely comparing temperature and

power density, it was found that the two systems produced highly comparable results.

In light of the issues raised by Hill, Flemming et al. [12] in regards to validating the results of CFD calculations, Luxat [13] remedies this concern by recommending that results produced by a coupled approach be judged on its “reasonableness”. This approach has been exercised by Hu et al. [17] and thus provides an important guideline to follow when assessing the results produced by the coupling methodology developed for this thesis.

The summary of the research described in this sub-section has revealed that CFD and radiation transport techniques have been used in concert to perform nuclear reactor safety analysis. The key differences, however, between the coupling approaches used for nuclear reactor safety analysis and radioactive particulate resuspension are outlined in Table 1.1.

Coupling Purpose Coupling Attribute	Reactor Safety Analysis	Radioactive Particulate Resuspension
Front End of Coupling Sequence	Radiation transport calculations	CFD calculations
Parameter used for Coupling	Reactor Power/Temperature/ Density	Airborne particulate activity
Coupling Type	Cyclical; information exchanged between codes until results converge	Sequential (see Figure 1.3 for more details)

Table 1.1 – Difference between Coupling Approaches for Reactor Safety Analysis and Radioactive Particulate Resuspension

Thus, the contents of Table 1.1 re-affirm the fact that the coupling performed for radioactive particulate resuspension studies is unique and has not been addressed by the hybrid studies outlined above.

There do exist, however, computer codes that assess the radiological impact on humans and the environment from a contamination event. Despite the presence of these codes, they possess a number of limitations which hamper their ability to perform realistic resuspension calculations and produce reliable dose estimates. These codes are discussed in the next section and as will be shown, the lack of hybrid techniques and computer codes to quantify the radiological impact of a resuspension event identifies a technology gap that will be addressed by the methodology developed in this thesis to couple CFD and radiation transport techniques.

1.2 Motivation of Research

Presently, there are no simulation systems that can couple radioactive particulate resuspension and subsequent radiation field determination. Instead, the current state-of-the-art is to [19]:

- (1) Conduct an analysis of the flow of particulates in order to determine the extent of the transport and deposition of radioactive material, and
- (2) Perform a separate and independent assessment of the radiation field

Thus, the current practice does not use the results of the particulate flow calculation to predict the corresponding radiation field and hence there exists a total disconnect between these two calculations.

There are presently a few computer codes that are capable of providing results that link aerosol transport with radiation field determination. The names and a brief description of these codes are outlined below:

- *Hazard Predication and Assessment Capability (HPAC)*
This code allows the user to define terrain, atmospheric, and release conditions and provides the user with radiation field data [20].
- *Consequent Assessment Tool Set (CATS)*
CATS performs similar functions as HPAC but can also be used to analyze a greater set of population threats, such as natural disasters [21].
- *HOTSPOT*
HOTSPOT is used exclusively for radiological releases but is unable to incorporate intricate modelling features such as complex terrains [22].

There are a number of limitations to the above codes, the foremost of which is that they use a Gaussian plume model for particulate transport. Examples of problems associated with the use of the Gaussian plume model are as follows:

- Details of terrain are incorporated into the model by making elementary surface roughness modifications to the Gaussian plume model. As a result, intricate model details that are pertinent for advanced analysis are absent from the abovementioned codes.
- A Gaussian distribution is used to govern the movement of particulate. As such, a more realistic approach to modelling particulate transport (such as a *force-balance*⁸⁾ approach) is absent from the Gaussian plume model. Appendix F will compare and contrast the use of Gaussian plume modelling and the force-balance approach for particulate tracking.

⁸⁾ The *force-balance* approach balances the different forces acting on a particulate, in order to determine the movement of the particulate when subjected to these forces. Examples of such forces are gravity, adhesion, and fluid forces, amongst others.

Further to the codes described above, there are additional codes that have been employed extensively for the purposes of nuclear reactor safety analyses and a brief description of these codes are provided below:

- *GOTHIC*
GOTHIC models thermal-hydraulic phenomena in nuclear power plant containment and other confinement buildings, particularly under nuclear plant accident scenarios. This code also tracks the movement of radioactive particulates that are released from the accident scenarios under investigation [23].
- *PEAR*
PEAR computes the radiation dose that members of the public receive, particularly under nuclear plant accident scenarios, from the atmospheric release of radioactive material. This code performs such calculations by prompting the user to specify multiple inputs to characterize the scenario under investigation, such as the height and spatial location at which radioactive material is released to the environment and the weather conditions [24].

The primary limitation with the GOTHIC and PEAR nuclear codes, in terms of their employment for use in analyzing the resuspension of radioactive particulates and subsequent radiation field determination, is that they are primarily used for calculating the radiation dose members of the public receive from nuclear plant accidents. Unlike the resuspension scenario whereby radioactive particulates settle to the ground only to be later resuspended by a resuspension agent, the radioactive particulates examined in GOTHIC and PEAR emanate from elevated structures such as cooling towers and chimneys. However, the use of Computational Fluid Dynamics provides a greater amount of flexibility in defining the spatial locations at which radioactive particulates can emanate from, which affords the modeller to fully characterize the resuspension scenario just described, unlike the GOTHIC and PEAR codes for the reasons just discussed.

Despite the fact that CFD codes are capable of modelling extremely detailed physical and geometric properties, there is presently no generic code available that can perform radioactive particulate transport in conjunction with radiation field modelling. It is clearly evident that there is a research need to couple CFD with radiation transport techniques for the aforesaid purpose. The respective roles of these computational tools in developing a coupling methodology are described below:

- The *CFD simulation*, with the aid of particulate injections, will displace particulates initially at rest in the flow domain via fluid flow (such as air flow). Therefore, a particulate spatial distribution will be attained and will be used by the radiation transport calculations.
- For the given particulate spatial distribution, the *MC radiation transport simulation* will characterize the resultant radiation field by calculating various radiation-related quantities such as radiation flux and radiation dose, amongst others.

The modelling flexibilities offered by the abovementioned computational tools will allow for the analysis of radioactive particulate resuspension and resultant radiation field determination in geometries that emulate urban topographies. Such geometries contain bluff bodies (an example of bluff bodies are houses, buildings, etc.) and are of practical importance to the analysis of the radiological impact of a RDD event, the reasons for which are outlined in Figure 1.2.

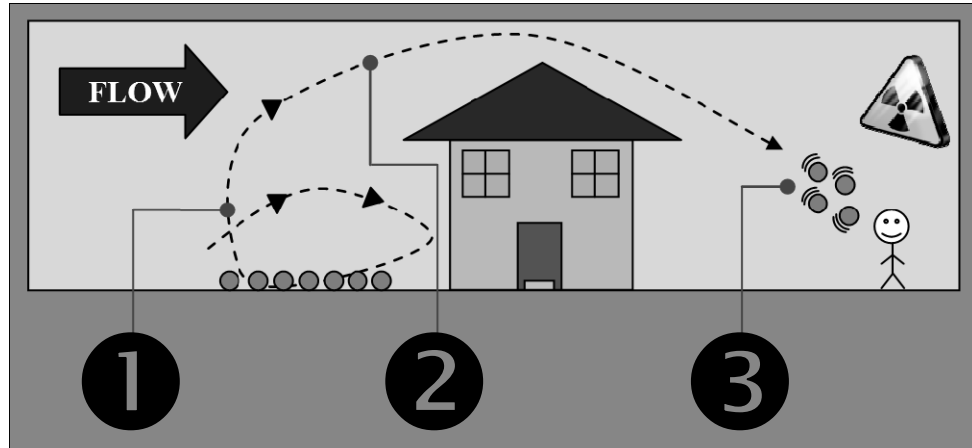


Figure 1.2 – Impact of Urban Topographies on Radioactive Particulate Resuspension

As shown in Figure 1.2, when released radioactive material (such as those from a RDD event) in the form of particulate settle in front of bluff bodies (such as the house shown) it can be resuspended by a resuspension agent (such as wind). This figure also illustrates the basic steps in the resuspension process, described in Table 1.2.

Step	Description
1	A resuspension agent, such as wind, has its flow obstructed by the presence of the house. The interaction of the flow stream with the house produces a vortex (also called a <i>flow structure</i>).
2	The vortex can, depending upon how energetic it is, penetrate the boundary layer and resuspend the resident particulates. These resuspended particulates can acquire a significant vertical trajectory, enabling them to be resuspended over the house.
3	The resuspended particulates enter into the breathing space. This can cause humans, who are in the vicinity of the resuspended particulates, to not only be <i>externally</i> exposed, but also <i>internally</i> exposed to the radioactive particulates via the inhalation of the particulates. Thus, the resuspended radioactive particulate can deliver both an internal and external radiation dose.

Consequently, in urban environments where the population levels are high,

there is an enormous potential for a large amount of the populace to receive a radiation dose.
--

Table 1.2 – Description of the Basic Steps of Resuspension in Urban Environments

It is paramount that a basic blueprint be provided on how the coupling methodology will be developed, such that radiological particulate resuspension events such as the one illustrated in Figure 1.2 can be effectively simulated. This blueprint will be discussed in the following section.

1.3 Objective of Research

Before discussing the blueprint, a clear statement of the objective of the research conducted in this thesis is presented as follows:

The objective of this thesis is to develop and implement a methodology that will allow for the coupling of CFD and MC radiation transport simulations such that the radiological hazard arising from the resuspension of radioactive particulates will be assessed.

Further to the roles of the CFD and MC radiation transport simulations described earlier, it is crucial that a concrete blueprint be put forth such that the above stated objective can be achieved. Figure 1.3 illustrates the blueprint that will be employed in order to achieve the above stated research objective.

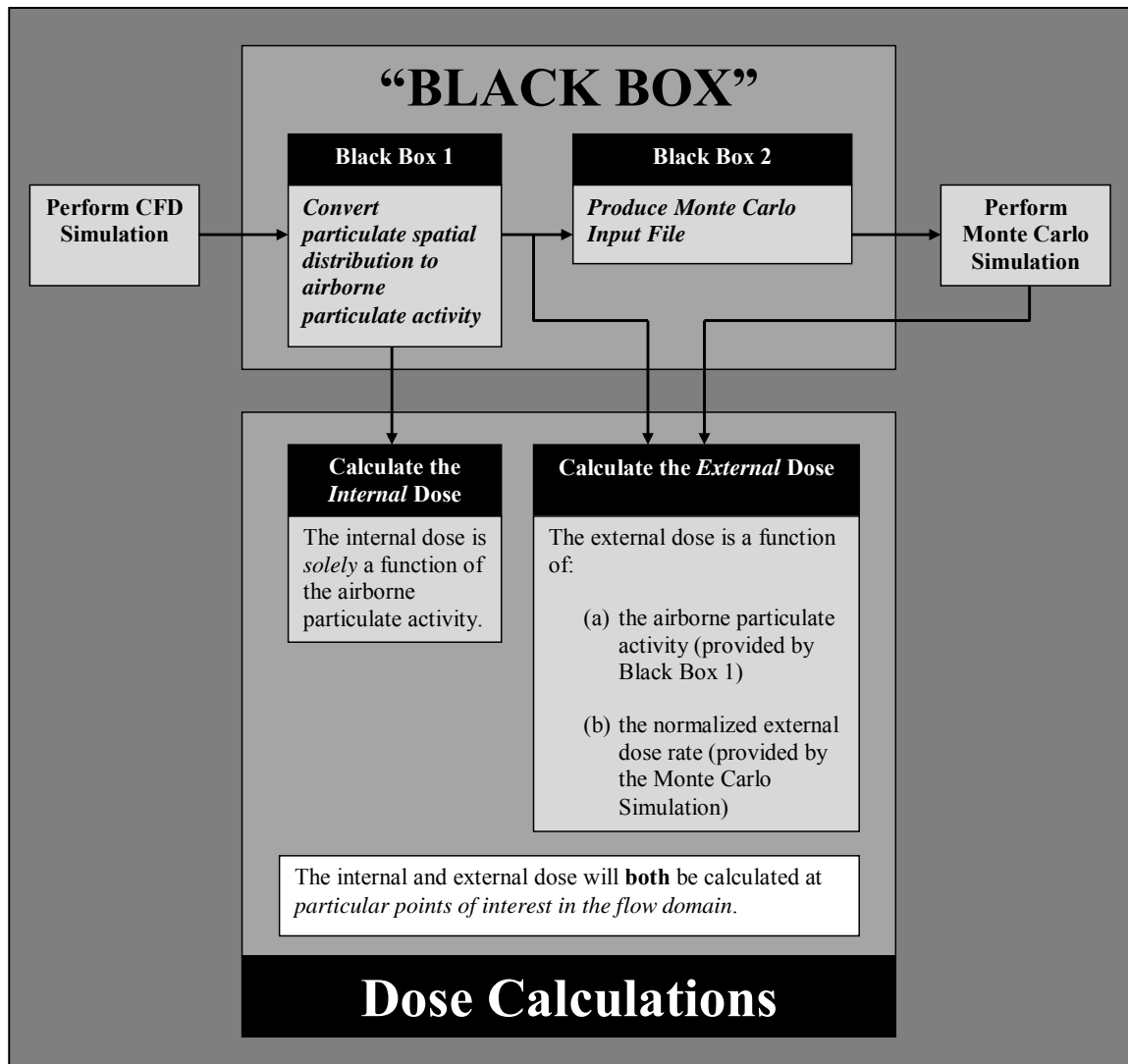


Figure 1.3 – Illustration of the Research Blueprint

The airborne particulate activity serves as the liaison by which the particulate spatial distribution produced by the CFD calculation can be used to perform a dose estimate. To complement the work flow shown in Figure 1.3, the following describes the major steps of the coupling framework:

- (1) In the CFD simulation, once the particulates have been displaced via the fluid flow, most CFD codes have a feature that allows the user to export particulate data to an external text file. This text file contains attributes of each of the

particulates placed in the domain, such as position, velocity, diameter, amongst others.

- (2) The text file is then read into a “Black Box” whose purpose is to process the data in the text file. The “Black Box” consists of two black boxes each of which performs separate tasks. Black Box 1 converts the particulate spatial distribution, contained in the text file, to an airborne particulate activity. The airborne particulate activity is then fed into Black Box 2 which uses the airborne particulate activity to create an input file for the MC radiation transport simulation.
- (3) Once the input file is created, the MC radiation transport simulation is performed, and the results of this simulation are stored in an external text file.
- (4) Dose calculations now proceed, whereby the internal and external dose will both be calculated via equations provided in Section 3.2.4.

Now that the objective of the research performed in this thesis and a discussion on the blueprint employed to achieve this objective has been provided, a brief description of how this research can be used to provide military field commanders with simplified guidance to perform risk assessments when responding to a RDD event will now follow.

1.4 Applicability of Research

It has been alluded to at the beginning of this chapter that military field commanders require knowledge of how much radioactivity exists in the breathing space after the detonation of a RDD. This quantity is embodied by the airborne particulate activity and is indicative of how much internal and external radiation exposure one can incur from exposure to the resuspended radioactive particulates.

Typically, field commanders quantify the airborne particulate activity by possessing two quantities which are (1) measuring the *surface particulate activity*, which is a measure of how much particulate activity is present on the surface that hosts the radioactive particulates divided by the area of the surface and (2) knowledge of the *resuspension factor*, which is defined via equation (1.1).

$$K(t) = \frac{A_v(t)}{A_s} \quad (1.1)$$

Where:

$K(t)$ = resuspension factor at time t (unit: m^{-1})

$A_v(t)$ = airborne particulate activity at time t (unit: $Bq \cdot m^{-3}$)

A_s = surface particulate activity (unit: $Bq \cdot m^{-2}$)

It is clear from equation (1.1) that the airborne particulate activity can be calculated via the product of the resuspension factor and surface particulate activity. It is important to acknowledge the fact that in equation (1.1), the surface particulate activity is not a function of time. The reason being is that this quantity is a measure of how much radiation is initially present on a surface prior to the introduction of a resuspension agent into the contamination premises. However, amount of particulates that are resuspended from the surface and into the breathing space is dependent on time. Thus, the airborne particulate activity and resuspension factor are dependent on time.

Typically, a member of the military unit that responds to a RDD detonation event measures the surface particulate activity via a pancake probe while the resuspension factor is often assumed to be equivalent to the “magic number” of $10^{-6} m^{-1}$ [3]. There are several problems associated with this assumption and are outlined below:

- (1) This assumption is not necessarily accurate in that the resuspension factor is dependent on multiple factors including the direction of resuspension agent flow, velocity of resuspension agent flow, and the physical make-up of the

contamination premises (such as the number and size of buildings), amongst others. Thus, the resuspension factor changes from scenario to scenario.

- (2) Resuspension factors have been quantified from measurements made at nuclear weapons fallout sites. These weapons have been detonated decades ago and so the radioactive particulates on the surfaces of this site have been present for decades and are termed “aged fallout”. The primary difference between a nuclear weapons detonation scenario and a RDD detonation scenario is that in the former case, the released radioactive particulates are of a high temperature and complex chemistry and so the particulates tend to mix with the soil (or host surface) of the contamination site. Thus, resuspended matter from the nuclear weapons fallout site is a mixture of radioactive particulates and soil. In the RDD detonation scenario, a fresh, not aged, fallout field is produced and the released radioactive particulates do not possess a highly complex physical chemistry as their nuclear weapons counterpart and so they tend to lie on top of the host surface without mixing with the host surface material. Thus, resuspended matter from this fresh fallout field will consist primarily of radioactive particulates that have been released from the RDD.

It will be made evident, however, throughout Chapter 3 that the CFD-MC radiation transport coupling methodology developed in this thesis can be employed to quantify the resuspension factor for various fresh fallout field scenarios since CFD and MC radiation transport simulations affords the modeller the flexibility to analyze an infinite amount of resuspension scenarios, not just the one discussed in Chapter 3. Hence, the research conducted in this thesis will make great strides in tabulating the resuspension factor for various resuspension scenarios such that the field commander can employ this list to quickly assess the radiological hazards associated with the contamination zone being dealt with and to then implement the appropriate precautionary measures.

With this framework in mind, the thesis has been arranged as follows. Chapter 2 will present theory pertinent to the fields of fluid dynamics, particulate resuspension, and radiation transport. Chapter 3 will describe the geometry used as a basis for developing the CFD-MC radiation transport coupling methodology and will provide a step-by-step explanation of the coupling methodology that has been developed. Chapter 4 will present both qualitative and quantitative results of the CFD and MC radiation transport simulations performed and a discussion of these results will then ensue. Chapter 5 will summarize the results and discuss possible future investigations.

CHAPTER 2

THEORETICAL BACKGROUND

The research undertaken in this thesis is multi-disciplinary and requires input from the fields of fluid dynamics and radiation transport. It is imperative that a theoretical background be provided in these respective fields such that a basis for the understanding of pertinent quantities and important phenomena be established. This chapter will commence with a discussion of fluid dynamics theory followed by a presentation of particulate resuspension theory. A description of radiation transport theory will then ensue and a discussion of how the fields of fluid dynamics and radiation transport theory are integrated will conclude the chapter.

This chapter is designed to provide an understanding of how the theories pertinent to the abovementioned fields relate to each other, such that a unified description of how the resuspension of radioactive particulate can be used for subsequent radiation field determination be provided.

2.1 Fluid Dynamics Theory

The roles of the CFD calculation are to calculate the three-dimensional flow and resuspend particulates placed in the flow geometry under investigation. It has been shown that when the fluid interacts with the bluff body, a rotational flow pattern is produced. This flow pattern is called a *vortex* or *flow structure* and is the primary vehicle by which particulates are transported from the *boundary layer* up into the main flow stream⁹⁾.

It is apparent that the boundary layer and vortex have a significant impact on the resuspension of particulates and so this section will begin with a description of the characteristics of the boundary layer and will then conclude with a discussion on the

⁹⁾ With respect to flow geometries, the *main flow stream* is the part of the flow geometry that is far removed from surfaces (where the boundary layer is present).

basic principles of CFD. Section 2.2 will then commence with a detailed explanation of how vortices impact the resuspension of particulates.

2.1.1 Shear Stress

A fluid velocity gradient exists in the boundary layer and it arises from the fact that at the lower end of the boundary layer, a stationary solid surface, the fluid velocity is zero via the “no-slip” boundary condition while at the upper end (which is in motion), the fluid velocity is approximately equal to that of the main flow stream. This dynamic creates a *shear stress* that is exerted on fluid flowing throughout the boundary layer region.

The shear stress is defined in equation (2.1).

$$\tau = \mu \left(\frac{\partial u}{\partial y} \right) \quad (2.1)$$

Where:

- $\tau =$ shear stress in the boundary layer (unit: Pa)
- $\mu =$ dynamic viscosity of the fluid (unit: Pa·s)
- $u =$ fluid velocity (unit: m·s⁻¹)
- $y =$ height of the boundary layer (unit: m)
- $\frac{\partial u}{\partial y} =$ “strain rate”/velocity gradient in the boundary layer (unit: s⁻¹)

As per equation (2.1), shear stress is directly proportional to viscosity. To place the concept of viscosity in greater perspective, one can consider the fact that a fluid that moves faster possesses a low viscosity compared to a slower moving fluid. In essence, viscosity has a frictional effect on the movement of a fluid where the more viscous a fluid is, the less mobile it becomes. Viscosity plays a dominant role in the movement of fluid in the (a) near-wall (boundary layer) region of the flow domain and (b) downstream

(wake) region of a flow obstructor. Equation (2.1) establishes the fact that the shear stress is a viscous effect and so the regions of the flow domain that possess the highest velocity gradients will have the flow confined within these regions be governed by a viscous regime. It therefore follows that since the boundary layer and wake region hosts considerably higher velocity gradients than those in the remainder of the flow domain in question, viscous effects are confined to these respective regions.

It is therefore evident that the effect of viscosity is greatest in the vicinity of a solid surface. As will now be discussed, viscosity constitutes an integral characteristic of the boundary layer.

2.1.2 Reynolds Number

The Reynolds Number is an important quantity in the field of fluid dynamics and serves to characterize the nature of the flow in question. There exist two regions of flow in a flow volume, namely:

- (1) *Main Flow Stream*, which is far removed from the solid surfaces. Here, the fluid is inviscid and is governed by inertia effects which sustains the flow in this region, and
- (2) *Boundary Layer/Wake Region*. In the case of the boundary layer, this region resides in the vicinity of the solid surfaces whereas the wake region resides downstream of a bluff body¹⁰⁾. In these respective locations, the flow is governed by viscous effects

The Reynolds Number seeks to relate the strength of the force governing the flow in the first flow region to that of the second. Thus, an extremely high Reynolds Number

¹⁰⁾ Note that a bluff body is composed of solid surfaces. Thus, the boundary layer resides in the vicinity of the solid surfaces of the bluff body whereas the wake region resides in the region downstream of the bluff body.

indicates the flow in the flow volume is dominated by inertia effects while a very low Reynolds Number signifies that viscous effects are dominant. Equation (2.2) is the formal equation for Reynolds Number.

$$\text{Re} = \frac{\rho u L}{\mu} \quad (2.2)$$

Where:

Re = Reynolds Number

ρ = density of the fluid (unit: $\text{kg}\cdot\text{m}^{-3}$)

u = fluid velocity¹¹⁾ (unit: $\text{m}\cdot\text{s}^{-1}$)

L = characteristic length of fluid domain feature¹²⁾ (unit: m)

μ = dynamic viscosity of the fluid (unit: $\text{Pa}\cdot\text{s}$)

In addition to the properties of the Reynolds Number described above, it also serves as an indicator as to how large the boundary layer is for a given flow scenario. The importance of this is that it will allow for one to determine the physical extent to which the viscous regime governing the boundary layer will exert its influence onto the main flow stream. For low-Reynolds Number flow, the size of the boundary layer region is very large, extending from the immediate vicinity of a solid surface to a considerable distance away from the solid surface. When analyzing high-Reynolds Number flow, the size of the boundary layer region becomes very small and forms in the immediate vicinity of the solid surface and when bluff bodies are present in the flow domain, the viscous effects of the boundary layer are also “convected” further downstream from the bluff body. This downstream region is called the *wake region* and hosts negative pressure vortices¹³⁾ [25].

¹¹⁾ The fluid velocity at the inlet of the flow geometry is substituted for this quantity [10].

¹²⁾ The Reynolds Number is calculated based on the features of the domain. For example, if there is a flow scenario where the flow approaches a bluff body, the *height of the bluff body* will be substituted for this quantity [25].

¹³⁾ The terms *vortex/vortices* and *wakes* are equivalent.

It is evident that the boundary layer plays an important role in any flow scenario. This is particularly true for turbulent flows since the boundary layer along with the presence of a bluff body create a wake region that hosts vortices. These vortices that are created will go on to play a crucial role in the resuspension of particulates. Thus, it is only fitting that a discussion of the boundary layer now follows.

2.1.3 Boundary Layer

The fluid velocity gradient in the boundary layer constitutes one distinguishing characteristic of this region, and is illustrated in Figure 2.1.

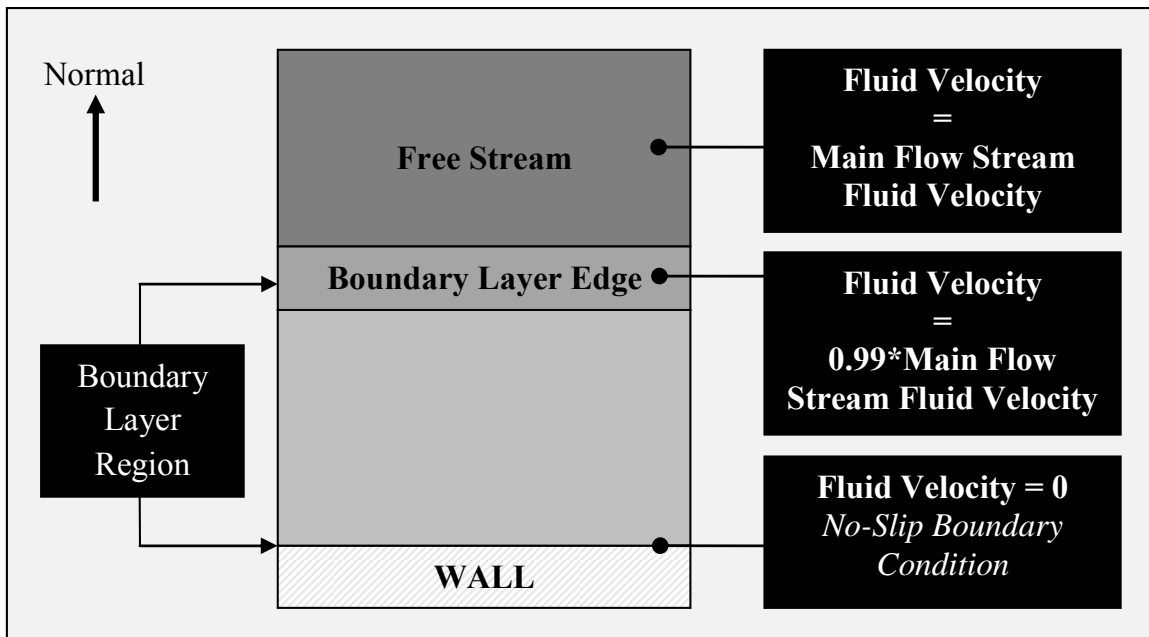


Figure 2.1 – Illustration of Boundary Layer Location and Variation of Fluid Velocity Within this Region [25]

As shown in Figure 2.1, the boundary layer region is defined as the region of the flow where the fluid velocity ranges from zero (at the wall¹⁴⁾) to 99% of the main flow

¹⁴⁾ The term *wall* and the terms *solid surface* and *surface* are all equivalent to each other.

stream fluid velocity¹⁵⁾. This property of the boundary layer coupled with the fact that this region is governed by a viscous regime reveals the second distinguishing characteristic of the boundary layer which is that it is a region of slow moving fluid.

Further to what has been stated about the boundary layer, it is also composed of two regions which are described below, in increasing distance from the wall [26]:

- The *inner region* is composed of three constituent zones:
 - Zone 1: Known as the *viscous sub-layer*, viscous effects are dominant
 - Zone 2: Known as the *buffer layer*, the effects of viscosity and inertia are equivalent
 - Zone 3: Known as the *log-law layer*, inertia effects are dominant
- The *outer region*, known as the *law-of-the-wake layer*, is dominated by inertia effects

It is crucial that the flow field in both the boundary layer/wake and main flow stream regions of the flow domain be calculated since this flow field serves as a prerequisite for particulate resuspension calculations. The manner in which a flow field can be calculated, especially in complex flow domains, is via the use of Computational Fluid Dynamics whose principles will now be discussed.

2.1.4 Computational Fluid Dynamics

CFD is the use of numerical algorithms to characterize a two-dimensional or three-dimensional fluid flow field. To illustrate the major principle of CFD, consider the

¹⁵⁾ As a rule of thumb, an approximation to the value of the main flow stream velocity is that of the inlet flow velocity.

need to conserve¹⁶⁾ some flow variable, denoted by ξ , within a finite control volume. Figure 2.2 illustrates the control volume used to conserve the flow variable ξ .



Figure 2.2 – Finite Control Volume

The conservation equation for ξ in the finite control volume shown in Figure 2.2 is qualitatively stated in equation 2.3 [26].

$$\begin{aligned}
 & \left[\begin{array}{c} \text{Rate of Change of } \xi \\ \text{in the control volume} \\ \text{with respect to time} \end{array} \right] \\
 & \quad = \\
 & \left[\begin{array}{c} \text{Net rate of increase of } \xi \\ \text{due to convection into the} \\ \text{control volume} \end{array} \right] + \left[\begin{array}{c} \text{Net rate of increase of } \xi \\ \text{due to diffusion into the} \\ \text{control volume} \end{array} \right] + \left[\begin{array}{c} \text{Net rate of creation of } \xi \\ \text{inside the control} \\ \text{volume} \end{array} \right] \\
 & \quad \underbrace{\hspace{10em}}_{\text{Transport of } \xi \text{ due to fluid flow}} \quad \underbrace{\hspace{10em}}_{\text{Transport due to the variation of } \xi \text{ from point to point}}
 \end{aligned} \tag{2.3}$$

The mathematical description of equation (2.3) is embodied by the *Navier-Stokes equation*, which is one of the two equations that govern the flow of incompressible fluids. This equation is formulated on the basis that the acceleration undergone by a fluid is directly proportional to the forces acting on the fluid. The Navier Stokes equation is stated in equation (2.4) [25].

¹⁶⁾ The term *conserve* implies the need to strike a balance between the means that increase and decrease a quantity.

$$\underbrace{\rho \left(\frac{\partial \vec{V}}{\partial t} + \vec{V} \cdot \nabla \vec{V} \right)}_{\text{Fluid Acceleration}} = \underbrace{-\nabla p}_{\substack{\text{Pressure Force} \\ \text{acting on the} \\ \text{fluid}}} + \underbrace{\rho \vec{g}}_{\substack{\text{Force due to} \\ \text{Gravity acting} \\ \text{on the fluid}}} + \underbrace{\mu \nabla^2 \vec{V}}_{\substack{\text{Viscous Force} \\ \text{acting on the} \\ \text{fluid}}} \quad (2.4)$$

Forces acting on the fluid

Where:

ρ = density of the fluid (unit: $\text{kg} \cdot \text{m}^{-3}$)

μ = dynamic viscosity of the fluid (unit: $\text{Pa} \cdot \text{s}$)

t = time (unit: s)

\vec{V} = fluid velocity vector (unit: $\text{m} \cdot \text{s}^{-1}$)

p = fluid pressure (unit: Pa)

\vec{g} = acceleration due to gravity (unit: $\text{m} \cdot \text{s}^{-2}$)

The second equation that governs the flow of incompressible fluids is the continuity equation. This equation states that the rate at which mass enters a control volume is equal to the rate at which it leaves. The mathematical description of this equation is shown in equation (2.5).

$$\nabla \cdot \vec{V} = 0 \quad (2.5)$$

Where:

\vec{V} = fluid velocity vector (unit: $\text{m} \cdot \text{s}^{-1}$)

Once the control volume has been identified in the flow domain, both the Navier-Stokes and continuity equations will be used to characterize the fluid flow in this control volume. For complex flow geometries, the Navier Stokes equation cannot be solved analytically and thus the use of numerical methods is required. In a CFD code, one establishes the spatial locations of nodes within the flow geometry at which fluid quantities such as pressure and velocity will be calculated via the Navier-Stokes equation (or by other turbulence models). The user must also specify initial and boundary conditions for fluid quantities of interest. Since numerical methods are used, the CFD

calculations will be iterative in nature and so the fluid quantities at each of the nodes will be updated for each iteration (if a steady-state simulation is performed) or time step (if a transient simulation is performed) until the value of the fluid quantities have converged¹⁷⁾.

When modelling turbulent flow, approximations to the Navier-Stokes equations have been made in order to model such flow and a description of these approximations will now be discussed.

2.1.5 Turbulence Modelling

When modelling turbulent flow, one would expect that the Navier-Stokes equation shown in equation (2.4) will be solved. This approach, known as Direct Numerical Simulation, has been deemed too computationally expensive and is not used to model industrial flows [27]. To circumvent this issue, several turbulence models have been formulated that approximate the solution to the Navier Stokes equation, each with their own advantages and disadvantages.

It has been described that vortices are hallmarks of turbulent flows. A turbulent flow field consists of both small and large vortices and as a rule of thumb, small vortices tend to stay close to walls while large vortices reside in the main flow stream. The large vortices obtain their energy from the main flow stream and pass some of that energy to the small vortices, in order to sustain them. Each turbulence model seeks to capture this energy extraction process.

It has been set out at the beginning of Section 2.1 that the fundamental properties of the boundary layer be established and the discussion thus far has been dedicated to this. Addressed in the next section is how the presence of the boundary layer and vortices impact the resuspension of particulate.

¹⁷⁾ Convergence represents the state of a numerical simulation where the change in the value of a quantity of interest is negligible for successive iterations/time steps.

2.2 Particulate Resuspension Theory

Particulates residing in the boundary layer are subjected to several forces whose origins are attributed to the nature of the flow, the physical and material properties of the particulates, and the material characteristics of the surface that the particulates are placed on. Some of these forces act to encourage particulate resuspension while others serve to ensure that particulates remain in the boundary layer. This section seeks to provide a qualitative description of the nature of particulate resuspension beginning with a discussion of the aforementioned forces followed by a description of the effect that the size of a particulate has on its ability to be resuspended. The time-dependent nature of particulate resuspension will then be outlined and the section will then conclude with a cumulative list of parameters that affect particulate resuspension. For the sake of clarity, the discussions contained in this chapter will be in reference to a single, individual particulate unless otherwise specified.

2.2.1 Forces Acting on a Particulate

Particulates reside in the boundary layer only to be resuspended by the vortices that are present in the flow. Figure 2.3 further describes the categorization of these forces.

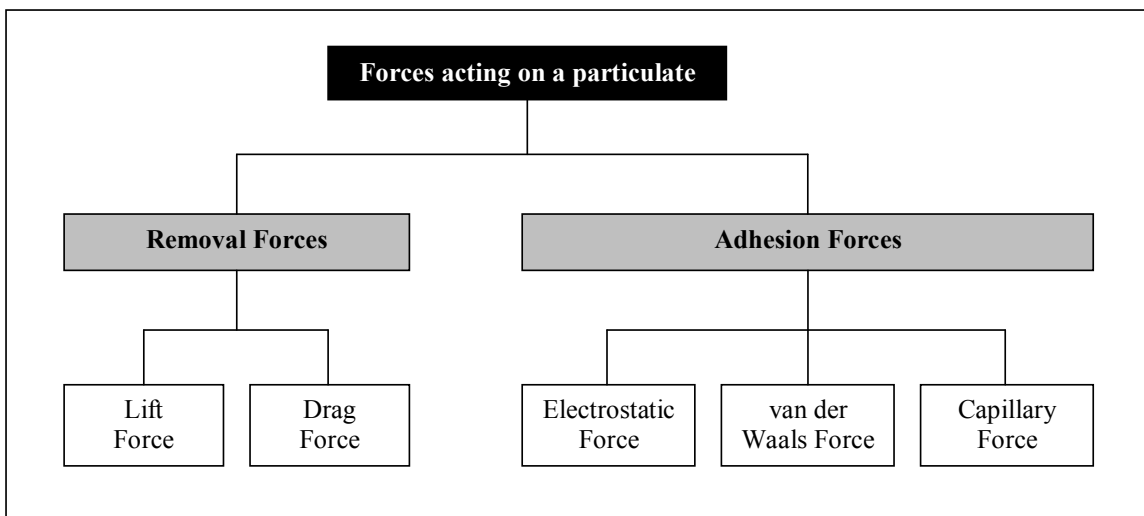


Figure 2.3 – Description of the Forces Acting on a Particulate

In Figure 2.3, the term *removal forces* represent the forces that encourage particulate resuspension while the term *adhesion forces* represent the forces that discourage particulate resuspension. It is clear that each of these forces is comprised of several sub-forces and it is only fitting that a description of the removal and adhesion forces along with their constituent sub-forces be provided. The next section will discuss the removal forces.

2.2.1.1 Removal Forces

Prior to discussing removal forces, a preliminary description of the constituent removal forces, the lift and drag force is provided. The lift force is the vertical component of the removal force acting on the particulate while the drag force is the horizontal component of the removal force acting on the particulate. A more detailed explanation of these forces is developed throughout this section.

Removal forces serve as the foremost catalyst for particulate resuspension. A prime example of a removal force is the force exerted on a particulate by a vortex that is present in the flow stream. It is important, however, to clearly acknowledge the different types of vortices that form in a flow stream. There are two such types and are described below [28]:

- (1) the vortex such as the one shown in Figure 1.2 penetrates the boundary layer and resuspends the resident particulates, and
- (2) the vortices that form in the wake region of a bluff body are present in the main flow stream and act to keep the resuspended particulates in suspension

Section 2.1.2 discussed the latter vortex type and so it is imperative that a description of the first vortex type now proceed. To ascertain the exact nature of this vortex that penetrates the boundary layer and resuspend the resident particulates, Kaftori et al. [28] conducted an experiment where particulates were initially placed on a surface and then

subjected to turbulent flow. With the aid of flow visualization apparatus, a description of the physical appearance of this vortex has been provided and is outlined below:

- In the *streamwise direction*¹⁸⁾, there is a vortex that expands outward from the wall in the form of an expanding spiral
- In the *spanwise direction*¹⁹⁾, this vortex possesses a funnel-like shape

A pictorial description of this flow structure is shown in Figure 2.4.

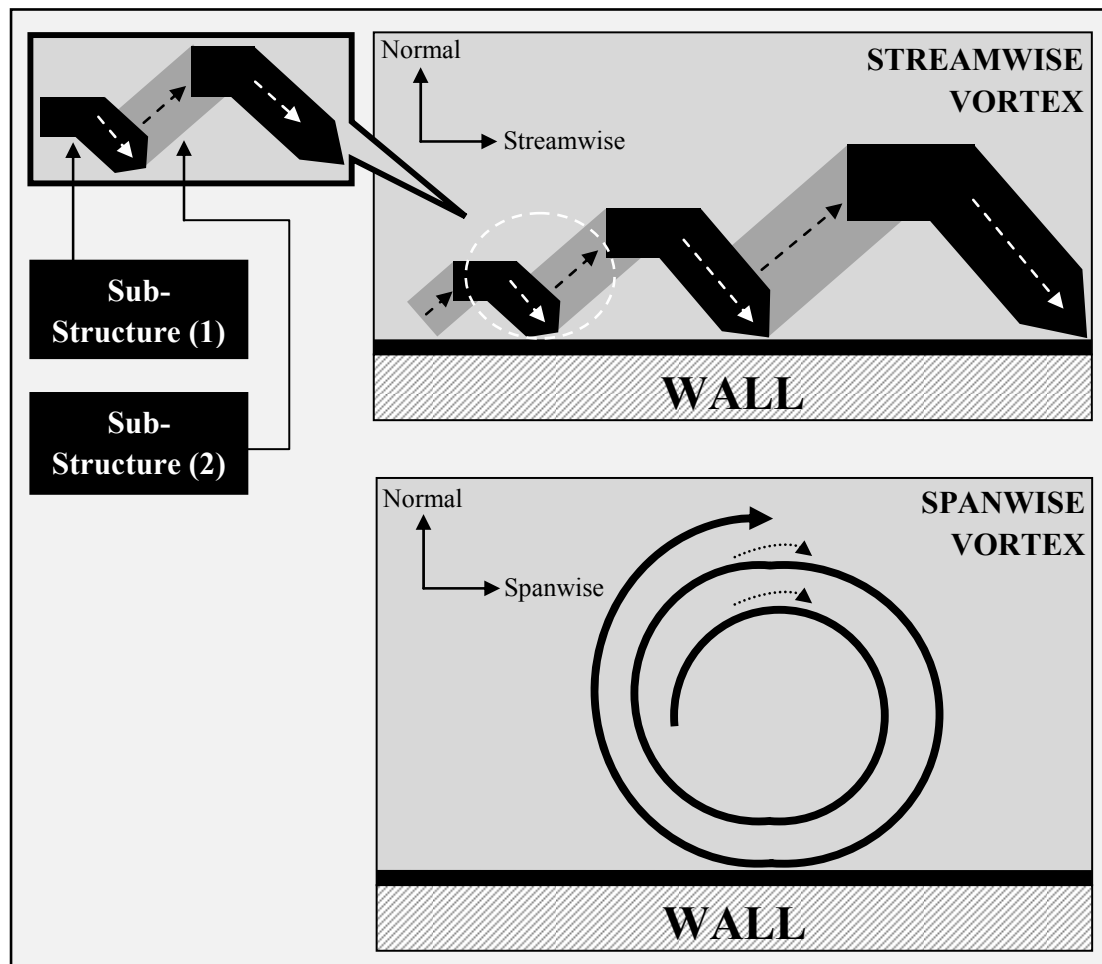


Figure 2.4 – Illustration of Boundary Layer Vortex [28]

¹⁸⁾ The *streamwise direction* is the direction that is parallel to the direction of the flow.

¹⁹⁾ The *spanwise direction* is in the direction that crosses the flow and the *normal direction* is the direction that is perpendicular to the flow.

Figure 2.4 describes the streamwise version of the vortex as consisting of two sub-structures, discussed below:

- Sub-Structure (1): Known as the *sweep structure*, it captures particulates in an attempt to re-entrain them into the main flow stream. The fluid velocity within the sweep structure is high.
- Sub-Structure (2): Known as the *ejection structure*, the particulates captured by the sweep structure are then passed to the ejection structure in an attempt to entrain these particulates into the main flow stream. The fluid velocity within the ejection structure is low.

The presence of this vortex and its influence on particulate resuspension has also been observed by Braaten et al. [29] who conducted an experiment where monodisperse particulates²⁰⁾, that reportedly possessed small cohesion forces²¹⁾ and whose median diameter was 27.8 μm , were placed on the floor of a wind tunnel and exposed to a turbulent flow stream. Based on the experimental data acquired, a “sweeping Eddy concept of particle resuspension” is supported. This concept describes an energetic vortex penetrating the boundary layer (specifically the viscous sub-layer) and subsequently removing particulates from this region and entraining (i.e. resuspending) them into the main flow stream.

The challenge for this vortex is that it must be energetic enough such that it can overcome the viscous regime governing the boundary layer in order to interact with the resident particulates. The Reynolds Number has an enormous influence on the strength of this vortex and this relationship will now be analyzed.

²⁰⁾ *Monodisperse* particulates imply that the group of particulates in question share roughly the same diameter.

²¹⁾ The *cohesion force* is a measure of how particulates tend to “stick” to each other such that they can then form a larger, agglomerated particulate.

2.2.1.1.1 Influence of Reynolds Number

A high Reynolds Number indicates that the flow in question is dominated by inertia. Since flow streams contain both large and small vortices where the large vortices extract their energy from the main flow stream and pass some of that energy onto the smaller vortices, it therefore follows that the more energetic the flow stream, the more energetic the large and small vortices will be. Thus, the first vortex type discussed in Section 2.2.1.1 will be more energetic and will go on to penetrate the boundary layer and resuspend a large amount of resident particulates. This relationship has been confirmed by the experimental results of Kaftori et al. [28] who found the following relationships between the magnitude of the Reynolds Number and the amount of particulate resuspension:

- (1) In *high Reynolds Number flow*, most of the particulates are in suspension, since the flow is energetic enough to entrain particulates from the boundary layer into the main flow stream

- (2) In *low Reynolds Number flow*, most of the particulates reside in the wall/boundary layer region, since the flow is NOT energetic enough to entrain particulates from the boundary layer into the main flow stream

Kaftori et al. [28] provides greater insight to the above relationships as shown in Figures 2.5 and 2.6.

Figure 2.5 illustrates the resuspension process for low Reynolds Number flow and is elaborated on in Table 2.1.

Step	Description
1	The vortex interacts with particulates in the boundary layer.
2	Since the flow structure is not energetic enough (due to low Reynolds Number), only a few particulates from the boundary layer will be entrained

	into the main flow stream.
3	The majority of particulates in the boundary layer will be pushed aside by the vortex, forming “streaks”, since this flow structure will not be energetic enough to transport these particulates to the main flow stream. Since many particulates remain in the boundary layer, the streaks will be long, wide, and massive and will be several particulate layers thick, since many large particulates will not be entrained and will therefore be present in these streaks.

Table 2.1 – Description of the Resuspension Process for Low Reynolds Number Flow

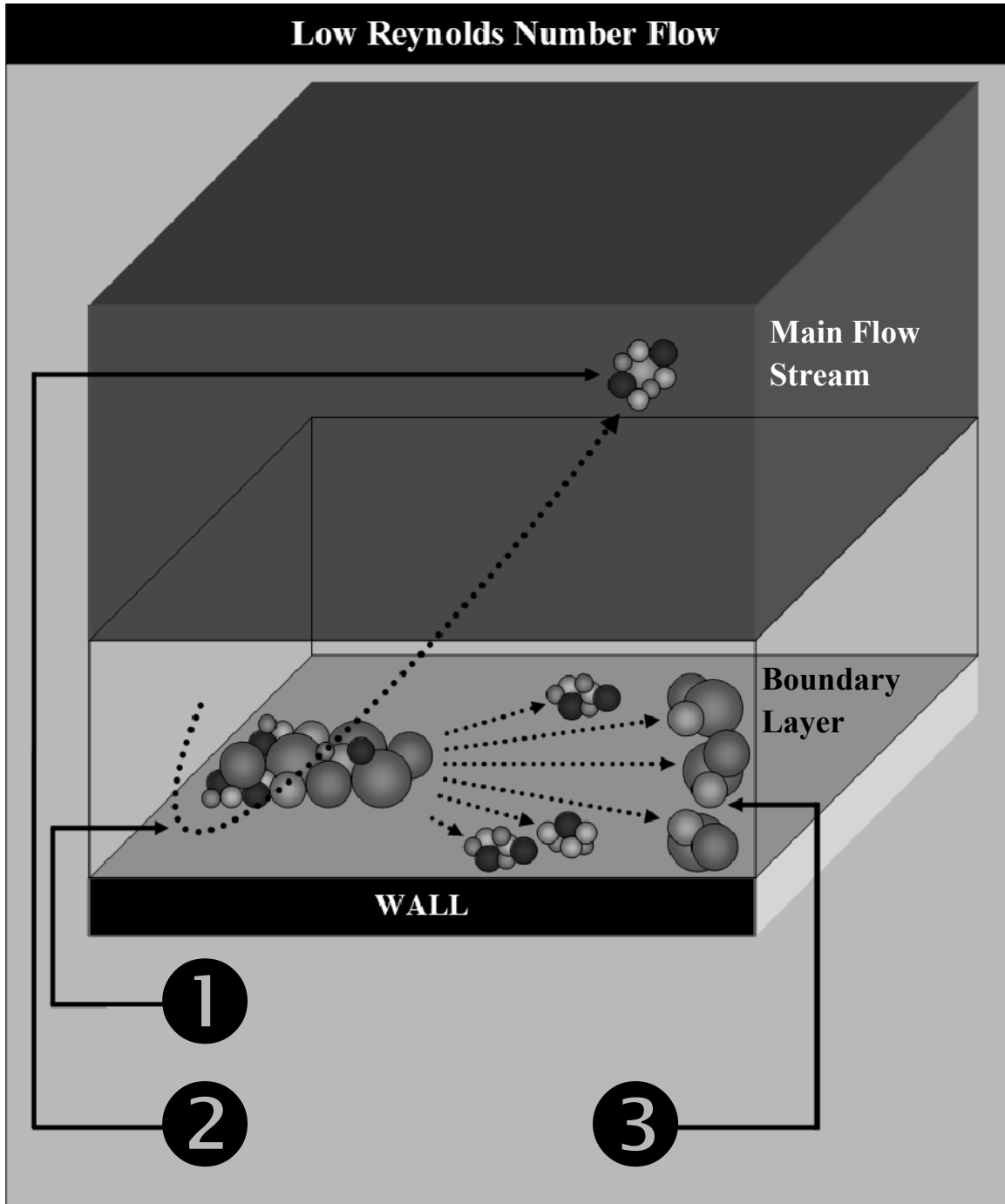


Figure 2.5 – Effect of Low Reynolds Number Flow on Particulate Resuspension [28]

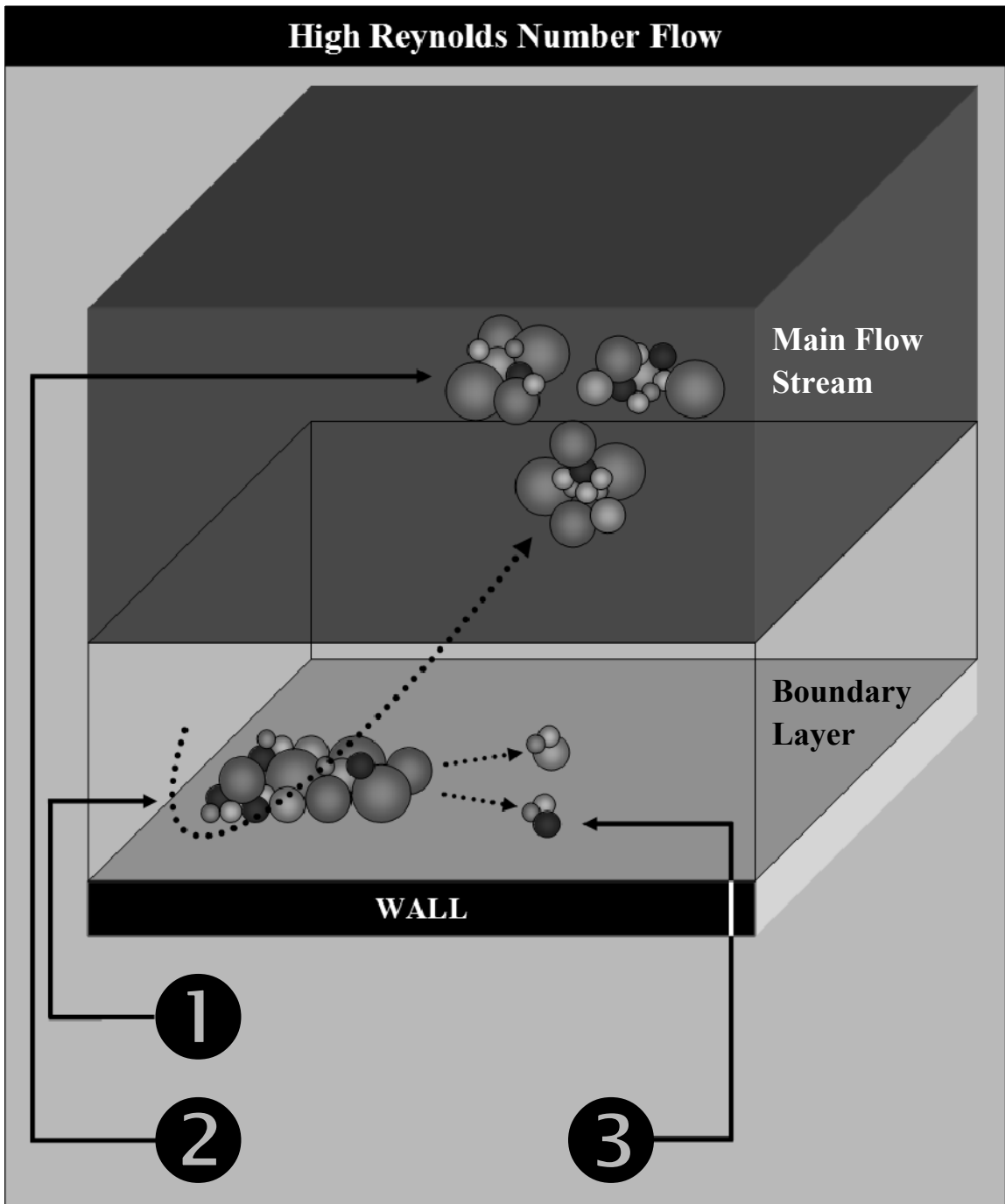


Figure 2.6 – Effect of High Reynolds Number Flow on Particulate Resuspension [28]

Figure 2.6 illustrates the resuspension process for high Reynolds Number flow and is elaborated on in Table 2.2.

Step	Description
1	The flow structure interacts with particulates in the boundary layer.
2	Since the flow structure is energetic enough (due to high Reynolds Number), more particulates from the boundary layer will be entrained into the main flow stream.
3	As a result of the energetic flow, there will be few particulates left in the boundary layer after the flow structure passes through. As a result of the flow structure's inability to entrain these particular particulates, these particulates will be pushed aside by the flow structure forming "streaks". These streaks, however, will be very short, narrow, and contain very few particulates, since most of the large particulates will have been entrained.

Table 2.2 – Description of the Resuspension Process for High Reynolds Number Flow

Clearly, the flow that possesses a higher Reynolds Number will produce energetic vortices that will go on to resuspend a greater amount of particulates. Aside from the effect that the fluid flow has on particulate resuspension, the material characteristics of the surface that the particulates are placed on also play a role in this phenomenon. This will be the topic of the next section.

2.2.1.1.2 Influence of Rock 'n' Roll Motion

In reality, surfaces are not perfectly smooth as they possess some sort of roughness/unevenness at least on a sub-microscopic scale. The unevenness possessed by a surface is characterized by what are known as *asperities*. When exposed to the flow stream, the particulate that is placed on a surface with asperities (often placed between asperities) will experience "Rock 'n' Roll" motion [30]. Figure 2.7 depicts how a particulate is situated on a surface with asperities.

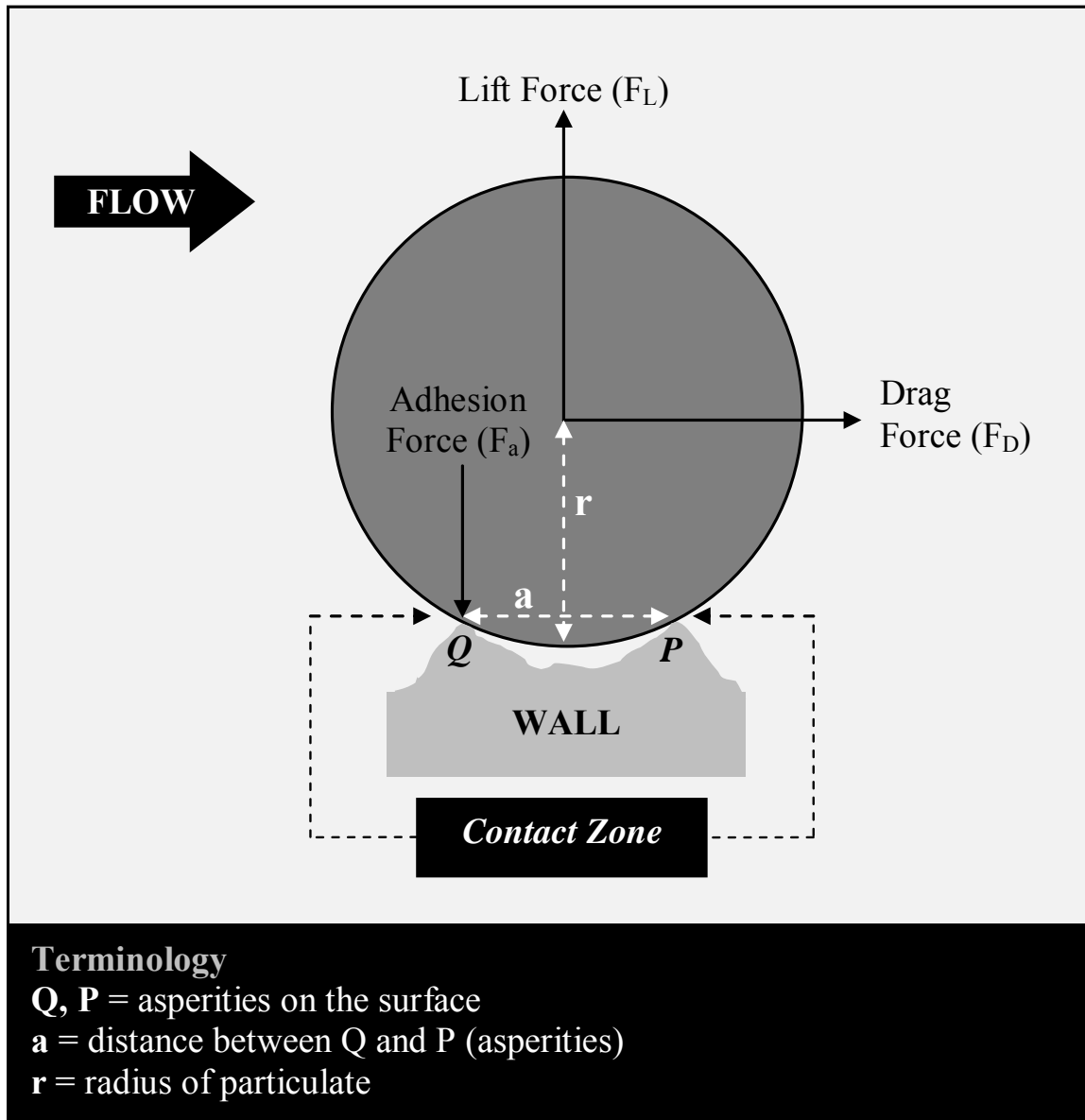


Figure 2.7 – Rock ‘n’ Roll Motion of a Particulate Exposed to Boundary Layer Flow [30]

As alluded to in Figure 2.3, the removal force is composed of lift and drag forces, which will be discussed in detail later. It is of interest to determine which of the two removal forces, lift or drag, play a dominant role in the resuspension of the particulate. To address this, Biasi et al. [30] developed the configuration shown in Figure 2.7. To determine which of the two constituent removal forces have a greater influence on resuspension, the moment of the particulate about asperity P was taken. The reason why this particular asperity was chosen is because since the fluid motion traverses the

particulate from left to right, the particulate will “rock” about asperity P via the action of the *removal force* but “rolls” back to Q due to the action of the *adhesion force*. This motion will result in the particulate accumulating rotational energy which in turn will assist the particulate in eventually being resuspended.

The moment of inertia about asperity P is given by equation (2.6).

$$\Gamma_P = (r)(F_D) + \left(\frac{1}{2}a\right)(F_L) \quad (2.6)$$

Where:

Γ_P = moment of particulate about asperity P (unit: $N \cdot m$)

r = radius of particulate (unit: m)

a = distance between asperities P and Q (unit: m)

F_D = drag force acting on particulate (unit: N)

F_L = lift force acting on particulate (unit: N)

The particulate of interest to this thesis are those that have diameters in the microscopic range (i.e. diameters that are greater than or equal to 10^{-6} m). It has also been mentioned that the distance between the asperities are on the sub-microscopic scale and so it follows that, in reference to the nomenclature shown in Figure 2.7 that $r \gg a$ (that is, the radius of the particulate is much greater than the distance between asperities). When this statement is applied to equation (2.6), it is evident that the particulate’s moment of inertia about asperity P is dominated by the drag force.

In summary, the particulate shown in Figure 2.7 will exhibit Rock ‘n’ Roll behaviour under the following conditions:

- (1) The particulate will be subjected to removal forces (lift and drag forces) and adhesion forces. The former acts to resuspend the particulate from the surface

while the latter seeks to keep the particulate grounded at the surface.

- (2) The removal forces will cause the particulate to ROCK about asperity P but the adhesive forces (acting downwards towards the surface) will force the particulate to ROLL back to asperity Q.
- (3) This rocking and rolling motion of the particulate will cause it to accumulate enough rotational energy such that it will eventually be able to break its contact with the surface at asperity Q.
- (4) The particulate can then break its contact with the surface at asperity P, either by rolling off of or lifting off at asperity P, if there is sufficient lift force such that the adhesive forces can be overcome. The particulate is considered to be resuspended at this point.

It is clear that as a result of the drag force dominating the movement of the particulate in the presence of asperities, the particulate will undergo significant horizontal displacement. As the particulate rolls along the surface, it will encounter asperities along the way and will undergo the Rock 'n' Roll motion described above. The successive encounters with asperities will enable the particulate to attain a skipping motion whereby it will gain a small (with respect to the extent of the particulate's horizontal displacement) vertical trajectory periodically. The significance of this lay in the fact that this small vertical trajectory can enable the particulate to escape the innermost layer of the boundary layer – the viscous sub-layer, and enter the less viscous portion of the boundary layer. This will enhance the chances of the particulate to be swept up by and ejected into the main flow stream by the vortex shown in Figure 2.4.

An aspect of the flow that enhances this phenomenon is the shear stress in the boundary layer. The rolling and skipping motion of the particulate described thus far is attributed to the particulate encountering asperities on the surface. It will be shown in the next section that the presence of shear stress will enable the particulate to roll more

vigorously along the surface such that it can gain a greater vertical trajectory when experiencing the skipping motion.

2.2.1.1.3 Influence of Shear Stress

The shear stress arises from the fluid velocity gradient that is present in the boundary layer and equation (2.1) states that the shear stress is directly proportional to the fluid velocity gradient in the boundary layer. To explore the effect that the shear stress/fluid velocity gradient has on particulate motion in the boundary layer, consider Figure 2.8.

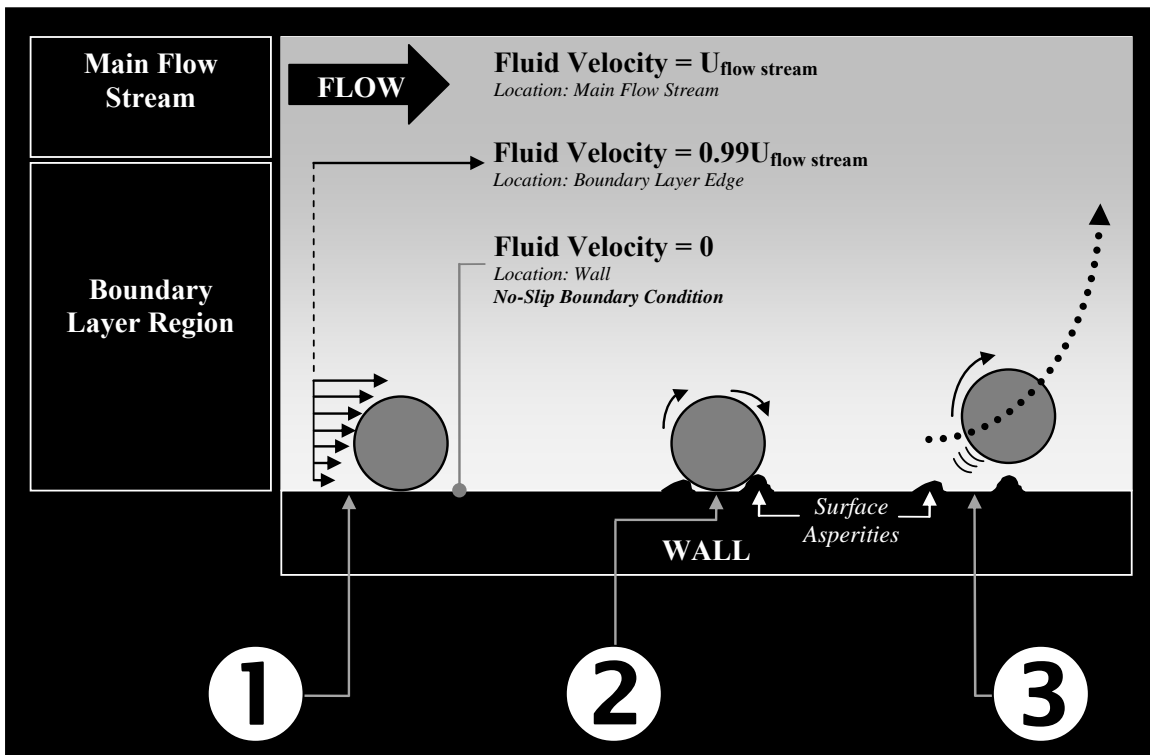


Figure 2.8 – Effect of Shear Stress on Particulate Motion in the Boundary Layer²²⁾

Figure 2.8 illustrates the relationship between shear stress and particulate motion in the boundary layer in three steps, and is explained in Table 2.3.

²²⁾ As a rule of thumb, $U_{\text{flow stream}}$ is equivalent to the inlet fluid velocity.

Step	Description
1	The fluid velocity gradient present in the boundary layer acts in the normal direction and increases in this direction (hence the increasing size of the arrows as one moves further away from the wall). The particulate present in the boundary layer will be subjected to this velocity gradient and as a result, it will have a lower velocity on its lower half and will have a higher velocity on its upper half.
2	This velocity gradient on the particulate's surface results in a torque, which will cause it to roll in the direction of the flow. Since most surfaces have asperities, the rolling of the particulate as a result of the velocity gradient in the boundary layer will cause the particulate to experience "Rock 'n' Roll" motion.
3	Due to the rolling of the particulate induced by the fluid velocity gradient and the presence of surface asperities, the particulate will experience a skipping motion as a result of encountering successive asperities. This results in the particulate gaining a measureable vertical trajectory. This will enable the particulate to leave the innermost portion of the boundary layer, the viscous sub-layer, and enter a less viscous region of the boundary layer. The increased elevation experienced by the particulate will enhance its chances of being resuspended into the main flow stream by the vortex described in Figure 2.4.

Table 2.3 – Description of the Influence of Shear Stress on Particulate Resuspension

Based on the discussion on removal forces, it is evident that efforts to resuspend a particulate are conducted on multiple fronts. The action of vortices that penetrate the boundary layer and resuspend the resident particulates coupled with the influence of the particulate's Rock 'n' Roll motion which in turn is complimented by the presence of shear stress in the boundary layer culminate in the formation of a *removal force* that is exerted on a particulate such that it can be resuspended into the main flow stream. The removal force consists of the lift and drag forces whereby the lift force represents the vertical component of the removal force while the drag force represents the horizontal component of the removal force.

This concludes the discussion of the nature of removal forces and a description of the second type of force acting on particulates, adhesion forces, will now ensue.

2.2.1.2 Adhesion Forces

Adhesion forces seek to have the particulate resist the actions of the removal forces. There are three such forces and it will be shown that each of these three constituent adhesion forces are dependent on the material properties of both the particulate and the surface it is placed on and the properties of the fluid flow. A discussion of each adhesion forces will now commence.

2.2.1.2.1 Electrostatic Force

Particulates that possess a diameter of 0.1 μm or larger carry a small net charge [8]. When in the vicinity of the surface it is placed on, the charge of the particulate induces an equal but opposite charge in the surface (note the space between the particulate and the surface; see Figure 2.10). As a result, an attractive force between the two mediums is created. This attractive force is called the *Electrostatic Force* and its formation is illustrated in Figure 2.9.

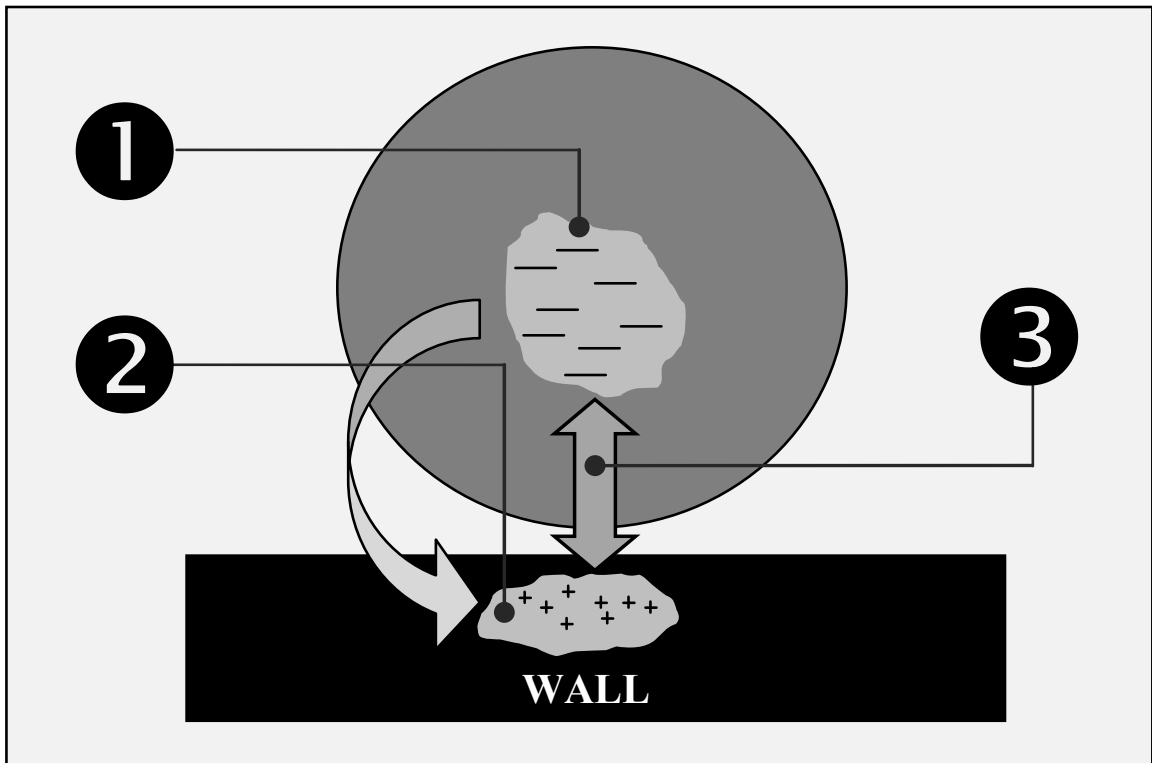


Figure 2.9 – Formation of the Electrostatic Force [8]

Figure 2.9 depicts the steps in the formation of the Electrostatic Force, and is discussed further in Table 2.4.

Step	Description
1	Particulates that possess diameters of 0.1 μm and above carry a small net charge.
2	The charge possessed by the particulate induces an equal but opposite charge in the surface (wall).
3	The dipoles in both the particulate and the wall create an attractive force between the particulate and the wall.

Table 2.4 – Description of the Formation of the Electrostatic Force

Another attractive force between the particulate and the surface based on electric charges is called the van der Waals Force and is described in the next section.

2.2.1.2.2 van der Waals Force

The van der Waals force is one that arises from an attraction between the particulate and the surface based on the electric charges of these two mediums. Here, the random movement of positive and negative charges in the particulate creates areas of concentrated charge called *dipoles*. These dipoles induce complimentary dipoles in the surface, thereby forming an attractive force between the two mediums – the particulate and the surface. This attractive force is called the *van der Waals Force* and its formation is illustrated in Figure 2.10.

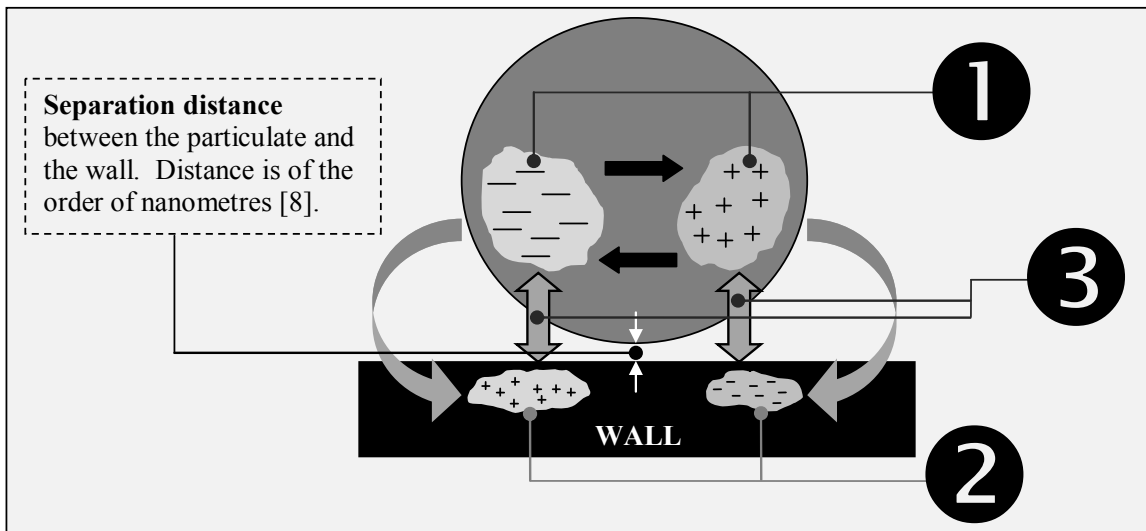


Figure 2.10 – Formation of the van der Waals force [8]

The steps in the formation of the van der Waals force shown in Figure 2.10 are elaborated on in Table 2.5.

Step	Description
1	The random movement of electric charges within the particulate creates momentary areas of concentrated charge called dipoles.

2	These dipoles of the particulate induce dipoles of equal but opposite charge in the neighbouring material (the wall).
3	These dipoles become attracted to one another thereby creating an attractive force between the particulate and the wall.

Table 2.5 – Description of the Formation of the van der Waals Force

Thus far, the attraction between the particulate and the surface has been based on the electric charges possessed by these mediums. In addition to these attractive forces, another arises when fluid “seeps” into the separation distance outlined in Figure 2.10. The following section will discuss this phenomenon.

2.2.1.2.3 Capillary Force

Depending on the relative humidity²³⁾, water vapour in the air can condense in the capillary space (characterized by the separation distance) between the particulate and the surface. This results in the formation of an adhesive force that forms between the particulate and the surface, via the surface tension possessed by the condensed water vapour. This force is called the *Capillary Force* and its formation is illustrated in Figure 2.11.

²³⁾ The relative humidity is a measure of the amount of water vapour in the air.

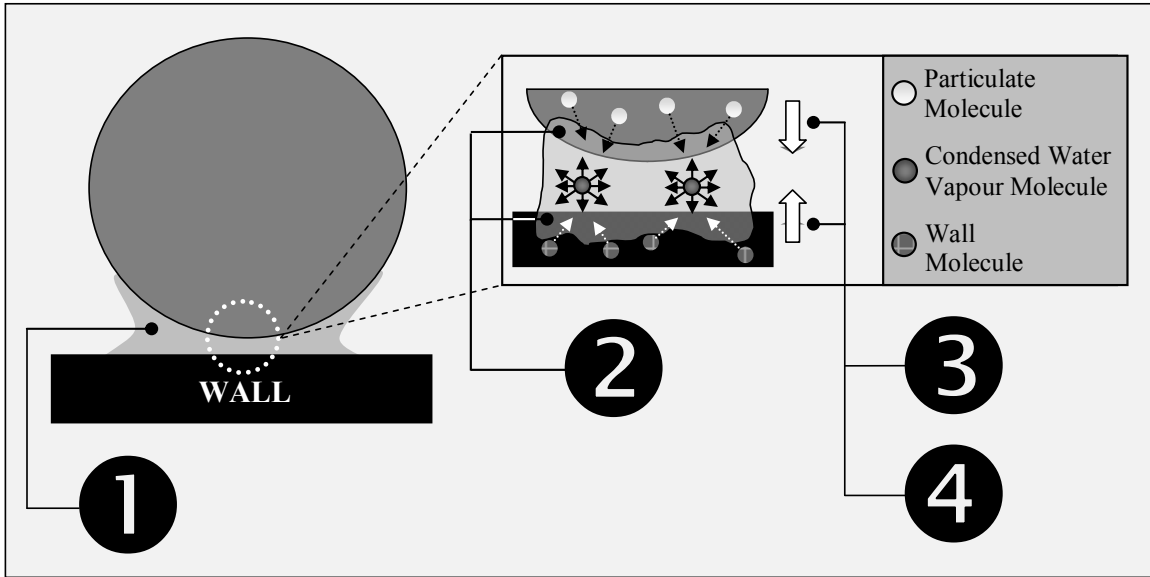


Figure 2.11 – Formation of the Capillary Force [8]

Figure 2.11 illustrates the steps in the formation of the Capillary Force and is elaborated on in Table 2.6.

Step	Description
1	Depending on the relative humidity, water vapour in the air can condense in the capillary space (characterized by the separation distance) between the particulate and the wall.
2	As a result of the condensed water vapour being in contact with both the particulate and the wall, the particulate and the wall will absorb some of the condensed water vapour. This contact will cause a surface tension to form around the condensed water vapour in the capillary space.
3	The surface tension of the condensed water vapour causes the molecules of this vapour to exert a pulling force on the molecules of the mediums that are in contact with it – the particulate and the wall.
4	The attractive force between (1) the particulate and the condensed water vapour and (2) the condensed water vapour and the wall causes the vapour to act as an intermediary by which the particulate is adhered to the wall.

Table 2.6 – Description of the Formation of the Capillary Force

A description of the forces acting on a particulate residing in the boundary layer has been provided. It has been emphasized that vortices produced by the flow must be energetic enough to penetrate the boundary layer such that it can then go on to resuspend the resident particulates. At the same time, the particulates are being forced to adhere to the surface via the adhesion forces. Of course, the strength of the removal forces must overcome that of the adhesion forces, which constitutes a key condition for resuspension.

The discussion thus far has focused on how the properties of the flow and the material characteristics of both the particulate and the surface it is placed on affect the prospects for particulate resuspension. What has not been discussed is how the actual size of the particulate affects its ability to be resuspended. This factor is relevant to the overall probability of a particulate being resuspended and will be the topic of discussion in the next section.

2.2.2 Effect of Particulate Size on Resuspension

Based on the results of their resuspension experiment, Kaftori et al. [28] made the following general observations on the size of the particulates that became resuspended:

- For smaller particulates (i.e. those with small diameters), most will be entrained into the main flow stream while only a few will be pushed aside by the vortex penetrating the boundary layer, forming short and narrow streaks.
- For larger particulates (i.e. those with large diameters), few of them will be entrained while most will be pushed aside by the vortex penetrating the boundary layer, forming massive streaks.

To shed some light on these observations, one can make the inference that when a vortex penetrates the boundary layer and interacts with the resident particulates, smaller particulates are more apt to be resuspended than the larger particulates due to the fact that smaller particulates possess lower mass than their larger counterparts. As a result, the

vortex does not have to expend much of its own energy in transporting the small particulates from the boundary layer and into the main flow stream.

The concept presented thus far, in that smaller particulates are more capable of resuspension than larger particulates, is challenged by the work of Kim et al. [31]. Here, equations that modelled the magnitude of the removal and adhesion forces acting on a particulate were cited. Hinds (1999) provided an empirical equation for the adhesion force acting on a hard non-deformable particulate that is placed on a clean surface (as cited in Kim et al. [31]), and this equation is shown below.

$$F_a = 15d_p(0.5 + 0.0045(\%RH)) \quad (2.7)$$

Where:

F_a = adhesion force acting on the particulate (unit: N)

d_p = particulate diameter (unit: μm)

$\%RH$ = relative humidity (unit: unitless)

Hall (1988) derived an empirical correlation for the mean lift and drag force acting on a particulate (as cited in Kim et al. [31]) and are shown in the following respective equations.

$$\frac{\langle F_L \rangle}{\rho_a \nu^2} \approx 20.9 \left(\frac{1}{2} \left(\frac{d_p u_*}{\nu} \right) \right)^{2.31} \quad \text{for} \quad 1.8 < \frac{1}{2} \left(\frac{d_p u_*}{\nu} \right) < 70 \quad (2.8)$$

Where:

F_L = mean lift force acting on the particulate (unit: N)

ρ_a = density of air (unit: $\text{kg}\cdot\text{m}^{-3}$)

d_p = particulate diameter (unit: m)

u_* = friction velocity (unit: $\text{m}\cdot\text{s}^{-1}$)

ν = kinematic viscosity of air (unit: $\text{m}^2\cdot\text{s}^{-1}$)

$$\frac{\langle F_D \rangle}{\rho_a v^2} \approx 32 \left(\frac{1}{2} \left(\frac{d_p u_*}{\nu} \right) \right)^2 \quad (2.9)$$

Where:

F_D = mean drag force acting on the particulate (unit: N)

Equations (2.7)-(2.9) possess two major features:

- The adhesion force is directly proportional to the particulate diameter to the first order
- The mean lift and drag forces (i.e., the removal force) are directly proportional to the particulate diameter at least to the second order

These features imply that as the size of the particulate decreases, the removal forces will become smaller than the adhesion forces. As a result, smaller particulates adhere to the surface to a greater extent, in comparison to larger particulates, and are therefore harder to resuspend. To further this argument, Kim et al. [31] outlined the effect of particulate size on their ability to be resuspended in relation to the boundary layer zones the particulates are situated in, and is discussed in Figure 2.12.

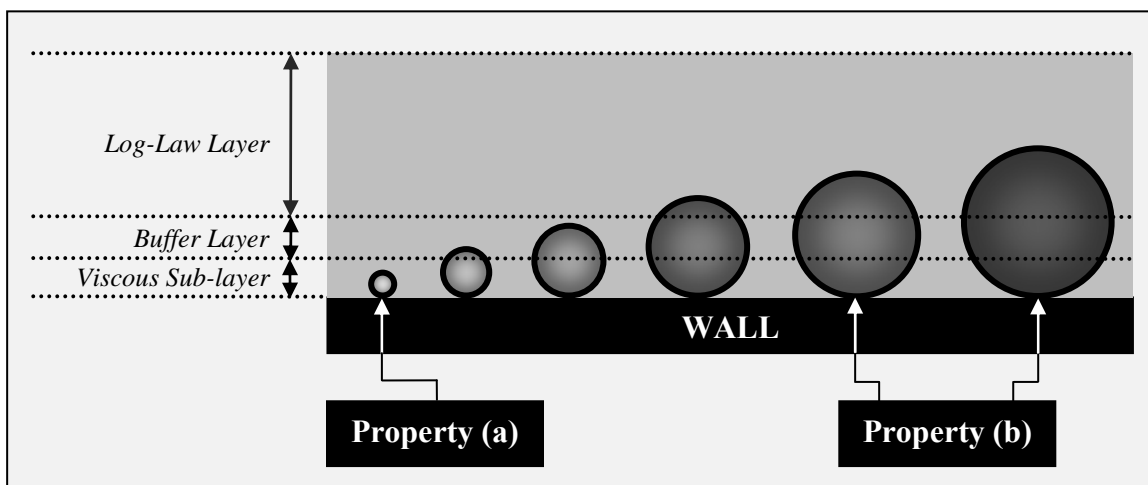


Figure 2.12 – Effect of Particulate Size on Resuspension

Figure 2.12 depicts two properties which are described in Table 2.7.

Property	Description
a	<p>Small particulates suffer from two deficiencies and are outlined below:</p> <p>(1) Due to their size, small particulates are trapped/enclosed in the viscous sub-layer. This particular zone of the boundary layer is the most viscous and so the resuspension vortex will have to expend much energy in order to penetrate the viscous sub-layer and resuspend the small particulates that reside.</p> <p>(2) As one moves further away from the wall, the fluid velocity gradient will increase. This implies that the fluid velocity gradient in the viscous sub-layer will be small in comparison to that of the other boundary layer zones. As a result, the small particulates of the viscous sub-layer will be unable to experience the skipping motion described earlier.</p> <p>An energetic resuspension vortex coupled with skipping motion is favourable for resuspension. These deficiencies, however, hamper the ability of small particulates to become resuspended.</p>
b	<p>Large particulates, due to their size, are able to “stick out” of the viscous sub-layer. This not only allows large particulates to be subjected to viscous forces (particularly on their lower ends), but also the inertia effects present in the boundary layer zones outside the viscous sub-layer. This has the following implications:</p> <p>(1) The resuspension vortex does not have to expend much energy in interacting with the large particulates in comparison to its energy expense when penetrating the viscous sub-layer.</p>

	<p>(2) Large particulates, due to their increased height, are subjected to a higher velocity gradient and will experience greater skipping motion, in comparison to smaller particulates.</p> <p>Contrary to small particulates, these properties of the large particulates are conducive to resuspension.</p>
--	--

Table 2.7 – Effect of Particulate Size on Its Resuspension Potential

The proposition stated by Kim et al. [31], in that larger particulates are resuspended more easily than smaller particulates, are also supported by several other works, and are briefly discussed below:

- Hill [32] analyzed the results of an experiment where radioactive particulates, initially placed on a plate, were resuspended by air flow, and noted that larger particulates were easier to resuspend.
- Nicholson [2] stated that a particulate projecting from the viscous sub-layer (as is the case with large particulates) has a greater chance of being rapidly resuspended as opposed to a particulate enclosed in a slow moving air flow (such as small particulates in the viscous sub-layer).

Clearly, there is some contradiction in what has been discussed in this section thus far. On one hand, Kaftori et al. [28] state that smaller particulates are easier to resuspend while Nicholson [2], Kim et al. [31], and Hill [32] advocate that larger particulates are more conducive for resuspension. To begin to find a middle ground, one can refer back to the work of Nicholson [2], who outlined the effect of particulate size on its ability to remain in suspension, once resuspended. This relationship is described in Table 2.8.

Particulate Diameter Range	Particulate Motion
$<\sim 10\mu\text{m}$	Particulates are resuspended for a <i>considerable</i> amount of time.
$<\sim 100\mu\text{m}$	Particulates are resuspended for a <i>smaller</i> amount of time (in comparison to the motion of particulates whose diameter is less than $10\mu\text{m}$).
$100\mu\text{m}$ to $500\mu\text{m}$	Particulates experience what is known as <i>saltation</i> . Here, the particulates are ejected almost vertically into the main flow stream and gain considerable horizontal momentum but then fall back to the surface.
$500\mu\text{m}$ to $1000\mu\text{m}$	Particulates gain no significant vertical motion; they are confined to rolling along the surface (this is known as <i>surface creep</i>). Note that this rolling is different than the one described earlier which is attributed to shear stress and surface asperities.

Table 2.8 – Relationship between Particulate Diameter and Particulate Motion

Table 2.8 illustrates an important feature of particulate resuspension, in that *as the particulates become larger, their ability to remain in suspension for an extended period of time becomes hampered*. In light of this, one can now draw the following consensus on the effect of particulate size on its ability to be resuspended:

- (1) Removal forces cannot easily penetrate the viscous sub-layer and resuspend the resident particulates. However, if the resuspension vortex is energetic enough (for example, if a high Reynolds Number flow is considered), it can penetrate the viscous sub-layer and resuspend the small particulates. These small particulates will go on to remain in suspension for a considerable amount of time.
- (2) Removal forces can easily access larger particulates in comparison to smaller particulates. However, once the large particulates are captured by the

resuspension vortex, the vortex may have difficulty in transporting these particulates from the boundary layer and into the main flow stream. This is attributed to the fact that larger particulates are more massive than their smaller counterparts. The large particulates can have two possible fates at this stage. The first is that the particulate is able to enter the main flow stream but due to the large force of gravity acting upon it (in comparison to lighter particulates), the particulate will fall back to surface. The second fate is that, for particularly massive particulates such as those that fall into the last particulate diameter range shown in Table 2.8, the resuspension vortex is unable to capture these particulates. Instead, as a result of the vortex's attempt to "pick up" the particulate, the particulate simply rolls along the surface.

The discussions that have taken place thus far have focused on how the forces acting on a particulate and the size of the particulate affect the particulate's ability to be resuspended. In experimental setups, a particulate's ability to be resuspended also becomes time-dependent and will thus be the subject of the next section.

2.2.3 Time-Dependence of Particulate Resuspension

In a typical particulate resuspension experiment, particulates will initially be placed on the floor of the flow domain, such as that of a wind tunnel. The flow field will be transient in nature since the inlet fluid velocity will initially change over time. This enables the experimentalist to explore how the number of resuspended particulate changes over time and how the size of a particulate dictates when it will be resuspended.

The experiment conducted by Braaten et al. [29] involved the use of monodisperse particulates. Here, particulates were placed on the floor of a wind tunnel and exposed to an initially transient flow stream. To assess the affect of particulate characteristics on when a particulate will be resuspended, an adhesion force distribution was measured for the particulates placed on the floor of the wind tunnel. Based on the experimental data obtained, a qualitative and quantitative description of how the

cumulative fraction of particulates resuspended (normalized to the total number of particulates initially placed on the wind tunnel floor) changes over time has been attained. This description is shown in Figure 2.13.

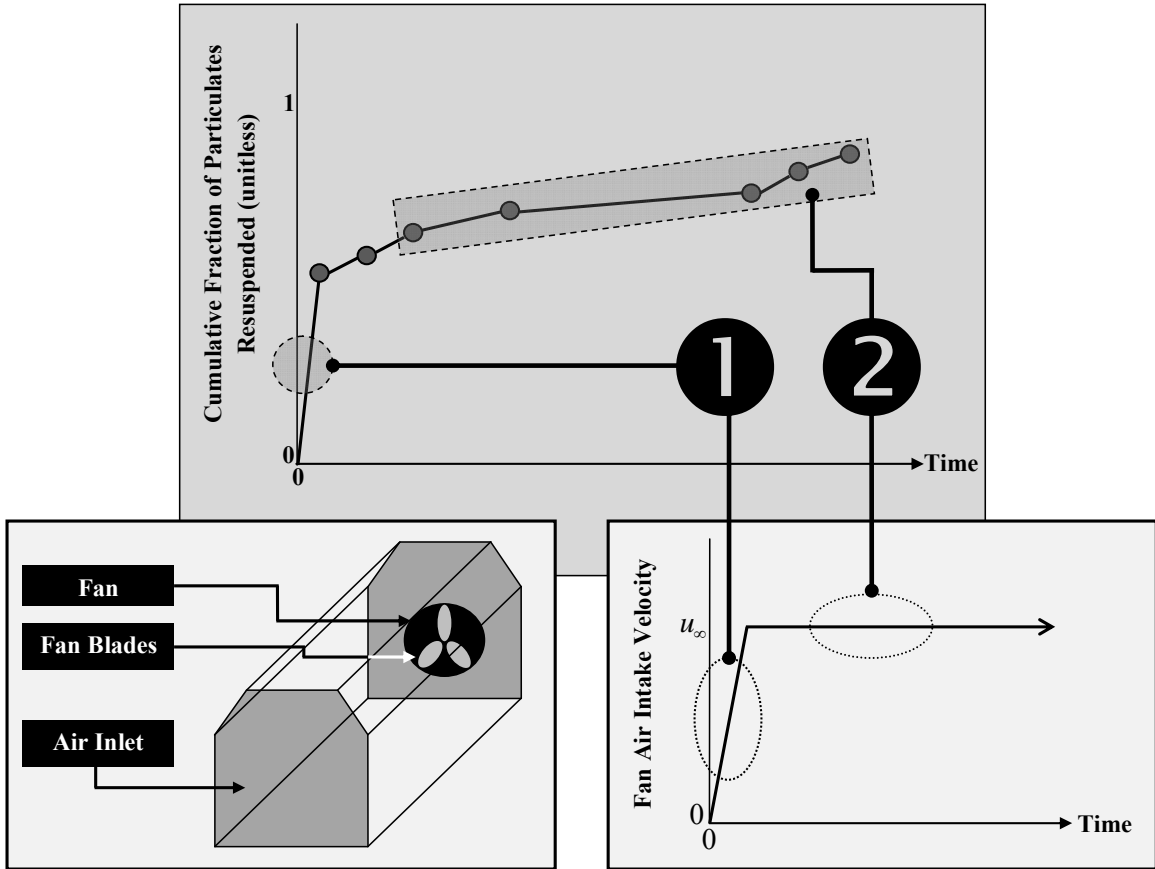


Figure 2.13 – Qualitative Description of the Variation of the Cumulative Fraction of Particulates Resuspended with Time [29]

Before a discussion on the main plot shown in Figure 2.13 ensues, the transient flow field characteristic of resuspension experiments must first be discussed. In these experiments, a motor-based apparatus such as a fan is used to inject air into the domain at the desired inlet fluid velocity (denoted by u_∞). However, these fans cannot rotate at a rate that will yield the equivalent of the desired inlet fluid velocity as soon as it is turned on. Rather, the fan will “ramp up” from zero velocity to the desired inlet fluid velocity over a short time interval and will maintain this velocity for as long as required. This

change in inlet fluid velocity over time is shown in the plot in the lower right inset of Figure 2.13.

Air is injected into the domain not from the inlet, but by a fan that is placed at the back of the flow domain as illustrated in the figure in the lower left inset of Figure 2.13. Once turned on, the fan will rotate such that a “sucking” effect will be produced that will draw air towards it. The overall effect is that air will be drawn into the flow domain through the inlet at the desired inlet velocity. Of course, the fan will operate in the manner described above in regards to the “ramp up” shown in the lower right inset of Figure 2.13.

The main plot in Figure 2.13 indicates a relationship between the cumulative fraction of particulates resuspended over time with respect to the transient characteristic of the fan air intake velocity. This relationship is described further in Table 2.9.

Relationship	Description
1	<p>As per the profile shown on the lower right inset of Figure 2.13, the fan air intake “ramps up” from rest to the desired inlet air velocity u_{∞}. It has been documented that a higher Reynolds Number yields more energetic resuspension vortices. Since the Reynolds Number is directly proportional to the inlet air velocity, it follows that the resuspension vortices during this transient period will not be as energetic as it would be in the post-transient, steady-state period illustrated in the plot on the lower right inset of Figure 2.13.</p> <p>However, Braaten et al. [29] notes that a very large fraction of particulates were resuspended during this transient period and is evident in the sharp rise in the main plot shown in Figure 2.13. Termed the <i>initial “blow-off” period</i>, Braaten, et al. [29] noted that based on the particulate adhesion distribution, the resuspended particulates were subjected to low adhesion forces. As a result of the lower energy flow</p>

	structures present during this period, it was noted that the resuspension vortices did not have to expend much energy to resuspend these particulates.
2	This is the steady-state phase, with respect to the fan air intake velocity, and it follows from the discussion in Relationship 1 that since the air intake velocity is at its maximum, the flow structures will be the most energetic during this period. It was noted, however, that a smaller amount of particulates were resuspended during this period, as evidenced by the relatively small growth shown in main plot in Figure 2.13 in the post-transient period. Based on the particulate adhesion distribution, Braaten, et al. [29] noted that the resuspended particulates were subjected to higher adhesion forces and that the energetic flow structures were much more persistent in resuspending these particulates.

Table 2.9 – Relationship between the Amount of Resuspension and the Transient Nature of the Fan Air Intake Velocity

The adhesion force equation cited by Kim et al. [31] stated that the adhesion force is directly proportional to the particulate diameter to the first order. This implies that for a set of monodisperse particulates, each particulate should be subjected to the same magnitude of adhesion force. However, the experiment by Braaten et al. [29] measured an adhesion force distribution for the monodisperse particulate used and as discussed in Table 2.9, the resuspension of particulates during the transient and steady-state phases were still attributed to the variation in the magnitude of the adhesion forces that the particulates were subjected to.

To justify this observance, one can refer to Hinds [8] who lists several factors that affect the adhesion forces acting on a particulate and of these, surface roughness is mentioned. Surfaces in reality are not perfectly smooth and possess asperities, which are an embodiment of surface roughness. Figure 2.7 illustrates such asperities and how it affects the motion of particulates. It has been stated in the aforesaid section that a

particulate placed between asperities must acquire enough rotational energy imparted by the removal forces in order to escape the “potential well” formed by the asperities. Certainly, the physical depth to which a particulate is embedded between asperities will affect the resuspension potential of the particulate. For example, if the lower portion of a particulate simply rests on the asperities, the potential well it must escape will not be as steep as that of a particulate, of the same size, whose sides are resting against the asperities. Thus, the major factor in these two respective situations is the distance between the asperities and in most materials, this distance is not uniform throughout. As such, this will enable one to measure an adhesion force distribution for a monodisperse group of particulates.

Nevertheless, the time-dependent nature of particulate resuspension has been discussed and it is clear that as the flow field develops, so too does the resuspension vortices. These vortices, although of low energy, go on to resuspend particulates that are subjected to low adhesion forces. When the flow field becomes fully developed, it will produce energetic resuspension vortices. These high energy vortices will go on to resuspend particulates that possess high adhesion forces.

The discussion that has taken place thus far in Section 2.2 has focused on the complex nature of particulate resuspension. Emphasis has been placed on how (a) the forces interacting with a particulate and (b) the particulate size influences a particulate’s ability to become resuspended. Particulate resuspension has been shown to be dependent on the nature of the flow, the physical and material properties of the particulate, and the material characteristics of the surface that the particulates are placed on. This section will now conclude with a cumulative list of parameters that directly affect particulate resuspension, and will therefore be the subject of the next section.

2.2.4 Parameters Affecting Particulate Resuspension

Kim et al. [31] sought to develop a cumulative list of parameters that have a direct affect on the resuspension of particulates. These parameters are pertinent to the physical and material characteristics of the flow stream, the particulate, and the surface that the particulates are placed on. This list is shown in Figure 2.14 and the parameters presented are grouped into respective categories.

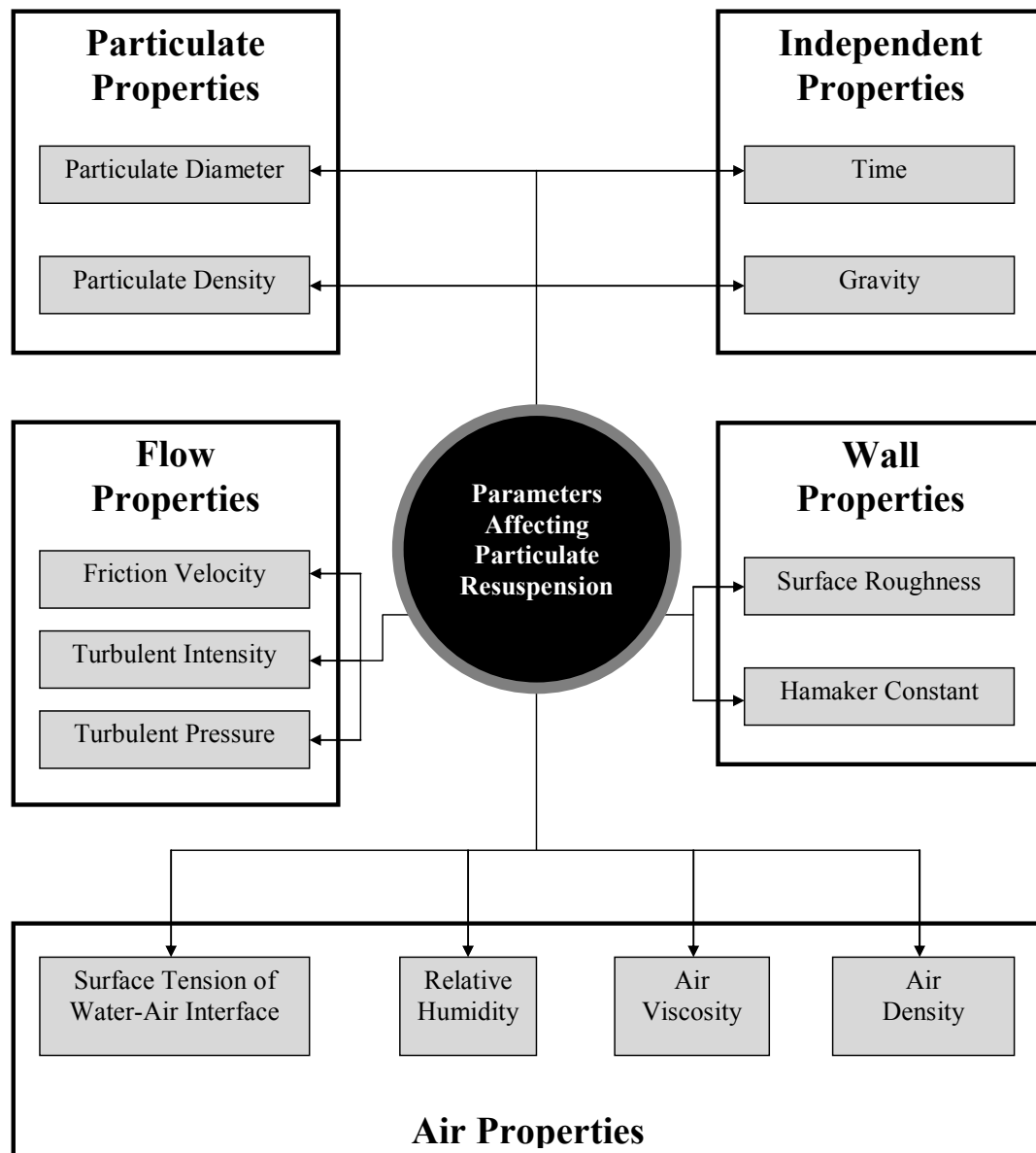


Figure 2.14 – Parameters Affecting Particulate Resuspension [31]

Table 2.10 discusses how each of the parameters listed in Figure 2.14 affect particulate resuspension.

Parameter	Description
<i>Particulate Properties</i>	
Particulate Diameter	The diameter of a particulate affects the magnitude of the removal and adhesion forces it is subjected to.
Particulate Density	The density of the particulate dictates (a) the degree to which its presence impacts the flow stream and (b) the importance of particulate-to-particulate interactions.
<i>Air Properties</i>	
Surface Tension of Water-Air Interface	Surface tension is a measure of how the surface of one medium is attracted to that of another. The discussion on Capillary Force illustrates the importance of this quantity whereby the surface tension of the condensed water vapour in the capillary space acts as an intermediary by which the particulate is adhered to the wall.
Relative Humidity	Depending on the temperature in the flow domain, water vapour in the air can condense in the capillary space between the particulate and the surface. The condensed water vapour forms an attractive force between the particulate and the surface.
Air Viscosity	The viscosity of air will affect the Reynolds Number of the flow and will dictate the movement of particulates in the boundary layer. The more viscous the fluid, the more effective it is in trapping small particulates in the viscous sub-layer.
Air Density	The density of air is directly proportional to the Reynolds Number. Thus, this quantity will influence how energetic the air flow and the resultant resuspension vortices will be.
<i>Flow Properties</i>	
Friction Velocity	The friction velocity is a characteristic velocity (that is derived from scaling fluid-based equations). Based on the equation for friction

	velocity, it is directly proportional to the shear stress. A higher shear stress, and therefore a higher friction velocity, greatly enhances a particulate's ability to be resuspended.
Turbulent Intensity	The turbulent intensity is a measure of how energetic a flow is and more particularly, how energetic the flow structures (such as resuspension vortices) are. Highly energetic flow structures are more capable of penetrating deeper into the boundary layer (particularly the viscous sub-layer) and are more forceful in dislodging particulates on the surface and resuspending them into the main flow stream.
Turbulent Pressure	The turbulent pressure is a function of what is known as the <i>Reynolds Stress</i> . A higher Reynolds Stress indicates that adjacent fluid layers experience greater friction against each other's movement.
<i>Wall Properties</i>	
Surface Roughness	The presence of asperities on a surface causes particulates to experience "Rock 'n' Roll" motion, which will result in the particulates experiencing an additional lift force.
Hamaker Constant	The Hamaker Constant is a force constant that is used in quantifying the van der Waals force that exists between two mediums which in the case of Figure 2.10 are the particulate and the surface. The value of the Hamaker Constant is indicative of the strength of the van der Waals force that exists between the two aforesaid mediums. In the context of Figure 2.10, this constant is calculated via material properties of the particulate, the surface, and the condensed water vapour that exists in the separation distance [33].
<i>Independent Properties</i>	
Time	Section 2.2.3 has established the fact that the amount of particulates resuspended from a surface is a function of time.
Gravity	Once resuspended, the ability of a particulate to remain in suspension is dependent upon the effect that gravity has on its motion. Kaftori et al. [28] found that gravity has a significant impact on the motion of larger

particulates. Since these particulates possess a larger force of gravity, this hampered their ability to remain in suspension for an extended period of time.

Table 2.10 – Description of Parameters Directly Affecting Particulate Resuspension

In summary, the theory behind the resuspension of particulates has been discussed. Section 2.1 outlined the physical nature of the boundary layer while Section 2.2 looked at how the boundary layer hinders and how vortices encourage particulate resuspension. In addition, the effect of particulate size on the particulate’s ability to become resuspended has also been examined. What is important to recognize is that the particulate of interest to this thesis are radioactive and will therefore emit radiation. Thus, the next section will explore the theory of radiation transport.

2.3 Radiation Transport Theory

Quantifying the dose from the resuspension of radioactive particulates constitute a major component of the CFD-MC radiation transport coupling methodology developed in this thesis. Nuclear radiation arises from the situation where there is an imbalance between the number of protons and neutrons in the nucleus of an atom. Here, the nucleus is left in an excited state (i.e. has excess energy) and will seek to go to the ground state. It will get rid of this excess energy by emitting *radiation*. There are several types of radiation, and these will be discussed below.

2.3.1 Description of Radiation Types

There are four principal radiation types, each of which has an associated energy and charge. As will be discussed, the energy level and the charge each radiation type possesses are of importance when assessing the radiological hazard posed by the radiation type in question. Table 2.11 lists the different attributes of each radiation type.

Radiation Type	Range	Energy	Charge	Internal Hazard	External Hazard
Alpha	Short	High	Positive	High	Low
Beta	Moderate	Low to High (varies)	Negative	High	Medium
Gamma	Long	High	Neutral	Medium	High
Neutron	Long	Low to High (varies)	Neutral	N/A	High

Table 2.11 – Attributes of Different Radiation Types [34]

To assess the hazard that each radiation type poses to humans, the charge that it possesses is of primary importance. The charge dictates whether or not the radiation type in question manifests itself as an internal hazard (i.e. can cause damaging affects to internal tissues and organs of a human if ingested or inhaled) or an external hazard (i.e. can cause damaging effects when one is externally exposed to radiation). The reality is that charged radiation, when interacting with the organs and tissue of a human which also possesses a charge, can produce biological damage to varying degrees. For instance, charged radiation can affect the coding of DNA strands thereby causing cell mutation or death.

Moreover, the energy of the radiation is another important attribute that will also determine the amount of biological damage induced to the human. Simply put, the more energetic the radiation is, the more energy it can deposit in the organs and tissue of the human and the greater its ability to penetrate deeper into the human body.

Indeed, the movement of radioactive particles in an absorbing mass will deliver a radiation dose. Hence, the transport of radioactive particles is a prerequisite to dose calculations. As per the research blueprint presented in Chapter 1, MC techniques will be used as the basis for radiation transport calculations and so it is essential that a description of how this technique will be used for radiation transport calculations be provided. This will be the topic of the next section.

2.3.2 Monte Carlo Radiation Transport

MC radiation transport seeks not to solve the actual transport equation for the particular radiation type, but uses approximations (with the aid of random numbers) to simulate the physics of how the radiation interacts with the atoms of the host material it is travelling in. The basic steps of a MC radiation transport simulation are shown in Figure 2.15.

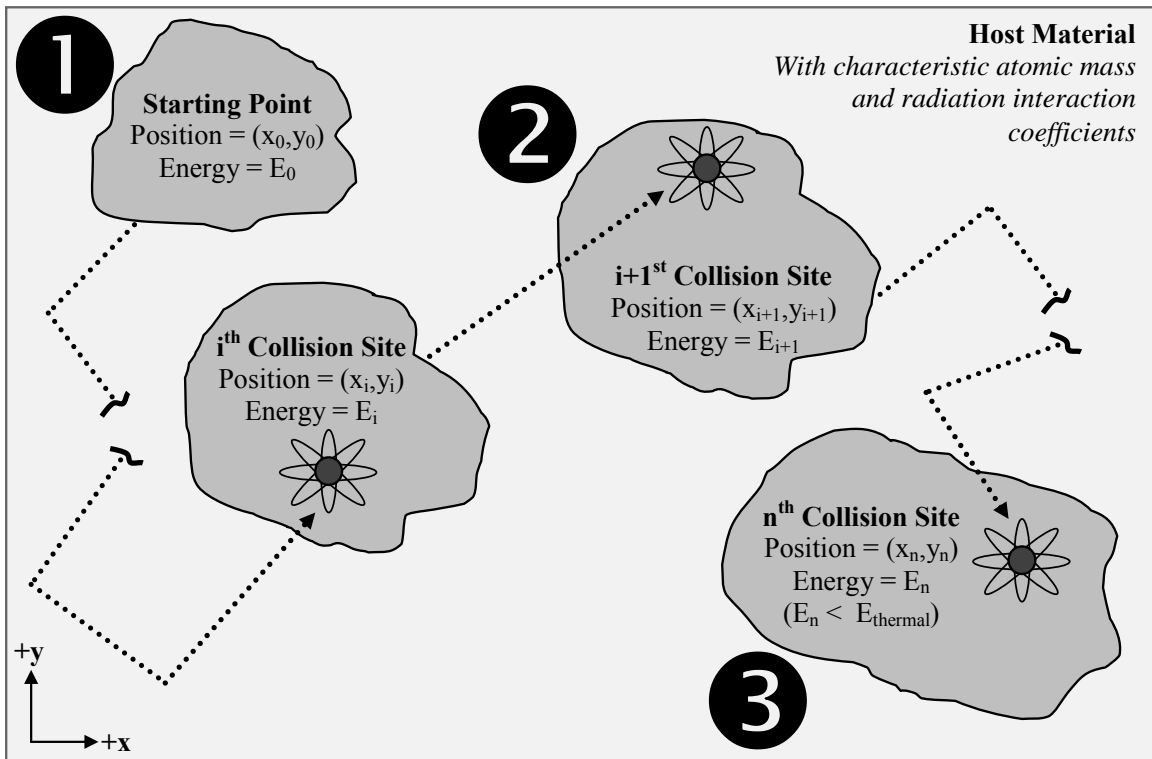


Figure 2.15 – Illustration of the Basic Steps of a MC Radiation Transport Simulation

Figure 2.15 depicts the basics steps in a MC radiation transport simulation, and is elaborated on in Table 2.12.

Step	Description
1	Provide each radioactive particle with initial values (such as initial position, initial energy, etc).
2	Calculate the properties of the radioactive particle (such as position and energy) at each collision site using the approximations made to solve the

	transport equation for the radiation type whose transport is simulated. At particular spatial locations within the domain of interest, one can calculate (i.e. <i>tally</i>), amongst others:
	(1) Particle flux (2) Dose delivered by particle flux
3	To perform a realistic simulation, the radioactive particle will eventually attain an energy below some threshold energy. This indicates that the particle has reached the end of its life and at this point will no longer be tracked.

Table 2.12 – Description of the Basic Steps of a MC Radiation Transport Simulation

It is important to mention that in a MC radiation transport simulation, the movement of each radioactive particle is analyzed. As a result, there are two key features that a MC simulation provides, and are outlined below:

- (1) The tally that the user seeks (such as particle flux) is normalized to the number of source particles (i.e., the number of radioactive particles whose transport is simulated). The purpose of this normalization is that it allows the user to vary the number of source particles until the normalized tally result becomes independent of the number of source particles whose transport are simulated.

- (2) Statistics are central to the use of MC methods as witnessed by the fact that multiple samples in the form of particles are used to calculate the mean value of the quantity of interest (i.e. the tally). As a result, statistical quantities can be used to quantify and assess the accuracy of the tally result obtained.

Once the normalized tally becomes independent of the number of source particles chosen and the fractional standard deviation²⁴⁾ of the normalized tally is below an

²⁴⁾ The *fractional standard deviation* is defined as the standard deviation divided by the mean value of the tally of interest.

acceptable limit²⁵⁾, it can then be concluded that the MC simulation has been successfully performed.

In light of the theories presented on fluid dynamics, particulate resuspension, and radiation transport, a description of how these fields interface with each other for the purpose of this thesis will now be presented. This discussion will assist in understanding what exactly is being simulated and how these respective fields are used in concert in order to simulate the resuspension of radioactive particulate and the resultant radiation field.

2.4 Integration of Fluid Dynamics and Monte Carlo Radiation Transport

With reference to the fundamental principals governing the fields of Fluid Dynamics²⁶⁾ and MC Radiation Transport as described previously, it is essential to describe how these two fields of study can be integrated in order to study the resuspension of radioactive particulates and the resultant radiation field. To provide a simple description of this coupling, consider Figure 2.16 where the movement of a single radioactive particulate is used to illustrate how the coupling is performed.

²⁵⁾ The “acceptable limit” is defined as having the fractional standard deviation of the tally being less than 5% [35].

²⁶⁾ It is evident from the discussion in Section 2.2 that particulate resuspension theory is closely tied to that of fluid dynamics. For simplicity, the term *Fluid Dynamics* is an umbrella term used to describe the fields of both fluid dynamics and particulate transport.

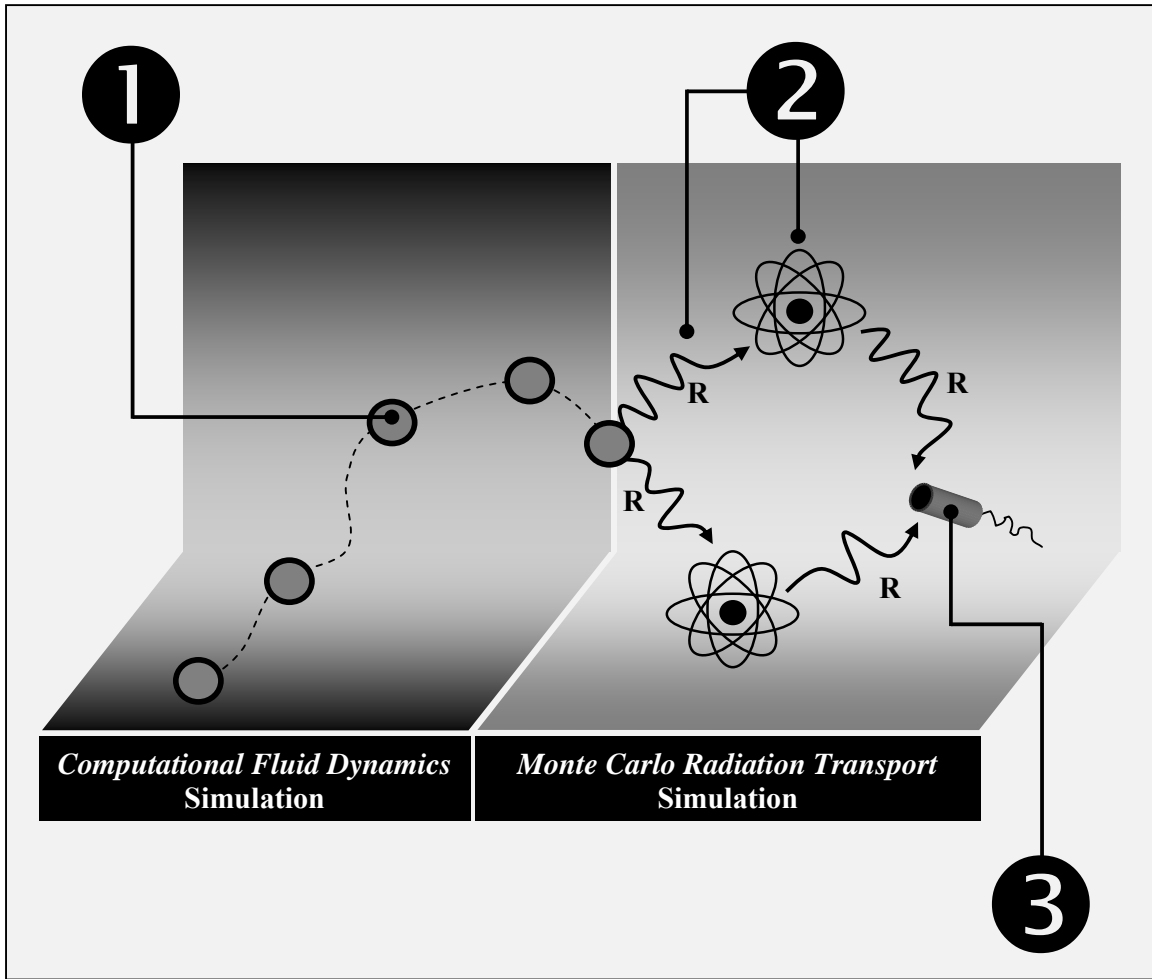


Figure 2.16 – Description of CFD-MC Radiation Transport Coupling

Figure 2.16 illustrates the steps required for the coupling of CFD and MC radiation transport simulations, and is elaborated on in Table 2.13.

Step	Description
1	In the <i>CFD simulation</i> , the fluid flow displaces the particulate. Thus, each particulate will acquire a new spatial location in the flow domain.
2	In reality, each particulate is radioactive and emits radiation (whose type is denoted by R). The emitted radiation will go on to interact with the atoms of the material it is surrounded by (for example, air in a wind tunnel).
3	In the <i>MC radiation transport simulation</i> , a “source” is placed in the exact location that each particulate has been displaced to. This source will replicate

the physical and radiological characteristics of the particulate, such as density, diameter, radiation type emitted, radiation energy, etc.

In the radiation transport simulation, radiation will be emitted from the source and “detectors” (in the form of *tallies*) will be placed in spatial position(s) of interest. These tallies will detect radiation quantities such as radiation flux, radiation dose, etc. In fact, the spatial distribution of radiation quantities such as radiation flux can be obtained via the use of tallies in that tallies can be placed at multiple spatial positions of interest within the flow domain.

Table 2.13 – Basic Steps of the CFD-MC Radiation Transport Coupling Procedure

Figure 2.16 and Table 2.13 have established the basis on which CFD and MC radiation transport simulations are coupled. The coupling procedure will be discussed in much greater detail in Chapter 3.

The theoretical background presented in this chapter is diverse in that theories pertinent to fluid dynamics, particulate resuspension, and radiation transport have been presented. A glimpse into how these respective fields interface with each other for the purpose of this thesis has just been provided. It is fitting that at this point, a brief summary of what has been presented in this chapter now ensue.

2.5 Summary

This chapter has presented the theoretical background of the fields pertinent to this thesis – fluid dynamics, particulate resuspension, and radiation transport. An overview of how these fields are coupled for the purpose of simulating radioactive particulate resuspension and subsequent radiation field determination has been provided, and this will serve as a prelude to Chapter 3. Chapter 3 will discuss in detail the methodology that has been developed for the aforementioned purpose. Once this methodology is described, Chapter 4 will then present the results of the methodology developed for the resuspension scenario described in Section 3.1.

CHAPTER 3

EXPERIMENTAL SETUP AND MODELLING METHODOLOGY

The purpose of this chapter is twofold. The first is to provide a description of the geometry that will be employed in the CFD and MC radiation transport simulations. Of course, the fluid flow and radioactive particulate resuspension will be characterized in this geometry and so the geometry is pivotal in illustrating how the aforementioned simulations are coupled. Once this geometry is described, the methodology developed to couple these two simulations will be documented.

The geometry that is used is similar to that of the WIS Wind Tunnel located in Munster, Germany [1]. This wind tunnel is used for radioactive particulate resuspension experiments and was built in support of the international collaboration on particulate resuspension described at the beginning of Chapter 1.

3.1 Description of the WIS Wind Tunnel

This section is partitioned into two parts. The first will describe the physical configuration of the WIS Wind Tunnel, discussing its important features. The second will describe the radioactive particulates used for the resuspension experiments in this wind tunnel.

3.1.1 Physical Configuration of the WIS Wind Tunnel

Figure 3.1 shows an exterior view of the wind tunnel.

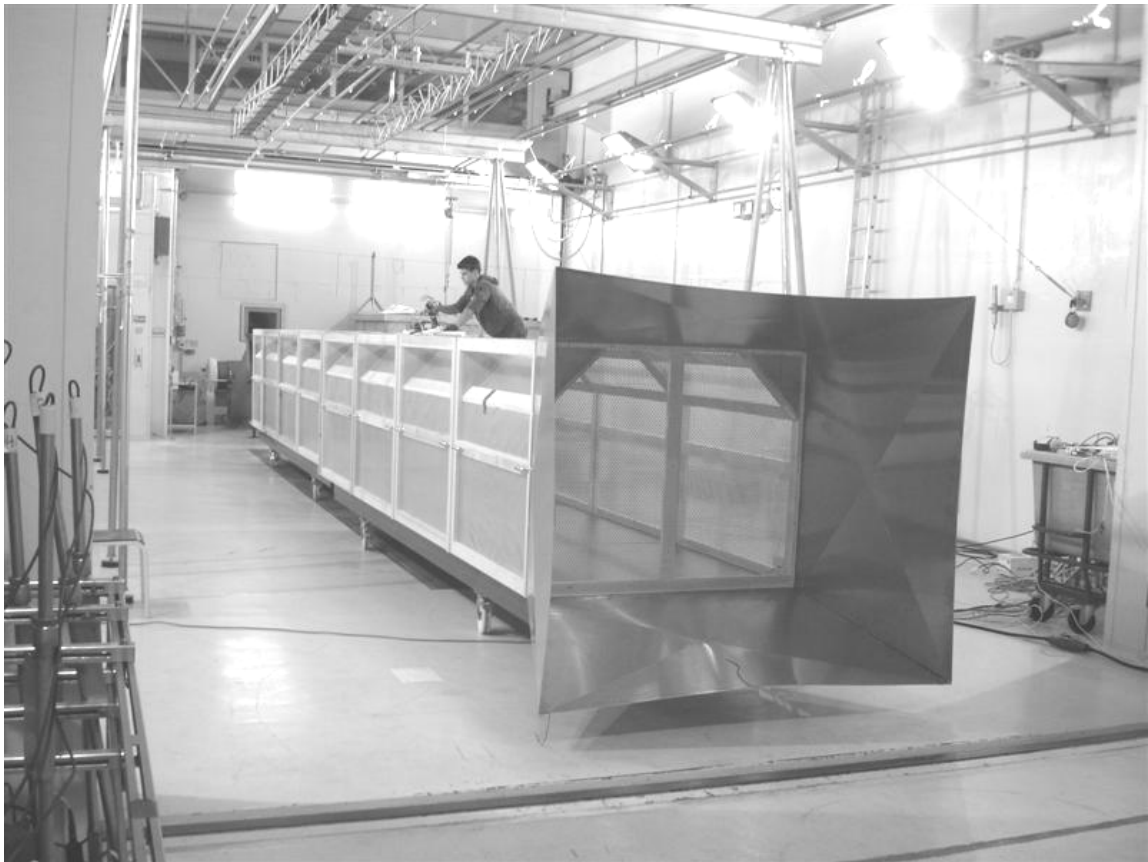


Figure 3.1 – Exterior View of WIS Wind Tunnel

The foreground of Figure 3.1 illustrates that the wind tunnel has a quasi-hexagonal cross section. Figure 3.2 provides an interior view and identifies key features located within the wind tunnel.

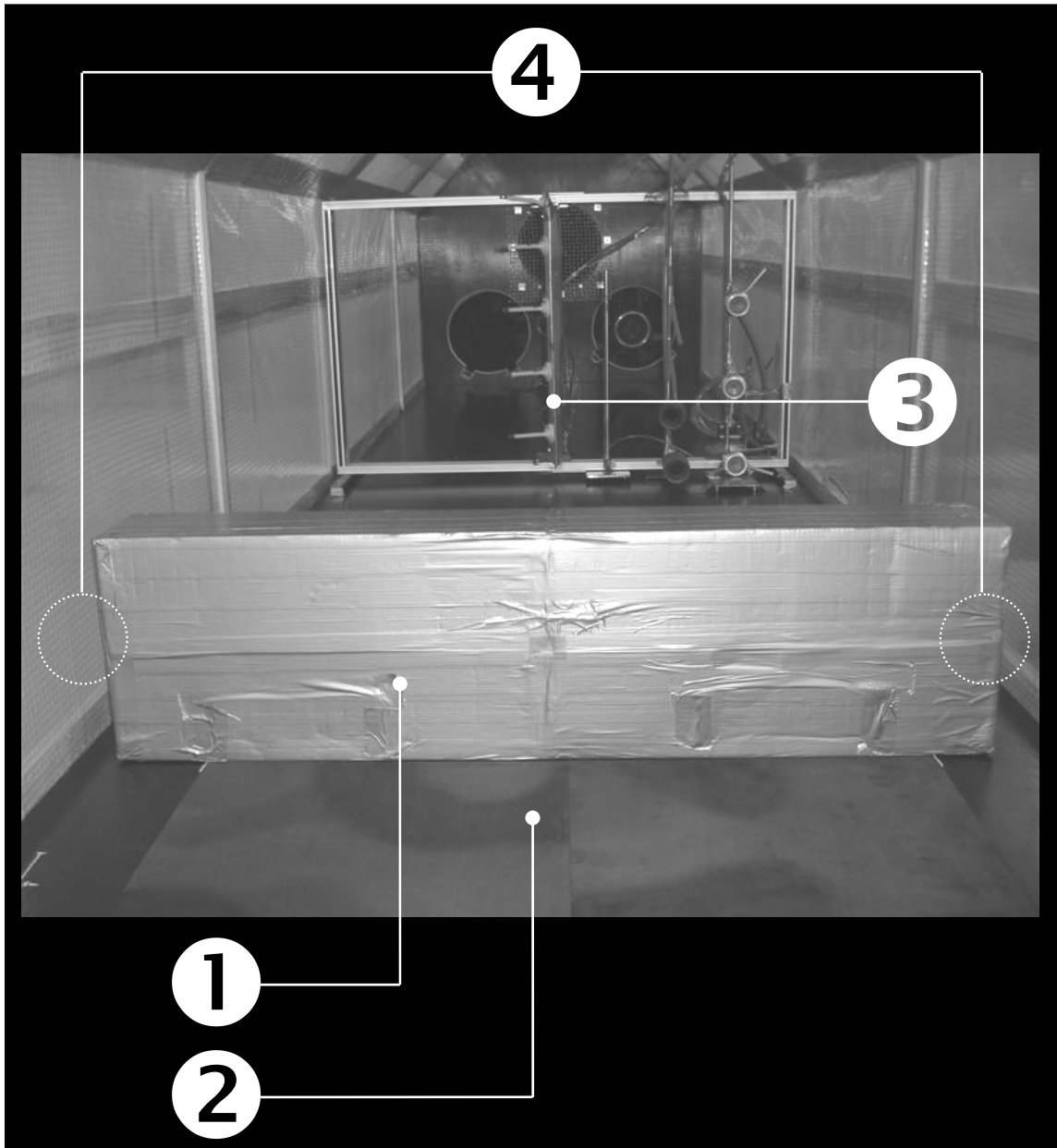


Figure 3.2 – Interior View of WIS Wind Tunnel (Downstream View): 1 - Bluff Body, 2 - Plate, 3 - Velocity Probes, 4 - Openings

Figure 3.2 shows a barrier at the bottom of the wind tunnel acting as a bluff body. As per the schematics of the WIS Wind Tunnel provided in Appendix A, the distance between the velocity inlet and the bluff body is considerably large and so as the flow approaches the bluff body over this distance, a mature boundary layer will develop. However, the growth of this boundary layer along the aforementioned distance abruptly halts once the flow interacts with the bluff body, since the flow is not traversing over a flat surface but rather traversing over an elevated surface at this point and so in essence, the bluff body trips the boundary layer. The floor in front of the bluff body serves as a plate surface on which radioactive particulates are placed prior to the injection of high speed air flow into the wind tunnel. Velocity probes are placed at location 3 and will measure the air velocity downstream of the bluff body (Table A.2 in Appendix A contains air velocity data measured by these probes for various experimental conditions). Figure 3.2 also identifies small openings to each side of the bluff body which allow for air to flow around the bluff body inducing the formation of vortices behind this structure.

Further to the features identified in Figure 3.2, Figure 3.3 displays apparatus pertinent to the injection of high speed air flow into the wind tunnel.



Figure 3.3 – Interior View of WIS Wind Tunnel (Downstream View Without Bluff Body)

Figure 3.3 shows fans in the background. High speed air flow is injected into the domain in the manner described in Figure 2.13. Here, the fans, located at the back of the wind tunnel, will rotate at a rate that will draw in air through the inlet (shown in the foreground of Figure 3.1) at the desired inlet velocity.

Although interior and exterior views of the WIS Wind Tunnel have been shown, a comprehensive view of the wind tunnel will be provided. This view will enable one to fully visualize the processes taking place within the wind tunnel. Figure 3.4 shows a three-dimensional rendering of the wind tunnel.

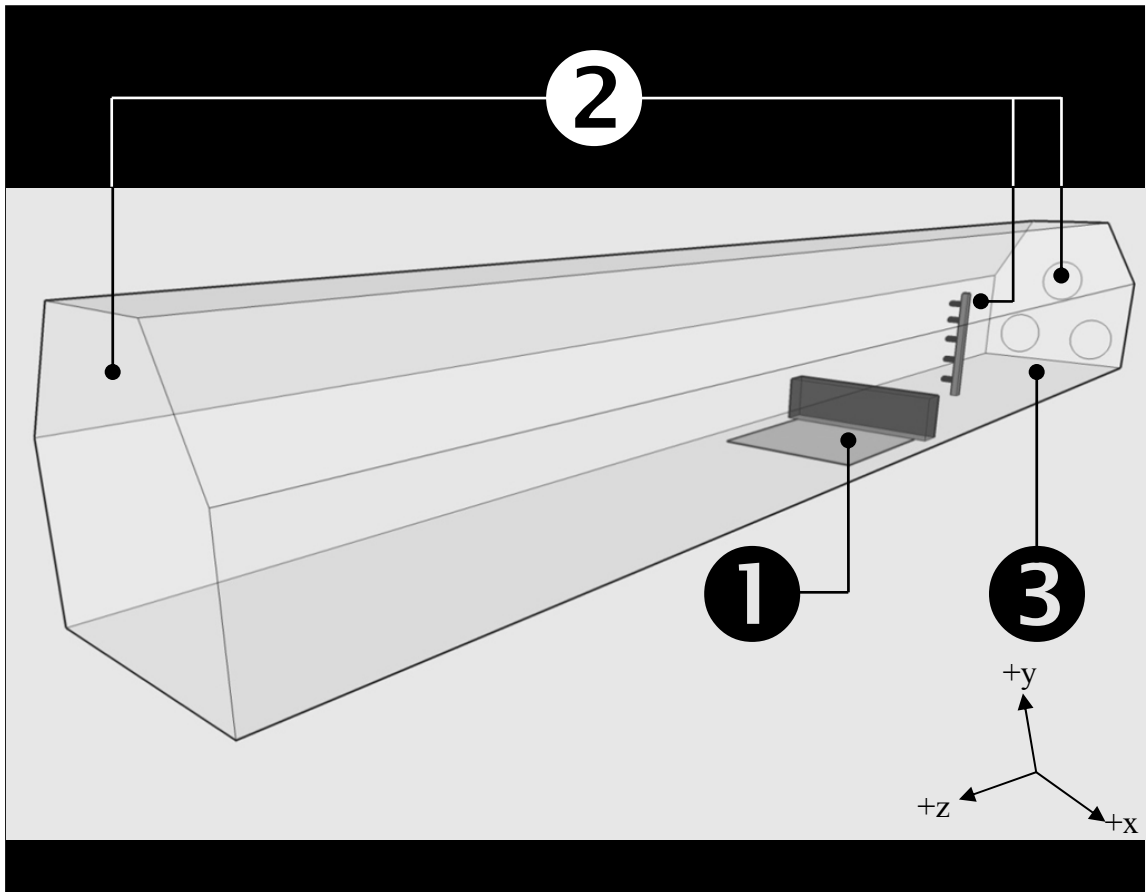


Figure 3.4 – Three-Dimensional Rendering of the WIS Wind Tunnel

Figure 3.4 shows a three-dimensional view of the WIS Wind Tunnel, complete with those of the bluff body, plate, and velocity probes. This figure also indicates the major phenomena occurring in the radioactive particulate resuspension experiments that take place in the WIS Wind Tunnel. These phenomena will be discussed in a step-wise manner and will begin with the first step which involves the placement of radioactive particulates on the plate, at rest. Secondly, fans are turned on and eventually rotate at a rate such that air entering the inlet is equal to 6 m/s (see Figure A.4 in Appendix A). Once the flow becomes fully developed, the velocity probes will record the air velocity downstream of the bluff body. Finally, as high speed air flow is injected into the wind tunnel, particulates will be displaced (i.e., resuspended) from the plate, enabling particulates to acquire new spatial locations.

The wind tunnel materials are described in Table 3.1. When performing radiation transport calculations, knowledge of the material type through which the radiation is

traversing is of critical importance since solving the transport equation for the radiation type in question requires the use of radiation interaction coefficients which in turn are dependent on the material being dealt with.

WIS Wind Tunnel Feature	Material
Bluff Body	Plywood
Plate	Plywood
Fluid	Air

Table 3.1 – Description of the Materials Used in the WIS Wind Tunnel

In addition to the materials described above, the material composition of the particulate is of interest and is discussed in the following section.

3.1.2 Radionuclide Properties of Resuspension Particulate

Particulate that possess a resuspension radiation hazard are of interest to this thesis. The resuspension experiments performed in the WIS Wind Tunnel employ particulates composed of the compound $^{140}\text{La}_2\text{O}_3$ (Lanthanum Oxide Powder). From a radiation perspective, Oxygen is naturally stable while Lanthanum-140 emits both beta and gamma radiation, *and thus Lanthanum-140 poses a resuspension radiation hazard.* The decay chain for Lanthanum-140 is shown in Figure 3.5.

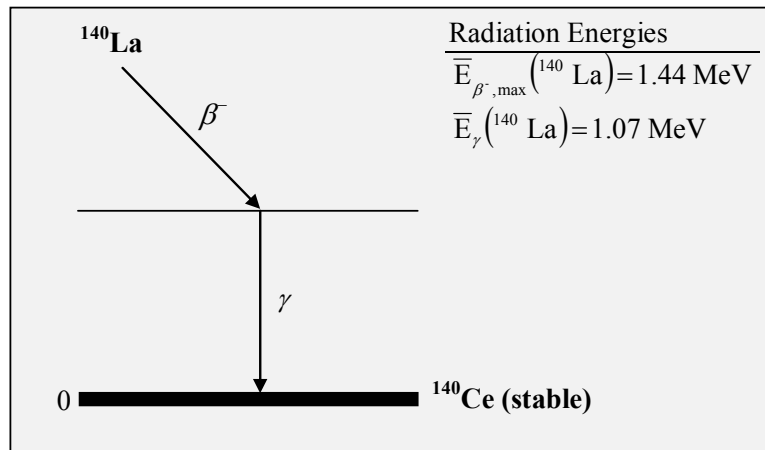


Figure 3.5 – Decay Chain for Lanthanum-140 [36]

It is of note that the radiation energies listed in Figure 3.5 are weighted based on the radiation emission probabilities. The beta and gamma radiation emitted from Lanthanum-140 will be accounted for in the MC radiation transport modelling and dose calculation segments of the CFD-MC radiation transport coupling blueprint that has been outlined in Chapter 1.

It is worthy to note that there are two appendices that contain information related to the physical configuration of the WIS Wind Tunnel and the materials employed. Appendix A contains detailed schematics of the WIS Wind Tunnel and Appendix B contains radiation data for Lanthanum-140 and physical data for the materials listed in Table 3.1. The information contained in these appendices is vital to the coupling methodology described in the next section. As mentioned at the beginning of this chapter, the physical configuration of the WIS Wind Tunnel and the resuspension process described in Figure 3.4 will be used as the basis by which CFD and MC radiation transport simulations will be coupled for the purposes of simulating the resuspension of radioactive particulates and characterizing the resultant radiation field. The next section will describe how this is done.

3.2 Modelling Methodology

To begin the process of developing a methodology to couple CFD and MC radiation transport simulations, the codes that (a) perform these respective calculations, (b) couples these calculations, and (c) perform a dose estimate from the radiation field produced from the resuspension of particulates, must first be identified. Table 3.2 lists the selected codes.

Discipline	Code Selected
CFD	GAMBIT + FLUENT
MC Radiation Transport	MCNPX
Black Box/Dose Calculations	MATLAB (original code produced for this thesis)

Table 3.2 – Identification of Codes Selected

GAMBIT is similar to a three-dimensional Computer Aided Design (CAD) software package in that it allows the user to build the geometry in which fluid flow will be analyzed [37]. The user also “meshes” this volume whereby the spatial locations of *nodes* will be specified. Nodes are essentially points in space at which fluid based properties, such as velocity and pressure, are calculated. Lastly, the user specifies the boundary type of each surface in the flow domain. Examples of boundary types include velocity inlet, wall, and pressure outlet.

GAMBIT then exports to FLUENT the geometrical details of the user defined fluid domain along with the node locations and boundary types. FLUENT contains advanced numerical algorithms that, for the purposes of this thesis, characterizes the fluid flow in the defined flow domain and simulates the resuspension of particulates from the fluid flow via particulate transport calculations (see Section F.2 of Appendix F) [38]. Using the information provided by GAMBIT, FLUENT prompts the user to provide information related to boundary conditions, initial conditions, selection of a turbulence model (see Appendix E), and material data for both the fluid and particulates.

MCNPX (which stands for Monte Carlo N-Particle eXtended) is the code selected for the MC radiation transport calculations [35]. As with GAMBIT, this code also requires the user to model the geometry in which radiation transport will take place. The user must also specify attributes of the materials found in the specified geometry (see Section B.2 of Appendix B) and initial conditions of the radioactive particles whose transport in and reactions with the specified materials are to be simulated. Examples of such initial conditions are initial spatial position within the geometry and initial energy, amongst others.

To complete the list of the codes selected, MATLAB, a scientific computing language, is used for the black box data processing and dose calculations.

It is important to describe the computational infrastructure used for this thesis. The CFD simulations were performed on a quad core HP xw6600 Workstation equipped

with the Ubuntu operating system. The presence of multiple processors on this machine enabled the use of a parallelized version of FLUENT. Parallelization allows for the distribution of calculations to each processor involved, which results in lower run times for computationally intensive simulations such as CFD simulations, in comparison to those that are run using a smaller number of processors. Moreover, the black box data processing, dose calculations, and MC radiation transport simulations were performed on a dual core HP Pavilion dv6000 laptop.

The objective of this thesis is to couple these two code sets (i.e. GAMBIT/FLUENT and MCNPX) in order to provide a methodology by which the resuspension of radioactive particulates and the evaluation of the resultant radiation field can be simulated. This will thus be the focus of Section 3.2. The research blueprint shown in Figure 1.3 serves as the framework that will be employed to perform the aforementioned coupling and this figure states that the CFD simulation constitutes the first step in the coupling methodology and will be discussed in the following section.

3.2.1 Computational Fluid Dynamics Modelling

GAMBIT serves as the “front end” of the CFD simulation in that the user must build and mesh the flow geometry and specify the boundary type for each surface in the flow domain. The information specified by the user here will then be exported to FLUENT. Performing these tasks in GAMBIT will now be discussed.

3.2.1.1 GAMBIT Setup

It has been established that the WIS Wind Tunnel geometry presented in this chapter will serve as the basis for the development of the coupling methodology. As such, the geometry that is modelled in GAMBIT is based on that of the WIS Wind Tunnel with a few exceptions that will be discussed.

The first step in fully defining the flow domain in GAMBIT is to build the flow geometry. Figures 3.6 and 3.7 display the wind tunnel geometry modelled in GAMBIT and it must be noted that these figures display one-half of the lateral section of the wind tunnel, and the reason for this will be discussed shortly.

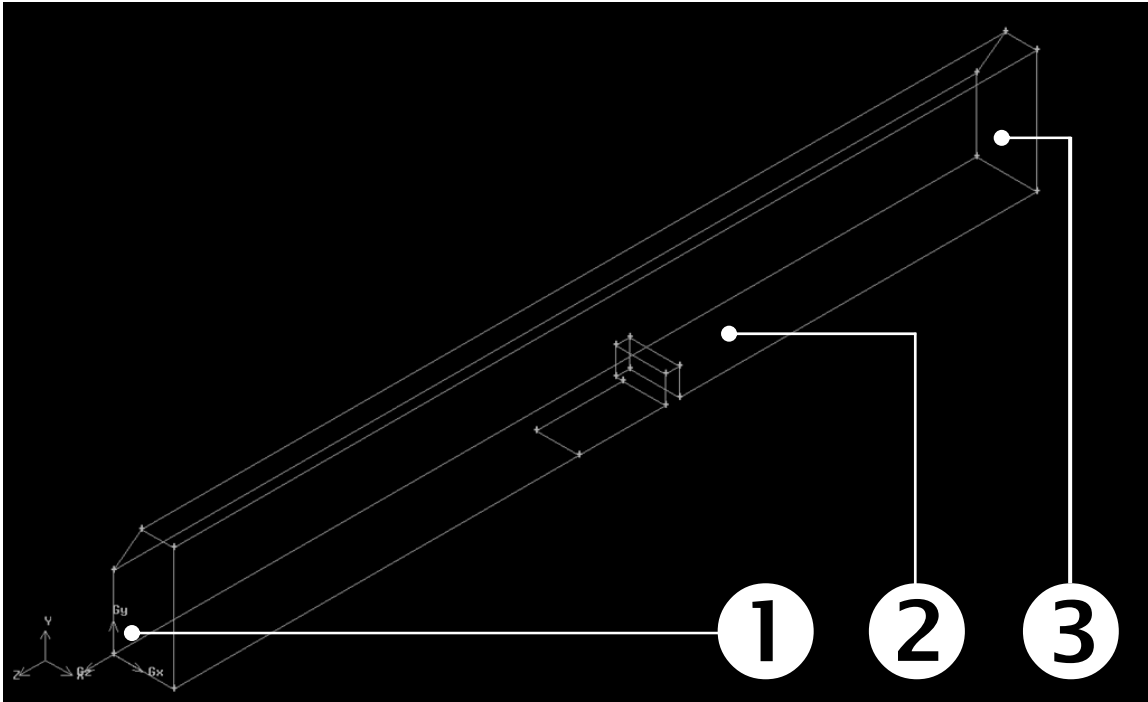


Figure 3.6 – Three-Dimensional View of Wind Tunnel Geometry in GAMBIT

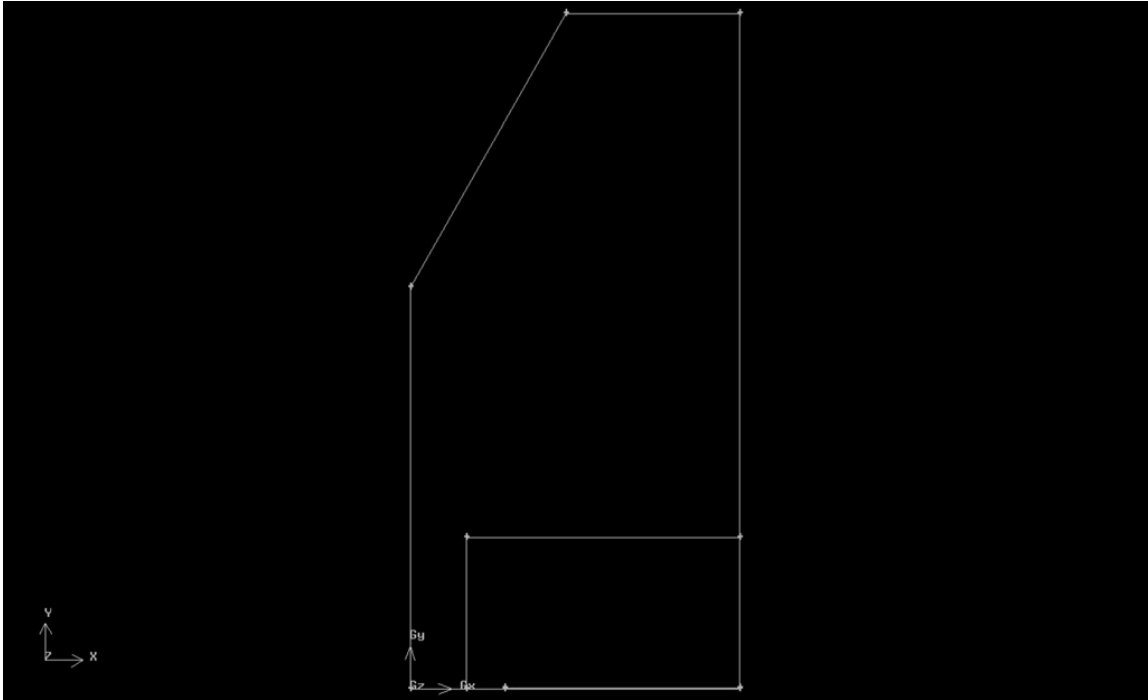


Figure 3.7 – Two-Dimensional View of Wind Tunnel Geometry in GAMBIT (Looking Downstream from Inlet)

When comparing the wind tunnel geometric model shown in Figures 3.6 and 3.7 with the schematics shown in Appendix A, there are two deviations.

The first deviation is the absence of the fans located at the back of the wind tunnel and the second is that only half of the wind tunnel is modelled. To address the first deviation, one can refer to the work of Harwell [11] who performed CFD simulations to model particulate resuspension. Here, the WIS Wind Tunnel was modelled without the bluff body. Instead of explicitly modelling the fans, Harwell [11] modelled the effect of the fans by first representing the face through which air flows into the wind tunnel (the left most face in Figure 3.4) and the face that contains the fans (the right most face in Figure 3.4) as planar faces. The former face was designated as a velocity inlet whilst the latter was assigned as a pressure outlet. This affords the modeller to explicitly specify the fluid velocity at the inlet and the gauge pressure at the pressure outlet (which will be discussed further in Section 3.2.1.2). This technique formulated by Harwell [11] has been applied to the wind tunnel geometric model employed in this thesis.

With respect to the second deviation mentioned above (i.e. only half of the wind tunnel being modelled in GAMBIT), this can be justified by first referring to the schematics shown in Appendix A. It is evident that the WIS Wind Tunnel geometry is symmetric about the $x=70$ cm plane²⁷⁾. As a result of this property of the wind tunnel geometry, only half of it was modelled in GAMBIT. When FLUENT calculates the flow field and particulate resuspension in the half-geometry shown in Figures 3.6 and 3.7, it then “reflects” the results of its calculations onto the other half of the wind tunnel geometry (this will be made clear in the results shown in Chapter 4). The foremost advantage in this approach is the reduction in the computational overhead since a lesser amount of calculations are performed relative to that required to characterize the flow field and particulate resuspension in the fully modelled geometry.

Figure 3.6 identifies planes of interest in the wind tunnel geometry. These planes represent important boundary types in the flow geometry and will be outlined in Table 3.3.

Plane	Boundary Type
1	Velocity Inlet
2	Symmetry
3	Pressure Outlet
Other	Wall

Table 3.3 – Boundary Types Employed in the GAMBIT Model

Figure A.4 in Appendix A illustrates that the inlet air velocity is 6 m/s. The relationship between the fans in an experimental setup and the resultant inlet fluid velocity has been described in Figure 2.13, with the net result being that the fans will rotate at a rate such that the fluid will enter the inlet at the desired velocity. This is also the case in the WIS Wind Tunnel and as per the discussion on the exclusion of the fans in

²⁷⁾ Referring to Figure A.1 in Appendix A, the cross section of the wind tunnel is symmetric about the $x=70$ cm plane. This plane will be herein referred to as the *symmetry plane*.

the GAMBIT model, plane 1 identified in Figure 3.6 is then designated as a velocity inlet. In light of the discussion on the use of symmetry in the GAMBIT model, plane 2 is designated as a symmetry boundary type. To determine the boundary type of plane 3, one must refer to Figure A.4 in Appendix A. Here, it is stated the static pressure at the flow outlet (i.e. plane 3) is equivalent to the atmospheric pressure. One can think of plane 3 as having two sides whereby the first side faces the interior of the wind tunnel and the second is exposed to outside environment surrounding the wind tunnel. As a result, the latter side is exposed to the atmosphere (i.e. the static pressure here is equivalent to the atmospheric pressure). In order to maintain continuity on both sides of plane 3, then the static pressure on the inner side of plane 3 must also be equal to the atmospheric pressure. To accommodate this continuity requirement, plane 3 is designated as a pressure outlet and the reasons for this choice will be discussed in Table 3.4. It is also important to mention that the surfaces of the wind tunnel not identified by the plane numbering in Figure 3.6 such as those of the plate and bluff body, have been designated as a *wall* boundary type.

Lastly, a word on the meshing of the wind tunnel geometry shown in Figures 3.6 and 3.7. An unstructured mesh²⁸⁾ comprised of tetrahedral elements and consisting of approximately two million nodes is employed.

Once the modeller has fully characterized the flow domain in GAMBIT, GAMBIT will then export the attributes of the domain to FLUENT. These attributes are the geometry of the fluid domain, node locations, and boundary types. A discussion on how FLUENT uses the information provided by GAMBIT to calculate the flow field and particulate resuspension within the flow domain shown in Figure 3.6 will now ensue.

3.2.1.2 FLUENT Setup

When FLUENT imports the attributes of the flow domain, it will observe the presence of the symmetry plane and will allow the user to view the full geometry of that

²⁸⁾ A *mesh* is defined as a network of nodes.

in Figure 3.6. This is shown in Figure 3.8. Note that in this figure, the vertical plane dissecting the cross section of the geometry shown denotes the plane of symmetry.

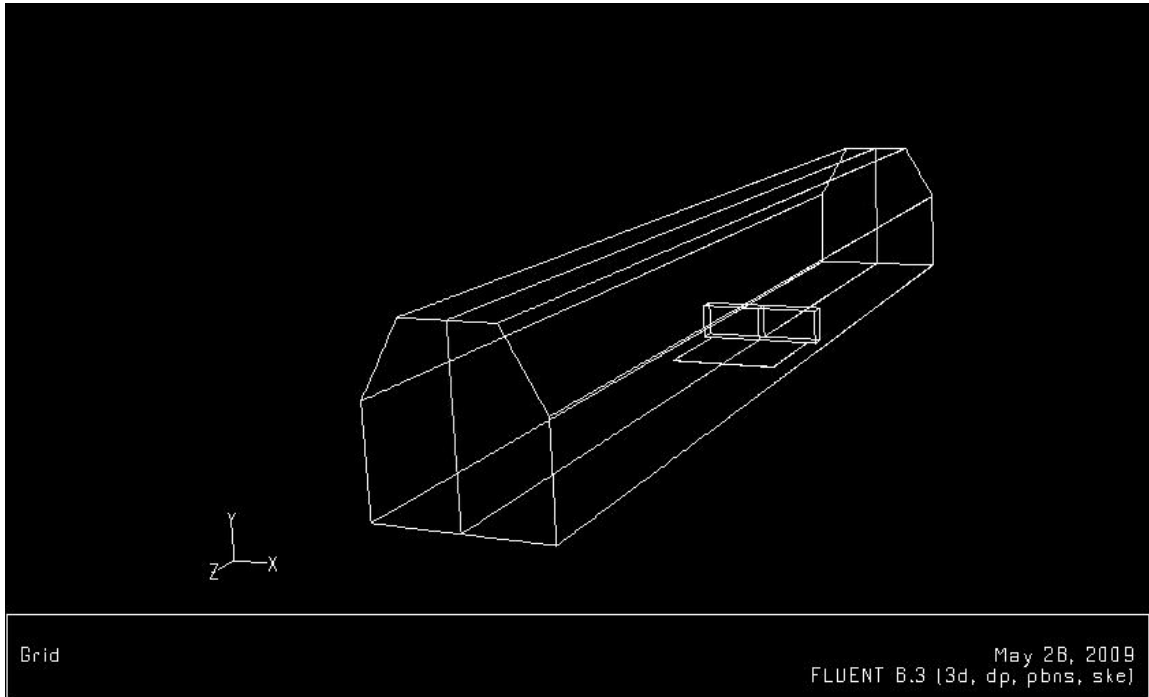


Figure 3.8 – View of Full Wind Tunnel Geometry in FLUENT

Before FLUENT can calculate the flow field and particulate resuspension in the flow domain shown in Figure 3.6, there are several types of input required from the user. These input types have been grouped into several categories, which will now be discussed.

The first input category is related to the boundary conditions that must be imposed at the respective planes displayed in Figure 3.6 and outlined in Table 3.3. Table 3.4 will describe these boundary conditions in further detail.

Plane	Boundary Type	Input Description
1	Velocity Inlet	Figure A.4 in Appendix A states that the inlet air velocity is 6 m/s. This velocity value will serve as input to the velocity inlet boundary condition along with the direction of the

		flow, which will be along the $-z$ axis (streamwise direction; see Section A.1 and Figure A.4 in Appendix A).
2	Symmetry	No input required.
3	Pressure Outlet	The static pressure at plane 3 must be equal to that of the atmosphere. In order to achieve this, the gauge pressure at this plane must be equal to zero. The pressure outlet boundary type in FLUENT permits the user to impose a gauge pressure at this plane. Thus, a gauge pressure of zero will serve as input to the pressure outlet boundary condition.
Other	Wall	<p>There are three boundary conditions which must be imposed at the wall surfaces, and are described below:</p> <ul style="list-style-type: none"> (1) The no-slip boundary condition must be enforced (i.e., the air velocity at the wall is zero) (2) The wall surfaces are smooth (i.e., they possess no surface roughness) (3) The walls are adiabatic (i.e., they do not exchange heat with the air flow or with other mediums)

Table 3.4 – Description of Boundary Conditions Employed by the Wind Tunnel Geometry in GAMBIT

The second input category deals with characterizing the flow conditions, and will be described in Table 3.5.

Flow Condition	Input Description
Gravity	It has been made clear in the schematics shown in Appendix A that the $+y$ axis represents the vertical direction. As such, the force of gravity will act <i>counter</i> to this direction and so the acceleration due

	to gravity along this axis will be specified as -9.81 m/s^2 .
Air Flow	Air is the default flow material in FLUENT. The default values assigned to the properties of air are employed, namely those of dynamic viscosity and density. The default values for these quantities are $1.79 \times 10^{-5} \text{ Pa}\cdot\text{s}$ [39] and $1.23 \text{ kg}\cdot\text{m}^{-3}$ [39], respectively. The default temperature is based on the default inlet air temperature which is 300K (27°C) [40]. Moreover, the Mach Number calculation in Section A.3 of Appendix A documents the fact that the air flow for the scenario being modelled in this thesis is incompressible.
Turbulence	<p>Section A.2 of Appendix A documents the fact that the flow in the WIS Wind Tunnel described in Figure 3.4 qualifies as turbulent. As such, a turbulence model must be selected to model the flow in the wind tunnel shown in Figure 3.6. Section 2.1.5 sheds light on the existence of turbulence models, as they serve to approximate the solution to the Navier-Stokes equation for the given flow scenario. Appendix E contains a discussion on the different turbulence models. Of the models described here, the Standard k-ϵ turbulence model has been selected, for the following reasons [26]:</p> <ul style="list-style-type: none"> • Well established and widely validated turbulence model • Performs well when modelling confined flows²⁹⁾, as is the case with the flow being modelled in Figure 3.6 • Well established for modelling many industrially relevant flows <p>Two important parameters employed by the Standard k-ϵ turbulence</p>

²⁹⁾ Confined flow is one that is bounded by the surfaces of the flow volume.

model are k , which represents the turbulent kinetic energy per unit mass, and ε which represents the rate of dissipation of turbulent kinetic energy per unit mass. In reference to the discussion on large and small vortices in Section 2.1.5, one can think of the k quantity as an indicator as to how energetic the large vortices, which reside in the main flow stream, are. Moreover, one can think of the ε quantity as an indicator of how the viscous regime governing the boundary layer attenuates the energy of the small vortices residing in the near-wall region [41].

Since the k and ε quantities dictate the nature of the vortices in the flow domain, it follows that they also indicate the nature of the turbulent flow. Since the turbulent fluid flow commences from the inlet of the flow domain, the values of k and ε must be specified as an inlet boundary condition. Rarely does the modeller have the precise values of these quantities for the flow scenario being analyzed, and so it is advisable that one perform a sensitivity analysis of the values chosen on the results produced by the CFD simulation [26].

Indeed, it is preferable that the CFD simulation, as in any numerical simulation, achieve a faster rate of convergence. Guidance exists on the selection of the value of k and ε such that a faster convergence rate be attained. It is advisable that the k quantity be assigned a very small value in comparison to that given to the ε quantity [41].

In light of the guidance provided, the following values were assigned to k and ε , respectively [41]:

$$k = 10^{-4} \text{ m}^2 \cdot \text{s}^{-2}$$

$$\varepsilon = 5 \text{ m}^2 \cdot \text{s}^{-3}$$

Lastly, it is also of note that the k- ϵ turbulence model is a steady-state turbulence model (i.e. no time-dependence) and so it employs an iteration-based approach to achieve a converged flow field.
--

Table 3.5 – Description of Input Required to Characterize the Flow Conditions

Upon convergence of the flow field, particulates can then be injected into the flow domain. This leads to a discussion of the third input category, which is related to particulate injections. To begin, one must first make assumptions on the physical nature of the particulates being modelled and how these particulates interact with the air flow. To make sound assumptions, Lavezzo et.al [42], whom modelled the dispersion of solid particulates in a stirring tank, states that the ratio of the fluid density to particulate density must first be taken. Having achieved a value of 0.2, the authors made the following assumptions:

- (1) Particulate-to-particulate interactions are negligible
- (2) Particulate density is large compared to fluid density
- (3) The effect of particulates on the flow field is negligible

Thus, it is prudent to take the ratio stated above for the flow scenario modelled for this thesis. Prior to this ratio being taken, the material composition of the particulate that is modelled in this thesis must be discussed. Particulates composed of Lanthanum Oxide powder were employed in the resuspension experiments performed in the WIS Wind Tunnel and so the radiation field produced by the resuspension of particulates composed of Lanthanum Oxide powder is attributed to the beta and gamma radiation emitted by Lanthanum-140, as Oxygen is naturally stable. In light of this fact and the need in this thesis to simulate particulates whose resuspension will result in a radiation hazard, *particulates composed solely of Lanthanum-140 will be modelled in FLUENT*. With this being said, the calculation of the ratio of the densities of air (fluid material) to that of Lanthanum-140 (particulate material) can now proceed.

The densities for air and Lanthanum-140 can be found in Section A.2 in Appendix A and Table B.1 in Appendix B, respectively (as per the discussion in Section A.2 of Appendix A, the stated density of air corresponds to a temperature of 25°C while the density of Lanthanum-140 is nominal). The ratio is now taken:

$$\frac{\rho_{\text{air}}}{\rho_{^{140}\text{La}}} = \frac{(1.18 \text{ kg} \cdot \text{m}^{-3})(1000 \text{ g} \cdot \text{kg}^{-1})(100 \text{ cm} \cdot \text{m}^{-1})^{-3}}{6.19 \text{ g} \cdot \text{cm}^{-3}}$$

$$\frac{\rho_{\text{air}}}{\rho_{^{140}\text{La}}} = 1.91 \times 10^{-4} \tag{3.1}$$

It is clear that the ratio stated in equation (3.1) is much less than that calculated in [42]. As a result, the assumptions used in [42] are also applicable to the flow scenario modelled in this thesis. For the sake of clarity, these assumptions will be stated below along with assumptions pertaining to the physical nature of the particulates (which are independent of the density of fluid to particulate ratio):

- (1) Particulates are non-deformable spheres
- (2) Particulate-to-Particulate interactions are negligible
- (3) Particulate density is very large in comparison to the air density
- (4) The effect of particulates on the flow is negligible
- (5) Particulates are inert

With these assumptions in mind, the next particulate modelling inputs pertain to particulate trajectory calculations. As described in Section F.2 in Appendix F, the equations of motion used by FLUENT to calculate the trajectory of a particulate is time dependent and therefore requires the use of a time step to solve numerically. FLUENT requires the user to specify attributes of this time step which are discussed in Table 3.6.

Time Step Attribute	Description
Time Step Calculation	<p data-bbox="597 256 1398 510">FLUENT provides several options to calculate the time step used for particulate trajectory calculations. The option chosen for modelling the particulate resuspension in the wind tunnel shown in Figure 3.6 is the <u>length scale</u> approach. Here, the time step is calculated as follows:</p> $\Delta t = \frac{\text{Length}}{u_p + u} \quad (3.2)$ <p data-bbox="597 751 695 783">Where:</p> <ul style="list-style-type: none"> <li data-bbox="695 804 1003 835">Δt = time step (unit: s) <li data-bbox="638 856 1052 888">Length = length scale (unit: m) <li data-bbox="703 909 1190 940">u_p = particulate velocity (unit: $\text{m}\cdot\text{s}^{-1}$) <li data-bbox="711 961 1084 993">u = air velocity (unit: $\text{m}\cdot\text{s}^{-1}$) <p data-bbox="597 1077 1414 1497">The length scale represents the distance the particulate will travel before its motion equations will be solved again such that its trajectory will be updated. It is important to note that when a particulate enters/leaves a computational cell³⁰⁾ in the flow domain, its spatial position is always calculated. So even in the case that a large length scale is specified, the time step calculated via equation (3.2) will be used such that the computational cell is traversed in one time step [43].</p> <p data-bbox="597 1570 1398 1717">The reason why the length scale option has been chosen is due to the fact that as shown in equation (3.2), the time step is reflective of local conditions, in that the velocity of the</p>

³⁰⁾ A computational cell is essentially a control volume and in the context of the flow domain mesh in the GAMBIT model, a computational cell/control volume is formed on the basis of node locations.

	<p>particulate and the surrounding fluid at time step i is used to calculate the particulate's spatial position at time step $i+1$. This illustrates the recursive nature of the length scale approach.</p> <p>Lastly, the default value of the length scale, 0.01 m, will be used.</p>
<p>Maximum Number of Time Steps</p>	<p>This quantity represents the maximum number of time steps used to compute a single particulate trajectory. The reason why this must be specified lies in the fact that there are situations where a particulate either remains in the fluid domain for a prolonged period of time or ends up not leaving the domain. An example of such a situation is a particulate that, after being resuspended by a resuspension vortex, becomes trapped by a vortex in the main flow stream.</p> <p>As a rule of thumb, the value specified for the maximum number of time steps must not be too small or too large. The reason why is that if it is too small, the particulate's full trajectory will not be calculated (i.e., the trajectory calculations will be terminated prematurely) and if it is too large, the particulate will be tracked for a longer period of time and thus a large computational overhead will be incurred.</p> <p>In order to find a middle ground, a value of 10,000 has been designated as the maximum number of steps. This is large in comparison to the default value of 500.</p>

Table 3.6 – Inputs Required by Particulate Trajectory-based Time Step Calculations

Once the inputs described in Table 3.6 have been made in FLUENT, the material properties of the particulates must then be declared. As discussed earlier, the particulates that are to be modelled in FLUENT are composed of Lanthanum-140. Moreover, the list

of assumptions used for particulate modelling indicate that the particulates are inert and so no considerations need to be made about the particulates undergoing chemical reactions, heat transfer, melting, etc. However, the particulate trajectory equations used by FLUENT to track a particulate (see Section F.2 in Appendix F) do require the particulate density. Thus, the density of Lanthanum-140 is the only physical property of this element that must be defined in the list of material attributes of the particulates in FLUENT.

The last input pertinent to particulate modelling deals with defining the diameter of the particulates and the spatial locations in which they are placed in the flow domain. As per Figure 3.4, particulates are to be initially placed on the plate. However, the wind tunnel that is being modelled (see Figure 3.6) is half modelled and so the flow field and particulate resuspension are calculated on the portion of the wind tunnel that is modelled. The results of these calculations are then “reflected” on to the un-modelled, symmetric portion of the wind tunnel. As a result, particulates can only be placed on the portion of the plate shown in Figure 3.6. Particulates of varying diameters are placed on the plate in order to model a more realistic scenario as is the case with an RDD whereby the released particulates will not be of uniform diameter.

The particulates are placed in the domain in the following manner:

- Particulates are placed in groups on the plate whereby the grouping is based on particulate diameter. For example, particulates that possess a diameter of 1 μm will be placed in their own group; particulates that possess a diameter of 2 μm will be placed in their own group, etc.
- Each group will contain 100 particulates.
- The placement of groups on the plate will take the form of placing the constituent particulates in a row-like manner whereby the row is parallel to the z axis (see Figure 3.6).

- A uniform distance will separate each particulate placed in a row.

In order to accommodate the manner in which particulates will be placed on the plate as described above, the *rake tool* available in FLUENT will be employed. This tool allows the user to specify a line in the flow domain. On this line, the user will define the spatial extent of the line and the number of points the line shall possess. FLUENT will automatically calculate the distance between the points by dividing the line length by the number of points requested minus one. Thus, the spacing between each point will be uniform, as desired. As per the input above, the modeller will specify 100 points to be placed on a line atop the plate and parallel to the z axis (the modeller will define the spatial extent of this line along the z axis). These properties of the rake will allow for the particulates to be placed in the row-like manner described above whereby a particulate will be placed at each point on the line. These lines are created for each particulate group.

Table 3.7 documents the rakes employed to inject particulates into the flow domain shown in Figure 3.6. Note that the spatial extents of the rakes are with respect to the schematics of the WIS Wind Tunnel provided in Appendix A.

Rake/Group Number	Spatial Extent (unit: cm)	Number of points/particulates released	Particulate Diameter (unit: μm)
1	$x = 25$ $y = 0.2$ $-562 \leq z \leq -482$	100	1
2	$x = 30$ $y = 0.2$ $-562 \leq z \leq -482$	100	2

3	$x = 40$ $y = 0.2$ $-562 \leq z \leq -482$	100	3
4	$x = 50$ $y = 0.2$ $-562 \leq z \leq -482$	100	4
5	$x = 60$ $y = 0.2$ $-562 \leq z \leq -482$	100	5
6	$x = 70$ $y = 0.2$ $-562 \leq z \leq -482$	100	6

Table 3.7 – Description of Rakes Employed for Particulate Injections

Each of the particulates that are placed in the domain will be tracked until either (a) the maximum number of time steps (see Table 3.6) is exceeded when computing the particulate trajectory or (b) it exits the flow domain. At each time step, the attributes of each particulate injected into the domain will be recorded. Examples of particulate attributes are its spatial position, velocity, and diameter, amongst others. When the tracking of all particulates are terminated, for the reasons just outlined, FLUENT allows the modeller to export the particulate attributes to an external data file. Figure 3.9 shows an example of a particulate data file that is exported by FLUENT.

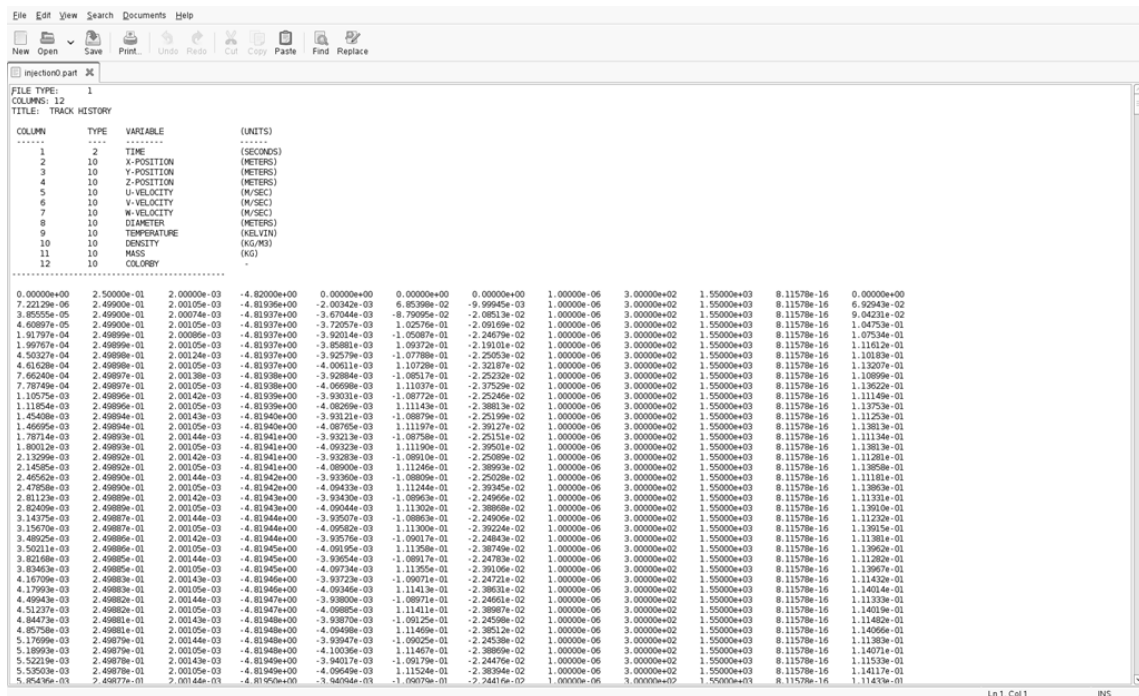


Figure 3.9 – Screenshot of Particulate Data File Exported by FLUENT

The efforts to build a CFD model of the wind tunnel shown in Figure 3.6 have been the focus of Section 3.2.1. The series of inputs in both the GAMBIT and FLUENT software pertain to the modelling of both the flow field and the resuspension of particulates. These inputs along with the convergence of the FLUENT calculation results in the exportation of a data file that contains attributes of each particulate placed in the domain. As per the research blueprint described in Figure 1.3, the Black Box coupling code was required. Here, the Black Box will convert the particulate spatial distribution contained in the external particulate data file into an airborne particulate activity and will then use this airborne activity to create an input file for the MCNPX simulation. The development of the Black Box constitutes the second step in the coupling methodology and will be discussed in the following section.

3.2.2 Black Box Data Processing

The purpose of the Black Box is to process the particulate data that is exported by FLUENT. The airborne particulate activity is the parameter that will be used to couple

the CFD simulation with the MC radiation transport simulation. Thus, the mandate of the Black Box will be twofold:

- (1) Convert the particulate spatial distribution contained in the particulate data file exported by FLUENT to airborne particulate activity
- (2) Use the airborne particulate activity to create an input file for the MC radiation transport simulations

The purpose of this section is to document how the Black Box interprets the particulate data exported by FLUENT such that its mandates described above can be achieved. Figure 1.3 illustrates that the Black Box consists of two “sub” Black Boxes, the first dedicated to the conversion of the particulate spatial distribution to airborne particulate activity while the second focuses on using the airborne particulate activity to create an input file for the MC radiation transport simulations. The Black Box takes the form of MATLAB m-files (commonly referred to as MATLAB codes) whereby three pieces of MATLAB code have been developed in order to implement the above mandates and are briefly described in Table 3.8.

Black Box Number	MATLAB Code Name	Description
1	Activity_Calculations.m	This code will convert the particulate spatial distribution exported by FLUENT to airborne particulate activity.
2	Source_Bias.m	This code uses the airborne particulate activity to calculate what is known as a source bias. The concept of source bias along with the means by which it is calculated will be discussed in Section 3.2.2.2.

	MCNPX_Black_Box.m	Based on the source bias calculated in Source_Bias.m, an input file for the MCNPX simulation is created.
--	-------------------	--

Table 3.8 – Description of MATLAB Codes Created for Black Box Development

It is important to keep in mind that the results of the calculations produced by both the Black Box and MCNPX simulations are used to calculate the dose delivered by the resuspension of particulates. This is realized in Section 3.2.4, which discusses how the dose calculations are performed.

3.2.2.1 Black Box 1 Development

The purpose of Black Box 1 is to convert the particulate spatial distribution contained in the particulate data file exported by FLUENT to airborne particulate activity. In order to achieve this, several tasks must be performed, and will be discussed in the following sections.

3.2.2.1.1 Selection of Time Steps

The equations FLUENT uses to calculate the trajectory of a particulate is time-dependent and therefore requires the use of a time step to solve numerically. The process of solving these equations numerically implies that an iterative approach will be taken to calculate the trajectory of a particulate in the flow domain. The reality of particulate tracking in FLUENT is that each particulate is tracked at the same time step. The term time step implies the iteration number for which a particulate is tracked (this will herein be known as the *time step iteration*). For example, at time step iteration 1, each particulate will have its spatial position computed and at time step iteration 2, the spatial position of each particulate is computed again, and so on. However, the actual value of the time step used to solve the particulate trajectory equations used by FLUENT, as shown in equation (3.2), will be different for each particulate. The reasons being are as follows:

- Equation (3.2) is dependent on the particulate velocity and the velocity of the surrounding air. According to Section F.2 in Appendix F, the trajectory equations FLUENT employs state that the particulate velocity is a function of the particulate diameter and air velocity. As described in Table 3.7, the particulates injected into the flow domain shown in Figure 3.6 will not have the same diameter and it therefore follows that the velocity of each particulate will not be the same.
- With the presence of the plate and bluff body shown in Figure 3.6, these wind tunnel features will obstruct the flow and cause the air velocity to spatially vary throughout the flow domain. Since each particulate injected into the domain will be resuspended (i.e. displaced) to different spatial locations via the air flow, it follows that the air velocity surrounding each particulate will not be the same.

As the time step iterations proceed to solve the FLUENT trajectory equations for each particulate, the *elapsed time*³¹⁾ that a particulate is being tracked is also recorded. Of course, the elapsed time is calculated using the time step computed via equation (3.2). As a result, the elapsed time computed for the corresponding time step iteration will not be the same for each particulate. For the sake of clarity, it will be reiterated that as particulates are tracked in FLUENT, they will be tracked at the same time step iteration but the corresponding elapsed time for which it is tracked will be different.

The fact that the spatial position of particulates is a function of time allows the modeller to essentially take a snapshot of the radiation field. That is, one can compute the airborne particulate activity and the resultant dose using the particulate spatial distribution at selected times. This provides the modeller with some flexibility in selecting the times at which each snapshot will be taken. The methodology used to determine these times will now be described. One of the major concerns of the resuspension of radioactive particulates is the occurrence of particulates being resuspended into the breathing space. In other words, this concern is based on the vertical heights the resuspended particulates can attain. As a result, the selection of time

³¹⁾ The terms *elapsed time* and *time* are herein interchangeable.

steps will be based on the heights that the particulates in the wind tunnel shown in Figure 3.6 are resuspended to. The following height ranges are considered (it must be noted that in the ranges listed below, the “[” and “]” symbols denotes inclusiveness and the “)” symbol denotes exclusiveness):

- $[10^{-2}, 10^{-1})\text{m}$
- $[10^{-1}, 8.5 \times 10^{-1}]\text{m}$

These height ranges essentially split the vertical domain into two parts, the first being close to the wind tunnel floor and the second being at higher elevations. The reason why this is done is that it allows the modeller to observe the range of vertical trajectories that the resuspended particulates attain. With respect to the second range shown above, it is of note that the upper limit is 85 cm. As per Figure A.1 in Appendix A, the cross section of the wind tunnel is rectangular from the floor (at $y=0$ cm) to $y=85$ cm. As will be discussed shortly, this choice of the upper limit will affect the way in which the radiation field is analyzed. Using the particulate data file exported by FLUENT, the heights of each $1 \mu\text{m}$ particulate will be analyzed for each of the height ranges listed above. The reason why the heights achieved by $1 \mu\text{m}$ particulates are specifically employed in this analysis is that as discussed in Section 2.2.2, small particulates, once resuspended, can attain significant vertical trajectories and can remain in suspension for long periods of time. Thus, smaller particulates are better able in delivering a resuspension dose than their larger counterparts and since the $1 \mu\text{m}$ particulates represent the smallest particulate size class employed in this thesis, their vertical heights will be analyzed when selecting the time steps at which the radiation field in the wind tunnel will be examined.

In this analysis, for whichever respective $1 \mu\text{m}$ particulate that attains the smallest or largest height in the above ranges, the radiation field will be analyzed at the corresponding time step iteration number. For example, if a given $1 \mu\text{m}$ particulate attains the lowest height in the first range at time step iteration number 300, then the airborne particulate activity and radiation dose will be calculated at this specific time step

iteration number using the particulate spatial distribution. Once these time step iteration numbers are identified, time step iterations that are intermediary to the ones selected will also be chosen to analyze the radiation field as well. For example, if the time step iteration numbers 300 and 600 have been identified in the above analysis, a time step iteration number of 450 will also be selected. The reason for selecting additional time step iterations to analyze the radiation field is so that the modeller will have more data to better understand how the particulate airborne activity and resultant radiation dose change over time.

Not all particulates initially placed in the flow domain will be present in the wind tunnel at a particular time step iteration number as some might have already exited the domain prior to the time step iteration taking place. As discussed, each particulate is tracked at the same time step iteration number, but will have different corresponding elapsed times. Nonetheless, it is imperative that an average elapsed time be calculated at each of the time step iteration number at which the radiation field in the wind tunnel is being analyzed. In Section 3.2.4, it will be shown that the use of the average elapsed time will be required in the calculation of radiation dose. When analyzing the radiation field at each time step iteration number, a counter must be put into place to detect the number of particulates that have exited the domain. With this in mind, the average elapsed time for a corresponding time step iteration number is calculated as follows:

$$\bar{t}_{\text{elapsed}}(i) = \left(\frac{1}{n_{\text{total}} - n_{\text{exit}}(i)} \right) \left(\sum_{j=1}^{n_{\text{total}} - n_{\text{exit}}(i)} t_{\text{elapsed},j}(i) \right) \quad (3.3)$$

Where:

$\bar{t}_{\text{elapsed}}(i)$ = average elapsed particulate tracking time at the i^{th} time step iteration
(unit: s)

$t_{\text{elapsed},j}$ = elapsed time that the j^{th} particulate residing in the domain at the i^{th} time step iteration is tracked (unit: s)

n_{total} = total number of particulates initially placed in the domain

$n_{\text{exit}}(i)$ = total number of particulates that have exited the domain prior to the i^{th} time

step iteration

Note that in equation (3.3), the term $n_{\text{total}} - n_{\text{exit}}(i)$ represents the number of particulates remaining in the flow domain at the i^{th} time step iteration. Thus, equation (3.3) simply represents the sum of the elapsed time that each particulate residing in the flow domain at the i^{th} time step iteration is being tracked divided by the number of particulates remaining in the flow domain at the i^{th} time step iteration.

Now that the methodology to select the time step iterations at which the radiation field will be analyzed has been described, the means by which the radiation field will be characterized will now be discussed.

3.2.2.1.2 Spatial Partitioning and Particulate Airborne Activity Calculations

At any time step iteration, the particulates will be spatially distributed throughout the flow domain. Since the particulates simulated in this thesis are radioactive, the radiation field will spatially vary as well. In order to quantify this spatial variation, the following approach has been formulated. The approach is centred on spatially partitioning a part of the wind tunnel domain shown in Figure 3.6. This is illustrated in Figure 3.10.

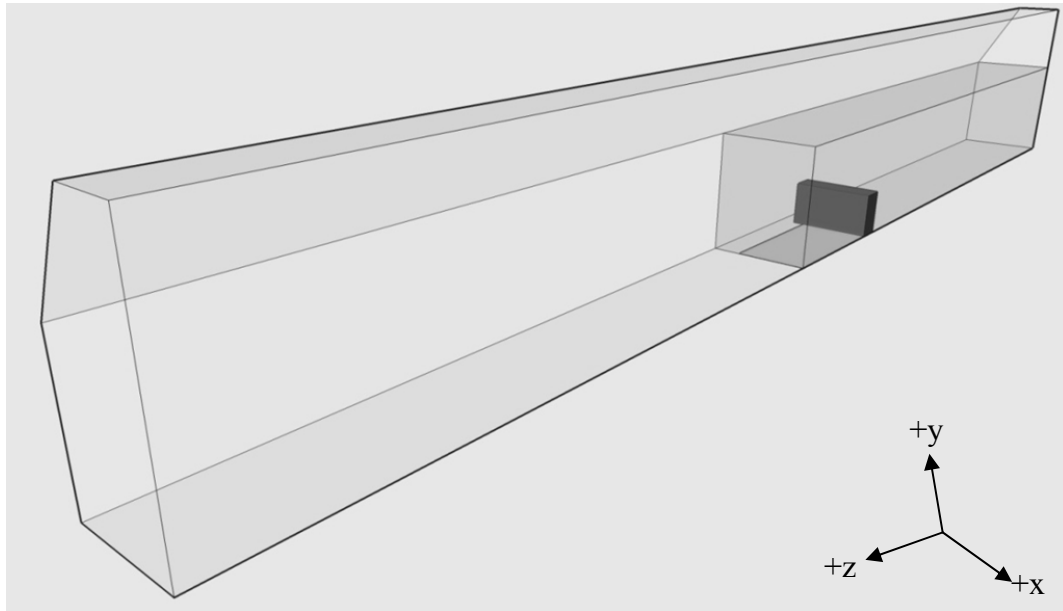


Figure 3.10 – Identification of Wind Tunnel Region to be Partitioned

The shaded volume in Figure 3.10 identifies the portion of the wind tunnel that will be spatially partitioned. *The term spatial partitioning embodies the process by which the shaded region shown in Figure 3.10 is split into different sub-volumes (herein known as partitions) and the particulate spatial distribution within each of these partitions are then converted to an airborne particulate activity.* The reason why this particular portion of the wind tunnel is being partitioned is based on the following assumptions pertaining to the resuspension of particulates:

- (1) Particulates will not be transported upstream (i.e., in the direction opposite the flow)
- (2) Particulates will not attain vertical heights greater than $y=85$ cm
- (3) Particulates will only be transported downstream

Recalling the selection of time step iterations to perform radiation field analysis, the second height range mentioned had an upper bound of $y=85$ cm. The reason for the selection of this particular value as the upper limit is due to the second assumption stated above. Since the cross section of the wind tunnel from $y=0$ cm to $y=85$ cm is rectangular

(see Figure A.1 in Appendix A), this then explains why the shaded region in Figure 3.10 also has a rectangular cross section.

It will be shown in Chapter 4 that the assumptions stated above in regards to the transport of particulate is justified in that the analysis of the radiation field for each of the selected time step iterations accounts for all particulates placed in the domain.

Bearing in mind the fact that the wind tunnel modelled in GAMBIT and FLUENT is only half modelled, FLUENT will model the flow field and particulate resuspension in this portion alone. Afterwards, the results of the calculations carried out by FLUENT will then be “reflected” onto the other un-modelled symmetric half of the wind tunnel. The implication of this on the radiation field analysis is that the particulate distribution data exported by FLUENT is only available for the half of the wind tunnel that is actually modelled. However, the analysis of the entire radiation field requires that particulate data in the other un-modelled half of the wind tunnel be available as well. To address this need, the modeller operates under the premise that the spatial distribution of particulate are symmetric about the symmetry plane and this of course is guaranteed by the use of the symmetry plane in the GAMBIT model. With this being said, the spatial partitioning of the shaded region shown in Figure 3.10 and its counterpart in the other half of the wind tunnel is shown in Figure 3.11.

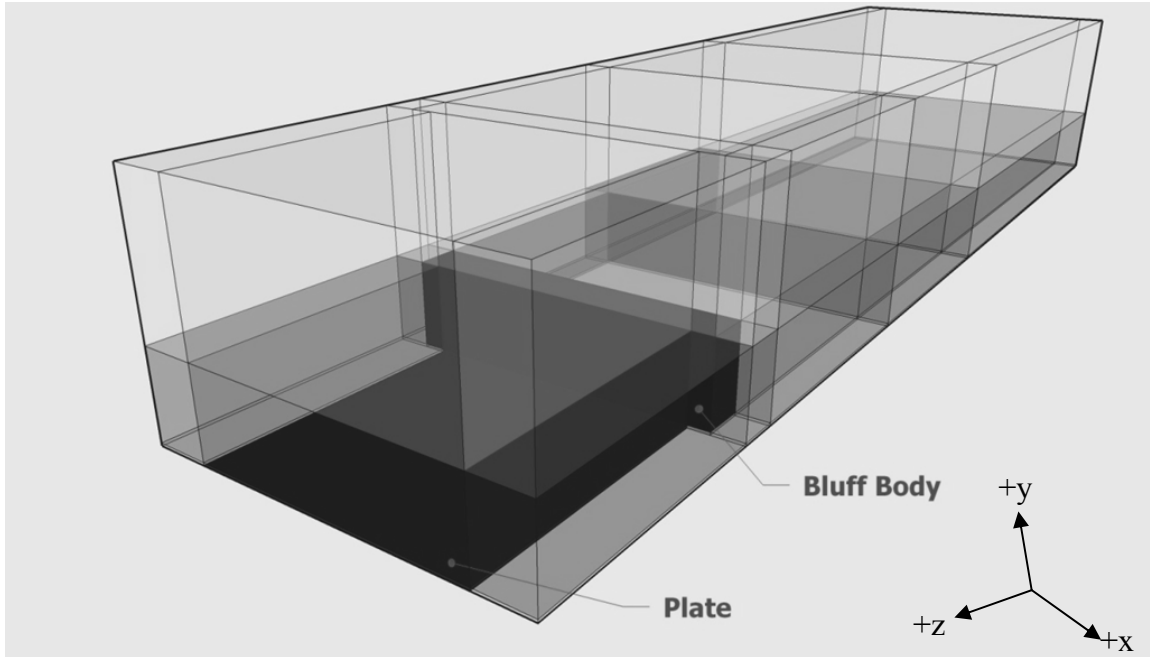


Figure 3.11 – Partitioning of Wind Tunnel Geometry

As shown in Figure 3.11, the region of the wind tunnel in the vicinity of and downstream of the plate and bluff body has been split up into different partitions. To get a better view of these partitions, consider Figures 3.12a-3.12c which shows an exploded view of Figure 3.11.

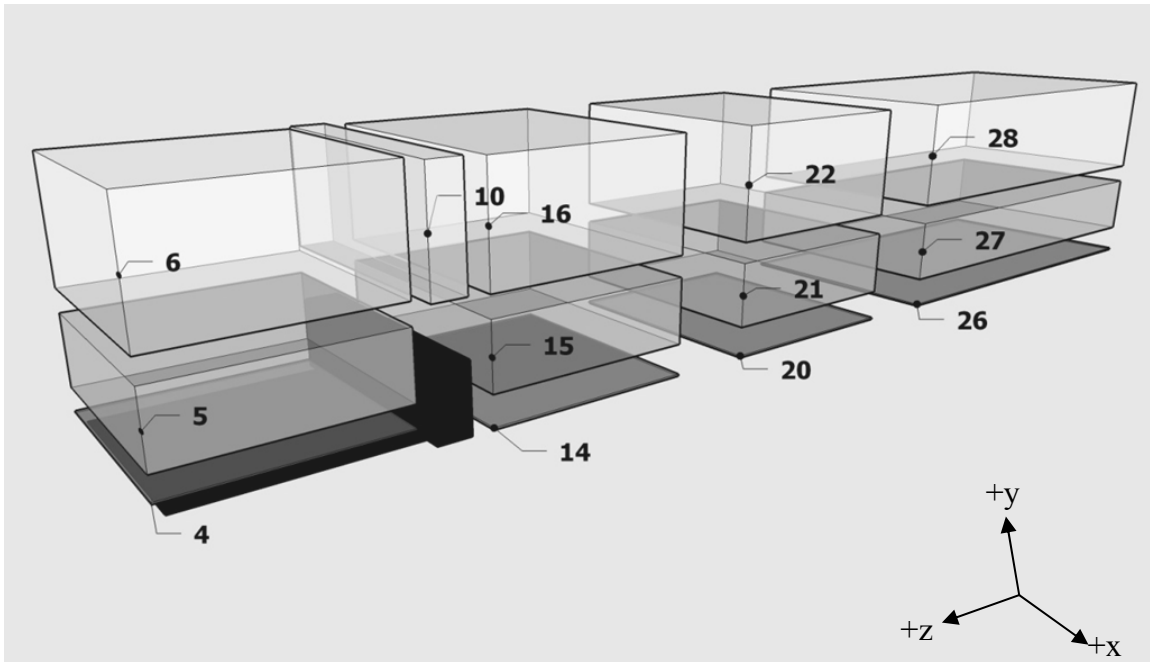


Figure 3.12a – Spatial Partitions about the Symmetry Plane

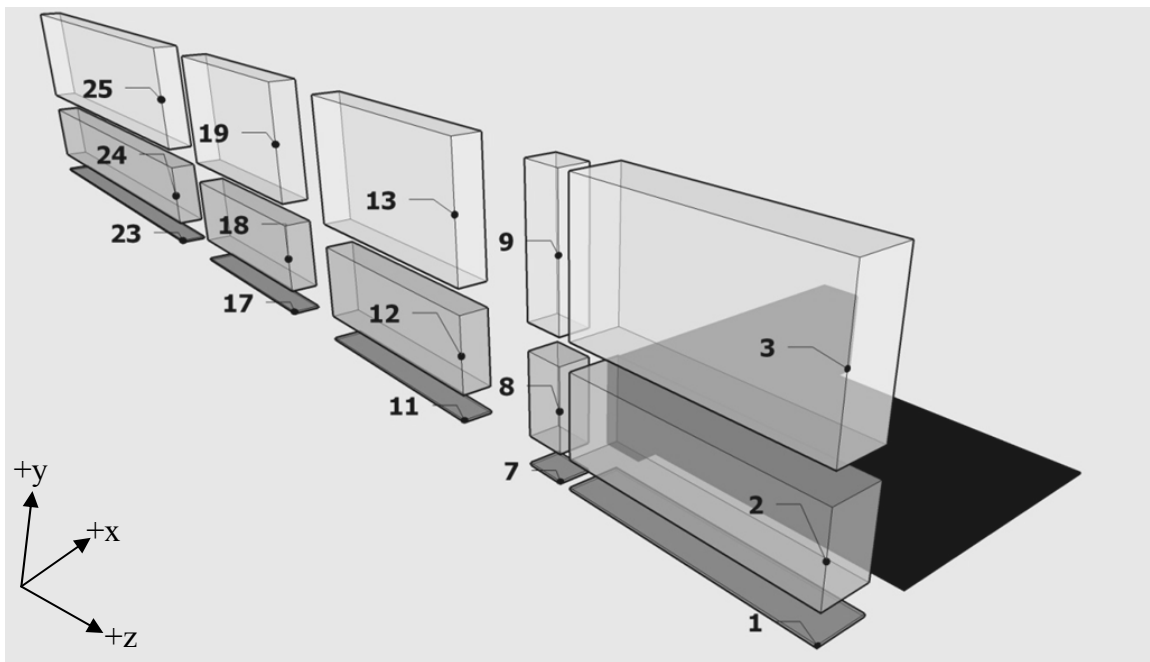


Figure 3.12b – Spatial Partitions to the Left of the Plate and Bluff Body

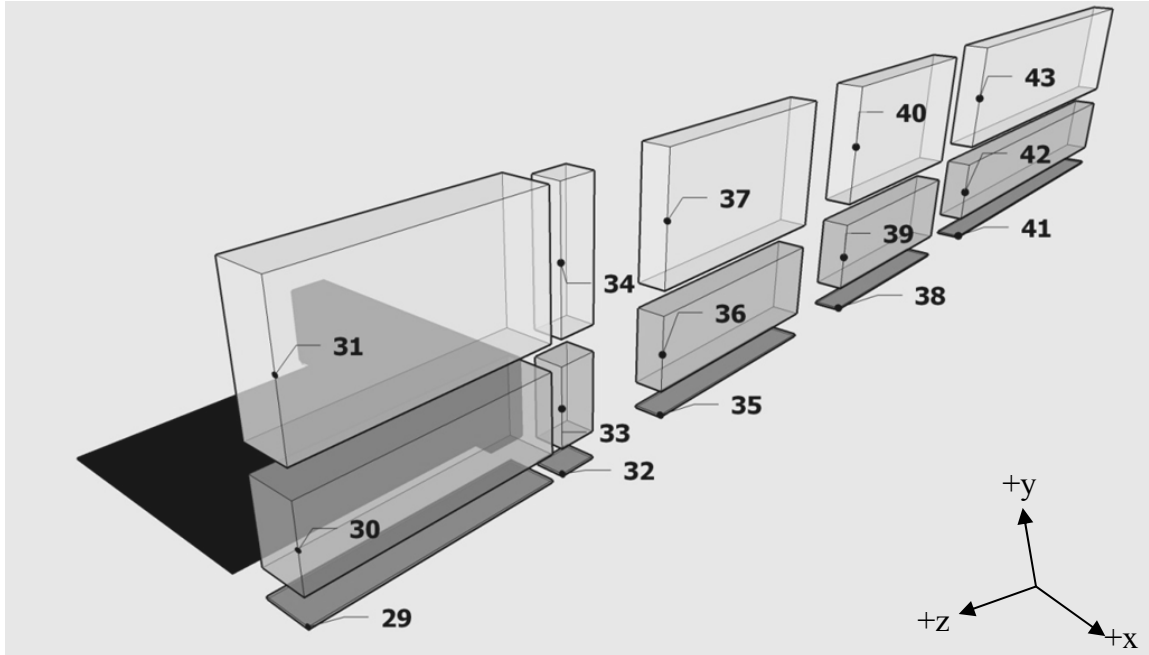


Figure 3.12c – Spatial Partitions to the Right of the Plate and Bluff Body

The configuration of the partitions shown in Figures 3.12a-3.12c exhibit two major features. The first is related to the vertical placements of the partitions in that they have been placed on the three levels. The first level is close to the floor of the wind tunnel, the second is up to the $y=32$ cm plane (this coincides with the height of the bluff body), and the third encompasses the region of space above the $y=32$ cm plane. The second feature of the partition configuration is in its streamwise placements. As shown in the abovementioned figures, partitions have been placed progressively downstream. These two features will allow the modeller to observe the following:

- (1) The vertical trajectories particulate can attain
- (2) How far the particulate is transported downstream and the region of space the particulates tend to accumulate in

Thus, this configuration ultimately affords the modeller to fully capture the spatial distribution of particulate at any given time step iteration.

In light of the partitions shown in Figures 3.12a-3.12c, there are two properties that must be acknowledged, and are described in Table 3.9.

Property	Description
1	The partitions shown in Figure 3.12a are those that intersect the symmetry plane ($x=70$ cm plane). These partitions have been placed such that when the partition is intersected by the symmetry plane, the volume of the partition on either side of the symmetry plane is equal. In addition, with respect to Figures 3.12b and 3.12c, the partitions shown in the latter figure are a mere reflection of those in former.
2	As mentioned previously, particulate distribution data is only available for the partitions shown in Figure 3.12b and the left half of the partitions shown in Figure 3.12a. Note that the sum of these partitions for which particulate data is available constitute the shaded region shown in Figure 3.10 (these partitions are herein known as <i>shaded partitions</i>).

Table 3.9 – Properties of Spatial Partitions

The properties described in Table 3.9 will play a pivotal role is fully characterizing the radiation field in the entire flow domain. Once the spatial partitions have been established (i.e., the spatial bounds of each partition shown in Figures 3.12a-3.12c have been determined; see Appendix C), the modeller can then focus on the second step in assessing the radiation field. This step focuses on converting the particulate spatial distribution within each partition at a given time step iteration to an airborne particulate activity. The means by which this conversion is accomplished will be described in Table 3.10.

Step	Description
1	Import the particulate data file exported by FLUENT into MATLAB.
2	Store the following data in the MATLAB input file:

- The spatial bounds for each of the shaded partitions
- The time step iterations for which the radiation field will be analyzed

3 For each time step iteration, bin the number of particulates, as a function of diameter, that reside in each shaded partition. Convert this distribution to activity via the following equation (see Appendix G):

$$A_j(i) = \frac{1}{6} \pi \left(\frac{\ln(2)}{T_{\frac{1}{2}}(^{140}\text{La})} \right) \left(\frac{N_A \rho_{^{140}\text{La}}}{M_M^{^{140}\text{La}}} \right) \left(\sum_{q=1}^{n_j(i)} D_{q,j}^3 \right) \quad (3.4)$$

Where:

$A_j(i)$ = activity of the ^{140}La particulates in shaded partition j at the i^{th} time step iteration (unit: Bq)

$T_{\frac{1}{2}}(^{140}\text{La})$ = half life of ^{140}La (unit: s)

N_A = 6.02×10^{23} nuclei \cdot mol $^{-1}$ (Avogadro's Constant)

$\rho_{^{140}\text{La}}$ = density of ^{140}La (unit: g \cdot cm $^{-3}$)

$M_M^{^{140}\text{La}}$ = molar mass of ^{140}La (unit: g \cdot mol $^{-1}$)

$n_j(i)$ = number of particulates residing in shaded partition j at the i^{th} time step iteration

$D_{q,j}$ = diameter of the q^{th} particulate residing in partition j at the i^{th} time step iteration (unit: cm)

Store in a matrix the activity of each shaded partition for each time step iteration.

It is important to note the absence of an exponential decay term on the right hand side of equation (3.4) to account for the radioactive decay of the ^{140}La particulates. For clarity, the exponential term is stated as $e^{-\lambda t}$, where λ is the decay constant for ^{140}La and t is the average elapsed time for which the radiation field in the wind tunnel is being analyzed.

As per Table 4.1, the average elapsed times for which the radiation field within the wind tunnel is being analyzed are negligible in comparison to the half life of ^{140}La (see Table B.1 in Appendix B). Thus, the exponential decay term will be close to unity and as such, it is not required to be present in equation (3.4).

- 4 For each time step iteration, calculate the volumetric activity in each shaded partition via the following equation:

$$A_{\forall,j}(i) = \frac{A_j(i)}{\forall_j} \quad (3.5)$$

Where:

$A_{\forall,j}(i)$ = volumetric activity of the ^{140}La particulates in partition j at the i^{th} time step iteration (unit: $\text{Bq}\cdot\text{m}^{-3}$)

$A_j(i)$ = activity of the ^{140}La particulates in partition j at the i^{th} time step iteration (unit: Bq)

\forall_j = volume of the shaded partition j (unit: m^3)

Store in a matrix the volumetric activity in each shaded partition for each time step iteration.

- 5 The volumetric activity calculated in step 4 must now be “reflected” onto the other un-modelled symmetric half of the wind tunnel domain. To do this, the properties stated in Table 3.9 must be used. With respect to property 1, the volumetric activity calculated in the partitions shown in Figure 3.12b will be “reflected” onto the partitions shown in Figure 3.12c. That is, the volumetric activity in partition 1 will be assigned to partition 29 and the volumetric activity in partition 2 will be assigned to partition 30, and so on. The partitions shown in Figures 3.12b and 3.12c that possess the same volumetric activity are fully listed below:

1 and 29	7 and 32	11 and 35	17 and 38	23 and 41
2 and 30	8 and 33	12 and 36	18 and 39	24 and 42
3 and 31	9 and 34	13 and 37	19 and 40	25 and 43

The partitions shown in Figure 3.12a have the activity and volumetric activity calculated in its left half (see property 2 in Table 3.9) in steps 3 and 4 respectively. However, when the left half of the partition is appended to its right half as per the “reflection” of results described above, the volumetric activity in this new partition will be the same as that in its left half calculated in step 4. To understand this, consider the following:

- As the left half and right half of the partition are appended, the new partition volume will double with respect to that of the left half.
- As per the symmetry plane employed in the GAMBIT model, the activity on the right half of the partition will be the same as that of the left half. Consequently, when the left and right halves of the partition are appended, the activity in the new partition will double with respect to that of the left half calculated in step 4.

If one were to substitute the activity and volume of the newly formed partition, both as a function of those of the left half, into equation (3.5), one finds that the volumetric activity of the new partition is the same as that of the left half.

The volume for each partition shown in Figures 3.12a-3.12c must also be computed. Using the spatial bounds for each shaded partition (see Appendix C), the volume can be calculated for each shaded partition. Then, these volumes can be used to find the volumes of the partitions shown in Figure 3.12a and 3.12c in the manner described above.

	Once the volumetric activity for each time step iteration and the volume are calculated for each of the partitions shown in Figures 3.12a-3.12c, they must be stored in their respective matrices.
6	Based on the calculations in the step 5, the following data are to be exported to data files: <ul style="list-style-type: none"> • Volume of each partition • Volumetric activity of each partition as a function of time step iteration • The average elapsed time for the corresponding time step iteration at which the radiation field is analyzed

Table 3.10 – Description of Particulate Spatial Distribution to Airborne Particulate Activity Conversion Algorithm

The steps shown in Table 3.10 have been used as the basis for developing the Activity_Calculations.m MATLAB code.

The modelling strategy developed thus far has effectively provided the framework by which a snapshot of the radiation field is taken for any given time step iteration. This is witnessed by the fact that via the spatial partitioning of the shaded region of the wind tunnel shown in Figure 3.10, the particulate spatial distribution in each of the partitions shown in Figures 3.12a-3.12c is converted to a volumetric activity. As a result, this strategy allows for the radiation field to effectively be mapped throughout the flow domain as a function of the time step iteration. Thus, the goal of Black Box 1 has been achieved.

Via the exported data described in step 6 of Table 3.10, the development of Black Box 2 will be discussed in the next section.

3.2.2.2 Black Box 2 Development

Table 3.8 states that the purpose of Black Box 2 is to use the volumetric activity data exported by Black Box 1 to calculate what is known as the *source bias*. The reality of the modelling strategy developed thus far is that at any time step iteration, there will be several partitions that will have a non-zero volumetric activity (herein, such partitions will be known as *active partitions*). Of course, this indicates that radiation is present in the partition and that the partition represents a radiation source. Further to the MC radiation transport theory presented in Chapter 2, when performing a MC radiation transport simulation with multiple sources, each source must be assigned a bias. A bias represents how much more radioactive one partition is relative to another. For example, if the volumetric activity data exported by Black Box 1 indicates that for a particular time step iteration, partition 1 has a volumetric activity of $7 \text{ kBq}\cdot\text{m}^{-3}$ and partition 15 has a volumetric activity of $10 \text{ MBq}\cdot\text{m}^{-3}$, then the MC source routine will sample partition 15 more than partition 1. Thus, partition 15 will possess a higher bias than partition 1.

The MC radiation transport simulation models the transport of radioactive particles and so in MCNPX, the user specifies how many of such radioactive particles will be simulated. Of course, the radioactive particles will emanate from the sources described above and so the MC simulation will use the bias calculated for each active partition to assign how many radioactive particles will be emitted from each. As per the example above, a higher fraction of the number of radioactive particles requested by the user will be assigned to emanate from partition 15 than from partition 1. Thus, the number of radioactive particles allotted to a partition based on its bias is a testament to how radioactive it is.

The bias is calculated as follows:

$$\text{Bias}_j(i) = \frac{A_{v,j}(i)}{\sum_{b=1}^{p(i)} A_{v,b}(i)} \quad (3.6)$$

Where:

$\text{Bias}_j(i) =$ bias that the j^{th} active partition possesses at the i^{th} time step iteration

$A_{v,j}(i) =$ volumetric activity of the j^{th} active partition at the i^{th} time step iteration
(unit: $\text{Bq}\cdot\text{m}^{-3}$)

$p(i) =$ number of active partitions at the i^{th} time step iteration

$A_{v,b}(i) =$ volumetric activity of the b^{th} active partition at the i^{th} time step iteration
(unit: $\text{Bq}\cdot\text{m}^{-3}$)

Equation (3.6) states that to calculate the bias of an active partition at the i^{th} time step iteration, divide the volumetric activity of this active partition by the sum of the volumetric activities of the partitions that are active at the i^{th} time step iteration.

Moreover, it is important to state the reason why the volumetric activity, instead of the activity, is used to compute the bias of a partition. Bearing in mind that the partitions employed in this thesis do not possess the same volume, it is important to acknowledge the fact that the volumetric activity is a measure of how distributed the activity is throughout a volume. As per equation (3.5), the activity in a small volume is more concentrated than it would be in a larger volume and as such, the volumetric activity will be higher for the smaller volume than it would be for the larger one. Herein lays the importance of accounting for volume. The bias calculations provide the perfect avenue by which the effect of partition volume can be accounted for in the MC radiation transport simulations.

The bias calculation methodology that has been presented essentially takes the snapshot of the radiation field provided by Black Box 1 and quantifies how radioactive each partition is with respect to each other. The results of these calculations act as a liaison by which the radiation field captured in Black Box 1 can be translated into a MC radiation transport model. The process by which this is done will be discussed in the next section.

The algorithm described above for bias calculations have been implemented in the `Source_Bias.m` MATLAB code. Once this code computes the bias for each active

partition at each time step iteration, the bias will then be exported to an external data file. The data contained in this file will be used to create an MCNPX input file for each time step iteration. As per Figure 1.3, the process of creating MCNPX input files is done in Black Box 2. However since this portion of the Black Box essentially deals with MC radiation transport modelling, its development will be discussed in the next section.

3.2.3 Monte Carlo Radiation Transport Modelling

Of course, quantifying the dose delivered by the resuspension of radioactive particulates constitute a major component of the CFD-MC radiation transport coupling methodology developed in this thesis. When assessing the radiological hazard arising from a resuspension event, the internal and external dose delivered by the resuspended particulates is of concern. Figure 1.3 broadly depicts how the dose will be calculated; however Section 3.2.4 will discuss this in greater detail. In the aforesaid figure, it is stated that the calculation of the external dose from the radiation field produced by radioactive particulate resuspension requires the external dose rate that must be computed by the MC simulation. The reason why the MC simulation can calculate the external dose rate is attributed to its ability to simulate the movement of energetic radiation emitted from radioactive decay, particularly in complex geometries where analytical solutions to radiation transport equations are not easily attained. Once the movement of radiation can be simulated, tallies can be placed at spatial locations of interest in the flow domain - tallies such as particle flux and external dose rate³²⁾, amongst others.

Of course, the MC simulation requires some prerequisite information in order to calculate the normalized external dose rate. The following steps will outline the information required and how the MC simulation will go about calculating the

³²⁾ Tallies calculated by MCNPX are normalized to the number of radioactive particles whose transport has been simulated. Due to this normalization, tallies have the word “normalized” appended to its name. For example, the external dose rate tally is called *normalized external dose rate*. Herein, this term will be used to discuss the external dose rate calculated by MCNPX.

normalized external dose rate (note that the following steps must be performed for each time step iteration):

- (1) Obtain the snapshot of the radiation field provided by Black Box 1
- (2) Insert rectangular parallelepiped sources in the place of each active partition (since each partition has this shape)
- (3) With the aid of the bias calculations from Black Box 2, assign radioactive particles to emanate from each of the sources
- (4) Simulate the movement of the radioactive particles within the wind tunnel domain and at particular spatial points of interest, tally the normalized radioactive particle flux
- (5) Convert the normalized particle flux to a normalized external dose rate

The above steps must be embodied in an input file for the MC radiation transport simulation. MCNPX is the code selected to perform these simulations and it must be noted that every MCNPX input file is composed of three sets of inputs called *cards*³³⁾. These cards are the cell, surface, and data cards. To shed more light on how the steps described above are incorporated into the MCNPX input file, consider the discussion below. Note that as per the discussion at the end of Section 3.2.2.2, the MCNPX input file generation is part of Black Box 2, and so the input files will be created in MATLAB.

Before the cards are constructed, the following data must be imported into MATLAB:

³³⁾ A “card” represents a portion of the MCNPX input file. This term dates back to the early generations of computing whereby a computer code was arranged into a set of cards (each card was in the form of a punch card). These cards were collectively known as “decks”.

- The bias that each partition possesses for each time step iteration
- The spatial bounds of each partition
- The gamma energy spectrum of ^{140}La (see Table B.3 in Appendix B for more information)

Using the data contained in the above files, the cards can now be populated. The first card that must be constructed is the cell card. The purpose of this card is to define every region of space, both within the domain of interest and outside of it, and the material(s) it is composed of. In the case of the wind tunnel being modelled for this thesis, the following regions are identified along with their respective composition material:

Region	Material
Plate	Plywood
Bluff Body	Plywood
Inside the wind tunnel but outside the plate and bluff body	Air
Outside of the wind tunnel	Void

Table 3.11 – Regions to Be Defined in MCNPX

With respect to the material assignment in the last region stated above, radioactive particles that enter the outside of the wind tunnel are no longer tracked since this region of space is not of interest in the radiation field analysis. Hence, this region is deemed void.

The second card that must be constructed is the surface card. The purpose of the surface card is to essentially build the regions described in Table 3.11 in the MCNPX environment. For example, to build the bluff body, the modeller will instruct the surface card to place a rectangular parallelepiped that will have the exact spatial dimensions and spatial location as the bluff body. This will be done for all of the structures found in the domain of interest, which are the plate, bluff body, and the wind tunnel shell (which is defined as the wind tunnel minus the plate and bluff body). The cell card will take these

surface declarations and assign a material composition to each of them. See Appendix D for more information on constructing the wind tunnel in the MCNPX environment.

The final card that must be populated is the data card. The data card contains information related to the radioactive particles whose transport is to be simulated in MCNPX. The inputs required for this card are described in Table 3.12.

Data	Description
Radioactive Particle Type	^{140}La emits both beta and gamma radiation and of these radiation types, gamma radiation poses an external radiological hazard. Moreover, it is assumed that when quantifying the dose delivered by the resuspension of ^{140}La particulate, the hypothetical individual who is standing at the exact spatial locations at which the dose is being calculated is assumed to be fully clothed. As such, external exposure to beta radiation is negligible since the moderate range of beta radiation will cause it to be fully attenuated by the clothing. Since the normalized external dose rate is sought after in the MCNPX simulation, gamma particles will be the radiation type whose transport is simulated.
Gamma Energy Spectrum	^{140}La emits gamma radiation of varying energies. The Gamma Energy Spectrum lists these energies as a function of their probability of emission. MCNPX will use this information to select the energies of the gamma radiation whose transport will be simulated.
Source Locations	The radiation field snapshots described by the data exported by the bias calculation data from Black Box 2 will indicate to the modeller which partitions are active at each time step iteration and the bias they possess. This therefore implies that an MCNPX input file will be created for each time step iteration. In each input file, a rectangular parallelepiped source will be placed in the spatial location of each active partition for the corresponding time step

	<p>iteration. In addition, the emission of radiation from each active partition will be isotropic (i.e., radiation will be emitted in all directions without preference to any one particular direction).</p>
Number of radioactive source particles	<p>The modeller has to alter the number of radioactive particles simulated in MCNPX until the tally result becomes independent of the number chosen and that its associated fractional standard deviation is below 5%. The number that will be used for the first execution of each MCNPX input file will be 1,000,000 and will be increased for subsequent runs.</p>
Detector Locations	<p>The work of Nigro et al. [9] and Krajnović et al. [10] showed that vortices formed downstream of a cube around and over which flow was modelled. The flow being modelled in Figure 3.6 is of a similar configuration in that there is flow around and over the bluff body. This leads the modeller to make the following assumptions:</p> <ul style="list-style-type: none"> • Vortices will form downstream of the bluff body. • Since these vortices are present in the main flow stream, they will act to keep particulates that have already been resuspended, remaining in suspension. • The location of these vortices (i.e. downstream of the bluff body) are such that it will cause the majority of the resuspended particulates to accumulate in this downstream region <p>In light of these assumptions, it can then be asserted that the region of space downstream of the bluff body will host the highest radiation hazard. Figure 1.3 states that internal and external doses will be calculated at spatial points of interest in the flow domain. As a result of the assumptions stated above, the radiation dose will</p>

	<p>be quantified in this region of the wind tunnel. Two spatial locations, herein known as <i>detector locations</i>, have been selected, one close to the back of the bluff body and the other further downstream. The coordinates for these points are as follows:</p> <table border="1" data-bbox="722 464 1227 575"> <tr> <td>Detector 1 Location</td> <td>(70, 8, -638)</td> </tr> <tr> <td>Detector 2 Location</td> <td>(70, 8, -738)</td> </tr> </table> <p>Since the internal and external doses will be calculated at the above spatial locations, a normalized external dose rate tally will be placed at these positions. This tally is implemented in two stages whereby an F5 tally is first placed at each detector location. This tally will record the time-integrated normalized gamma flux at each location (i.e., the normalized gamma fluence). The DF5 tally will then be placed at each detector location and will convert the respective normalized gamma fluence to a normalized external dose rate via fluence-to-dose rate conversion factors tabulated in the ANSI/ANS-6.1.1-1991 database.</p>	Detector 1 Location	(70, 8, -638)	Detector 2 Location	(70, 8, -738)
Detector 1 Location	(70, 8, -638)				
Detector 2 Location	(70, 8, -738)				
Material Specifications	The materials shown in Table 3.11 must be declared in the MCNPX input file. The manner in which this is done is shown in Appendix B, Tables B.4 and B.5.				

Table 3.12 – Description of Data Card Contents in MCNPX Input File

Based on the description of the inputs required by the geometry (cell, surface, and data) cards, it is evident that the portion of the MCNPX input file that is dependent on the time step iteration for which it is created for is the source locations. Again, the data produced by Black Box 2 will indicate the partitions in the wind tunnel domain that are active for each time step iteration analyzed. The partitions that are active will be different for each time step iteration and so sources in the corresponding MCNPX input file will be placed accordingly (see discussion on *Source Locations* in Table 3.12). The

description above pertaining to the process of creating an MCNPX input file has been implemented in the MCNPX_Black_Box.m MATLAB code.

The development of Black Box 1 and 2 have been discussed. The formulation of these black boxes has allowed for the following to be attained:

- The spatial variation of the volumetric activity for each time step iteration
- The normalized external dose rate at each detector location described in Table 3.12, for each time step iteration

As per the research blueprint shown in Figure 1.3, the above two quantities serve as essential parameters by which the dose calculations can proceed. Carrying out these calculations will be the subject of the next section.

3.2.4 Dose Calculations

The objective of the dose calculations is to quantify the internal and external dose delivered by the resuspension of the radioactive particulates, at each detector location. As per Figure 1.3, these calculations represent the final stage in the coupling methodology. The fact that (a) the spatial variation of the volumetric activity and (b) the normalized external dose rate at each detector location has been calculated at each time step iteration allows for the temporal variation of the internal and external dose rate at each detector location to be quantified.

At each detector location, the dose calculations will be conducted in two phases, the first being the calculation of the internal and external dose rate (dose per unit time) and the second being the time-integrated internal and external dose. A discussion on the dose rate calculations follows.

3.2.4.1 Dose Rate Calculations

The internal dose rate at each detector location is calculated via equations (3.7) and (3.8) shown in Table 3.13.

Internal Dose Rate Equations		
Detector Location	Equation	Equation Number
1	$\dot{D}_{\text{internal},1}(\mathbf{i}) = A_{\text{V}}^{(15)}(\mathbf{i}) \cdot \text{BR} \cdot \text{DCF}$	(3.7)
2	$\dot{D}_{\text{internal},2}(\mathbf{i}) = A_{\text{V}}^{(21)}(\mathbf{i}) \cdot \text{BR} \cdot \text{DCF}$	(3.8)

Where:

$\dot{D}_{\text{internal},1}(\mathbf{i}), \dot{D}_{\text{internal},2}(\mathbf{i}) =$ internal dose rate at detector 1 and 2 locations, respectively, for i^{th} time step iteration (unit: $\text{Sv} \cdot \text{hr}^{-1}$)

$A_{\text{V}}^{(15)}(\mathbf{i}), A_{\text{V}}^{(21)}(\mathbf{i}) =$ volumetric activity in partitions 15 and 21, respectively, for i^{th} time step iteration (unit: $\text{Bq} \cdot \text{m}^{-3}$)

BR = breathing rate (unit: $\text{m}^3 \cdot \text{hr}^{-1}$)

DCF = dose conversion factor (unit: $\text{Sv} \cdot \text{Bq}^{-1}$)

Table 3.13 – Internal Dose Rate Equations

There are several assumptions pertaining to the quantities employed by the equations shown in Table 3.13, and are documented in Table 3.14.

Quantity	Assumption
Volumetric Activity	With respect to the partitions that detector locations 1 and 2 are placed in, Appendix C indicates that partitions 15 and 21 respectively host these detectors. The assumption pertaining to the volumetric activities in these respective partitions, as is the case with all partitions, is that it is uniformly distributed throughout the partition.

	<p>That is, the volumetric activity exhibits no spatial variation within the partition – it is the same at each point within the partition.</p>
Breathing Rate	<p>The breathing rate has been extracted using the following attributes:</p> <ul style="list-style-type: none"> • Target Group: Adult Men • Activity Type: Light <p>The breathing rate for the above attributes is $1.2 \text{ m}^3 \cdot \text{hr}^{-1}$ [34].</p>
Dose Conversion Factor	<p>The dose conversion factor has been extracted using the following attributes:</p> <ul style="list-style-type: none"> • Nuclide: ^{140}La • Intake Mode: Inhalation • Target Group: Adult, Public • Target Organ: Effective (ICRP 60) – Sum over all organs, Type M³⁴⁾ <p>The dose conversion factor for the above attributes is $1.10 \times 10^{-9} \text{ Sv} \cdot \text{Bq}^{-1}$ [44].</p> <p>It is important to mention that the dose conversion factor corresponding to the inhalation of $1 \mu\text{m } ^{140}\text{La}$ particulates are only available in [44]. Despite the fact that the transport of particulates whose diameters varied from $1 \mu\text{m}$ to $6 \mu\text{m}$ are modelled in this thesis, the dose conversion factor for the inhalation of $1 \mu\text{m}$ particulates must be employed to compute the internal dose that arises from the inhalation of particulates greater than this size as such factors for the inhalation of $2 \mu\text{m} - 6 \mu\text{m } ^{140}\text{La}$ particulates are</p>

³⁴⁾ The “type” classifies how fast radiation that is characteristic of a particular radionuclide (^{140}La) is absorbed/transferred out of lungs and into the blood streams that will then go on to interact with and distribute within other organs. “M” stands for medium and so a medium rate of distribution of ^{140}La throughout the body is being modelled.

unavailable at the time of this writing.

Table 3.14 – Internal Dose Rate Calculation Assumptions

As per the assumptions stated in Table 3.14, it is clear that the inhalation of ^{140}La is being modelled and the resultant internal dose is being analyzed over the entire body. If one were to visualize a human standing at each detector location, the local volumetric activity will contribute to the internal dose since the human will inhale this volumetric activity. Hence, the calculation of the internal dose rate at each detector location employs the volumetric activity of the host partition. Of course, since the internal dose seeks to quantify the biological damage from the inhalation of ^{140}La particulates, the internal dose is classified as an effective dose.

The external dose rate at each detector location is calculated via equations (3.9) and (3.10) which are shown in Table 3.15.

External Dose Rate Equations		
Detector Location	Equation	Equation Number
1	$\dot{D}_{\text{external},1}(\mathbf{i}) = DF_{\text{MCNPX},1}(\mathbf{i}) \cdot Y_{^{140}\text{La}} \cdot \left(\sum_{f=1}^{p(\mathbf{i})} A_{\nabla,f}(\mathbf{i}) \right) \cdot \left(\sum_{f=1}^{p(\mathbf{i})} \nabla_f \right)$	(3.9)
2	$\dot{D}_{\text{external},2}(\mathbf{i}) = DF_{\text{MCNPX},2}(\mathbf{i}) \cdot Y_{^{140}\text{La}} \cdot \left(\sum_{f=1}^{p(\mathbf{i})} A_{\nabla,f}(\mathbf{i}) \right) \cdot \left(\sum_{f=1}^{p(\mathbf{i})} \nabla_f \right)$	(3.10)

Where:

$\dot{D}_{\text{external},1}(\mathbf{i}), \dot{D}_{\text{external},2}(\mathbf{i}) =$ external dose rate at detector 1 and 2 locations, respectively, for i^{th} time step iteration (unit: $\text{Sv} \cdot \text{hr}^{-1}$)

$DF_{\text{MCNPX},1}(\mathbf{i}), DF_{\text{MCNPX},2}(\mathbf{i}) =$ MCNPX normalized external dose rate at detector 1 and 2 locations, respectively, for i^{th} time step iteration (unit: $\text{Sv} \cdot \text{hr}^{-1} \cdot \gamma_S^{-1}$)³⁵⁾

³⁵⁾ The symbol γ_S stands for gamma source particle and is equivalent to the number of gamma particles whose transport is simulated in MCNPX.

$Y_{140\text{La}}$ = gamma yield for ^{140}La (unit: $\gamma_s \cdot \text{decay}^{-1}$)

$p(i)$ = number of active partitions at the i^{th} time step iteration

$A_{\forall,f}(i)$ = volumetric activity of f^{th} active partition at the i^{th} time step iteration (unit: $\text{Bq} \cdot \text{m}^{-3}$)

\forall_f = volume of f^{th} active partition (unit: m^3)

Table 3.15 – External Dose Rate Equations

Further to what was described in Table 3.12 about the radioactive particle type being simulated in MCNPX, specifically the omission of beta contributions to the external dose rate, beta submersion dose is ignored in the external dose rate calculation as the external exposure to gamma radiation is of primary concern.

Contrary to the internal dose rate calculations, the volumetric activities of all active partitions must be included in the external dose rate calculations since the human standing at each detector location will be externally exposed to the radioactivity contained in *all* active partitions and so will receive a dose contribution from *all* active partitions. Since the external dose quantifies the biological damage due to external exposure to gamma radiation, the external dose is classified as an effective dose.

Based on the equations used to calculate the internal and external dose rates in Tables 3.13 and 3.15, respectively, there are two important properties of these dose rate types that must be emphasized. Equations (3.7) and (3.8) illustrate the fact that the internal dose rate is solely a function of the volumetric activity of the partitions that host the respective detectors. As shown in equation (3.4), the activity is calculated directly from the particulate data exported by FLUENT (as is the case with the volumetric activity which, via equation (3.5), is a function of the activity). Thus, the internal dose rate is calculated directly from the FLUENT results. However, equations (3.9) and (3.10) indicate that the external dose rate is a function of the volumetric activity of all active partitions and the normalized external dose rate calculated by MCNPX. Thus, the external dose rate is calculated from both FLUENT and MCNPX results. These properties conform to what was described about dose calculations in Figure 1.3 in that the

internal dose is a function of only the airborne particulate activity (calculated via FLUENT results) while the external dose is a function of both the airborne particulate activity and normalized external dose rate (calculated via FLUENT and MCNPX results, respectively).

The internal and external dose rate will be calculated at each detector location and at each time step iteration. As a result, the dose rates that are calculated are a function of time and it is of interest to the modeller to calculate the total dose³⁶⁾ delivered by the resuspension of ¹⁴⁰La particulates during the time of exposure (i.e., from the first to last time step iteration analyzed). The *total dose* is known as the *time-integrated dose* and the procedure by which this is calculated will be discussed in the next section.

3.2.4.2 Time-Integrated Dose Calculations

Generally speaking, the time-integrated dose is the area under the curve of dose rate versus time. To state this mathematically, first consider the hypothetical curve of dose rate versus time in Figure 3.13.

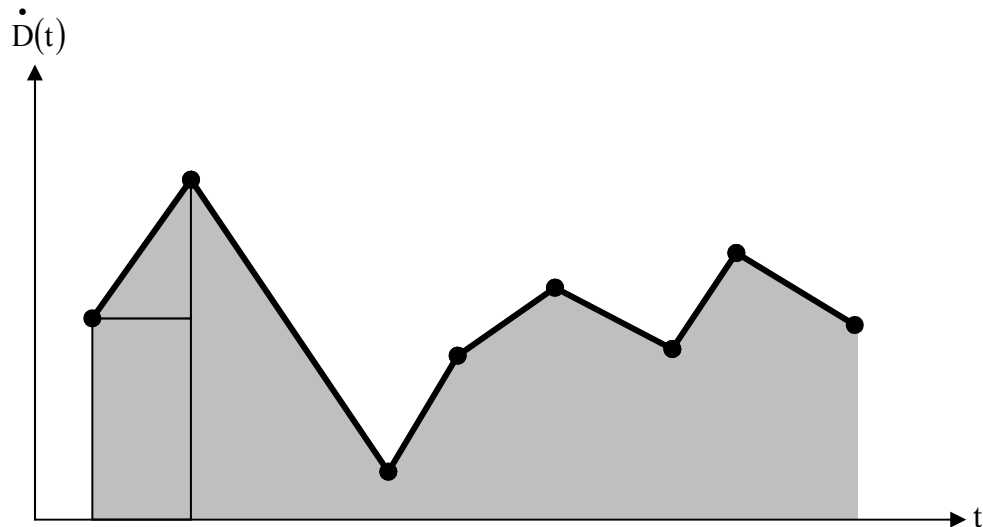


Figure 3.13 – Hypothetical Dose Rate Distribution Over Time

³⁶⁾ The term *total dose* encompasses the time-integrated internal dose and the time-integrated external dose at each detector location.

To find the area under the curve shown in Figure 3.13, one needs to first fragment the area into triangles and rectangles and then take the sum of the respective areas of these shapes, as shown in the above figure. With this in mind and the configuration shown in Figure 3.13, the equation to find the total dose is as follows:

$$D_{\text{total}} = \underbrace{\left(\frac{1}{2} \sum_{i=1}^{h-1} \left(\left| \dot{D}_{i+1} - \dot{D}_i \right| \right) (t_{i+1} - t_i) \right)}_{\text{Area of Triangle}} + \underbrace{\left(\sum_{i=1}^{h-1} \left(\dot{D}_i \right) (t_{i+1} - t_i) \right)}_{\text{Area of Rectangle}} \quad \text{if } \dot{D}_i < \dot{D}_{i+1} \quad (3.11)$$

$$D_{\text{total}} = \left(\frac{1}{2} \sum_{i=1}^{h-1} \left(\left| \dot{D}_{i+1} - \dot{D}_i \right| \right) (t_{i+1} - t_i) \right) + \left(\sum_{i=1}^{h-1} \left(\dot{D}_{i+1} \right) (t_{i+1} - t_i) \right) \quad \text{if } \dot{D}_{i+1} < \dot{D}_i$$

Where:

D_{total} = total (time-integrated) dose (unit: Sv)

h = number of time steps analyzed

\dot{D}_i = dose rate at the i^{th} time step iteration (unit: Sv·hr⁻¹)

t_i = averaged elapsed time for corresponding i^{th} time step iteration (unit: hr)

Since the internal and external dose rates at each detector location have been calculated for each time step iteration, equation (3.11) must be employed to compute the time-integrated internal and time-integrated external dose at each detector location.

Once the total dose is found, it must be re-stated with respect to some reference quantity in order to provide an indication of how intense the radiation field produced by the resuspension of the ¹⁴⁰La particulates is. The following section will expound upon this.

3.2.4.3 Surface Activity-to-Dose Conversion Factor Calculations

The means by which the total dose computed via equation (3.11) can be re-stated relative to some reference quantity is via the calculation of a surface activity-to-dose

conversion factor. This is not to be confused with the one employed in equations (3.7) and (3.8). Rather, the nature of this conversion factor is described by equation (3.12).

$$\eta = \frac{D_{\text{total}}}{A_{\text{S}}^{\text{plate}}} \quad (3.12)$$

Where:

η = surface activity-to-dose conversion factor (unit: Sv·Bq⁻¹·m²)

D_{total} = total dose (unit: Sv)

$A_{\text{S}}^{\text{plate}}$ = plate surface activity (unit: Bq·m⁻²)

As shown in equation (3.12), this conversion factor is the ratio of the total dose to the initial surface plate activity. As described earlier, the ¹⁴⁰La particulates are placed on the plate prior to the introduction of high speed air flow into the wind tunnel.

Consequently, the plate will possess a surface activity before any resuspension occurs. Thus, this surface activity provides an indication of how strong the radiation field is before resuspension while the total dose quantifies the strength of the radiation field as a result of resuspension. Therefore, taking the ratio of the latter quantity to the former will permit the modeller to understand how much total dose is delivered by the resuspension of ¹⁴⁰La particulates per unit plate surface activity. Thus, this ratio can be thought of as a measure of how intense the radiation field produced by the resuspension of ¹⁴⁰La particulates is in relation to the initial plate surface activity.

With respect to the denominator of equation (3.12), the initial plate surface activity can be computed by first calculating the activity on the plate and then dividing this quantity by the area of the plate. Equation (G.8) in Appendix G is used to compute the plate activity and using the particulate injection information in Table 3.7, the calculation proceeds as follows:

$$A_S^{\text{plate}} = \frac{1}{6} \pi \left(\frac{\ln(2)}{T_1 \left(\frac{140}{2} \text{La} \right)} \right) \left(\frac{N_A \rho_{140} \text{La}}{M_M^{140} \text{La}} \right) \left(\begin{array}{l} \sum_{i=1}^{100} D_{i,1}^3 + \sum_{j=1}^{100} D_{j,2}^3 + \sum_{k=1}^{100} D_{k,3}^3 \\ + \\ \sum_{l=1}^{100} D_{l,4}^3 + \sum_{m=1}^{100} D_{m,5}^3 + \sum_{n=1}^{100} D_{n,6}^3 \end{array} \right) \cdot \text{Area}_{\text{plate}}^{-1} \quad (3.13)$$

Where:

$D_{i,1}$ = diameter of i^{th} particulate from rake 1 (unit: cm)

$D_{j,2}$ = diameter of j^{th} particulate from rake 2 (unit: cm)

$D_{k,3}$ = diameter of k^{th} particulate from rake 3 (unit: cm)

$D_{l,4}$ = diameter of l^{th} particulate from rake 4 (unit: cm)

$D_{m,5}$ = diameter of m^{th} particulate from rake 5 (unit: cm)

$D_{n,6}$ = diameter of n^{th} particulate from rake 6 (unit: cm)

$\text{Area}_{\text{plate}}$ = area of the plate (unit: m^2)

The particulate injection information in Table 3.7 pertains to Figure 3.6, whereby the flow and particulate resuspension in only half of the wind tunnel is being modelled in GAMBIT and FLUENT. Once the plate activity is found, the area of the plate must be calculated. However, since the particulates are injected on half of the plate with respect to the 1x1 m plate shown in the schematics of Appendix A, then the area of the half plate must only be calculated. Hence, the area of the 0.5x1 m plate (0.5 m^2) must be employed. In light of the fact that the plate activity and plate area calculated above relate to the half-modelled plate shown in Figure 3.6, the ratio between these two quantities will be the same as it is for the ratio of that for the fully modelled plate. The reasons for this are analogous to that discussed in step 5 of Table 3.10.

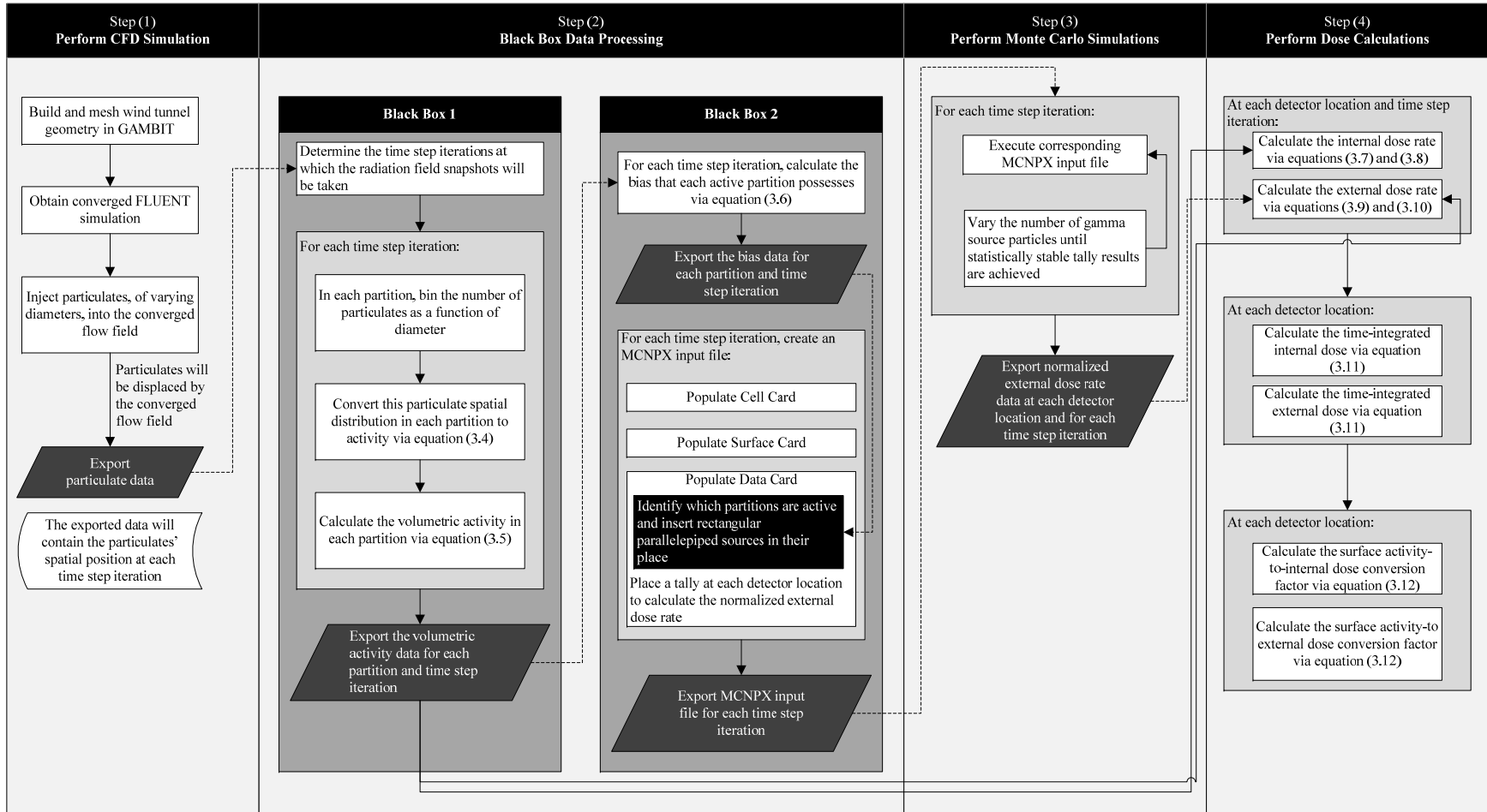
In equation (3.12), when the time-integrated internal dose at either detector location is substituted as the total dose, the surface activity-to-dose conversion factor is termed the *internal dose conversion factor*. Moreover, when the time-integrated external dose at either detector location is substituted into the numerator of equation (3.12), the surface activity-to-dose conversion factor is termed the *external dose conversion factor*.

3.3 Summary

This chapter commenced with a description of the geometry and radioactive particulates that were used as the basis for developing a coupling methodology to link CFD and MC radiation transport simulations for the purpose of simulating particulate resuspension and analyzing the resultant radiation field. Following this, a step-by-step description of the coupling methodology has been provided. For the sake of completion, Figure 3.14 provides a high level overview of the coupling methodology developed in this chapter.

With the coupling methodology shown in Figure 3.14 in mind, Chapter 4 will present the results of the CFD, MC radiation transport, and dose calculations performed in support of the coupling framework developed to model the scenario described in Figure 3.4.

Figure 3.14 – High-Level Overview of the CFD-MC Radiation Transport Coupling Methodology



CHAPTER 4

RESULTS AND DISCUSSION

Chapter 3 outlined and described the four major components of the methodology developed for coupling the CFD and MC radiation transport simulations that provides a framework to model the resuspension of radioactive particulates and analyze the resultant radiation field, and are relisted below:

- (1) CFD modelling
- (2) Black Box data processing
- (3) MC radiation transport modelling
- (4) Dose calculations

It is evident from Figure 3.14 that the coupling methodology employs a sequential execution. That is, a component passes data onto the next component of the coupling methodology without feedback from the latter to the former component. For example, the CFD simulation produces particulate data that will serve as input to the Black Box, however there is no transmission of data from the Black Box back to the CFD simulation. Nevertheless, each of these components produce output that is pivotal to the implementation of the coupling methodology developed in this thesis.

The purpose of this chapter is to present and analyze the results produced by each component of the coupling methodology. As mentioned on numerous occasions throughout this thesis, the coupling framework culminates in the calculation of the radiation dose. Hence, the ultimate aim of this chapter is to judge the ability of the coupling methodology developed to produce a reasonable dose estimate [13]. This chapter is structured to present and analyze the results produced by each component of the coupling methodology on a section-by-section basis. The results of the CFD simulation will first be presented, followed by the data produced by the Black Box. The results of the MCNPX simulation will then follow and finally the results of the dose calculations will be discussed.

4.1 CFD Simulation Results

Numerical-based simulations, such as CFD simulations, must be converged prior to the analysis of the results it produces. The manner in which FLUENT determines the convergence of a simulation is described in [45], and is summarized in the discussion below.

Several turbulence models have been derived to approximate the solution to the equations governing the flow of incompressible fluids (these equations will herein be known as conservation equations; see Section 2.1.4 for more information). Of course, these turbulence models require the use of numerical methods and as such, an iteration or time step approach is required to solve the respective constituent equations of these models at each node location specified in GAMBIT. For each iteration or time step, the solution yielded by the turbulence model does not fully satisfy the conservation equations, as these turbulence models are approximations to these equations. This discrepancy is known as the *residual* and the *total residual* of each flow variable that the turbulence model calculates (such as fluid pressure, fluid velocity, etc.) throughout the flow domain is calculated by taking the sum of the absolute value of the residual of each flow variable in each computational cell. The total residual is then divided by a scaling factor³⁷⁾ to produce a *scaled residual*. Total residuals are often divided by a common factor such that the residual for each flow quantity can be compared on a similar scale.

If the scaled residual of each flow quantity falls below a *residual threshold*, the simulation is deemed to be converged. In FLUENT, the default value of this threshold is 10^{-3} however this value can be changed by the user. As a rule of thumb, the smaller one makes this value, the longer the simulation will take to converge. To find a middle ground whereby a well-converged simulation can be produced over a non-exhaustive time frame, a residual threshold of 10^{-5} has been chosen for the CFD simulation performed for this thesis.

³⁷⁾ A scaling factor is selected from the properties of the main flow stream, such as average streamwise fluid velocity.

As per Table 3.5, the k- ϵ turbulence model has been selected to model the flow in the wind tunnel shown in Figure 3.6. To judge the convergence of this CFD simulation, FLUENT calculated the scaled residual of the following flow variables after each iteration: k, ϵ , fluid velocity, and the continuity equation³⁸⁾. If the scaled residual of each of these flow variables falls below 10^{-5} , the simulation is deemed to be converged. Figure 4.1 illustrates how the scaled residual for each of the aforesaid flow variables changes as the simulation progresses.

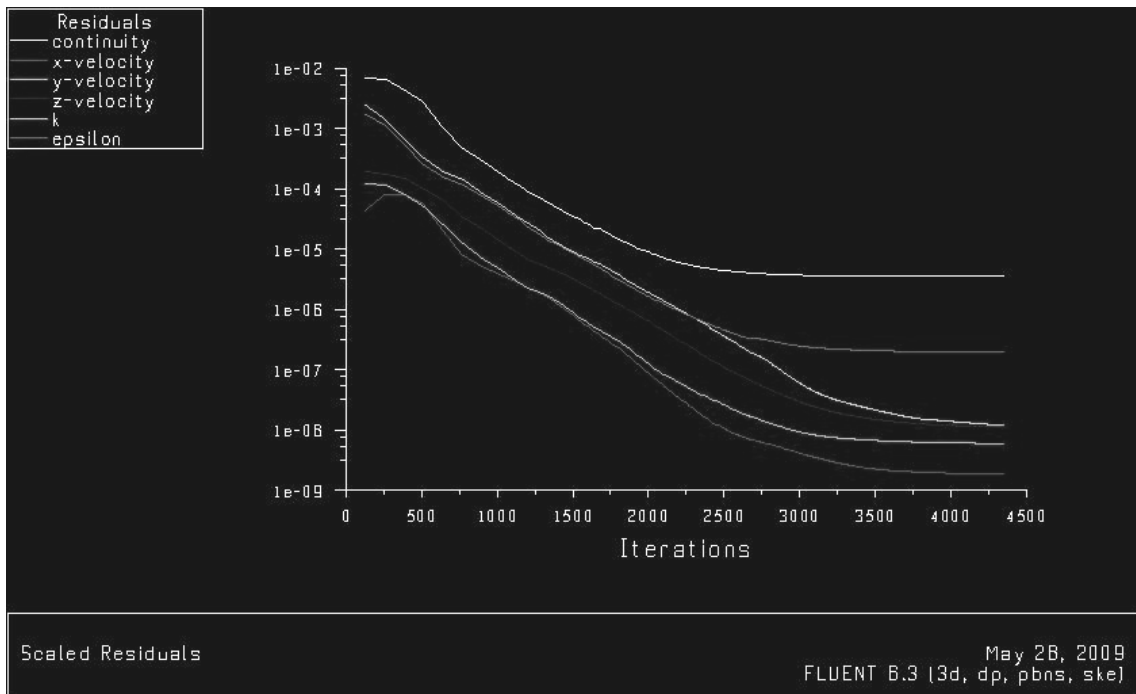


Figure 4.1 – Plot of Flow Quantity Scaled Residuals Versus Elapsed Number of Iterations

Figure 4.1 illustrates that at just over 4250 iterations, the scaled residual of all flow variables fall below the residual threshold of 10^{-5} and so the flow field calculated in the wind tunnel domain shown in Figure 3.6 is converged. At this point, the flow field produced in the wind tunnel can now be analyzed such that the flow structures produced by the bluff body can be visualized. The presence of a bluff body fosters the creation of a wake region to its downstream and an important feature of this region is the negative

³⁸⁾ The scaled residual of the continuity equation quantifies how the calculated flow field produced by the turbulence model selected over predicts or under predicts the solution to the continuity equation.

pressure vortices that it hosts. To visualize these vortices, two sets of figures will be shown whereby Figures 4.2-4.3 reveal the total fluid pressure distribution and vortices along the $+x/-z$ plane while Figures 4.4-4.6 will show those along the symmetry plane (i.e., see plane 2 in Figure 3.6). Of course, since it is of interest to visualize the total fluid pressure distributions and vortices in the vicinity of the bluff body, the contour plots pertaining to these quantities will intersect the bluff body along the abovementioned planes. Finally, before the aforementioned figures are presented, it must be noted that the arrows shown in Figures 4.3, 4.5, and 4.6 are indicative of two features of the fluid property to which the figure corresponds to, which are (1) the size of the arrow is directly proportional to the magnitude of the fluid property whose distribution is illustrated in the figure and (2) the direction of the arrow indicates the spatial direction in which the fluid is flowing in the domain.

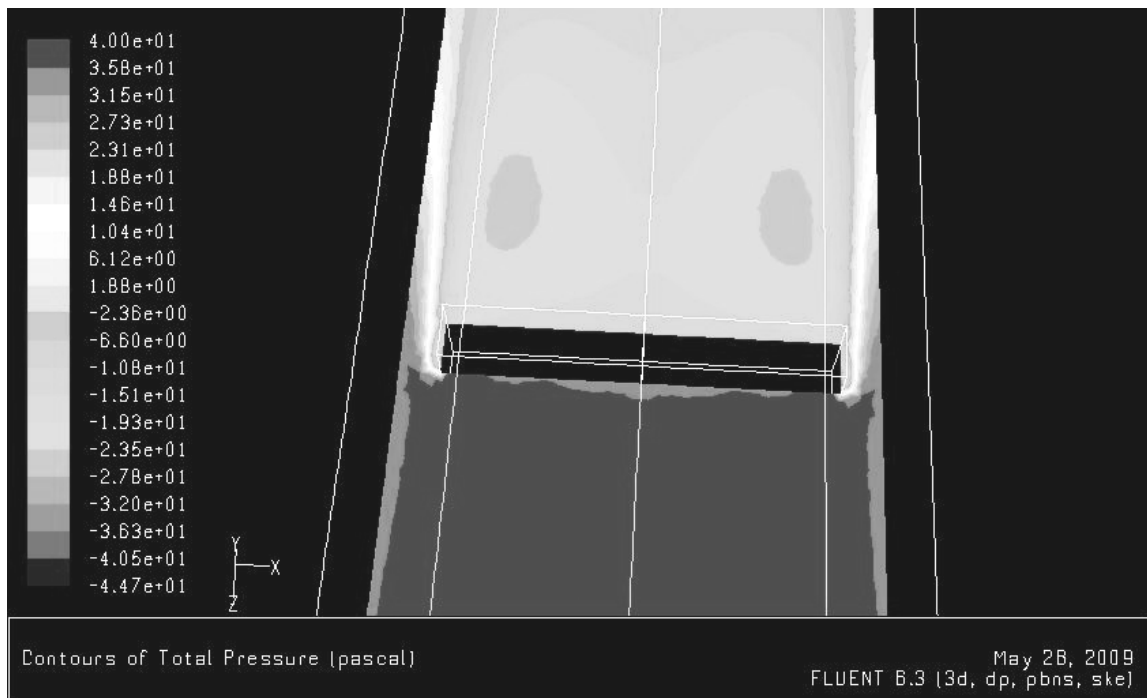


Figure 4.2 – Total Pressure Distribution along the $+x/-z$ Plane

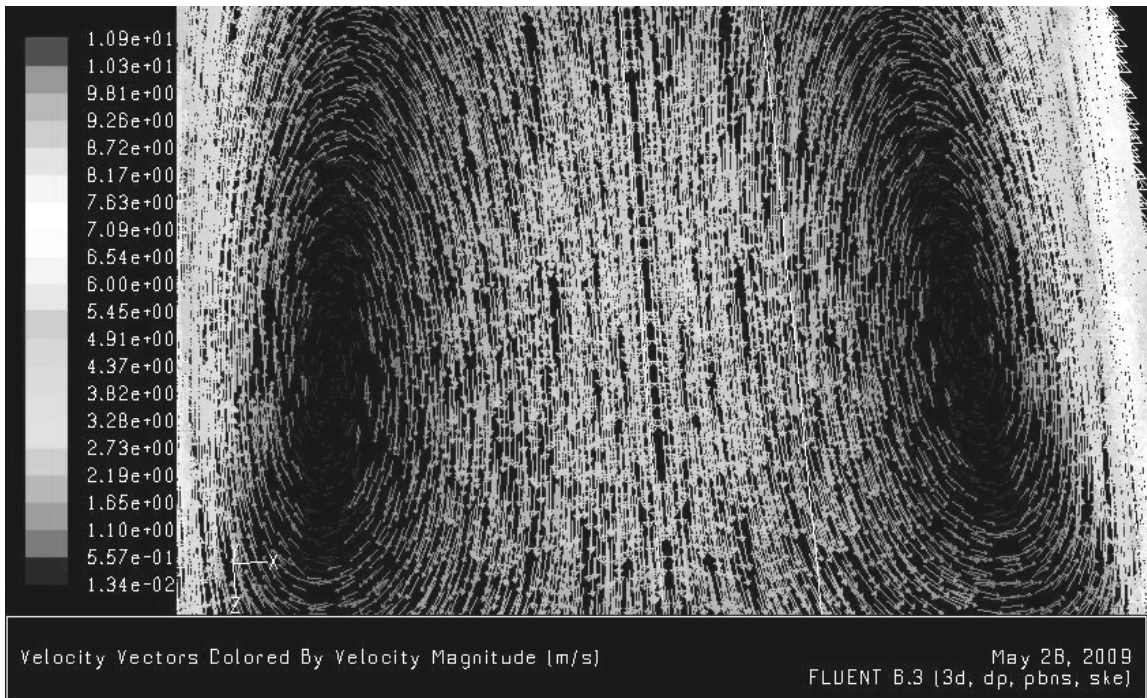


Figure 4.3 – Vortices Present Behind the Bluff Body along the +x/-z Plane

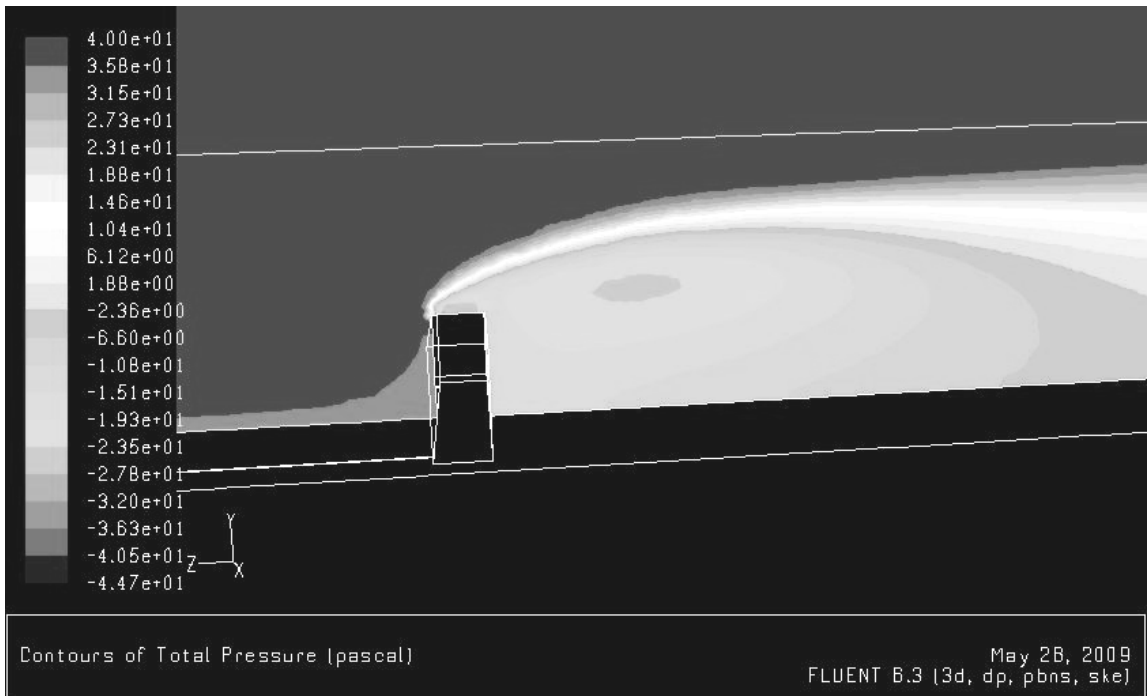


Figure 4.4 – Total Pressure Distribution along the +y/-z Plane

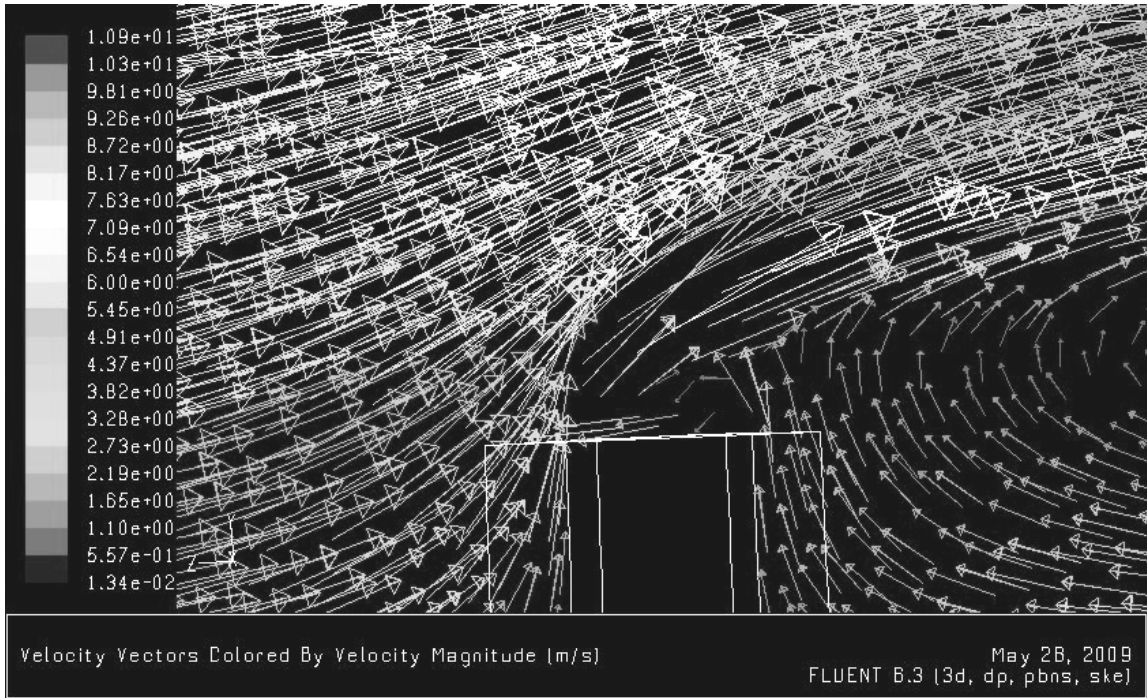


Figure 4.5 – Vortices Present Atop the Bluff Body along the +y/-z Plane

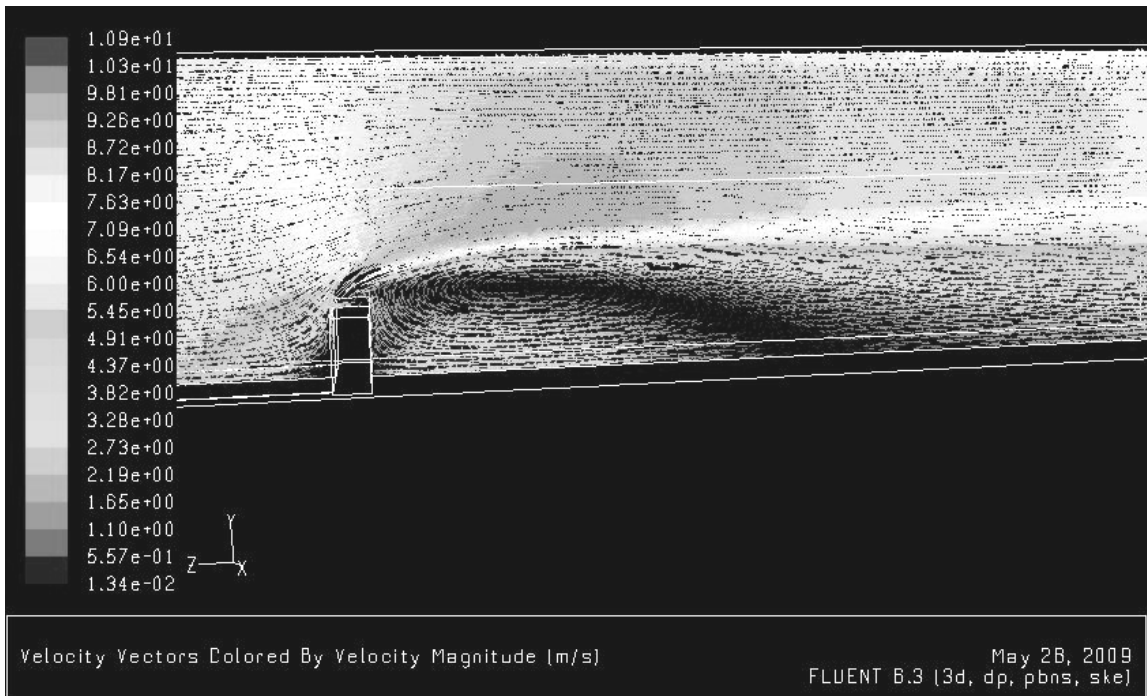


Figure 4.6 – Vortices Present Behind the Bluff Body along the +y/-z Plane

As discussed earlier, the presence of negative pressure serves as the prerequisite to the formation of vortices. This is the case shown in the respective total pressure distributions of Figures 4.2 and 4.4 whereby vortices form in the immediate vicinity of these negative pressure regions (see Figures 4.3, 4.5, and 4.6).

The presence of the vortices shown in Figures 4.3, 4.5, and 4.6 are justified by the findings in [9] and [10] whereby fluid flow was modelled over and around a cube (note that the flow has been modelled to approach the front of the cube). Here, the calculated flow field revealed the presence of (a) twin vortices, circulating in opposite directions, that are present behind the cube and (b) along the centreline of the cube, vortices are present in front of, above, and behind the cube. The flow fields shown in the abovementioned figures exhibit these vortices with the exception that the vortex in front of the bluff body is absent. To justify this absence, consider the following:

In [9] and [10], this vortex is shown to be of small size and positioned close to the ground surface of the flow domain. As per Section 2.1.5, such a vortex is classified as a near-wall vortex. However, the absence of this vortex in the results produced by the CFD simulation performed for this thesis is attributed to the flow inlet boundary conditions of k and ϵ . As per Table 3.5, it is mentioned that the numerical boundary condition of ϵ is made much larger than k . Since the former quantity is a measure of how the viscous regime governing the boundary layer attenuates the energy of near-wall vortices, a large value of ϵ increases the ability of the viscous boundary layer to reduce the energy possessed by near-wall vortices which eventually causes these vortices to either attain a weak energy state or be completely eliminated. Thus, the latter eventuality is the case with the near-wall vortex in front of the bluff body.

Moreover, the near-wall vortex above the bluff body shown in Figure 4.5 also appears to be affected by the use of the large inlet boundary condition value assigned to ϵ . This is witnessed by the fact that the appearance of this vortex in Figures 4.5 and 4.6 is of

a small physical size which may be indicative of the attenuation of its energy via the viscous boundary layer present in the top portion of the bluff body.

Nonetheless, it has been postulated in Table 3.12 that the resuspension of particulates and their ability to remain in suspension is attributed to the presence of the large vortices behind the bluff body. In addition, it is anticipated that the majority of the resuspended particulates will accumulate in both the immediate vicinity directly behind the bluff body and further downstream of it. Thus, it is assumed that the near-wall vortices in front and atop the bluff body will have a negligible role in the resuspension of particulates. Figure 4.7 illustrates the trajectory of each particulate placed in the wind tunnel shown in Figure 3.6.

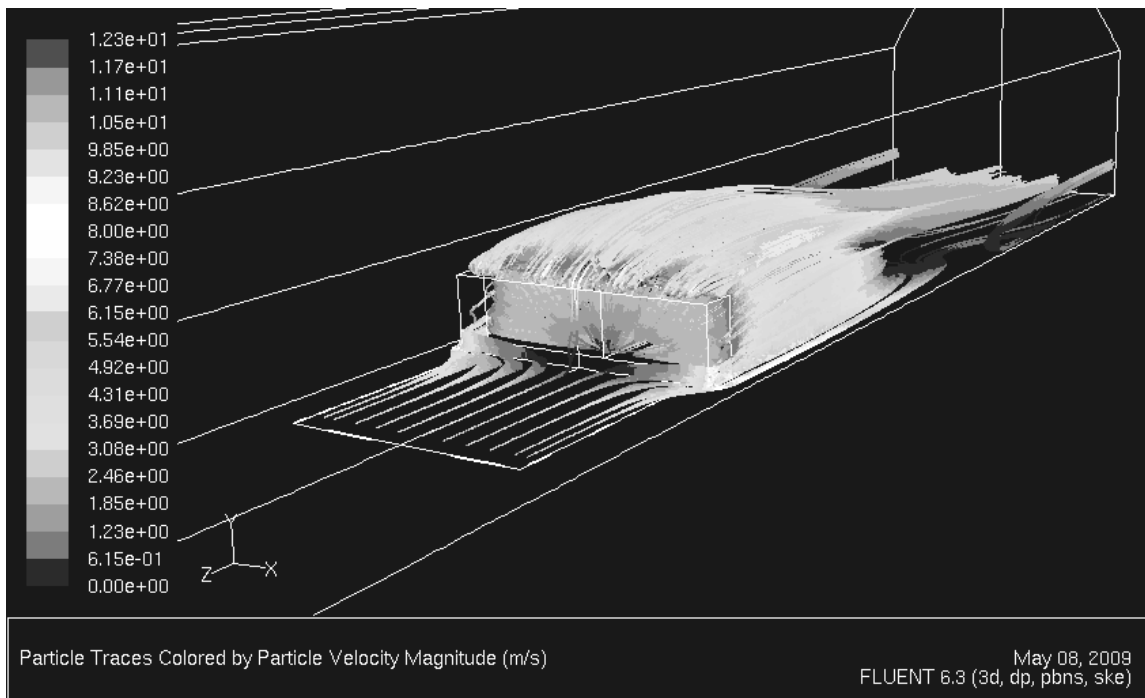


Figure 4.7 – Illustration of Particulates’ Trajectories in the Wind Tunnel Domain

It is evident, based on the particulates’ trajectories shown in Figure 4.7, that the assumptions made related to the spatial positioning of detectors (see Table 3.12) and the resuspension of particulates that have just been described are justified in that there is resuspension and accumulation of particulates directly behind the bluff body and further

downstream of it. Hence, due to the radioactive nature of the particulates simulated, the aforesaid regions of the wind tunnel will host the highest radiological hazard. As a result, the radiation field produced by the resuspension of particulates will be quantified in these regions via the placement of detectors at the two respective locations displayed in Table 3.12.

Finally, a means by which the results of the CFD simulation can be validated must be discussed. As per the discussion of feature 3 in Figure 3.2, the air velocity downstream of the bluff body has been recorded via velocity probes that have been positioned in this region of the wind tunnel. FLUENT affords the modeller the ability to view the air velocity distribution at any spatial location within the defined flow domain. As a result, this feature has been employed to extract the air velocity calculated at the exact spatial locations of the velocity probes (Figure A.4 in Appendix A provides the spatial location of the velocity probes). If there is agreement between the velocity probe data and the air velocity data extracted by FLUENT, this will be indicative that the correct flow field is being modelled in FLUENT. Thus, the velocity probe data constitutes a mean by which the flow field calculated by FLUENT can be validated. Figure 4.8 displays a plot which compares the two data sets.

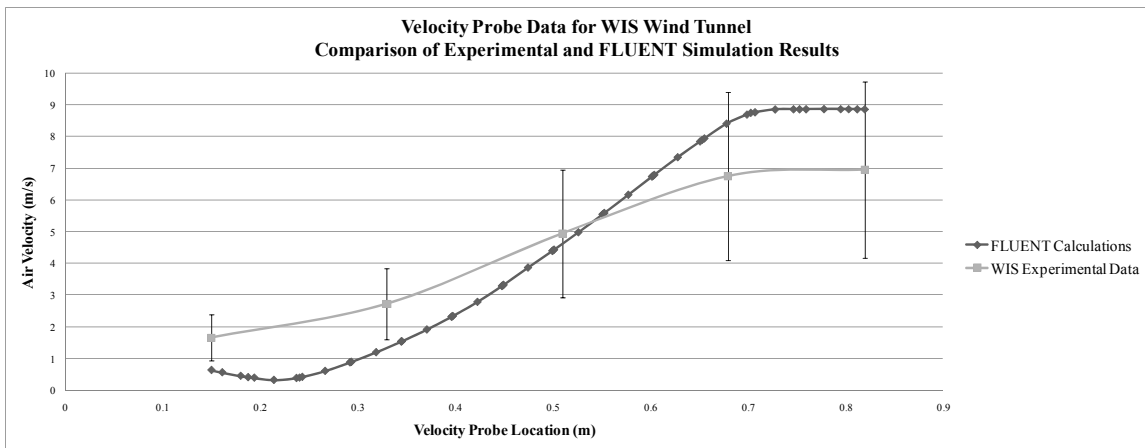


Figure 4.8 – Comparison of Velocity Probe Data with FLUENT Calculations

Figure 4.8 illustrates that the air velocity data extracted by FLUENT closely approximates the velocity probe data. Thus, this indicates that the correct flow field is

being modelled in FLUENT. In regards to the error associated with the FLUENT air velocity data, the discussion at the beginning of Section 4.1 outlined the fact that FLUENT quantifies a scaled residual for each flow quantity that the turbulence model in use calculates (examples of such quantities are fluid pressure, fluid velocity, etc.). In effect, the scaled residual represents the error associated with the flow quantity to which it corresponds. However, since the scaled residual quantifies the *magnitude* to which the calculated flow field produced by the turbulence model employed either over predicts or under predicts the solution to the conservation equations described in Section 2.1.4, the scaled residual is not a standard deviation of the flow quantity that it is associated with. Hence, the scaled residual of the FLUENT air velocity data is not plotted as an error bar in Figure 4.8.

Now that the results of the CFD simulation have been presented, the presentation of the data produced by the Black Box will now follow.

4.2 Black Box Data

The particulate data that is exported by FLUENT is then imported into the Black Box such that the radiation field can be characterized based on the particulate spatial distribution contained within the aforementioned data file. The data processing tasks conducted within the Black Box is initiated by the selection of time step iterations at which the radiation field will be analyzed. Table 4.1 displays the time step iterations and the corresponding average elapsed time for which the radiation field is analyzed via the selection methodology described in Section 3.2.2.1.1.

Time Step Number	Time Step Iteration	Average Elapsed Time (unit: s)
1	540	0.51
2	997	1.37
3	1150	1.77
4	1353	2.19

5	3189	4.51
6	3358	4.79
7	3915	5.61
8	4509	6.58
9	5149	7.56
10	9176	8.37

Table 4.1 – Time Step Iterations Where the Radiation Field is Characterized

Note that in Table 4.1, the data presented for the time step iteration and the corresponding average elapsed time are grouped under a corresponding *time step number*.

Another feature of the Black Box is the selection of the region of the wind tunnel shown in Figure 3.6 that will undergo spatial partitioning, as described in Section 3.2.2.1.2. This selection was based on several assumptions and it was addressed that despite only a fraction of the wind tunnel volume being partitioned, all of the particulates placed in the wind tunnel will be accounted for in the analysis of the radiation field produced via the resuspension of radioactive particulates. Table 4.2 displays, for each time step number, the number of particulates that are present in the wind tunnel domain and the number of particulates that have exited the domain prior to the time step iteration taking place.

Time Step Number	Number of Particulates Exited	Number of Particulates Present	Sum
1	0	600	600
2	4	596	600
3	73	527	600
4	100	500	600
5	194	406	600
6	198	402	600
7	265	335	600
8	277	323	600

9	368	232	600
10	590	10	600

Table 4.2 – Particulate Accounting Data for Each Time Step Iteration

Based on the data presented in Table 4.2, it is clear that as the time step iterations increase, the number of particulates that exit the domain increase and accordingly, the corresponding number of particulates present in the flow domain decreases. With respect to ensuring that all particulates have been accounted for in the spatial partitioning methodology presented in Section 3.2.2.1.2, it is shown in Table 4.2 that the sum of the number of particulates that have exited the domain and the number of those present in the domain at each time step iteration is equal to 600. Recalling the particulate injection data presented in Table 3.7, 600 particulates have been injected into the flow domain shown in Figure 3.6. Thus, the spatial partitioning methodology developed ensures that all particulates are being accounted for.

In each partition formed via the spatial partitioning mentioned above, the particulate spatial distribution within was converted to a volumetric activity. It is important to recall that the volumetric activity serves as the parameter by which CFD and MC radiation transport simulations will be coupled for the purpose of simulating radioactive particulate resuspension and analyzing the resultant radiation field. The mandate of the Black Box is to provide a snapshot, at each time step iteration, of the spatial variation of the volumetric activity. That is, the Black Box will calculate the volumetric activity in each partition as a function of time step iteration. Thus, it is prudent to display the temporal and spatial variation of the volumetric activity that is quantified via the Black Box. Figures 4.9-4.11 will illustrate this variation. Note that Appendix I numerically presents volumetric activity and bias data for each partition as a function of time step number.

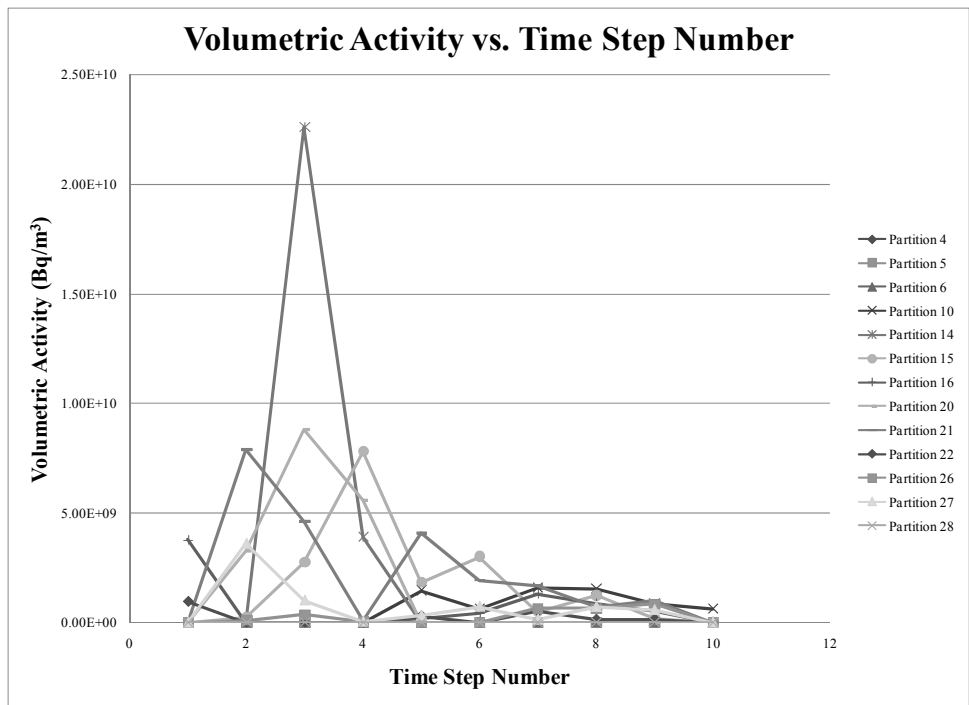


Figure 4.9 – Temporal Variation of Volumetric Activity for Partitions Centred About the Symmetry Plane

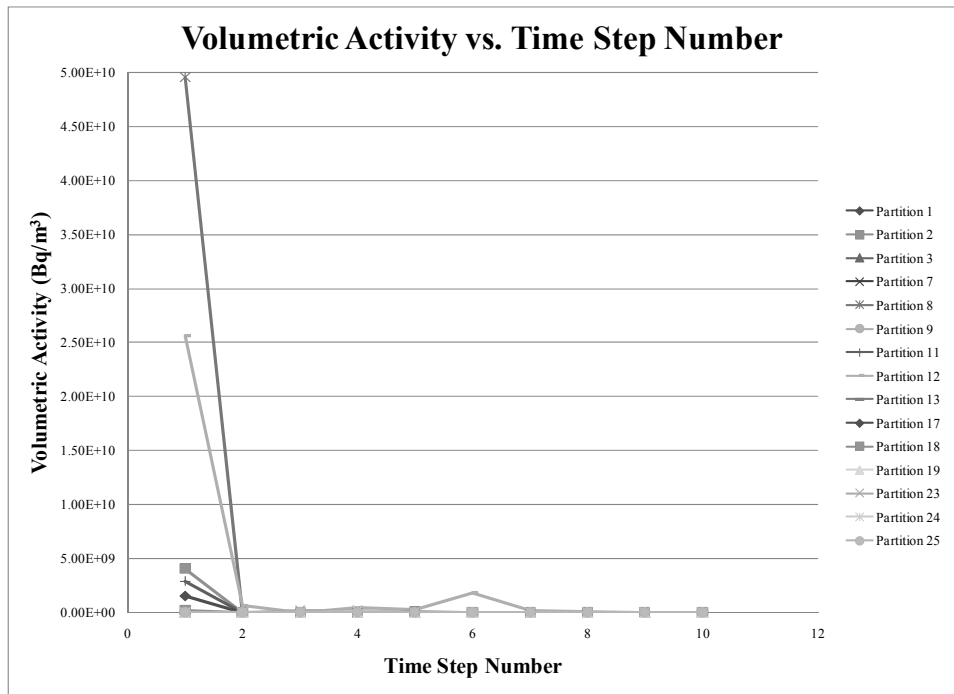


Figure 4.10 – Temporal Variation of Volumetric Activity for Partitions to the Left of the Plate and Bluff Body

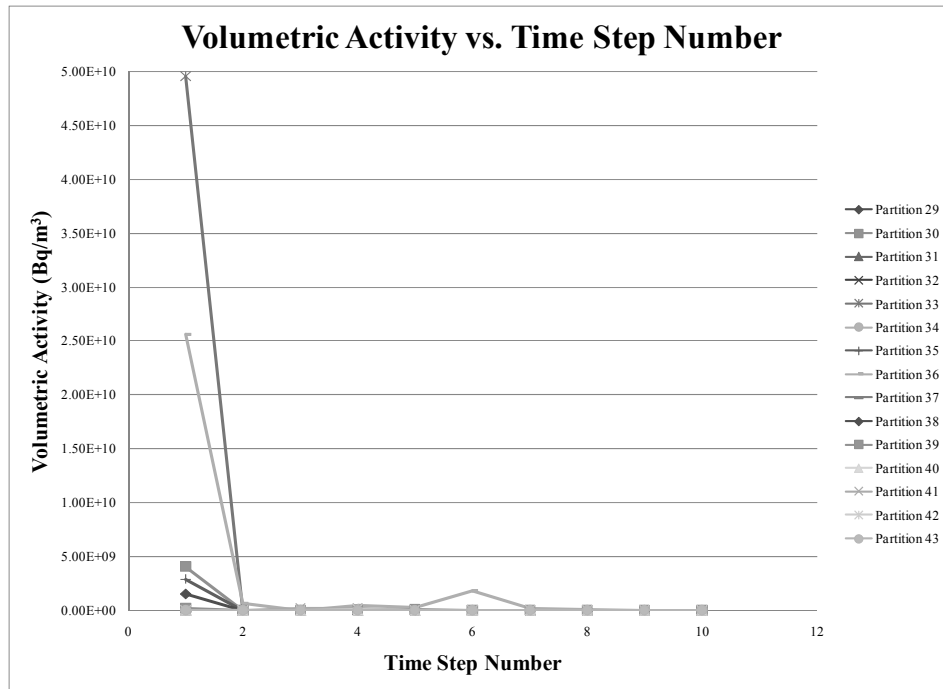


Figure 4.11 – Temporal Variation of Volumetric Activity for Partitions to the Right of the Plate and Bluff Body

Figures 4.9-4.11 illustrate how the volumetric activity, produced by the resuspension of ^{140}La particulates, for a given partition varies over time. The major patterns shown in these figures are as follows:

- As the time step iteration progresses, the particulates are transported further downstream
- The partitions directly behind and downstream of the bluff body are consistently active
- Partitions 15 and 21, which hosts each of the two detectors described in Table 3.12, are always active and are among the most active partitions at any given time step iteration. The exceptions to this are at step number 1 and 10 whereby at the former time step number, particulates are in the process of being transported downstream of the bluff body while at the latter time step, the majority of

particulates initially placed in the wind tunnel have exited the domain (see Table 4.2)

The above findings are in line with the assumptions made in the selection of the spatial locations of the detectors described in Table 3.12 namely that the downstream region of the bluff will host the highest radiological hazard produced by the resuspension of ^{140}La particulates. To quantify the radiological hazard, the internal and external dose is to be calculated at each detector location. As described in the internal and external dose rate equations shown in Tables 3.13 and 3.15, respectively, these respective dose rates are directly proportional to the volumetric activity. More specifically, the internal dose rate is a function of the volumetric activity in partitions 15 and 21 while the external dose rate is a function of the volumetric activity of all active partitions. While the external dose rate is not solely dependent on the volumetric activity of partitions 15 and 21, it is important to bear in mind that the closer an active partition is to the respective detector locations, the less attenuation the gamma radioactive particles emitted from the active partition will experience. Thus, the greater the volumetric activity possessed by the partitions that host and surround the detector locations, the greater the external dose rate that will be delivered to each dose point. Hence, the patterns described above indicate that the volumetric activities of the partitions in the vicinity of each detector location are amongst the highest of all active partitions, and so the assumption that the region of the wind tunnel downstream of the bluff body possesses the highest radiological hazard is justified.

The internal dose rate equations shown in Table 3.13 are solely a function of the volumetric activity calculated by the Black Box. However, the external dose rate equations shown in Table 3.15 are a function of both the volumetric activity calculated by the Black Box and the normalized external dose rate computed in MCNPX. The tabulation of this MCNPX quantity will be the focus of the next section.

4.3 MC Radiation Transport Results

The snapshots of the radiation field taken by the Black Box at each time step iteration are translated into the MCNPX model such that the normalized external dose rate delivered by gamma radiation emitted from all active partitions at the particular time step iteration is calculated at each detector location. Tables 4.3 and 4.4 will present the normalized external dose rates computed at each respective detector location for each time step iteration.

Time Step Number	Normalized External Dose Rate Data			
	Number of Gamma Source Particles = 1,000,000		Number of Gamma Source Particles = 10,000,000	
	Normalized External Dose Rate (unit: Sv · hr ⁻¹ · γ _s ⁻¹)	Fractional Standard Deviation (unitless)	Normalized External Dose Rate (unit: Sv · hr ⁻¹ · γ _s ⁻¹)	Fractional Standard Deviation (unitless)
1	1.94E-13	8.00E-04	1.94E-13	3.00E-04
2	1.54E-13	2.66E-02	1.50E-13	5.20E-03
3	9.92E-13	6.30E-03	9.89E-13	1.60E-03
4	1.03E-12	1.09E-02	1.03E-12	3.30E-03
5	4.53E-13	1.02E-02	4.55E-13	5.40E-03
6	6.09E-13	1.24E-02	6.06E-13	4.70E-03
7	2.98E-13	1.09E-02	2.94E-13	4.60E-03
8	4.60E-13	1.01E-02	4.59E-13	5.50E-03
9	2.13E-13	1.27E-02	2.13E-13	5.60E-03
10	1.99E-13	9.00E-04	1.99E-13	2.00E-04

Table 4.3 – Normalized External Dose Rate Data for Detector Location 1

Time Step Number	Normalized External Dose Rate Data			
	Number of Gamma Source Particles = 1,000,000		Number of Gamma Source Particles = 10,000,000	
	Normalized External Dose Rate (unit: Sv · hr ⁻¹ · γ _s ⁻¹)	Fractional Standard Deviation (unitless)	Normalized External Dose Rate (unit: Sv · hr ⁻¹ · γ _s ⁻¹)	Fractional Standard Deviation (unitless)
1	7.02E-14	1.00E-03	7.03E-14	3.00E-04
2	1.08E-12	1.06E-02	1.08E-12	3.30E-03
3	5.92E-13	4.70E-03	6.00E-13	3.30E-03
4	5.47E-13	3.10E-03	5.47E-13	1.00E-03
5	8.00E-13	1.60E-02	8.02E-13	4.70E-03
6	3.84E-13	1.75E-02	3.87E-13	5.20E-03
7	4.79E-13	1.43E-02	4.90E-13	5.00E-03
8	2.69E-13	1.00E-02	2.75E-13	5.50E-03
9	4.59E-13	2.29E-02	4.53E-13	5.80E-03
10	4.77E-14	2.40E-03	4.78E-14	1.80E-03

Table 4.4 – Normalized External Dose Rate Data for Detector Location 2

To determine if the data shown in Tables 4.3 and 4.4 are acceptable, one can refer to the guidance provided in Section 2.3.2 pertaining to the assessment of results produced by MC radiation transport simulations. Here, it is stated that a MC simulation is deemed to be successfully performed if the following are achieved:

- The value of the tally does not exhibit major changes as the number of radioactive particles whose transport is simulated in the MC simulation is changed
- The fractional standard deviation of the tally is below 5% (i.e., 5E-2)

The data shown in Tables 4.3 and 4.4 possess the above traits in that at each detector location and for each time step iteration, the normalized external dose rate does

not experience major changes in value as the number of gamma source particles is increased and its associated fractional standard deviation is below 5%. Thus, the MC simulations performed to quantify the normalized external dose rate at each detector location for each time step iteration are deemed to be successful.

The normalized external dose rate at each detector location and at each time step will serve as input to the external dose rate equations shown in Table 3.15. The normalized external dose rates pertaining to the use of 10,000,000 gamma source particles will be used to calculate the external dose rate. While the tallies pertaining to the use of 1,000,000 gamma source particles can be used as well, the fact that the fractional standard deviations of the former data set are lower than those of the latter (since, of course, more samples (i.e. source particles) are used to attain the tally and so the standard deviation and fractional standard deviation will decrease accordingly) provides an added advantage in that there is less statistical uncertainty possessed by the chosen data set.

The data produced by the Black Box and the MCNPX simulations are pivotal to the dose calculations, whose results will be discussed in the next section.

4.4 Dose Calculation Results

The internal and external dose rates have been calculated at each detector location for each time step iteration. As a result, the temporal variation of the internal and external dose rates at each detector location has been attained. It is important to the modeller, however, to calculate the total (i.e. time-integrated) internal and external dose delivered by the resuspension of ^{140}La particulates during the time of exposure (i.e., from the first to last time step iteration analyzed). With the aid of the radiation field snapshots taken by the Black Box and the normalized external dose rates calculated by the MCNPX simulations, the total internal and external dose delivered by the resuspension of ^{140}La particulates can be calculated at each detector location, and the results of these calculations are stated in Table 4.5.

	Detector 1 Location	Detector 2 Location
Total Internal Dose (unit: mSv)	6.52	6.06
Total External Dose (unit: μ Sv)	82.2	71.4

Table 4.5 – Total Internal and External Dose Delivered at Each Detector Location

It is necessary to provide a means by which the total internal and external doses shown in Table 4.5 can be related to some reference quantity such that an understanding of the intensity the radiation field produced by the resuspension of ^{140}La particulates can be achieved. The means chosen was the calculation of a surface activity-to-dose conversion factor whereby the total internal and external doses at each detector location, stated in Table 4.5, will be divided by the plate surface activity. It must be reemphasized that since this conversion factor is a function of the total (i.e. time-integrated) internal and external dose, the conversion factor is also a time-integrated quantity. The dose conversion factors are tabulated in Table 4.6.

	Detector 1 Location	Detector 2 Location
Internal Dose Conversion Factor (unit: $\text{Sv}\cdot\text{Bq}^{-1}\cdot\text{m}^2$)	1.10E-12	1.02E-12
External Dose Conversion Factor (unit: $\text{Sv}\cdot\text{Bq}^{-1}\cdot\text{m}^2$)	1.39E-14	1.20E-14

Table 4.6 – Internal and External Dose Conversion Factors at Each Detector Location

It is important to bear in mind that, as per the declaration of the spatial coordinates of the detectors stated in Table 3.12, detector 1 is closer to the bluff body than detector 2 which is placed further downstream, and so the data shown in Tables 4.5 and 4.6 indicate that there is a higher internal and external dose present in the immediate vicinity behind the bluff body. Nonetheless, the internal and external dose present at the detector 2 location is comparable to that of detector 1. Thus, the region of the wind tunnel in the immediate vicinity behind the bluff body and further downstream of it possess significant radiological hazards in that there is a quantifiable threat of biological

damage posed by the inhalation of beta radiation emitted by the ^{140}La particulates while there is a danger of external exposure to gamma radiation via the gamma decay of ^{140}La .

As per the surface activity-to-dose conversion factors shown in Table 4.6, this quantity measures the magnitude of the dose delivered by the resuspension of ^{140}La particulates per unit plate surface activity. In other words, one can think of the surface activity-to-dose conversion factor as an indicator of how much plate surface activity is translated into a resuspension dose. Based on the data shown in Table 4.6, it appears that a small fraction of the plate surface activity is converted into a resuspension dose.

The dose calculations represent the end-point of the CFD-MC radiation transport coupling methodology and as such, a judgment on the reasonableness of the dose results stated in Table 4.5 must now be passed [13], which will be the subject of the next section.

4.4.1 Assessment of Reasonableness

It is important to re-emphasize that the time-integrated external dose is calculated via the coupling of the CFD and MC radiation transport simulations while the time-integrated internal dose is calculated solely from the particulate spatial distributions exported by FLUENT. Indeed, as described by Luxat [13], the reasonableness of the time-integrated external dose produced by the coupling of the abovementioned simulations must be assessed. To perform such an assessment, it is imperative that alternative approaches to quantifying the time-integrated external dose that arise from the resuspension of radioactive particulates be employed. There are two approaches available to the modeller, which are the submersion dose technique and the point source technique, respectively. The time-integrated external dose produced by these two approaches will be compared to that produced by the CFD-MC radiation transport coupling. This comparison will lay the groundwork for a discussion on which approach to quantify the time-integrated external dose from the resuspension of radioactive particulates (i.e., the CFD-MC radiation transport coupling, submersion dose technique, and the point source technique) can produce realistic dose estimates. The application of

each of these techniques to calculate the time-integrated external dose will be discussed in the following two sections, respectively.

Of course, the spatial distribution of the volumetric activity is a prerequisite for performing any dose estimate and as such, the submersion dose technique and the point source technique will employ this distribution. In addition, these techniques will quantify the time-integrated external dose at each detector location (see discussion on *Detector Locations* in Table 3.12).

4.4.1.1 Submersion Dose Technique

The submersion dose technique is formulated on the premise that the detector is submersed in an infinite volume of radioactive material. To visualize the concept of the submersion dose, consider the spatial partitioning of the wind tunnel illustrated in Figure 3.11. The partitions shown in this figure allow for the spatial distribution of volumetric activity to be calculated at each time step iteration for which the radiation field in the wind tunnel is analyzed. As such, there are a selected amount of partitions that are active at any time step iteration. The submersion dose, however, seeks to express all partitions as being active. In other words, in reference to Figure 3.11, the volume of space occupied by all partitions is considered to be *uniformly* active and therefore represents a single radiation source. In order to convert the spatial distribution of volumetric activity afforded by the spatial partitioning of the wind tunnel shown in Figure 3.11 to a single radiation source that is placed in the region of space that is occupied by all partitions, the volumetric activity is said to be *spatially averaged*. Mathematically speaking, the spatially averaged volumetric activity is expressed in equation (4.1) and its values are tabulated in Table J.3 in Appendix J.

$$\bar{A}_v(i) = \frac{\sum_{j=1}^{P_{total}} A_{v,j}(i) \nabla_j}{\sum_{j=1}^{P_{total}} \nabla_j} \quad (4.1)$$

Where:

$\bar{A}_{\forall}(i)$ = spatially averaged volumetric activity at the i^{th} time step iteration
(unit: $\text{Bq}\cdot\text{m}^{-3}$)

$A_{\forall,j}(i)$ = volumetric activity of partition j at the i^{th} time step iteration
(unit: $\text{Bq}\cdot\text{m}^{-3}$)

\forall_j = volume of the j^{th} partition (unit: m^3)

p_{total} = total number of partitions

For the sake of clarity, the single radiation source, described above, is visually described in Figure 4.12.

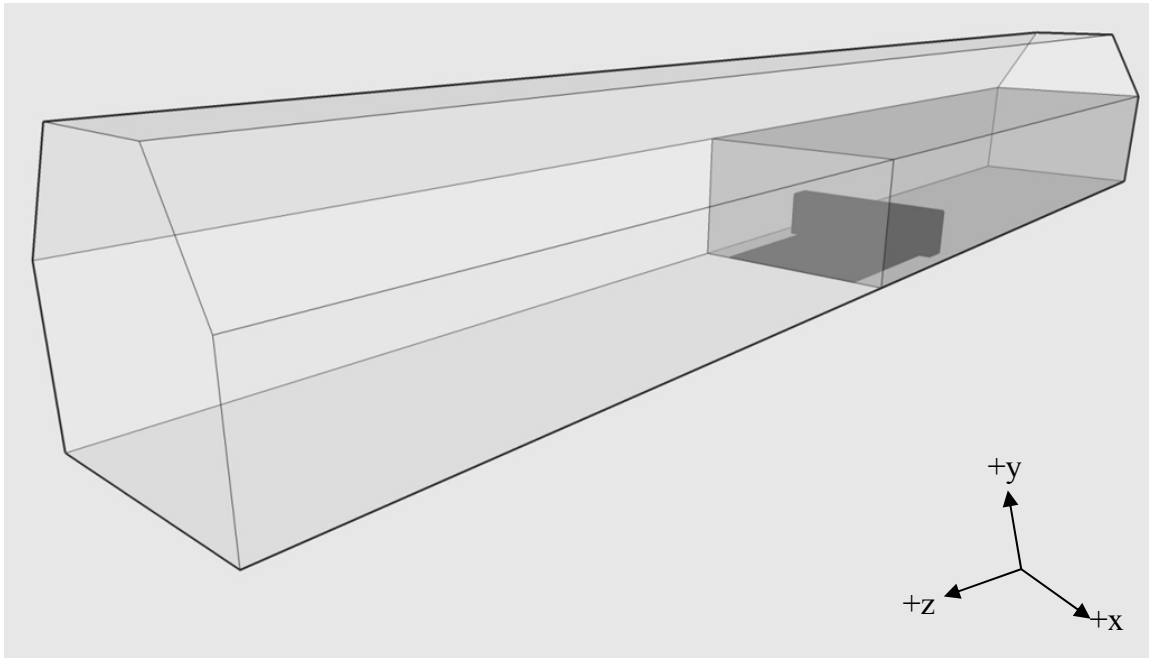


Figure 4.12 – Depiction of Single Radiation Source

Indeed, it is clear from Figure 4.12 that the partitions shown in Figure 3.11 have been unified into a single region of space (the shaded region shown in Figure 4.12) that possesses a volumetric activity, calculated from equation (4.1), that is uniformly distributed throughout this region.

With the concept of the submersion dose in relation to the wind tunnel analyzed for this thesis in mind, the manner in which the time-integrated external dose (herein known as the *time-integrated submersion dose*) can be quantified at each detector location via the submersion dose technique will now be discussed. As with the calculation of the time-integrated external dose via the CFD-MC radiation transport coupling, MCNPX will also be used with the exception that the gamma radiation source will possess the configuration of the source shown in Figure 4.12. On this note, the manner in which the single radiation source shown in Figure 4.12 will be implemented in MCNPX must now be examined. To state succinctly, the source will be fragmented into volumes of varying sizes but nonetheless will collectively occupy the region of space where the single radiation source shown in Figure 4.12 is placed. Figure 4.13 displays the fragmented volumes just described and these fragmented volumes will herein be known as sources.

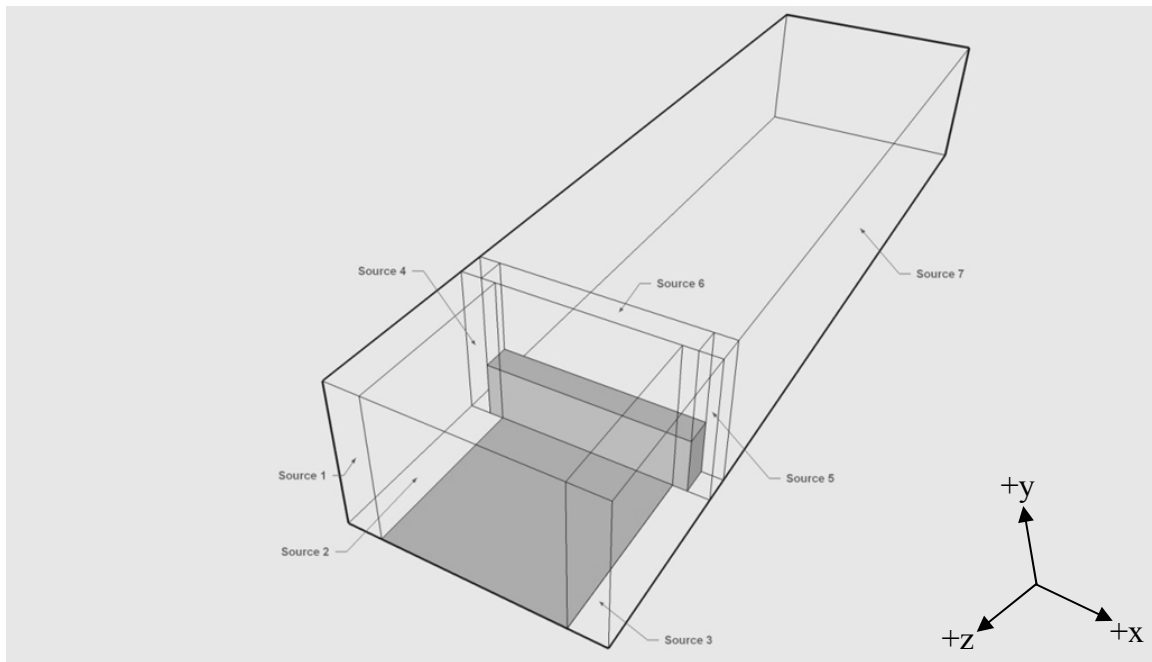


Figure 4.13 – Illustration of Source Locations

Each of the sources shown in Figure 4.13 must possess a bias and the discussion in Section J.1 of Appendix J outlines the fact that the biases of each of the aforementioned sources are calculated using the volume of the source (note that Table J.1

in Appendix J displays the spatial bounds and volume for each of the sources shown in Figure 4.13 while Table J.2 in this same appendix tabulates the bias that each source possesses). Of course, the volume of each source is constant and so the bias that each source possesses is independent of the time step iteration for which the radiation field in the wind tunnel is analyzed. Bearing this is mind, the bias of each of the sources shown in Figure 4.13 is calculated via equation (4.2).

$$\text{Bias}_j = \frac{\nabla_j}{\sum_{m=1}^n \nabla_m} \quad (4.2)$$

Where:

- Bias_j = bias that the jth source possesses
- ∇_j = volume of the jth source (unit: m³)
- n = number of sources (as per Figure 4.13, n=7)
- ∇_m = volume of the mth source (unit: m³)

With the source configuration and the source bias having been discussed, attention must be turned to calculating the time-integrated submersion dose at each detector location. The calculation of this dose will be analogous to the manner in which the time-integrated external dose was quantified for the CFD-MC radiation transport coupling with the exception of the following, in reference to the equations shown in Table 3.15:

- (1) the spatially averaged volumetric activity (calculated via equation (4.1)) will be used instead of the sum of the volumetric activities of all active partitions, and
- (2) the volume of the single radiation source shown in Figure 4.12, which is equivalent to the denominator of equations (4.1) and (4.2), will be used instead of the sum of the volumes of the active partitions

As described earlier, the concept of the submersion dose is that the detector at each detector location will be submersed in a large volume containing radioactive material (illustrated by the shaded region in Figure 4.12) that possesses a volumetric activity, that is calculated via equation (4.1)), and a volume that is equivalent to the denominator of equations (4.1) and (4.2). With this being said, the submersion dose rate at each detector location is calculated via equations (4.3) and (4.4) shown in Table (4.7).

Submersion Dose Rate Equations		
Detector Location	Equation	Equation Number
1	$\dot{D}_{\text{submersion},1}(i) = DF_{\text{MCNPX},1} \cdot Y_{140\text{La}} \cdot \bar{A}_{\text{v}}(i) \cdot \nabla_{\text{submersion source}}$	(4.3)
2	$\dot{D}_{\text{submersion},2}(i) = DF_{\text{MCNPX},2} \cdot Y_{140\text{La}} \cdot \bar{A}_{\text{v}}(i) \cdot \nabla_{\text{submersion source}}$	(4.4)

Where:

$\dot{D}_{\text{submersion},1}(i), \dot{D}_{\text{submersion},2}(i) =$ submersion dose rate at detector 1 and 2 locations, respectively, for the i^{th} time step iteration (unit: $\text{Sv} \cdot \text{hr}^{-1}$)

$DF_{\text{MCNPX},1}, DF_{\text{MCNPX},2} =$ MCNPX normalized submersion dose rate at detector 1 and 2 locations, respectively (unit: $\text{Sv} \cdot \text{hr}^{-1} \cdot \gamma_{\text{s}}^{-1}$)

$Y_{140\text{La}} =$ gamma yield for ^{140}La (unit: $\gamma_{\text{s}} \cdot \text{decay}^{-1}$)

$\bar{A}_{\text{v}}(i) =$ spatially averaged volumetric activity at the i^{th} time step iteration (unit: $\text{Bq} \cdot \text{m}^{-3}$)

$\nabla_{\text{submersion source}} =$ volume of the submersion source (equivalent to the denominators of equations (4.1) and (4.2)) (unit: m^3)

Table 4.7 – Submersion Dose Rate Equations

Once the submersion dose rate, at each detector location, is calculated for each time step iteration, the time-integrated submersion dose will be calculated via equation (3.11).

To conclude the discussion of the submersion dose calculations, there are two aspects of the MCNPX submersion dose simulation that affect the MCNPX normalized submersion dose rate employed by equations (4.3) and (4.4), and these are described as follows:

- (1) In regards to the sources shown in Figure 4.13, it has been outlined that the bias that each source possesses is independent of the time step iteration for which the radiation field in the wind tunnel is being analyzed. As such, the MCNPX normalized submersion dose rate will also be independent of the time step iteration

- (2) As per the discussion of the *number of radioactive source particles* in Table 3.12, the number of gamma source particles whose transport is simulated in MCNPX will be assigned a value of 1,000,000 and this number will then be increased for subsequent runs. This will allow the modeller to observe the effect of changing the number of source particles on the value of the MCNPX normalized submersion dose rate at each detector location

Now that the methodology to calculate the time-integrated submersion dose at each detector location has been outlined, the results produced by this methodology will now be presented. The first set of results are the MCNPX normalized submersion dose rate data and are shown in Table 4.8 while the second set of results, the time-integrated submersion dose rate data, is displayed in Table 4.9.

Detector Location	Normalized Submersion Dose Rate Data			
	Number of Gamma Source Particles = 1,000,000		Number of Gamma Source Particles = 10,000,000	
	Normalized Submersion Dose Rate (unit: Sv · hr ⁻¹ · γ _s ⁻¹)	Fractional Standard Deviation (unitless)	Normalized Submersion Dose Rate (unit: Sv · hr ⁻¹ · γ _s ⁻¹)	Fractional Standard Deviation (unitless)
1	1.80E-13	1.05E-02	1.85E-13	8.10E-03
2	1.93E-13	3.05E-02	1.91E-13	5.90E-03

Table 4.8 – Normalized Submersion Dose Rate Data

Detector Location	Time-Integrated Submersion Dose (unit: μSv)
1	2.50
2	2.58

Table 4.9 – Time-Integrated Submersion Dose Data

In order to determine whether the data shown in Table 4.8 are acceptable, one can again refer to the guidance provided in Section 2.3.2 which details the criteria that must be employed in order to determine the acceptability of the results produced by the MC radiation transport simulations. The criteria are namely that (a) the tally result (i.e., the normalized submersion dose rate) does not exhibit major changes as the number of gamma source particles change and (b) the fractional standard deviation of the tally is below 5% (i.e., 5E-2). Using these criteria, the data shown in Table 4.8 are deemed acceptable.

Now that the results of the use of the submersion dose technique to quantify the time-integrated submersion dose at each detector location have been presented, the use of the point source technique to quantify the time-integrated external dose at each detector location will now be discussed.

4.4.1.2 Point Source Technique

The point source technique is formulated on the basis that the radiation source in question occupies a *small volume* in space. As a result, the source can be thought of as a “point” in space. Now, consider Figure 4.14.

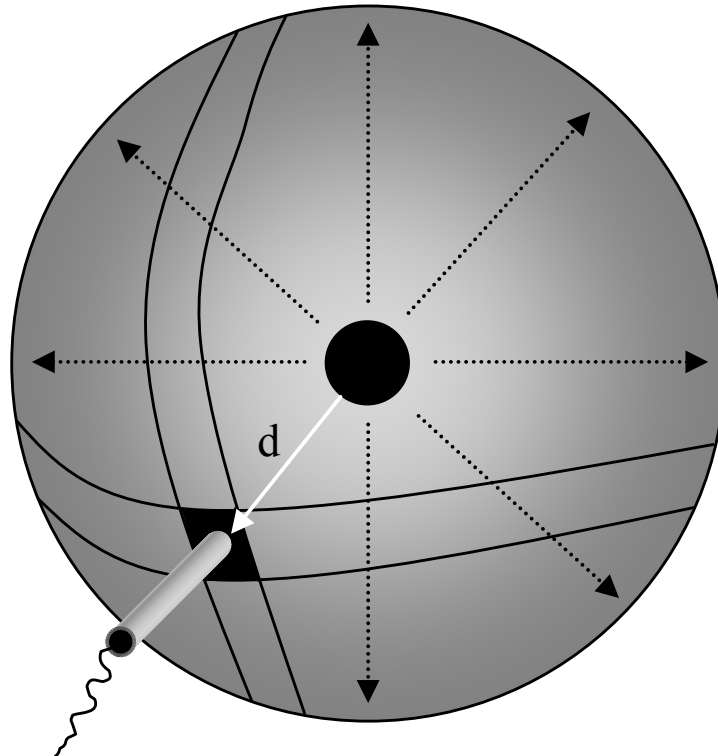


Figure 4.14 – Illustration of a Point Source

The radiation source, shown at the centre of the sphere in Figure 4.14, is enclosed in a small volume and thus qualifies as a point source. The point source emits radiation of type R and energy E_R in an *isotropic* manner. If a detector is placed at a distance d from the centre of the source enclosure volume, the flux of radioactive particles of type R at the detector location can be quantified. To do this, a sphere of radius d is formed whereby the radiation source is situated at the centre of the sphere and the detector is located at the sphere’s surface. Since radiation is emitted isotropically from the source,

the flux is defined as the ratio of the activity of the source to the surface area of the sphere. Equation (4.5) expresses this relationship.

$$\phi_R(d) = \frac{A}{4\pi d^2} \quad (4.5)$$

Where:

$\phi_R(d)$ = flux of radioactive particles of type R at a distance d from the source enclosure volume (unit: particles·cm⁻²·s⁻¹)

A = activity of the radiation source (unit: Bq)

d = distance between detector and centre of the source enclosure volume (unit: cm)

It must be stated that equation (4.5) is valid for situations where the attenuation of radioactive particles of type R from the radiation source to the detector is deemed negligible. This occurs for situations where the material that encompasses the region of space between the detector and the radiation source is a poor attenuator of radioactive particles of type R.

Once the flux of radioactive particles of type R is quantified at the detector location, the dose rate delivered by that flux can then be calculated via equation (4.6).

$$\dot{D}_R(d) = \phi_R(d) \cdot CF(E_R) \quad (4.6)$$

Where:

$\dot{D}_R(d)$ = dose rate delivered by the flux of radioactive particles of type R at a distance d from the centre of the source enclosure volume (unit: Sv·s⁻¹)

E_R = energy of radioactive particles of type R (unit: MeV)

$CF(E_R)$ = flux-to-dose rate conversion factor for radioactive particles of energy E_R (unit: Sv·cm²·particle⁻¹)

Now that the concept of the point source technique has been provided, a discussion of how this technique can be employed to quantify the time-integrated external dose (herein known as the *time-integrated point source dose*) at each detector location will now ensue. To begin, it is evident from Figure 3.11 that the coupling methodology developed in Chapter 3 quantifies the volumetric activity in each partition for each time step iteration at which the radiation field in the wind tunnel is analyzed. Thus, at every time step iteration, every partition will possess a unique volume and a volumetric activity. What the point source method seeks to do is to reduce the spatial distribution of volumetric activity at every time step iteration to a single partition that possesses a *representative* volume and a *representative* volumetric activity. In other words, this partition seeks to capture the spatial distribution of the volumetric activity into a single partition and so the attributes of this single partition (i.e., its volume and volumetric activity) will be equivalent to the *weighted average* of the volume of the partitions shown in Figure 3.11 and the *weighted average* of the volumetric activity within each partition at every time step iteration, respectively. Mathematically speaking, the volumetric activity of this *single representative partition* is calculated via equation (4.1) while the volume of this single representative partition is calculated via equation (4.7).

$$\bar{V}(i) = \frac{\sum_{j=1}^{p_{total}} V_j A_{v,j}(i)}{\sum_{j=1}^{p_{total}} A_{v,j}(i)} \quad (4.7)$$

Where:

$\bar{V}(i)$ = volume of the single representative partition at the i^{th} time step iteration
(unit: m^3)

$A_{v,j}(i)$ = volumetric activity of partition j at the i^{th} time step iteration (unit: $\text{Bq} \cdot \text{m}^{-3}$)

V_j = volume of the j^{th} partition (unit: m^3)

p_{total} = total number of partitions

Now that the volume and volumetric activity of the single representative partition can be quantified (note that this partition is assumed to be small enough such that it qualifies as a point source), the spatial location of this partition with respect to each detector location must be obtained. More precisely, the distance between the centre of this partition to detector locations 1 and 2 is required, and equations (4.8) and (4.9) computes these values, respectively.

Point Source to Detector Distance Equations		
Detector Location	Equation	Equation Number
1	$\bar{d}_1(i) = \frac{\sum_{j=1}^{p_{total}} d_{j,1} A_{v,j}(i)}{\sum_{j=1}^{p_{total}} A_{v,j}(i)}$	(4.8)
2	$\bar{d}_2(i) = \frac{\sum_{j=1}^{p_{total}} d_{j,2} A_{v,j}(i)}{\sum_{j=1}^{p_{total}} A_{v,j}(i)}$	(4.9)

Where:

$\bar{d}_1(i)$ = distance from detector location 1 to the centre of the single representative partition at the i^{th} time step iteration (unit: cm)

$\bar{d}_2(i)$ = distance from detector location 2 to the centre of the single representative partition at the i^{th} time step iteration (unit: cm)

$d_{j,1}$ = distance from the centre of the j^{th} partition to the location of detector 1 (unit: cm)

$d_{j,2}$ = distance from the centre of the j^{th} partition to the location of detector 2 (unit: cm)

$A_{v,j}(i)$ = volumetric activity of partition j at the i^{th} time step iteration (unit: $\text{Bq}\cdot\text{m}^{-3}$)

p_{total} = total number of partitions

Table 4.10 – Point Source to Detector Distance Equations

Note that Table J.3 in Appendix J contains the value of $\bar{V}(i)$, $\bar{d}_1(i)$, and $\bar{d}_2(i)$ for each time step iteration.

It must be stated that in equations (4.7)-(4.9), the quantity that is being calculated is weighted by the volumetric activity of each partition. Since the volumetric activity is employed to characterize the spatial distribution of radiation in the wind tunnel, it is therefore this quantity that is employed as the weights in the aforementioned equations. As a result, partitions with a high volumetric activity will contribute more to the value of the quantity being calculated than partitions with a low volumetric activity. In the case of equation (4.7), the volume of the single representative partition is comparable to the volume of the partitions that possess a high volumetric activity. Likewise, for the distances calculated in equations (4.8) and (4.9), the distance that separates the centre of the single representative partition and each detector will be comparable to the distance between partitions that host a high volumetric activity and each detector. As a result of these properties, the single representative partition will be placed at a distance away from the detectors that will coincide with the region where there is a high concentration of radioactivity and this partition will enclose a volumetric activity, equivalent to the spatially averaged volumetric activity, via a volume whose size is comparable to that of partitions that host a high volumetric activity.

The use of equations (4.1) and (4.7)-(4.9) allow for the single representative partition to be fully characterized such that the time-integrated point source dose can be quantified at each detector location. Figure 4.15 exemplifies this fact.

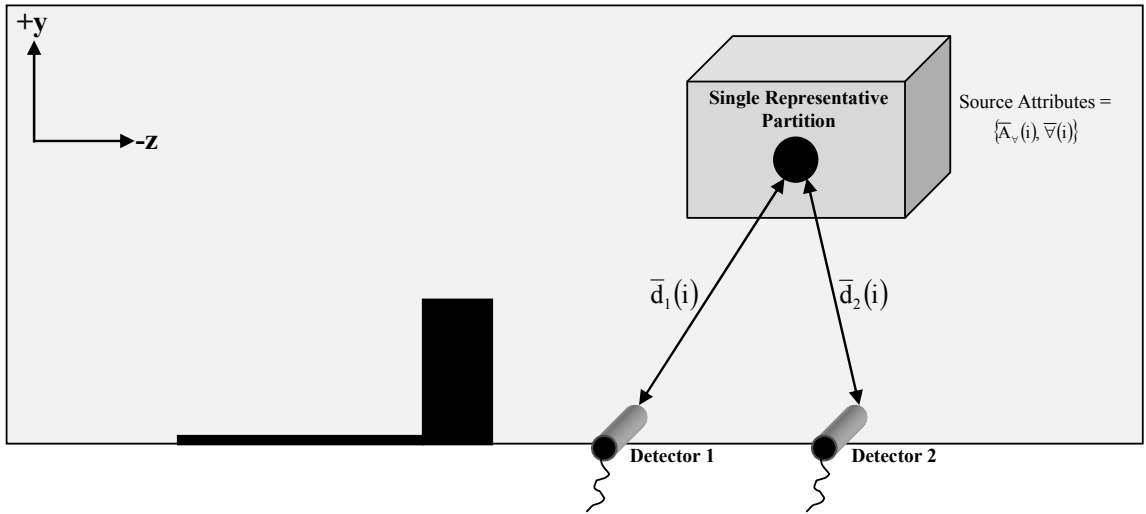


Figure 4.15 – Hypothetical Configuration of the Single Representative Partition at the i^{th} Time Step Iteration

Figure 4.15 states that a point source (i.e. the single representative partition) with an activity $\bar{A}_v(i)$, that is enclosed in a volume $\bar{V}(i)$, is located at a distance $\bar{d}_1(i)$ and $\bar{d}_2(i)$ from detectors 1 and 2 respectively at the i^{th} time step iteration.

It is clear from Figure 4.15 that equations (4.5) and (4.6) can be used in conjunction to calculate the gamma dose rate delivered from the gamma flux at each detector location. Equations (4.10) and (4.11) state the dose rate equation for each detector.

Point Source Dose Rate Equations		
Detector Location	Equation	Equation Number
1	$\dot{D}_{\gamma,1}(i) = \left(\frac{\bar{A}_v(i)\bar{V}(i)}{4\pi(\bar{d}_1(i))^2} \right) \cdot \text{CF}(\bar{E}_\gamma = 1.07 \text{ MeV})$	(4.10)
2	$\dot{D}_{\gamma,2}(i) = \left(\frac{\bar{A}_v(i)\bar{V}(i)}{4\pi(\bar{d}_2(i))^2} \right) \cdot \text{CF}(\bar{E}_\gamma = 1.07 \text{ MeV})$	(4.11)

Where:

$\dot{D}_{\gamma,1}(i), \dot{D}_{\gamma,2}(i) =$ point source dose rate at detector 1 and 2, respectively, at the i^{th} time step iteration (unit: $\text{Sv} \cdot \text{s}^{-1}$)

$\bar{A}_v(i)\bar{V}(i) =$ activity within the single representative partition at the i^{th} time step iteration (unit: Bq)

Since the single representative partition possesses a volumetric activity enclosed in a defined volume, the activity emitted from this partition is simply the product of the two aforementioned quantities.

$$\text{CF}(\bar{E}_{\gamma} = 1.07 \text{ MeV}) = 5.20 \times 10^{-12} \text{ Sv} \cdot \text{cm}^2 \cdot \gamma^{-1} \text{ [46]}$$

The flux-to-dose rate conversion factor is dependent on the energy of the gamma particles. The gamma energy weighted by the gamma radiation emission probabilities for ^{140}La has been used to extract the above stated conversion factor.

Table 4.11 – Point Source Dose Rate Equations

For simplicity, equations (4.10) and (4.11) do not account for the attenuation of gamma radiation and hence the absence of an exponential decay term in the aforementioned equations.

Once the point source dose rate, at each detector location, is calculated for each time step iteration, the time-integrated point source dose will be calculated via equation (3.11). The time-integrated point source dose, at each detector location, is stated in Table 4.12.

Detector Location	Time-Integrated Point Source Dose (unit: μSv)
1	0.06
2	0.07

Table 4.12 – Time-Integrated Point Source Dose Data

Of course, it is important to bear in mind that the point source technique has reduced the spatial distribution of the volumetric activity to a single representative partition. As such, the results shown in Table 4.12 display the time-integrated dose delivered by this single partition and therefore represents the average time-integrated dose delivered by each partition shown in Figure 3.11. With this being said, one can compute the time-integrated dose delivered by all partitions at each detector location by multiplying each value shown in Table 4.12 by the number of partitions (via Figures 3.12a-3.12c, the wind tunnel has been spatially divided into 43 partitions). Table 4.13 presents these values.

Detector Location	Time-Integrated Point Source Dose (unit: μSv)
1	2.58
2	3.01

Table 4.13 – Time-Integrated Point Source Dose Data (Scaled Up to the Number of Spatial Partitions)

With the results of the application of the point source technique to quantify the time-integrated external dose delivered by the resuspension of radioactive particulates being presented, a discussion on which approach to quantify the time-integrated external dose from the resuspension of radioactive particulates (i.e, the CFD-MC radiation transport coupling, submersion dose technique, and the point source technique) that can yield reasonable dose estimates will now take place, and will be the subject of the next section.

4.4.2 Comparison of Dose Calculation Techniques

In order to assess which of the three dose calculation techniques, as mentioned before are (1) CFD-MC radiation transport coupling, (2) submersion dose technique, and (3) point source technique, yield reasonable dose estimates, a brief recap of the principles of each of the aforementioned techniques will be first be provided. With respect to the first technique listed, the CFD-MC radiation transport coupling methodology has been extensively discussed in Chapter 3 and is centred on quantifying the spatial distribution of volumetric activity via the spatial partitioning system described in Section 3.2.2.1.2. The submersion dose technique seeks to express the entire region of space that has been spatially partitioned as a single radiation source that possesses a uniform volumetric activity (see Figure 4.12). The third and final technique, the point source technique, seeks to reduce the spatial distribution of volumetric activity into a single representative partition.

It is important to acknowledge that each of the three dose calculation techniques employ the spatial distribution of volumetric activity in order to arrive at a dose estimate and thus this distribution is common to each technique. However, the manner in which these techniques employ this distribution will dictate their ability to produce a reasonable dose estimate and this will now be the subject of discussion.

The submersion dose and point source techniques express the radiation source intensity as a spatially averaged volumetric activity that is calculated via equation (4.1). The qualitative interpretation of this equation is that it takes the total activity present in the region of the wind tunnel in which the radiation field is analyzed (the shaded region in Figure 4.12), as per the fact that the numerator of equation (4.1) computes the product of the volume and volumetric activity of each partition and takes the sum of this product over all partitions, and divides it by the volume of this region. The reality of this spatial averaging technique, however, is that albeit a uniform volumetric activity is found for the aforementioned region, the high intensity of the radiation field directly behind and further downstream of the bluff body (see Figures 4.9-4.11) is diluted in favour of uniformly

distributing this intensity throughout the shaded region in Figure 4.12. As a result, this technique places radiation in parts of the wind tunnel that were never active at any of the time step iterations at which the radiation field in the wind tunnel was analyzed. For example, radiation is placed in regions of the wind tunnel directly in front of the bluff body despite the fact that the radiation plots shown in Figures 4.9-4.11 clearly show otherwise. Consequently, the time-integrated external dose at each detector location that are calculated via the submersion dose and point source techniques are comparable to each other (see Tables 4.9 and 4.13), but are much smaller than those produced by the CFD-MC radiation transport coupling technique (see Table 4.5) for two reasons:

- (1) gamma radiation emanating from radiation sources placed at distances far removed from the detector locations, via the spatial averaging technique, do not contribute to the time-integrated external dose measured at each detector location because they must undergo a severe amount of attenuation prior to reaching the detector locations due to the distance between the source and each detector location, and
- (2) the strength of the radiation field in the immediate vicinity of each detector location, which are placed in the highly active downstream region of the bluff body, is weakened via the spatial averaging technique and as such, the time-integrated external dose measured at each detector location will be reduced

Contrary to the submersion dose and point source techniques, the CFD-MC radiation transport coupling technique does not manipulate the spatial distribution of volumetric activity. This distribution is acquired via the spatial partitioning system (see Section 3.2.2.1.2) and allows for the radiation field throughout the wind tunnel to be faithfully captured. Since the CFD-MC radiation transport coupling technique employs the unaltered spatial distribution of volumetric activity, the dose estimates produced by this technique are deemed to be reasonable. Of course, since the CFD-MC radiation transport coupling technique does not dilute the intensity of the radiation field in the vicinity of each detector location, a higher time-integrated external dose will be

calculated at each detector location (see Table 4.5) in comparison to those calculated by the submersion dose and point source techniques.

Now that the results produced by each of the four components of the CFD-MC radiation transport coupling methodology have been presented and discussed, a brief summary of what has been presented in this chapter will now be provided.

4.5 Summary

This chapter presented and discussed the results produced by each of the four components of the CFD-MC radiation transport coupling methodology. Bearing this in mind, Chapter 5 will contain concluding remarks on the research performed in this thesis and will discuss recommendations for future work.

CHAPTER 5

CONCLUSIONS AND RECOMMENDATIONS

5.1 Conclusions

The release of radioactive particulates from a radiological dispersal device and the subsequent resuspension of such particulates are of great concern to emergency response personnel and military field commanders. The impact of such resuspension is magnified in urban areas since the presence of bluff bodies in the form of buildings significantly increases the ability of the released radioactive particulates to be resuspended into the breathing space, thereby delivering both an internal and external radiation dose to members of the populace that are in the vicinity of the contaminated zone. Presently, there are no simulation systems that link the resuspension of radioactive particulates and the quantification of the resultant internal and external dose delivered by this resuspension. Thus, this thesis served to develop a methodology that provides a unified approach in simulating the aforementioned scenario. This approach consisted of employing Computational Fluid Dynamics, which simulated the resuspension of radioactive particulates, and Monte Carlo Radiation Transport, whose purpose was to convert the particulate spatial distribution provided by the CFD simulation into a radiation dose estimate.

The exact scenario that was used as a basis for developing the CFD-MC radiation transport coupling methodology was outlined in Figure 3.6 whereby a wind tunnel with a bluff body and plate in its interior was used to simulate the resuspension of radioactive particulates within this geometry. This configuration sought to replicate the urban geometry described above such that a realistic radioactive particulate resuspension scenario can be modelled in this thesis. Chapter 4 outlined the results produced by the two simulation tools employed in this thesis, CFD and MC radiation transport. With respect to the CFD results, there were two results that were of great interest to the modeller: (1) the presence of vortices in the vicinity of the bluff body and (2) the comparison of experimental air velocity data with those calculated by the CFD

simulation. With respect to the first result, it was found that the vortices were located in negative pressure regions of the wind tunnel and more notably, the locations of these vortices were in line with the findings of [9] and [10]. Figure 4.8 documents the comparison between the experimental velocity probe data and those of the CFD simulation, and it was found that two data sets are comparable. This is indicative of the fact that the correct flow field has been modelled in the CFD simulation.

The results produced by the MC radiation transport simulation are mainly those of the dose estimates that were performed. Here, the time-integrated internal and external dose was calculated at two spatial points in the wind tunnel, the first directly behind the bluff body and the second being further downstream. Of course, since two disparate disciplines have been used in concert to simulate the resuspension of radioactive particulates and perform subsequent radiation field determination, Luxat [13] states that the results produced by this coupling be assessed on their reasonableness. Indeed, the time-integrated external dose is calculated via data produced by both the CFD and MC radiation transport simulations and as such, this quantity must be assessed on its reasonableness. To do this, two alternative dose calculation techniques were employed namely the submersion dose and point source techniques. These approaches employ the spatial distribution of volumetric activity produced by the CFD simulation in order to perform a dose estimate. However, it was shown that the spatial averaging of volumetric activity performed by these techniques dilutes the high intensity of the radiation field directly behind the bluff body and further downstream from it. As a result, the time-integrated external dose calculated by these techniques is much lower than those produced by the CFD-MC radiation transport coupling. The comparison of these techniques with the hybrid approach employed in this thesis gave added confidence in the results that were produced by the CFD-MC radiation transport coupling in that (a) the spatial partitioning system developed in Section 3.2.2.1.2 allows for the spatial distribution of volumetric activity to be faithfully captured and (b) the coupling methodology does not manipulate the aforementioned distribution – rather, this distribution is directly translated into an MCNPX model such that a radiation dose estimate can then be performed.

The literature survey described in Chapter 1 yielded no evidence that CFD and radiation transport techniques have been used in conjunction to model the resuspension of radioactive particulates and perform subsequent radiation field determination. Hence, the research conducted in this thesis has made great strides in addressing this gap in simulation techniques and so the objective of this thesis, as set out in Section 1.3, has been achieved. It has been documented in Chapter 4 and in the discussion above that the results produced by the CFD and MC radiation transport simulations, which are the constituent simulation tools in the coupling methodology developed in this thesis, are in line with the literature reviewed and experimental data and it has also been shown that these results are deemed reasonable, as per Luxat [13].

On a larger scale, the CFD-MC radiation transport coupling methodology developed in this thesis to model the resuspension of radioactive particulates and characterize the resultant radiation field serves as a stepping stone by which this coupling procedure can be employed to develop resuspension factors for a plethora of RDD detonation scenarios. Tabulation of resuspension factors will allow the military field commander, when responding to a RDD detonation event, to quickly assess the radiological hazards associated with the contamination zone being dealt with and to then implement the appropriate precautionary measures.

Now that an overview of the work performed in this thesis and the results that were produced has been provided, a brief discussion of the recommendations for future work will now ensue.

5.2 Recommendations

There are three primary areas of work that greatly add to the research performed in this thesis, and they are outlined below:

- (1) The CFD simulation performed in this thesis was conducted on a quad core workstation. The use of other high performance computing clusters (such as

SHARCNET) which offer the use of four or more processors must be investigated. This will allow for the modeller to simulate particulate resuspension in more complex geometries than the one detailed in Figure 3.6. Nonetheless, the computational infrastructure required by the Black Box remains the same in that all that is needed is a single processor for its operation.

- (2) As described in Section F.2 in Appendix F, the particulate transport equations employed by FLUENT are dependent on the velocities of both the particulate and the air flow. The spatial variation of these quantities is achieved by the presence of nodes in the flow geometry, which is embodied by a mesh. It is known that the boundary layer region hosts a fluid velocity gradient and it has been shown that this gradient plays an important role in the resuspension of particulates that initially reside in the boundary layer. Thus, the modeller must incorporate a finer mesh resolution in the near-wall region of the flow geometry where the particulates are placed. This will allow for the fluid velocity gradient in this region to be fully quantified such that the influence of this fluid velocity gradient on particulate resuspension can be better captured.
- (3) The surface card, which constitute one-third of the input file for the MC radiation transport simulation, essentially builds the wind tunnel geometry shown in Figure 3.8 in the MCNPX environment. GAMBIT possesses a feature that allows the modeller to export data to a text file that contains the spatial coordinates of the vertices of the flow domain features such as those of the plate, bluff body, and the wind tunnel shell (which is the wind tunnel minus the plate and bluff body). In light of this feature, one can develop a generic algorithm, applicable to any geometry within which the resuspension of radioactive particulates is simulated, which translates the geometry in the GAMBIT environment (described via the vertex data exported by GAMBIT) into the MCNPX environment. In other words, this generic algorithm will employ the contents of the vertex data file exported by GAMBIT to build the surface card in the MCNPX input file. This will assist the modeller in applying the CFD-MC radiation transport coupling

methodology developed in this thesis to other resuspension scenarios aside from the one modelled in the wind tunnel shown in Figure 3.6.

APPENDIX A
WIS WIND TUNNEL DATA

The purpose of this appendix is to provide a detailed description of the WIS Wind Tunnel in the form of displaying schematics. Knowledge of these dimensions is integral to building the wind tunnel geometry that is used for both the CFD and MC radiation transport simulations. Based on the schematics provided, the Reynolds Number will be calculated in order to assess the nature of the fluid flow in the wind tunnel domain (i.e. laminar or turbulent). Also, the Mach Number will be calculated in order to determine if the flow in the WIS Wind Tunnel is either incompressible or compressible. This appendix will also present air velocity data measured by the velocity probes that are placed downstream of the bluff body. The schematics of the wind tunnel will now be addressed.

A.1 WIS Wind Tunnel Schematics

Before the schematics are presented, attention must be paid to the axis coordinate system employed by the schematics. It is evident that the $+x$ axis is in the *spanwise* direction, $+y$ axis is in the *normal* direction, and the $+z$ axis is in the *anti-streamwise* direction. The reason why the $+z$ axis is in the anti-streamwise direction is that as will be shown in Figure A.4, the flow is along the $-z$ axis. Hence, the $+z$ axis runs counter to the flow direction and is therefore anti-streamwise. It is also important to note that the axis coordinate system has its origin placed at vertex F shown in Figure A.5.

Bearing the axis coordinate system in mind, schematics for the WIS Wind Tunnel will now be shown beginning with Figure A.1 which illustrates the cross section of the wind tunnel, showing both the bluff body and plate.

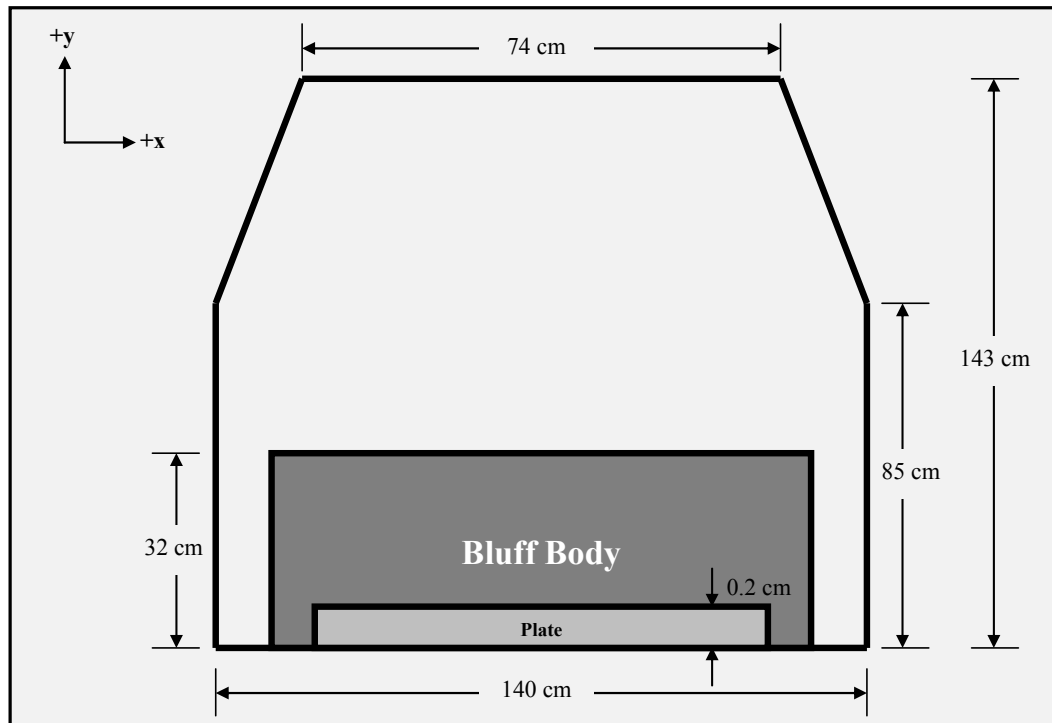


Figure A.1 – View of the WIS Wind Tunnel in the $+x/+y$ Plane

Figure A.2 displays the schematics for both the back of the wind tunnel and the fans that are placed on it.

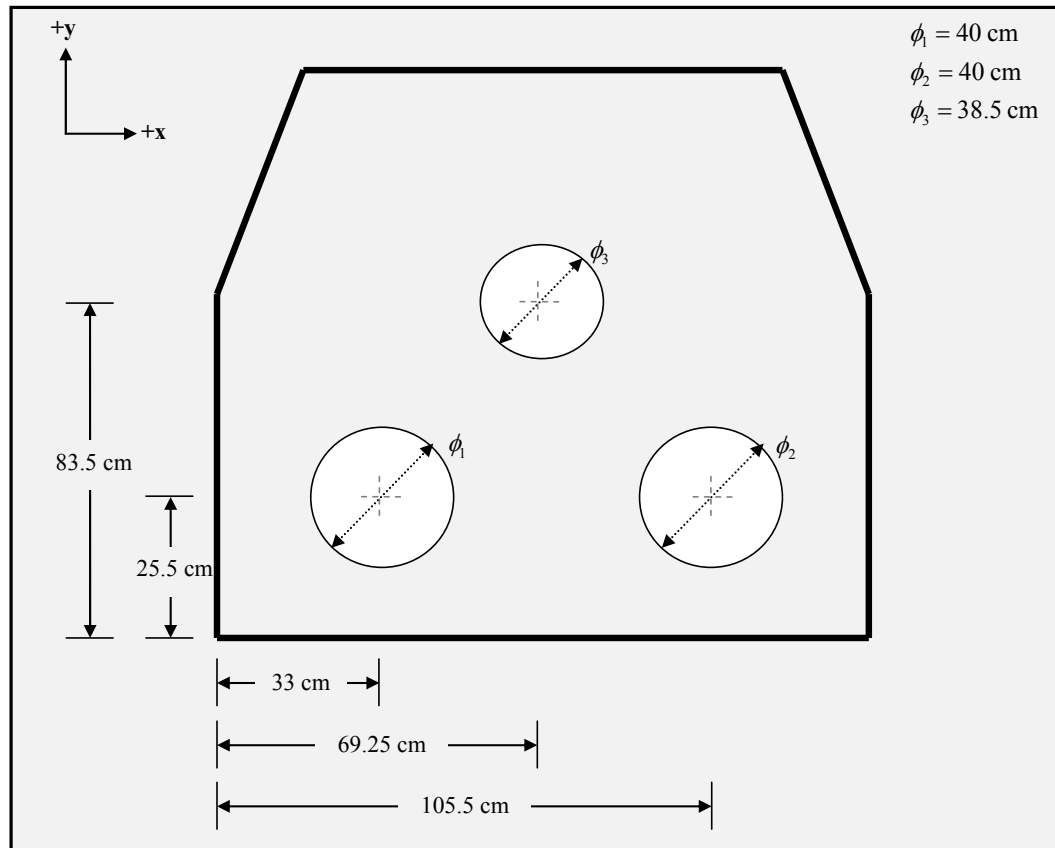


Figure A.2 – View of the Back of the WIS Wind Tunnel

Figure A.3 shows an overhead view of the bluff body and the plate.

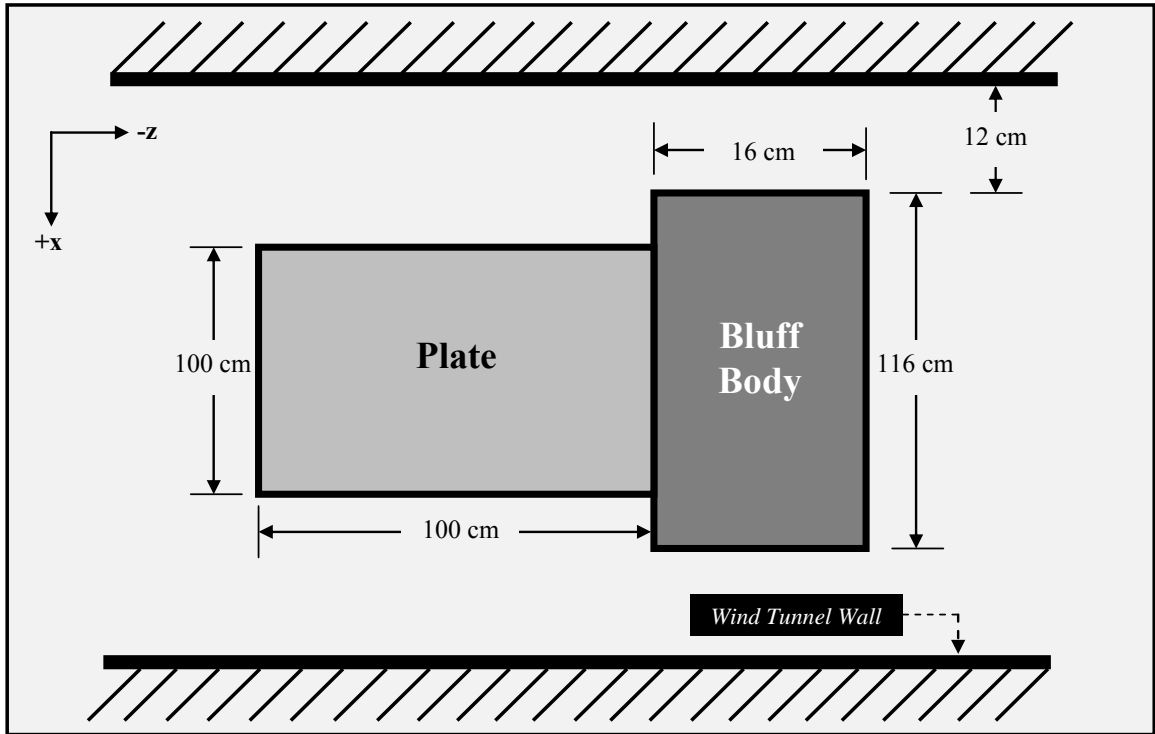


Figure A.3 – View of the WIS Wind Tunnel in the $+x/-z$ Plane

Figure A.4 displays a side view of the WIS Wind Tunnel (note the inlet air velocity).

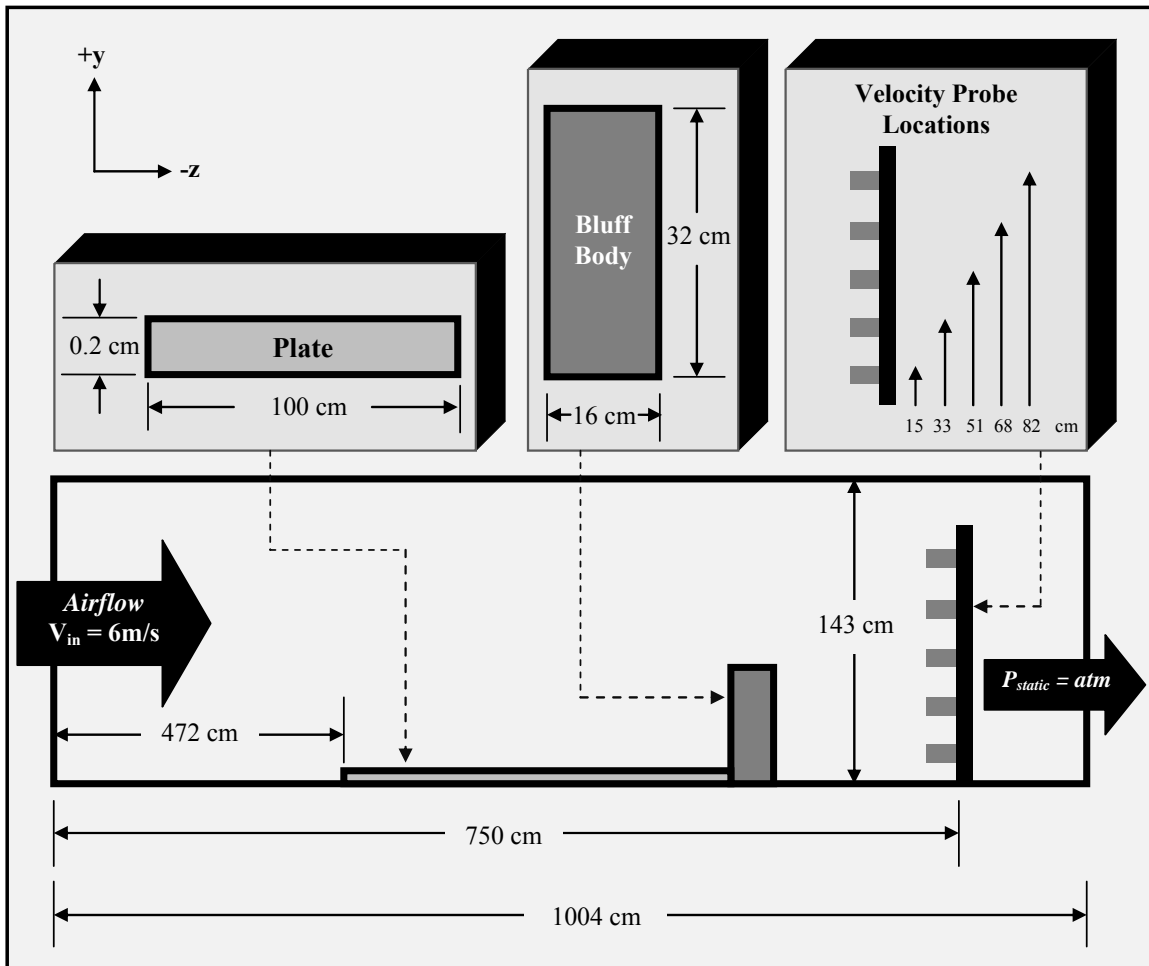


Figure A.4 – View of the WIS Wind Tunnel in the $+y/-z$ Plane

When building the wind tunnel geometry for use by the CFD and MC radiation transport calculations, knowing the spatial coordinates of the vertices of the bluff body, plate, and wind tunnel shell (which is the wind tunnel minus the plate and bluff body) are important. Figure A.5 will identify these vertices.

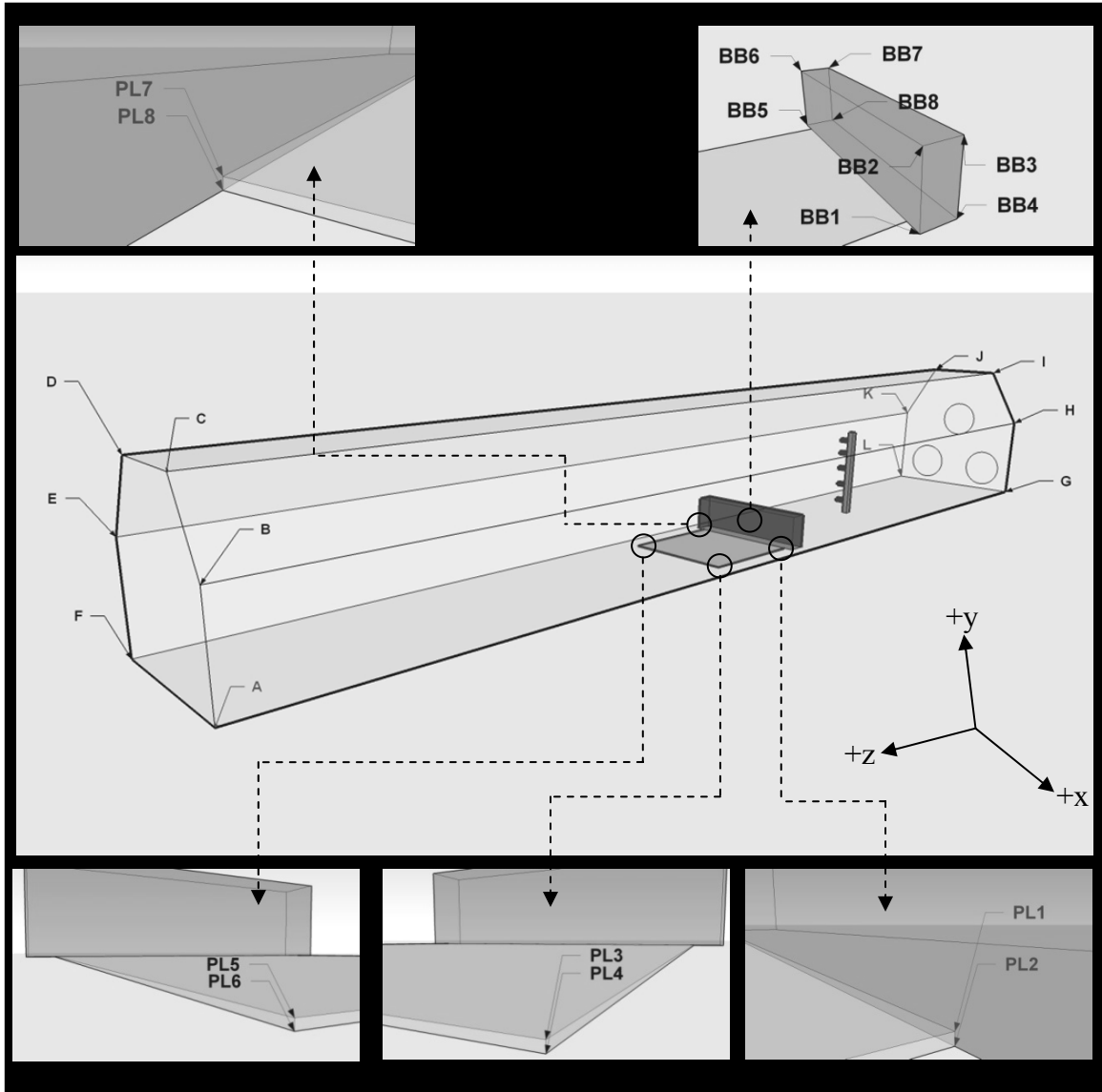


Figure A.5 – Identification of Vertices of the WIS Wind Tunnel Shell, Bluff Body, and Plate

Via the schematics shown in Figures A.1-A.4, the spatial coordinates of the vertices identified in Figure A.5 will be stated in Table A.1.

Vertex	(x,y,z) coordinates (unit: cm)
<i>Inlet Face Vertices</i>	
A	(140,0,0)
B	(140,85,0)
C	(107,143,0)
D	(33,143,0)

E	(0,85,0)
F	(0,0,0)
<i>Back Face Vertices</i>	
G	(140,0,-1004)
H	(140,85,-1004)
I	(107,143,-1004)
J	(33,143,-1004)
K	(0,85,-1004)
L	(0,0,-1004)
<i>Bluff Body Vertices</i>	
BB1	(128,0,-572)
BB2	(128,32,-572)
BB3	(128,32,-588)
BB4	(128,0,-588)
BB5	(12,0,-572)
BB6	(12,32,-572)
BB7	(12,32,-588)
BB8	(12,0,-588)
<i>Plate Vertices</i>	
PL1	(120,0.2,-572)
PL2	(120,0,-572)
PL3	(120,0.2,-472)
PL4	(120,0,-472)
PL5	(20,0.2,-472)
PL6	(20,0,-472)
PL7	(20,0.2,-572)
PL8	(20,0,-572)

Table A.1 – Coordinates of Vertices of the WIS Wind Tunnel Shell, Bluff Body, and Plate

A.2 Reynolds Number Calculation

In order to calculate the Reynolds Number for the flow in the WIS Wind Tunnel, attention must be turned to Figure A.4. This figure shows a streamwise view of the wind tunnel and as such, it provides a general understanding as to how the flow will move through the domain. This figure makes it clear that the major feature of the wind tunnel domain is the bluff body since it will foster the creation of a negative pressure wake region – a region that ultimately alters the nature of the flow.

As per equation (2.2), physical properties of air must be selected, namely the air density and air dynamic viscosity. It is desired to obtain the respective values of these quantities at a temperature equivalent to that of the air inlet temperature described in Table 3.5 to be 27°C. However, the physical properties of air listed in [25] does not contain data for air at this temperature and instead, data corresponding to the closest provided temperature of 25°C will be used. The following lists the values of abovementioned air properties [25].

$$\rho = 1.18 \text{ kg} \cdot \text{m}^{-3}$$

$$\mu = 1.85 \times 10^{-5} \text{ N} \cdot \text{s} \cdot \text{m}^{-2}$$

With respect to the mean fluid velocity, the inlet air velocity can be substituted for the aforementioned quantity. In addition, since the bluff body has been chosen as the flow feature of interest, the height of the bluff body will be used as the characteristic length of the flow domain feature [25]. Via Figure A.4, the values of these quantities are respectively:

$$u = 6 \text{ m} \cdot \text{s}^{-1}$$

$$L = 0.32 \text{ m}$$

Recalling equation (2.2), the expression for Reynolds Number is as follows:

$$\text{Re} = \frac{\rho u L}{\mu} \tag{A.1}$$

Substitute the values of the quantities shown into equation (A.1).

$$\text{Re} = \frac{(1.18 \text{ kg} \cdot \text{m}^{-3})(6 \text{ m} \cdot \text{s}^{-1})(0.32 \text{ m})}{(1.85 \times 10^{-5} \text{ N} \cdot \text{s} \cdot \text{m}^{-2})}$$

Simplifying the above expression yields a Reynolds Number of:

$$\text{Re} = 1.23 \times 10^5$$

(A.2)

For a flow around an obstacle that has a Reynolds Number that exceeds 20,000, this flow is deemed turbulent [27]. Thus, the calculated Reynolds Number shown in equation (A.2) exceeds this value and therefore the flow in the WIS Wind Tunnel is classified as turbulent.

Now that the Reynolds Number has been calculated, the Mach Number for the flow in WIS Wind Tunnel will now be calculated.

A.3 Mach Number Calculation

The purpose of quantifying the Mach Number for the flow scenario under investigation is to determine if the flow is either compressible or incompressible. The equation for the Mach Number is shown in equation (A.3).

$$\text{Ma} = \frac{u}{\sqrt{k(T)RT}} \quad (\text{A.3})$$

Where:

- Ma = mach number (unit: unitless)
- u = velocity of fluid (unit: $\text{m} \cdot \text{s}^{-1}$)
- k = ratio of specific heats of fluid at fluid temperature T (unit: unitless)
- R = $2.87 \times 10^2 \text{ J} \cdot \text{kg}^{-1} \cdot \text{K}^{-1}$ (gas constant of air)
- T = temperature of fluid (unit: $^{\circ}\text{K}$)

With respect to the quantities shown in equation (A.3), the inlet air velocity shown in Figure A.4 will be substituted for the numerator in the aforesaid equation.

$$u = 6 \text{ m} \cdot \text{s}^{-1}$$

The inlet air temperature employed by FLUENT is 27°C . As with the Reynolds Number calculation, the ratio of specific heats for air at this temperature is not available and so the value of this quantity for the closest temperature, 25°C , will be used.

$$k(25^{\circ}\text{C}) = 1.40$$

Substitute the values of the above quantities into equation (A.3).

$$\text{Ma} = \frac{6 \text{ m} \cdot \text{s}^{-1}}{\sqrt{(1.40)(2.87 \times 10^2 \text{ J} \cdot \text{kg}^{-1} \cdot \text{K}^{-1})(25^{\circ}\text{C} + 273.15)}}$$

Simplifying the above expression yields a Mach Number of:

$$\text{Ma} = 1.73 \times 10^{-2} \quad (\text{A.4})$$

Since the Mach Number is less than 0.3, the flow is deemed incompressible [25].

A.4 Velocity Probe Data

Table A.2 lists the velocity probe data. Note that five measurements have been made, each for the respective probe. This is in accordance with the probe configuration displayed in Figure A.4 which shows that five velocity probes were employed in the experimental setup.

Probe Location (m)	Air Velocity (m/s)	Standard Deviation (m/s)
0.15	1.65	0.73
0.33	2.72	1.13
0.51	4.94	2.03
0.68	6.75	2.65
0.82	6.96	2.79

Table A.2 – Velocity Probe Data

APPENDIX B
RADIATION DATA FOR WIS WIND TUNNEL MATERIALS

The properties of the material through which radiation traverses is of extreme importance and must be taken into account when the MC radiation transport calculations are performed.

The densities of air and Lanthanum-140 are the only material properties required for input in the CFD simulation. It is these same densities along with other radiation related quantities that are required for use by the Black Box, MC radiation transport calculations, and dose calculations. This appendix will be split into two parts; the first will describe the required material data for Lanthanum-140 while the second will pertain to that of the Bluff Body, Plate, and Air.

B.1 Radiation Data for Lanthanum-140

Table B.1 outlines radiation data for Lanthanum-140.

Quantity	Symbol	Value
Half-life of ^{140}La	$T_{\frac{1}{2}}(^{140}\text{La})$	40.22 hrs [36]
Nominal Density of ^{140}La	$\rho_{^{140}\text{La}}$	$6.19 \text{ g} \cdot \text{cm}^{-3}$ [47]
Molar Mass of ^{140}La	$M_M^{^{140}\text{La}}$	$138.91 \text{ g} \cdot \text{mol}^{-1}$ [36]
Avogadro's Constant	N_A	$6.02 \times 10^{23} \text{ nuclei} \cdot \text{mol}^{-1}$

Table B.1 – Radiation Data for Lanthanum-140

Table B.2 outlines the Beta Energy Spectrum data for Lanthanum-140.

Emission Probability	Maximum Beta Energy (unit: MeV)
1.62E-03	9.58E-01
6.40E-03	1.21E+00
1.19E-02	1.28E+00
5.08E-02	1.41E+00
5.20E-02	2.16E+00
5.63E-02	1.30E+00
5.89E-02	1.24E+00
1.11E-01	1.24E+00
2.07E-01	1.68E+00
4.45E-01	1.35E+00

Table B.2 – Beta Energy Spectrum for Lanthanum-140 [36]

Table B.3 outlines the Gamma Energy Spectrum data for Lanthanum-140.

Emission Probability	Gamma Energy (unit: MeV)
1.04E-03	2.55E+00
1.24E-03	1.74E-01
1.91E-03	1.09E-01
2.55E-03	4.84E-03
3.22E-03	3.93E-02
4.16E-03	1.21E+00
4.30E-03	2.42E-01
4.72E-03	3.43E-02
4.87E-03	2.67E-01
5.35E-03	9.51E-01
5.54E-03	1.31E-01
8.51E-03	2.35E+00
8.66E-03	3.47E-02
2.88E-02	9.20E-01
2.94E-02	4.33E-01
3.46E-02	2.52E+00
4.40E-02	7.52E-01
5.63E-02	8.68E-01
7.09E-02	9.25E-01
2.05E-01	3.29E-01
2.35E-01	8.16E-01
4.55E-01	4.87E-01
9.55E-01	1.60E+00
Gamma Yield = 2.17E+00	

Table B.3 – Gamma Energy Spectrum for Lanthanum-140 [36]

Based on the data shown in Tables B.2 and B.3, there are two important features to point out:

- (1) The Gamma Yield is found by taking the sum of all the emission probabilities stated in Table B.3
- (2) To find the weighted radiation energies stated in Figure 3.5, the sum of the products of the emission probability and the corresponding radiation energy must be taken, and this sum is then divided by the sum of the probabilities shown. This ratio is equivalent to the weighted radiation energy

Now that the radiation data for Lanthanum-140 has been provided, the radiation data for the Bluff Body, Plate, and Air will now be stated.

B.2 Radiation Data for Bluff Body, Plate, and Air

The radiation data for the Bluff Body, Plate, and Air are required for use by the MC radiation transport simulation. As per the material input requirements of MCNPX, the following quantities must be provided:

- Density of the material that the wind tunnel feature is composed of
- The constituent elements of these materials
- The atomic mass and atomic number for each of these elements
- The weight fraction of each element with respect to the compound (i.e. material) they belong to

It is important to note that in the third quantity mentioned above, the atomic mass and atomic number will be used to identify the data library which contains radiation interaction coefficients for the particular element. It is important to recall that the bluff body and the plate are composed of the same material, plywood, whereas the fluid flowing in the wind tunnel is composed of air. Tables B.4 and B.5 will contain the above quantities for two mentioned materials, respectively.

	Constituent Element	Cross Section Data Library	Weight Fraction (%)
Material: Plywood Density: 0.65 g·cm ⁻³	Hydrogen	1001.50c	6.2
	Carbon	6000.50c	44.5
	Oxygen	8016.50c	49.3

Table B.4 – MCNPX Input Data for Plywood [48]

	Constituent Element	Cross Section Data Library	Weight Fraction (%)
Material: Air Density: 1.24×10 ⁻³ g·cm ⁻³	Hydrogen	1001.50c	1.18
	Nitrogen	7014.50c	77.08
	Oxygen	8016.50c	21.28
	Argon	18000.35c	0.46

Table B.5 – MCNPX Input Data for Air [48]

Note that the data stated for air in Table B.5 is for the average meteorological conditions at the Army Pulse Radiation Facility [48].

APPENDIX C
SPATIAL BOUNDS FOR WIS WIND TUNNEL PARTITIONS

The purpose of this appendix is to provide the spatial bounds of the partitions shown in Figures 3.12a-3.12c in Chapter 3. These bounds are presented below in Table C.1.

Partition Number	Bounds (unit: cm)	Symmetrical Partition Number	Bounds (unit: cm)
1	$0 \leq x \leq 20$ $0 \leq y \leq 1$ $-572 \leq z \leq -472$	29	$120 \leq x \leq 140$ $0 \leq y \leq 1$ $-572 \leq z \leq -472$
2	$0 \leq x \leq 20$ $1 \leq y \leq 32$ $-572 \leq z \leq -472$	30	$120 \leq x \leq 140$ $1 \leq y \leq 32$ $-572 \leq z \leq -472$
3	$0 \leq x \leq 20$ $32 \leq y \leq 85$ $-572 \leq z \leq -472$	31	$120 \leq x \leq 140$ $32 \leq y \leq 85$ $-572 \leq z \leq -472$
4	$20 \leq x \leq 70$ $0.2 \leq y \leq 1$ $-572 \leq z \leq -472$	4	$20 \leq x \leq 120$ $0.2 \leq y \leq 1$ $-572 \leq z \leq -472$
5	$20 \leq x \leq 70$ $1 \leq y \leq 32$ $-572 \leq z \leq -472$	5	$20 \leq x \leq 120$ $1 \leq y \leq 32$ $-572 \leq z \leq -472$
6	$20 \leq x \leq 70$ $32 \leq y \leq 85$ $-572 \leq z \leq -472$	6	$20 \leq x \leq 120$ $32 \leq y \leq 85$ $-572 \leq z \leq -472$
7	$0 \leq x \leq 12$ $0 \leq y \leq 1$ $-588 \leq z \leq -572$	32	$128 \leq x \leq 140$ $0 \leq y \leq 1$ $-588 \leq z \leq -572$
8	$0 \leq x \leq 12$ $1 \leq y \leq 32$ $-588 \leq z \leq -572$	33	$128 \leq x \leq 140$ $1 \leq y \leq 32$ $-588 \leq z \leq -572$
9	$0 \leq x \leq 12$ $32 \leq y \leq 85$ $-588 \leq z \leq -572$	34	$128 \leq x \leq 140$ $32 \leq y \leq 85$ $-588 \leq z \leq -572$
10	$12 \leq x \leq 70$ $32 \leq y \leq 85$ $-588 \leq z \leq -572$	10	$12 \leq x \leq 128$ $32 \leq y \leq 85$ $-588 \leq z \leq -572$

11	$0 \leq x \leq 12$ $0 \leq y \leq 1$ $-688 \leq z \leq -588$	35	$128 \leq x \leq 140$ $0 \leq y \leq 1$ $-688 \leq z \leq -588$
12	$0 \leq x \leq 12$ $1 \leq y \leq 32$ $-688 \leq z \leq -588$	36	$128 \leq x \leq 140$ $1 \leq y \leq 32$ $-688 \leq z \leq -588$
13	$0 \leq x \leq 12$ $32 \leq y \leq 85$ $-688 \leq z \leq -588$	37	$128 \leq x \leq 140$ $32 \leq y \leq 85$ $-688 \leq z \leq -588$
14	$12 \leq x \leq 70$ $0 \leq y \leq 1$ $-688 \leq z \leq -588$	14	$12 \leq x \leq 128$ $0 \leq y \leq 1$ $-688 \leq z \leq -588$
15	$12 \leq x \leq 70$ $1 \leq y \leq 32$ $-688 \leq z \leq -588$	15	$12 \leq x \leq 128$ $1 \leq y \leq 32$ $-688 \leq z \leq -588$
16	$12 \leq x \leq 70$ $32 \leq y \leq 85$ $-688 \leq z \leq -588$	16	$12 \leq x \leq 128$ $32 \leq y \leq 85$ $-688 \leq z \leq -588$
17	$0 \leq x \leq 12$ $0 \leq y \leq 1$ $-788 \leq z \leq -688$	38	$128 \leq x \leq 140$ $0 \leq y \leq 1$ $-788 \leq z \leq -688$
18	$0 \leq x \leq 12$ $1 \leq y \leq 32$ $-788 \leq z \leq -688$	39	$128 \leq x \leq 140$ $1 \leq y \leq 32$ $-788 \leq z \leq -688$
19	$0 \leq x \leq 12$ $32 \leq y \leq 85$ $-788 \leq z \leq -688$	40	$128 \leq x \leq 140$ $32 \leq y \leq 85$ $-788 \leq z \leq -688$
20	$12 \leq x \leq 70$ $0 \leq y \leq 1$ $-788 \leq z \leq -688$	20	$12 \leq x \leq 128$ $0 \leq y \leq 1$ $-788 \leq z \leq -688$
21	$12 \leq x \leq 70$ $1 \leq y \leq 32$ $-788 \leq z \leq -688$	21	$12 \leq x \leq 128$ $1 \leq y \leq 32$ $-788 \leq z \leq -688$
22	$12 \leq x \leq 70$ $32 \leq y \leq 85$ $-788 \leq z \leq -688$	22	$12 \leq x \leq 128$ $32 \leq y \leq 85$ $-788 \leq z \leq -688$
23	$0 \leq x \leq 12$ $0 \leq y \leq 1$ $-1004 \leq z \leq -788$	41	$128 \leq x \leq 140$ $0 \leq y \leq 1$ $-1004 \leq z \leq -788$

24	$0 \leq x \leq 12$ $1 \leq y \leq 32$ $-1004 \leq z \leq -788$	42	$128 \leq x \leq 140$ $1 \leq y \leq 32$ $-1004 \leq z \leq -788$
25	$0 \leq x \leq 12$ $32 \leq y \leq 85$ $-1004 \leq z \leq -788$	43	$128 \leq x \leq 140$ $32 \leq y \leq 85$ $-1004 \leq z \leq -788$
26	$12 \leq x \leq 70$ $0 \leq y \leq 1$ $-1004 \leq z \leq -788$	26	$12 \leq x \leq 128$ $0 \leq y \leq 1$ $-1004 \leq z \leq -788$
27	$12 \leq x \leq 70$ $1 \leq y \leq 32$ $-1004 \leq z \leq -788$	27	$12 \leq x \leq 128$ $1 \leq y \leq 32$ $-1004 \leq z \leq -788$
28	$12 \leq x \leq 70$ $32 \leq y \leq 85$ $-1004 \leq z \leq -788$	28	$12 \leq x \leq 128$ $32 \leq y \leq 85$ $-1004 \leq z \leq -788$

Table C.1 – Spatial Bounds for WIS Wind Tunnel Partitions

APPENDIX D
CONSTRUCTION OF WIS WIND TUNNEL GEOMETRY IN MCNPX

The purpose of this appendix is to provide a detailed description of how the wind tunnel domain shown in Figure 3.6 is modelled in MCNPX. Of course, the wind tunnel shown in this figure is only half modelled and as such, the geometry that is constructed in MCNPX will be the one shown in Figure 3.8. As shown in these figures, the wind tunnel domain is composed of three structures which are the plate, bluff body, and the wind tunnel shell (which is defined as the wind tunnel minus the plate and bluff body). A description of how these respective structures are modelled in the MCNPX environment will be provided, commencing with a description of how the wind tunnel shell is constructed.

D.1 Construction of Wind Tunnel Shell

To begin, consider Figure D.1 which illustrates pertinent dimensions related to the wind tunnel cross section.

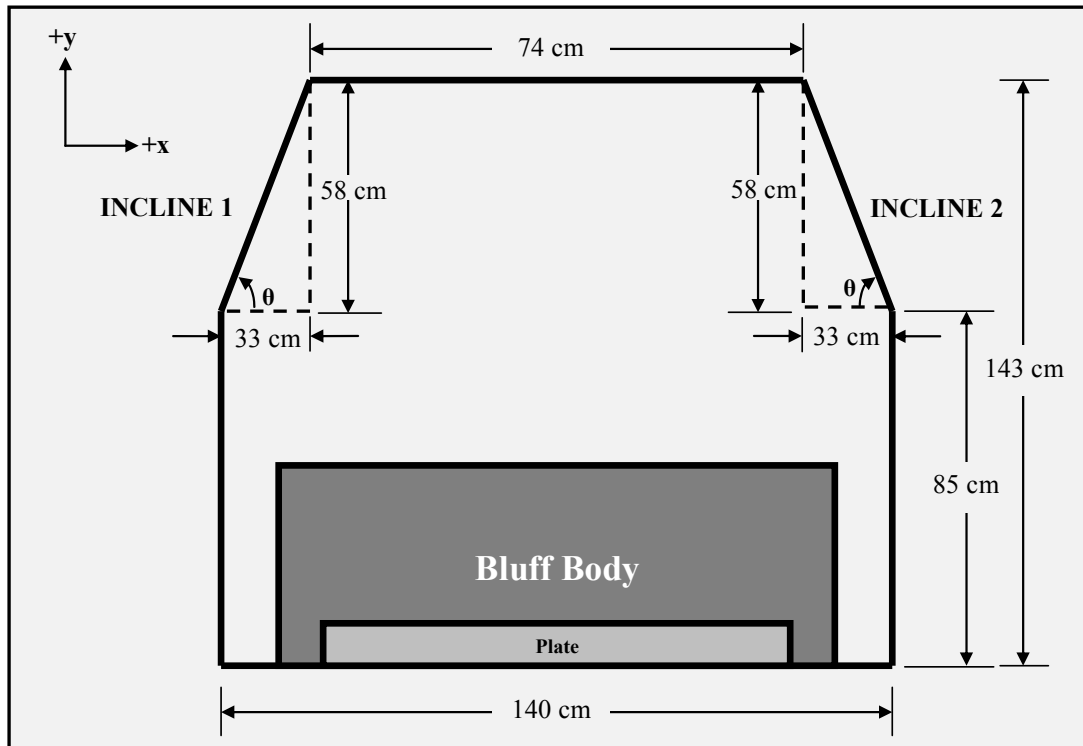


Figure D.1 – Cross Section of WIS Wind Tunnel

Figure D.1 identifies the two inclined upper sides of the wind tunnel, named Incline 1 and Incline 2 respectively. Characterizing these Inclines in MCNPX is pivotal in the creation of the wind tunnel shell and will be of much focus in this section. Before the attributes of the Inclines are discussed, a general description of how the wind tunnel shell is modelled in MCNPX must be provided, beginning with Figure D.2.

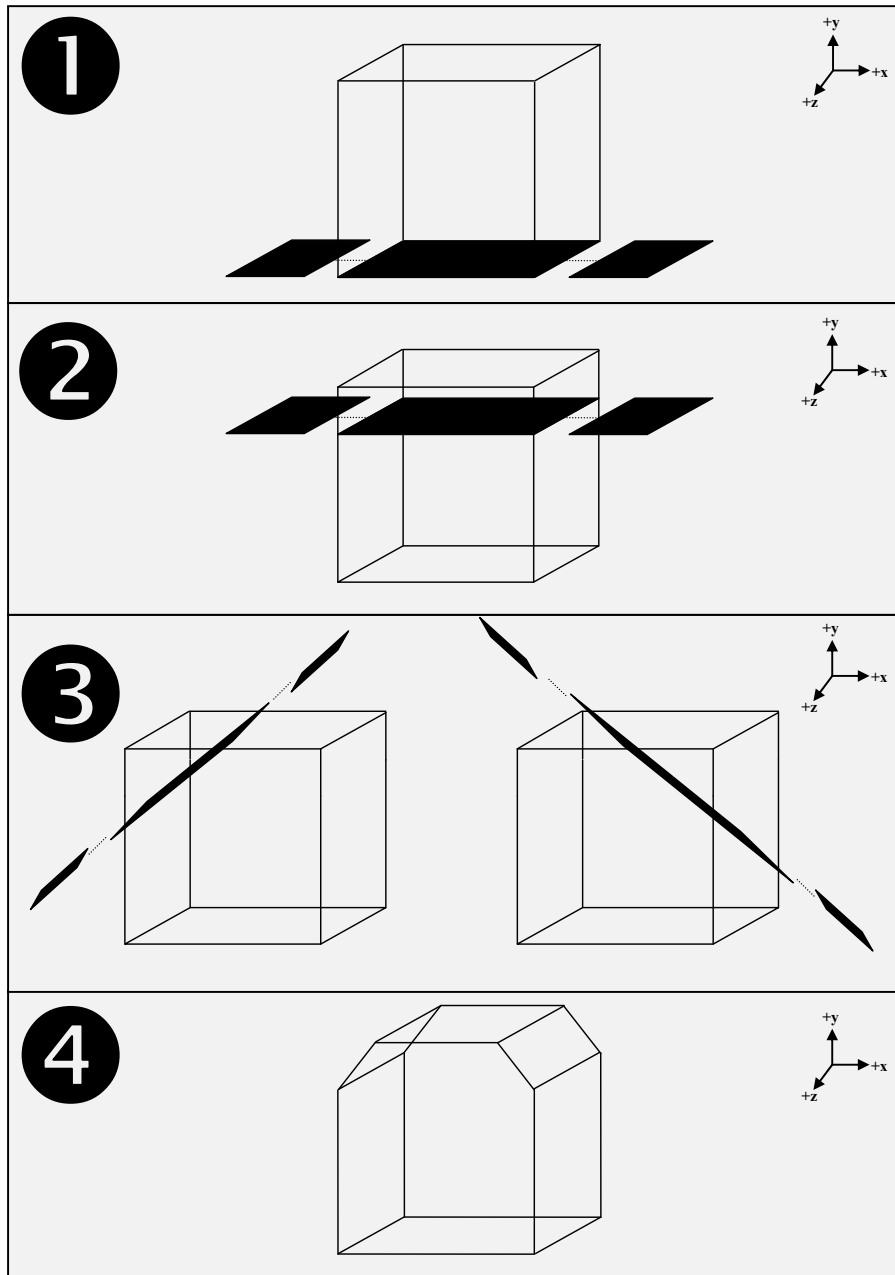


Figure D.2 – Steps in Constructing the Wind Tunnel Shell in MCNPX

Figure D.2 reveals the nature of the Inclines in that they are planes that intersect the wind tunnel frame at a certain height and angle to produce the cross section shown in Figure D.1. The steps illustrated in Figure D.2 are described further in Table D.1.

Step	Description
1	Build a rectangular parallelepiped whose dimensions are equivalent to the basic frame of the WIS wind tunnel. According to the schematics shown in Appendix A, the frame dimensions are 140 cm x 143 cm x 1004 cm. When constructing each Incline, begin by placing an infinite plane at y=0 cm.
2	It was stated at the beginning of Section A.1 that the origin is placed at the lower left corner of the wind tunnel cross section shown in Figure D.1. With this being said, it is clear that prior to rotation by an angle θ , the Incline 1 plane must be centred at the (0,+85,0) cm point while the Incline 2 plane must be centred at the (+140,+85,0) cm point. Thus, for the Incline 1 plane, translate it from y=0 cm to y=+85 cm while for the Incline 2 plane, translate it from y=0 cm to y=+85 cm and then from x=0 cm to x=+140 cm.
3	As per Figure D.1, rotate the Incline 1 plane by angle of θ about the +z axis in the counter clockwise direction. For the Incline 2 plane, rotate by angle of θ about the +z axis in the clockwise direction.
4	In MCNPX, perform an intersection operation between the rotated Incline 1 and 2 planes with the rectangular parallelepiped frame modelled in step 1.

Table D.1 – Description of Steps Required to Create Wind Tunnel Shell

In steps 2 and 3 described in Table D.1 where the Inclines 1 and 2 planes were translated and rotated about their respective centering points, MCNPX requires that these operations be described via a *rotation matrix*. To populate this matrix, the angle θ depicted in Figure D.1 must be calculated. Based on the dimensions provided in Figure D.1, the calculation of θ will be found via Figure D.3.

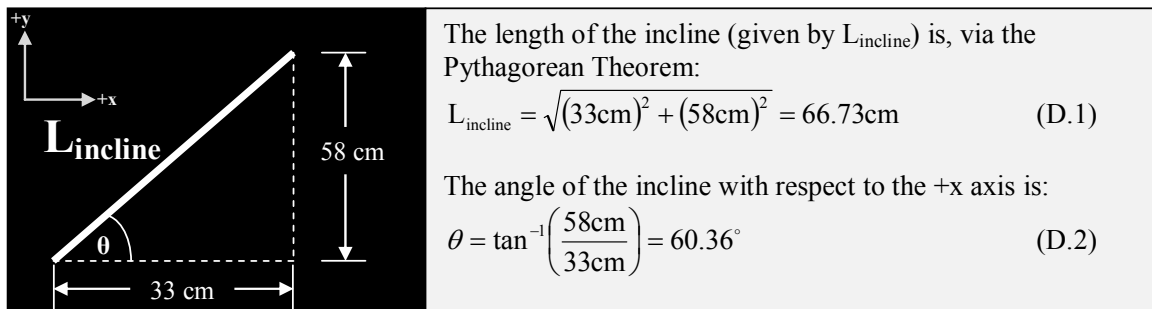


Figure D.3 – Calculation of Incline Plane Rotation Angle θ

To define the contents of the rotation matrix, first consider Figure D.4 which illustrates a hypothetical plane being rotated by an angle θ about the +z axis.

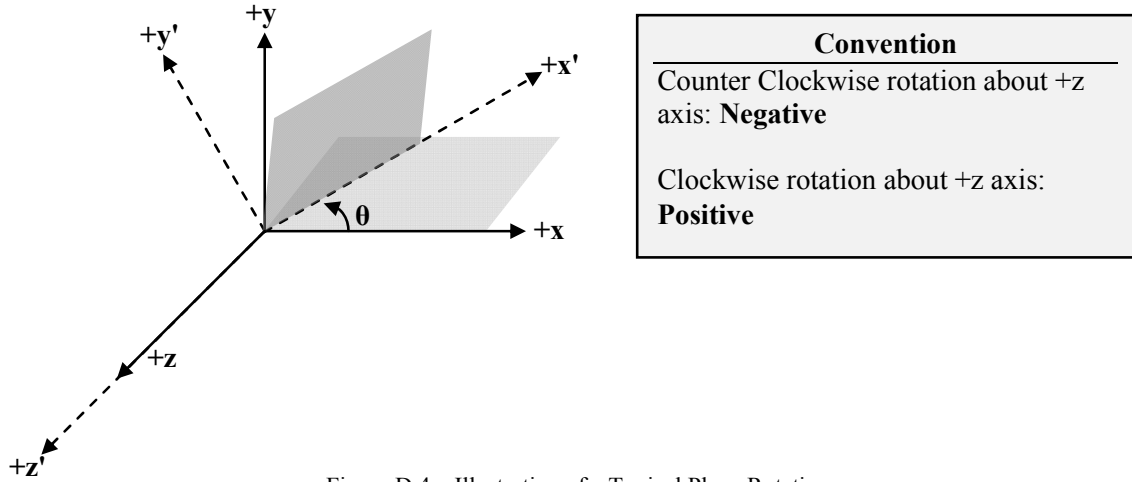


Figure D.4 – Illustration of a Typical Plane Rotation

The rotation matrix essentially holds the angles between the axes of the default coordinate system, shown as solid lines in Figure D.4, and those of the new coordinate system formed by the plane rotation, shown as dashed lines in Figure D.4. The rotation matrix has the following contents [35]:

$$\left[\begin{array}{c} \underbrace{O_1 O_2 O_3}_{\text{Displacement vector for the rotated plane}} \quad \underbrace{XX' \quad YX' \quad ZX' \quad XY' \quad YY' \quad ZY' \quad XZ' \quad YZ' \quad ZZ'}_{\text{Angles (in degrees) between the axes of the default coordinate system and those of the new coordinate system formed by the rotated plane}} \end{array} \right] \quad (D.3)$$

With respect to the left-most entry in the rotation matrix shown above, examples of a displacement vector are the centering points described for each Incline planes at the beginning of step 2 in Table D.1. In regards to the array of angles between the axes of the default and new coordinate system formed by the rotated plane, a convention must be employed when stating these respective angles. The convention is shown in Figure D.4 and to gain an understanding of it, consider the configuration of the two axes systems shown in this figure. The first entry in the angle array shown in equation (D.3) requires the angle between the X and X' axes. According to Figure D.4, a counter clockwise rotation is required to go from the X to X' axes. Thus, the angle between the two will be declared to be negative. Moreover, the second entry in the angle array requires the angle between the Y and X' axes. According to Figure D.4, a clockwise rotation is required to go from the Y to X' axes and so the angle between the two is declared to be positive.

Bearing in mind the contents of the rotation matrix shown in equation (D.3) and the angle sign convention just described, the rotation matrix will now be populated for Inclines 1 and 2 respectively.

As per the description of the displacement and rotation of the Incline 1 plane in steps 2 and 3 of Table D.1, the configuration of the axes of the new coordinates system formed by the plane translation and rotation to that of the default is shown in Figure D.5.

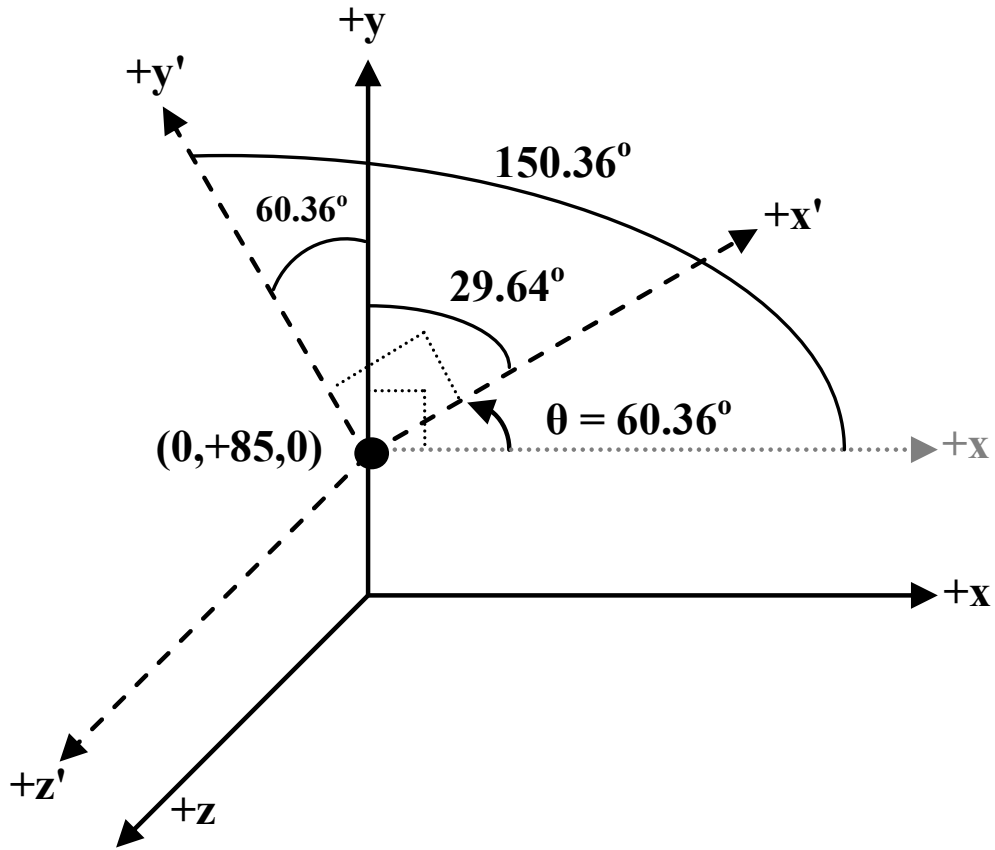


Figure D.5 - Incline 1 Coordinate System in Relation to that of the Default

Based on the contents of Figure D.5, the rotation matrix for the Incline 1 plane is shown in equation (D.4).

$$\begin{bmatrix} 0 \text{ cm} & 85 \text{ cm} & 0 \text{ cm} & -60.36^\circ & 29.64^\circ & 90^\circ & -150.36^\circ & -60.36^\circ & 90^\circ & 90^\circ & 90^\circ & 0^\circ \end{bmatrix} \quad (\text{D.4})$$

In regards to the rotation matrix for the Incline 2 plane, consider Figure D.6 which illustrates the configuration of the axes of the new coordinates system formed by the plane translation and rotation described in steps 2 and 3 of Table D.1 to that of the default.

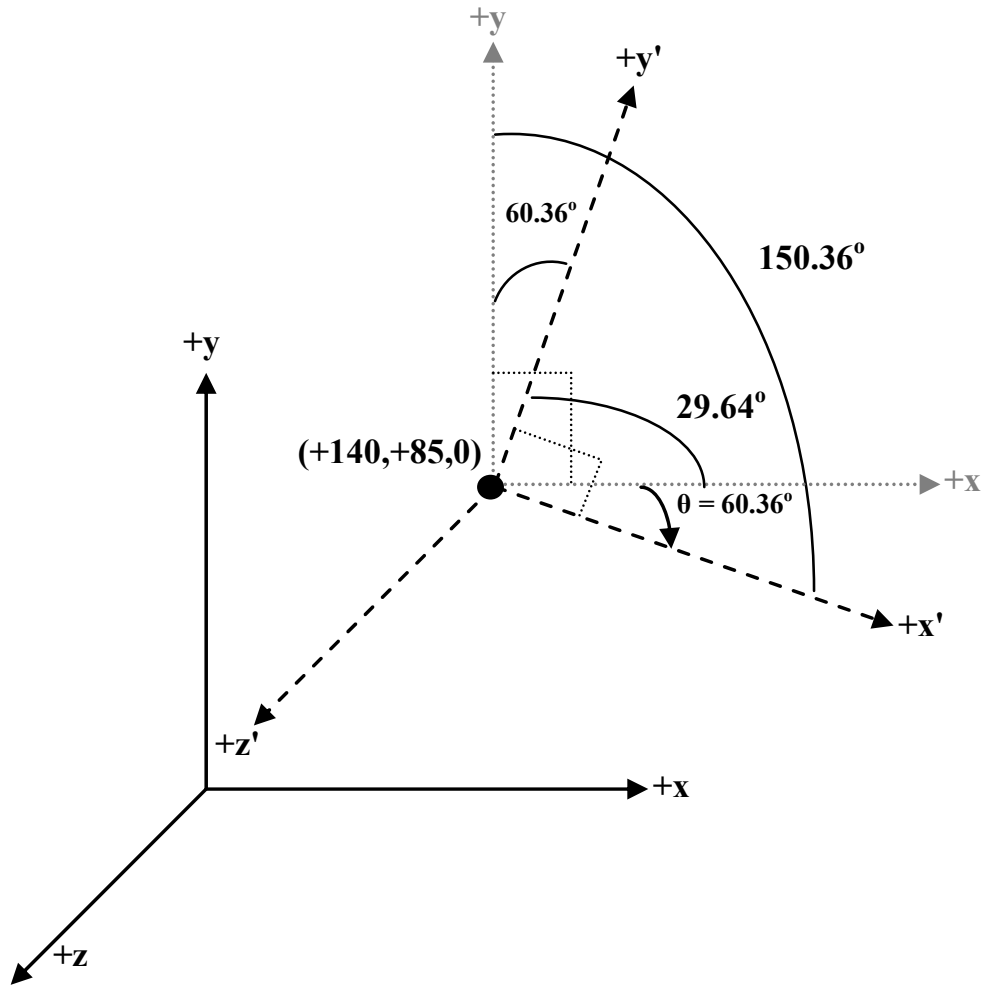


Figure D.6 - Incline 2 Coordinate System in Relation to that of the Default

Based on the contents of Figure D.6, the rotation matrix for the Incline 2 plane is shown in equation (D.5).

$$\begin{bmatrix} 140 \text{ cm} & 85 \text{ cm} & 0 \text{ cm} & 60.36^\circ & 150.36^\circ & 90^\circ & -29.64^\circ & 60.36^\circ & 90^\circ & 90^\circ & 90^\circ & 0^\circ \end{bmatrix} \quad (\text{D.5})$$

It is important to mention that the rotation of the Inclines shown in Figures D.5 and D.6 are independent of the sign of the angles specified between the +z and +z' axes and the +x and +y axes of the default and new coordinate system formed by the rotated Inclines. To understand why this is, consider the third entry in the angle array shown in equation (D.5) which corresponds to the angle between the +z and +x' axis. Of course, it has been mentioned that Inclines 1 and 2 are rotated about the +z axis and so the angle between the +x and +y axes of the default and new coordinates system formed by the rotated Inclines are perpendicular to the +z and +z' axes (note that since the Inclines are rotated about the +z axis, the z axis of the rotated Inclines, the +z' axis, will lie on top of the +z axis). With respect to the sign given to the 90° angle present between the +z and +x' axis, first consider Figure D.7.

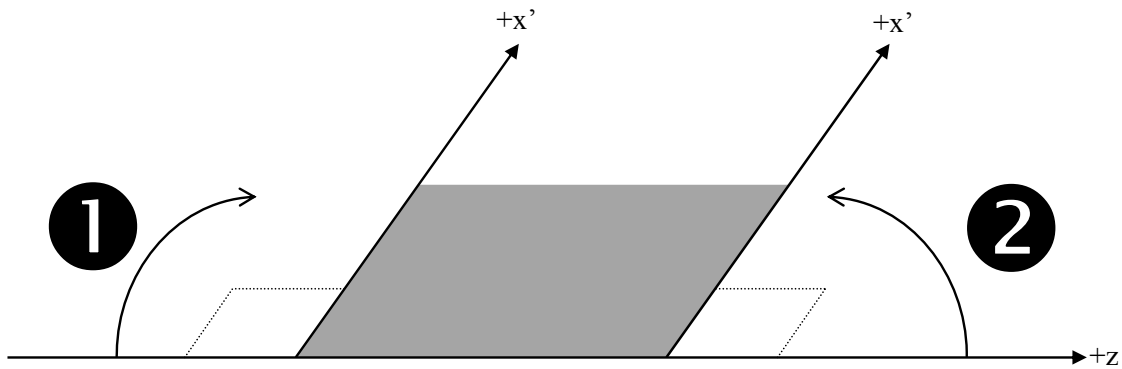


Figure D.7 - Orientation of a Plane Rotated About the +z Axis

Figure D.7 illustrates the two scenarios that are possible in regards to the sign assigned to the 90° angle present between the +z and +x' axis. As per the sign convention shown in Figure D.4, specifying an angle of $+90^\circ$ between the +z and +x' axis results in the first configuration shown in Figure D.7. Moreover, when an angle of -90° is specified between the +z and +x' axis, the second configuration shown in Figure D.7 arises. Nonetheless, it is shown in this figure that regardless of the sign of the angle specified between these axes, the orientation of the plane remains the same. This is the case not only with the angle between the +z and +x' axis, but also with all angles between the +x and +y axes of the default and new coordinate system of the rotated Inclines and the +z and +z' axes.

Now that a description of how the wind tunnel shell is modelled in the MCNPX environment, attention must now turn to constructing the plate and bluff body in MCNPX and this will be the subject of conversation in the next section.

D.2 Construction of the Plate and Bluff Body

As shown in the schematics in Appendix A, the plate and bluff body are rectangular parallelepipeds. To build such a volume in MCNPX, the following card is used:

RPP X_{min} X_{max} Y_{min} Y_{max} Z_{min} Z_{max}

The contents of the card shown above represent the lower and upper bounds of the spatial extents of the entity that the rectangular parallelepiped is created for. Via the schematics shown in Appendix A and in particular Table A.1 which identifies the spatial coordinates of the vertices of the plate and bluff body, the cards that must be declared for the plate and bluff body are respectively shown:

RPP 20 120 0 0.2 -572 -472

RPP 12 128 0 32 -588 -572

On this note, it was also mentioned in step 1 of Table D.1 that a 140 cm x 143 cm x 1004 cm rectangular parallelepiped be placed in the MCNPX model to represent the wind tunnel frame prior to the implementation of the inclines described in Section D.1. This frame is also constructed via the RPP card, and its entries are as follows:

```
RPP 0 140 0 143 -1004 0
```

A description of how the overall wind tunnel shown in Figure 3.8 is modelled in the MCNPX environment has been provided, whereby the manner in which the wind tunnel shell, plate, and bluff body are constructed in MCNPX has been documented. At this stage, the materials that these entities are composed of must be declared and the manner in which this is done is described in Tables B.4 and B.5. The material specifications in the aforesaid tables will allow the modeller to properly assign materials to these entities in the MCNPX environment.

APPENDIX E
DESCRIPTION OF TURBULENCE MODELS

Several mathematical models have been developed to model turbulent flow as an alternative to solving the Navier-Stokes equation. These models can be grouped into two categories: Reynolds-Averaged Navier Stokes (RANS) and Large Eddy Simulation (LES). These categories embody different computational approaches to modelling turbulent flow and their constituent turbulence models each possess a variation of the approach, which makes each model unique.

Reynolds-Averaged Navier-Stokes (RANS) Equations Models, pertain to models that solve the time-averaged Navier-Stokes equation. This time-averaged equation is formulated on the basis that each flow property, such as fluid pressure and fluid velocity, fluctuate about a mean value over time. The decomposition of each fluid property into a mean value and time-fluctuating component is substituted into the Navier-Stokes equation. The resultant equation, the time-averaged Navier-Stokes equation, results in additional terms, in comparison to the Navier-Stokes equation, that are a function of the time-dependent fluctuations of the fluid velocity, which constitute additional unknowns. These additional terms are called the *Reynolds Stresses*. The manner in which these additional terms are dealt with when solving the time-averaged Navier-Stokes equation for the mean value of each fluid property (herein known as *mean flow properties*) is dependent on the turbulence model employed.

Large Eddy Simulation (LES) is based on what is known as spatial filtering. Bearing in mind that a turbulent flow field consists of both small and large vortices (also known as eddies), the Large Eddy Simulation turbulence models employ a filter that essentially acts a threshold whereby eddies whose physical width exceeds this threshold are characterized by solving the “filtered” version of the Navier-Stokes equation (i.e., the Navier-Stokes equation subjected to a filter) whereas eddies whose physical width falls below the filter threshold are modelled via what is known as a sub-grid scale (SGS) model. There are several implementations of the sub-grid scale (SGS) model and each of these implementations is unique to a particular turbulence model.

Table E.1 provides a brief description of the constituent turbulence models in each of the abovementioned categories and Table E.2 outlines the applicability of these models to model specific flow scenarios. Note that the turbulence models discussed in these tables offer a non-exhaustive list of turbulence models that are available in FLUENT version 6.3 [27].

Of the turbulence models described in these tables, it is important to note that with the exception of the Reynolds Stress Model, the RANS turbulence models quantify the Reynolds Stresses via an *Eddy Viscosity*. The RANS turbulence model calculates the eddy viscosity in turn by computing a number of fluid related quantities, namely k (turbulent kinetic energy), ϵ (turbulent dissipation rate), and ω (specific dissipation rate). The Reynolds Stress Model, however, quantifies the Reynolds Stresses by solving transport equations for each Reynolds Stress.

Turbulence Model	Description
Reynolds-Averaged Navier-Stokes (RANS) Turbulence Models	
Spalart-Allmaras	The Spalart-Allmaras model employs a single transport equation that solves for a modified form of the eddy viscosity.
Standard k- ϵ (SKE)	The SKE model employs two transport equations that quantifies k and ϵ . The coefficients employed in these equations are empirically derived. The SKE model is valid only for fully turbulent flows.
Re-Normalization Group k- ϵ (RNG k- ϵ)	This is a variation of the SKE model whereby both the transport equations for k and ϵ and the coefficients employed by these equations are analytically derived. The changes found in the transport equation for ϵ improves the ability of the RNG k- ϵ turbulence model to model flows that possess large fluid velocity gradients.
Realizable k- ϵ (RKE)	The RKE model is another variation of the SKE model in that a different transport equation for ϵ is employed. Secondly, a coefficient found in the transport equations used by the RKE model is made to be a function of the mean flow and turbulence properties as opposed to being held constant, which is done in the SKE model [41].
Standard k- ω (SKO)	The SKO model employs two transport equations that quantifies k and ω . This model demonstrates superior performance for wall bounded and low Reynolds Number flow.
SST k- ω (SST KO)	The SST KO model is a variation of the SKO model whereby a combination of the Wilcox k- ω model to model flow in the vicinity of the walls of the flow domain and the Standard k- ϵ to model flow in the main flow stream is employed.
Reynolds Stress Model (RSM)	Instead of quantifying the Reynolds Stresses via the Eddy Viscosity, the RSM solves transport equations for each Reynolds Stress. The RSM is used for highly swirling flows.
Large Eddy Simulation (LES) Turbulence Models	
Detached Eddy Simulation (DES)	The DES model employs a hybrid approach to modelling turbulent flow whereby LES techniques are used to model flow in the main flow stream while techniques employed by the RANS turbulence models are used to model flow in the vicinity of the walls of the flow domain. More specifically, the DES model characterizes the flow in the near-wall region by using an approach based on the Spalart-Allmaras turbulence model.

Table E.1 – Description of Turbulence Models [27]

Turbulence Model	Description
Reynolds-Averaged Navier-Stokes (RANS) Turbulence Models	
Spalart-Allmaras	The Spalart-Allmaras turbulence model is designed specifically for aerospace applications. It performs poorly for three-dimensional flows but it suitable for use in mildly complex two-dimensional flow scenarios such as modelling flow past airfoils, wings, ship hulls, etc.
Standard k- ϵ (SKE)	The SKE turbulence model is a well established and widely validated turbulence model. The SKE model is the most widely-used turbulence model for modelling industrial flows and provides reasonably accurate flow field predictions. It performs well when modelling confined flows but it is not recommended for use in modelling flows that experience high fluid pressure gradients.
Re-Normalization Group k- ϵ (RNG k- ϵ)	The RNG k- ϵ model is appropriate for use when modelling flows involving moderate swirl and vortex production behind bluff bodies.
Realizable k- ϵ (RKE)	The RKE turbulence model offers the same benefits and has similar applications as the RNG k- ϵ turbulence model. The RKE turbulence model possibly offers more accurate flow field predictions and is easier to converge than the RNG k- ϵ turbulence model.
Standard k- ω (SKO)	The SKO turbulence model offers superior performance for wall-bounded and low Reynolds Number flow.
SST k- ω (SST KO)	The SST KO turbulence model offers similar benefits as the SKO model.
Reynolds Stress Model (RSM)	The RSM turbulence model is the most physically sound RANS model but requires more CPU time and memory. The RSM model is suitable for use when modelling three-dimensional flows with strong swirl/rotation.
Large Eddy Simulation (LES) Turbulence Models	
Detached Eddy Simulation (DES)	The DES turbulence model is suitable for use when modelling high Reynolds Number, wall bounded flows. DES is particularly useful for external aerodynamic applications such as modelling high Reynolds Number flow over bluff bodies.

Table E.2 – Applicability of Turbulence Models [27]

It is important to note that as one progresses down the list of turbulence models presented in Tables E.1 and E.2, there is an increase in computational cost per iteration [27].

APPENDIX F
DESCRIPTION OF METHODS FOR PARTICULATE TRANSPORT

The purpose of this appendix is to provide a review of methods employed for particulate transport and to assess the ability of these methods to provide realistic predictions for the transport of particulates. The two predominant methods are as follows:

- As discussed in Chapter 1, the present state-of-the-art computer codes that link particulate transport with radiation field determination (i.e. HPAC, CATS, and HOTSPOT) employ a Gaussian distribution as the basis for transporting particulates
- Particulate trajectory calculations in FLUENT employ a force-balance approach whereby the forces acting on a particulate are resolved in order to determine the movement of the particulate

The following two sections will discuss the above two particulate transport methods respectively, and this appendix will then conclude with a discussion on the ability of these methods to provide feasible particulate transport predictions.

F.1 Gaussian Plume Modelling

One of the most important accident scenarios that are considered when analyzing the safety of a nuclear installation is the release of radioactive material. A typical example of a release scenario is the discharge of radioactive particulates, contained in a plume, which emanates from an elevated structure such as a cooling tower at a nuclear power plant. Since this plume is exposed to the environment, it will be subjected to environmental phenomena such as wind. The abovementioned codes seek to model both the temporal and spatial variation of the radioactivity contained in the plume when exposed to wind.

In addition to wind speed and direction, the trajectory of the plume is also dependent on the stability of the atmosphere. To expound upon this, it is first important to mention the concept of the *inversion layer*. The exchange of energy between the atmosphere and the surface of the Earth causes the creation of large eddies (also known as vortices) and the region of space where these vortices are created is called the *Convective Boundary Layer (CBL)*. The CBL, which is situated in the vicinity of the Earth's surface, possesses air flow that is turbulent and thus fosters conditions that promote properties of air such as energy and momentum to be exchanged vertically. The upper extent of the CBL is termed the *inversion layer*, which denotes the region of space where the vertical mixing of air properties becomes limited [49].

To quantify the stability of the atmosphere, the *lapse rate* parameter is calculated, and its equation is shown below [49].

$$\Gamma = -\frac{dT}{dz} \tag{F.1}$$

Where:

- Γ = lapse rate (unit: $^{\circ}\text{C}\cdot\text{m}^{-1}$)
- T = air temperature (unit: $^{\circ}\text{C}$)
- z = altitude (unit: m)

As shown in equation (F.1), the lapse rate is defined as the rate of change of air temperature with elevation. When air expands with little to no exchange of heat with the surrounding air, the air is said to undergo adiabatic expansion. As such, when air adiabatically expands as it acquires higher elevation, the lack of heat addition to the air parcel causes the air temperature to decrease with increasing elevation. This fact is incorporated into the right hand side of equation (F.1), whereby the negative sign of the temperature gradient implies that the air temperature decreases with increasing elevation. From this equation, it is implied that a positive lapse rate indicates a decrease of air temperature with altitude while a negative lapse rate signifies an increase of air temperature with altitude.

Under dry conditions, when air expands adiabatically, the temperature of air decreases at a constant rate called the *dry adiabatic lapse rate*, and its approximate value is shown in equation (F.2) [49].

$$\Gamma_d = \frac{1^{\circ}\text{C}}{100\text{m}} \tag{F.2}$$

The dry adiabatic lapse rate is considered as an idealized reference value to compare with the environmental lapse rate (denoted by Γ_e), which represents the actual lapse rate being measured. When the temperature gradient is positive (and via equation (F.1), Γ_e is negative), vertical mixing is negligible and so the dispersion of radiation contained in the plume is minimal. This condition is particularly common during the winter season whereby as a result of the low dispersion of radioactive particulate contained in the plume, the spatial concentration of radiation is high.

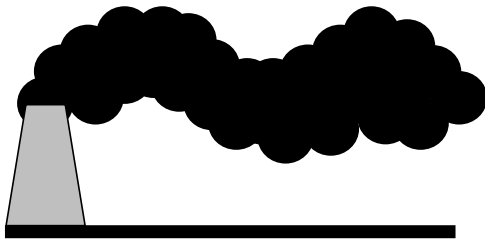
There are several regimes that govern the stability of the atmosphere, and these regimes are dependent upon the value of the environmental lapse rate in comparison to that of the dry adiabatic lapse rate. Table F.1 outlines the regimes that are encountered in the atmosphere in relation to the value of the environmental lapse rate.

Value of Environmental Lapse Rate	Stability of Atmosphere	Description
$\Gamma_e = \Gamma_d$	Neutral or Adiabatic	This condition is characterized by light winds and cloudy skies.
$\Gamma_e > \Gamma_d$	Super-Adiabatic	The environmental lapse rate is deemed to be strong and results in unstable conditions which foster good vertical mixing of radioactive particulates.
$0 < \Gamma_e < \Gamma_d$	Sub-Adiabatic	The environmental lapse rate is deemed to be weak and results in stable conditions. Here, vertical mixing of radioactive particulates is limited.

$\Gamma_e = 0$	Isothermal	This condition is characterized by stable conditions whereby vertical mixing of radioactive particulates is very limited.
$\Gamma_e < 0$	Thermal Inversion	This is a very stable condition and there is generally no vertical mixing of radioactive particulates.

Table F.1 – Atmospheric Stability as a Function of Environmental Lapse Rate [49]

As mentioned earlier, the trajectory of the plume is dependent on the atmospheric stability. The stability of the atmosphere also affects the shape of the plume and this relationship is described pictorially in Figure F.1.



Looping Plume
Unstable Conditions

Looping plumes occur under super-adiabatic conditions. The looping shape is attributed to the large vertical turbulences that are present in such regimes.



Coning Plume
Neutral Conditions

In neutral conditions, the shape of the plume is not confined by an inversion layer and expands outward from the top of the chimney stack.



Fanning Plume

Here, the plume is enclosed by an inversion layer. As a result, there is very little vertical mixing of radioactive particulates and the plume simply fans out with distance from the chimney.



Fumigation

An unstable regime exists below the inversion layer.



Lofting Plume

An inversion layer exists beneath the plume.

Figure F.1 – Relationship between Atmospheric Stability and Plume Shape [49]

In Figure F.1, it is shown that the presence of an inversion layer affects the shape of the plume. As stated earlier, an inversion layer is the region of space where very little vertical mixing of radioactive particulates occur. Hence, the plume shapes shown in Figure F.1 illustrate this fact since the spatial extent of the plume does not go beyond inversion layer demarcation(s).

It is evident that there are multiple factors that dictate the dispersion of radioactive particulates contained in the plume. The Gaussian plume model has emerged as the foremost tool that is employed to model the atmospheric dispersion of pollutants including radioactive particulates. Before the Gaussian *plume* model is shown, the Gaussian *puff* model must first be presented. A puff is essentially a physically smaller version of a plume and the equation used to model the dispersion of the pollutants contained in the puff serves as a stepping stone to derive the equation to model plume dispersion. The Gaussian puff model is shown in equation (F.3) [49].

$$\chi(x, y, z, t) = \frac{Q}{(2\pi)^{\frac{3}{2}}(\sigma_x\sigma_y\sigma_z)} \exp \left[- \left(\left(\frac{(x - \bar{u}t)^2}{2\sigma_x^2} \right) + \left(\frac{y^2}{2\sigma_y^2} \right) + \left(\frac{z^2}{2\sigma_z^2} \right) \right) \right] \quad (F.3)$$

Where:

$\chi(x, y, z, t)$ = concentration of pollutant at spatial position (x,y,z) at time t (unit: Bq·m⁻³·s⁻¹)

Q = pollutant source strength (unit: Bq·s⁻¹)

$$(\sigma_x, \sigma_y, \sigma_z) = (\sqrt{2K_x t}, \sqrt{2K_y t}, \sqrt{2K_z t})$$

σ_i is known as the *dispersion coefficient* of the plume in the ith direction. It is a function of the eddy diffusivity (denoted by K_i) in the ith direction.

Unit of σ_i : m

Unit of K_i : m²·s⁻¹

(x,y,z) = spatial coordinate of pollutant receptor (i.e., the spatial position where the pollutant concentration, χ , is measured)

Unit of (x,y,z): m

\bar{u} = mean wind velocity (unit: m·s⁻¹)

t = time (unit: s)

There are three important features of equation (F.3) that must be pointed out. The first is that this equation has been formulated on the basis that the mean wind velocity is constant. Secondly, the above equations assumes that the spatial diffusion of the pollutants contained within the plume is non-isotropic (i.e., the amount of diffusion of

pollutants in each spatial direction is different). Lastly, the value of the dispersion coefficients is attained in the following manner [49]:

- (1) Compute the environmental lapse rate
- (2) Using the environmental lapse rate, classify the atmospheric stability via what is known as the Pasquill-Gifford atmospheric stability categorization system
- (3) Knowing the stability category, compute the value of the dispersion coefficients via equations derived from tracer gas experiments. These equations are a function of several constants that are unique for each atmospheric stability category

Bearing the Gaussian puff model in mind, attention is turned to deriving the Gaussian plume model. As alluded to previously, a plume is considered to be an infinite number of puffs. The Gaussian plume model is developed based on the *slender plume approximation*, which is illustrated in Figure F.2.

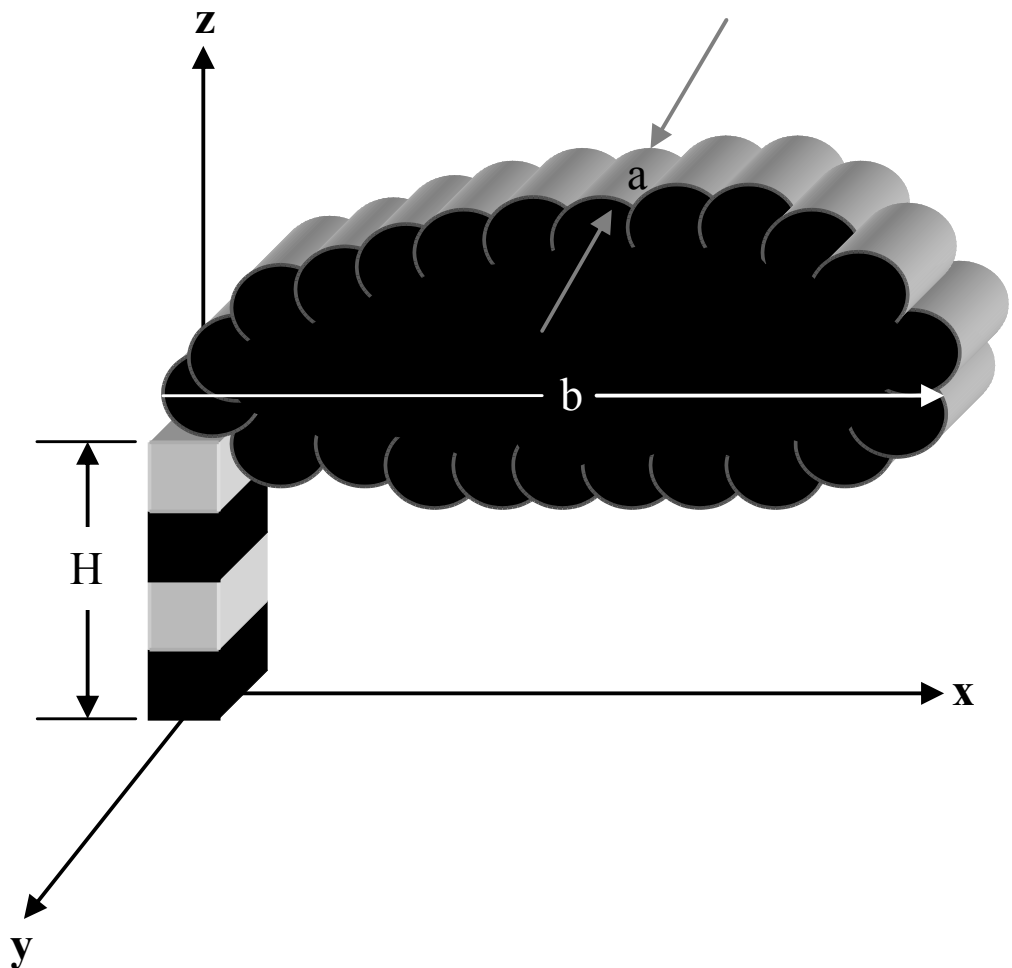


Figure F.2 – Illustration of Slender Plume Approximation [49]

In reference to Figure F.2, the slender plume approximation states that the spatial extent of the plume *about* the x axis (also known as the “spread”) is much smaller than the spatial extent of the plume *along* the x axis. In other words, the thickness of the plume, denoted by a , is much smaller than the length of the plume, denoted by b . This approximation gives the plume a “slender” shape.

Another aspect of plume transport that must be taken into account when developing the Gaussian plume model is the fact that plumes typically emanate from the top of structures, such as cooling towers and chimneys, that are elevated. As a result, the Earth’s surface acts as a physical barrier to the plume whereby there is no absorption or deposition of the pollutants contained in the plume into the surface of the Earth. In reference to Figure F.2, the Earth’s surface at $z=0$ is deemed to be totally reflecting of all pollutants contained in the plume. To ensure that this fact is incorporated into the Gaussian plume model, the reflection of the plume from the Earth’s surface is accounted for by calculating the pollutant concentration resulting from an imaginary source of an exact image of a real source. In other words, if a pollutant source is located at some elevation $z=H$ (as shown in Figure F.2), then an imaginary source will be placed at $z=-H$, which is located below the Earth’s surface [49].

The slender plume approximation and the pollutant source reflection boundary condition are incorporated into the Gaussian puff model, which then results in the Gaussian plume model (see equation (F.4) below) [49].

$$\chi(x, y, z, t) = \frac{Q}{2\pi\sigma_y\sigma_z\bar{u}} \left[\exp\left(-\frac{y^2}{2\sigma_y^2}\right) \right] \left[\exp\left(-\frac{(z-H)^2}{2\sigma_z^2}\right) + \exp\left(-\frac{(z+H)^2}{2\sigma_z^2}\right) \right] \quad (F.4)$$

Where:

- $\chi(x, y, z, t)$ = concentration of pollutant at spatial position (x,y,z) at time t (unit: $Bq \cdot m^{-3}$)
- H = effective height of pollutant source (unit: m)

The Gaussian plume model shown in equation (F.4) illustrates an important relationship in that the pollutant concentration is inversely proportional to the mean wind velocity. This relationship implies that the lower the mean wind velocity is, the less forceful the wind will be in dispersing the pollutants contained in the plume and thus a high spatial pollutant concentration will arise. Moreover, the greater the mean wind velocity is, the more forceful it is in dispersing the pollutants, resulting in low spatial pollutant concentration.

It is evident from the Gaussian plume model shown in equation (F.4) that the absence of any parameters pertaining to the physical, chemical, or radiological properties of the pollutant contained within the plume implies that the Gaussian plume model in the form shown in the abovementioned equation models the transport of inert pollutants. In reality, however, the pollutants will possess some form of toxicity and so the Gaussian plume model must be modified to reflect this. There are also other factors that play a prominent role in the transport of pollutant whose influence in this phenomenon must be incorporated into the Gaussian plume model. An example of such a factor is effect of complex terrain and buildings. Table F.2 summarizes the modifications that must be made to the Gaussian plume model in order to model a realistic pollutant transport scenario.

Modification	Description
Radioactive Decay	<p>A plume that contains radioactive pollutant will undergo radioactive decay. As such, the following correction factor must be calculated:</p> $C = e^{-\lambda\left(\frac{x}{u}\right)} \quad (F.5)$ <p>Where:</p> <p>C = correction factor</p> <p>λ = radioactive decay constant for the radionuclide that the pollutant is composed of (unit: s⁻¹)</p> <p>x = receptor distance from the pollutant source release point (unit: m)</p> <p>u = wind speed at the height of release (unit: m·s⁻¹)</p> <p>Once the correction factor is computed, it is then multiplied by either the pollutant source strength (Q) or the pollutant concentration (χ).</p>
Plume Rise	<p>Plumes emanating from elevated heights (such as from chimneys) may be released at high velocities or the density of the pollutants contained within the plume is lower than the surrounding air and so the plume is said to be buoyant. These two occurrences result in the plume rising to an elevation that is far greater than the chimney height. As a result, the effective release height (see equation (F.4)) may be much greater than the chimney height. The physical implication of this is that when one examines the pollutant concentration at a particular spatial location, the pollutant concentration will decrease when the effective release height is increased. This is due to the fact that a greater effective release height affords the pollutants to travel further before it reaches the ground, thereby allowing the pollutants more time to disperse before reaching the ground level. Thus, greater pollutant dispersion leads to lower pollutant concentration.</p> <p>When analyzing a plume transport scenario where there is potential for health and environmental hazards, it is important to ensure that the ground level pollutant concentration are as low as possible. Thus, this plume rise phenomenon must be taken into consideration such that an accurate effective height of release can be calculated.</p>
Complex Terrain and Effect of Buildings	<p>The presence of buildings will obstruct the wind flow, causing the formation of low-pressure vortices that form directly behind the building. These vortices will trap the pollutants, forming a region of high concentration of pollutants. Methods to account for complex terrain and buildings have been developed by Dupuis and Lipfert (1986) and Venkatram et al. (2001).</p>
Removal by Dry and Wet Deposition	<p><i>Dry Deposition</i> is where radioactive particulates are removed from the plume either by gravitational settling or when the plume impacts the Earth's surface. The dry deposition rate is calculated via equation (F.6).</p>

	<p>$D = v_g \chi$ (F.6)</p> <p>Where:</p> <p>D = dry deposition rate</p> <p>v_g = deposition velocity of particulates</p> <p>χ = pollutant concentration</p> <p>The deposition velocity is dependent on the physical characteristics of the particulates, meteorological conditions, and surface type.</p> <p><i>Wet Deposition</i> is the process by which radioactive particulates are removed from the plume from precipitation (such as rain and snow) via a “scavenging” process. This process is modelled via an exponential law shown in equation (F.7).</p> <p>$\chi_t = \chi_0 e^{-\Lambda t}$ (F.7)</p> <p>Where:</p> <p>χ_t = concentration of radioactive pollutant after time t</p> <p>χ_0 = original concentration of radioactive pollutant</p> <p>Λ = wash-out coefficient (this is dependent on rainfall and particulate size)</p> <p>t = time</p>
Resuspension of Particulates	<p>Radioactive particulates that settle on the ground can be resuspended especially under dry and windy conditions. The radioactive pollutant concentration in air that arises from resuspension is a function of the radioactive pollutant concentration on the ground via what is known as a <i>resuspension factor</i>. This is stated mathematically in equation (F.8).</p> <p>$\chi_a(t) = K(t)C_S$ (F.8)</p> <p>Where:</p> <p>$\chi_a(t)$ = radioactive pollutant concentration in air at time t (unit: Bq·m⁻³)</p> <p>K(t) = resuspension factor at time t (unit: m⁻¹)</p> <p>C_S = radioactive pollutant concentration on the ground (unit: Bq·m⁻²)</p> <p>t = time</p> <p>Resuspension phenomenon is a function of time and as such, the radioactive pollutant concentration in air (i.e. the concentration due to resuspension) and the resuspension factor, which determines how much radioactive particulates will be resuspended, are both dependent on time. The quantity that is not time-dependent is the radioactive pollutant concentration on</p>

	<p>the ground. The reason being is that this concentration represents the amount of radioactive particulates present on the ground prior to the introduction of a resuspension agent (such as wind).</p> <p>Further to what was described about the resuspension factor, information on quantifying this parameter can be found in Nair et al. (1997).</p>
--	--

Table F.2 – Description of Modifications made to the Gaussian Plume Model for Realistic Pollutant Transport Scenarios [49]

The Gaussian plume model has been presented along with modifications that must be made to the model in order to analyze realistic pollutant transport scenarios. The next section examines the method by which particulate transport is conducted via CFD techniques.

F.2 FLUENT Particulate Trajectory Calculations

A force-balance approach serves as the basis by which FLUENT particulate trajectory calculations are performed. As stated earlier, FLUENT resolves the forces acting on a particulate in order to determine the trajectory of that particulate. It is essential that the forces acting on a particulate be described, and they are as follows:

- When a particulate is being displaced by a flow field, it will experience a change in velocity. This change in velocity is embodied by the *force due to acceleration*
- Lift and drag forces act on a particulate, and of these forces, the *drag force* plays a more dominant role in the resuspension of a particulate
- The *force due to gravity* also acts on a particulate and it affects the ability of the particulate to remain in suspension

In the context of particulate transport, Newton’s second law states that the net external force acting on a particulate is equivalent to the mass of the particulate multiplied by its acceleration. In terms of the forces outlined above, the *force due to acceleration* is equal to the sum of the *drag force* and the *force due to gravity*. FLUENT incorporates this statement by employing equation (F.9) for particulate transport.

$$\underbrace{\frac{du_p}{dt}}_{\text{Force due to Acceleration}} = \underbrace{F_D(u - u_p)}_{\text{Drag Force}} + \underbrace{g \left(1 - \frac{\rho}{\rho_p} \right)}_{\text{Force due to Gravity}} \tag{F.9}$$

Where:

- u_p = particulate velocity (unit: $m \cdot s^{-1}$)
- u = fluid velocity (unit: $m \cdot s^{-1}$)

$$\begin{aligned}
F_D &= \text{drag force (unit: N)} \\
g &= -9.81 \text{ m}\cdot\text{s}^{-2} \text{ (acceleration due to gravity)} \\
\rho &= \text{density of fluid (unit: kg}\cdot\text{m}^{-3}\text{)} \\
\rho_p &= \text{density of particulate (unit: kg}\cdot\text{m}^{-3}\text{)}
\end{aligned}$$

Note that each of the forces stated in equation (F.9) are normalized to the mass of the particulate and that air is the fluid used for the CFD-MC radiation transport coupling methodology described in Chapter 3.

The drag force shown in equation (F.9) is given by equation (F.10) [43].

$$F_D = \left(\frac{18\mu}{\rho_p D_p^2} \right) \left(\frac{1}{24} C_D \text{Re}_p \right) \quad (\text{F.10})$$

Where:

$$\begin{aligned}
\mu &= \text{dynamic viscosity of fluid (unit: Pa}\cdot\text{s)} \\
D_p &= \text{diameter of particulate (unit: m)} \\
C_D &= \text{drag coefficient} \\
\text{Re}_p &= \text{particulate Reynolds Number}
\end{aligned}$$

The particulate Reynolds Number shown in equation (F.10) is given by equation (F.11) [43].

$$\text{Re}_p = \frac{\rho D_p |u_p - u|}{\mu} \quad (\text{F.11})$$

The drag coefficient shown in equation (F.10) is given by equation (F.12) [43].

$$C_D = a_1 + \frac{a_2}{\text{Re}_p} + \frac{a_3}{\text{Re}_p^2} \quad (\text{F.12})$$

Note that a_1 , a_2 , and a_3 , are constants that apply to smooth spherical particulates for wide ranges of Re_p .

Equations (F.9) to (F.12) are used to compute the particulate velocity. Once this quantity is known, the particulate trajectory is found by integrating equation (F.13) with respect to time [43].

$$u_p = \frac{dL_T}{dt} \quad (\text{F.13})$$

Where:

$$L_T = [L_{Tx}, L_{Ty}, L_{Tz}]$$

L_T represents the particulate trajectory and is a vector quantity that consists of three components. L_{Tx} , L_{Ty} , and L_{Tz} represent the trajectory of the particulate in the x, y, and z directions, respectively.

The manner in which FLUENT conducts particulate trajectory calculations has been outlined. Since FLUENT quantifies the forces acting on a particulate such that the trajectory can be computed makes it evident that the complete physical lifecycle of each individual particulate is followed in FLUENT.

The next section will conclude this appendix and will discuss the feasibility of each of the two particulate transport methods to provide realistic predictions of particulate transport.

F.3 Feasibility Analysis

Bearing in mind the two particulate transport methods discussed, a discussion on the ability of these models to produce realistic predictions of particulate transport must now ensue. With respect to the Gaussian plume model, it is an established tool employed for the atmospheric transport of pollutants such as radioactive particulates. This model inherently seeks to examine a scenario whereby a plume containing pollutant emanates from the top of an elevated structure and is then displaced over a flat terrain by environmental phenomena such as wind. However, it has been documented in Section F.1 that the plume model in the form shown in equation (F.4) cannot model a realistic particulate transport scenario namely the particulate transport in the vicinity of buildings and over complex terrain. Thus, modifications are required to be made to the Gaussian plume model, and these modifications are described in Table F.2.

The second particulate transport method involves the use of CFD techniques as the basis for particulate trajectory calculations. As shown in Chapter 3, CFD codes permit the user to define a geometry in which there will be fluid flow and to specify attributes of a resuspension problem, namely the number of particulates that will be placed in the flow domain and their respective diameters and the spatial locations that each particulate will be placed at. Once the CFD code calculates a converged flow field, the flow field will then be used to displace (i.e. resuspend) the particulates initially placed in the flow domain. As documented in Section F.2, the forces acting on each particulate are resolved, which will then enable the calculation of the particulate's trajectory. It is therefore evident that the method by which particulate transport is quantified via CFD techniques (see Section F.2) is much different than that employed by the Gaussian plume model in that no modifications are required to be made to the particulate transport method employed by FLUENT. Rather, the complexities involved in a realistic particulate transport scenario are built-in to the manner in which particulate transport is conducted in the CFD environment.

In light of the analysis conducted in this section, it is clear that the method by which FLUENT performs particulate trajectory calculations provides a more realistic assessment of particulate transport in resuspension problems.

APPENDIX G
CONVERSION OF PARTICULATE SPATIAL DISTRIBUTION TO ACTIVITY

The purpose of this appendix is to derive a mathematical expression that calculates the activity of a particulate composed of Lanthanum-140. This appendix is divided in two parts, the first containing the derivation of this equation and the second containing a unit analysis of the derived equation.

G.1 Derivation of Activity Equation

To begin, the first order equation for activity is defined as:

$$A_{\text{particulate}} = \lambda_{140\text{La}} N_{140\text{La}} \quad (\text{G.1})$$

Where:

$$\begin{aligned} \lambda_{140\text{La}} &= \text{decay constant for Lanthanum-140 (unit: s}^{-1}\text{)} \\ N_{140\text{La}} &= \text{number density of Lanthanum-140 (unit: nuclei}\cdot\text{cm}^{-3}\text{)} \end{aligned}$$

The equation for the decay constant is found in equation (G.2).

$$\lambda_{140\text{La}} = \frac{\ln(2)}{T_{1/2}({}^{140}\text{La})} \quad (\text{G.2})$$

Where:

$$T_{1/2}({}^{140}\text{La}) = \text{half life of Lanthanum-140 (unit: s)}$$

The equation for the number density is stated in equation (G.3).

$$N_{140\text{La}} = \frac{N_A \rho_{140\text{La}}}{M_M^{140\text{La}}} \quad (\text{G.3})$$

Where:

$$\begin{aligned} N_A &= 6.02 \times 10^{23} \text{ nuclei}\cdot\text{mol}^{-1} \text{ (Avogadro's Constant)} \\ \rho_{140\text{La}} &= \text{density of Lanthanum-140 (unit: g}\cdot\text{cm}^{-3}\text{)} \\ M_M^{140\text{La}} &= \text{molar mass of Lanthanum-140 (unit: g}\cdot\text{mol}^{-1}\text{)} \end{aligned}$$

If one were to substitute equations (G.2) and (G.3) into equation (G.1), the activity will have the following unit:

$$\begin{aligned} [A_{\text{particle}}] &= [\lambda_{140\text{La}} [N_{140\text{La}}]] \\ [A_{\text{particle}}] &= [\text{s}^{-1}] [\text{nuclei} \cdot \text{cm}^{-3}] = [\text{nuclei} \cdot \text{cm}^{-3} \cdot \text{s}^{-1}] \end{aligned}$$

This unit of activity is incorrect as there is a volume quantity in the denominator of the unit. To correct this, the right hand side of equation (G.1) must be multiplied by some volume quantity. Since the objective is to calculate the activity of a particulate composed of Lanthanum-140, the right hand side of equation (G.1) will be multiplied by the particulate volume, as shown in equation (G.4).

$$A_{\text{particulate}} = \lambda_{140\text{La}} N_{140\text{La}} \forall_{\text{particulate}} \quad (\text{G.4})$$

Where:

$$\forall_{\text{particulate}} = \text{volume of particulate (unit: cm}^3\text{)}$$

The particulates simulated in FLUENT are spherical and as such, the particulate volume is given by equation (G.5).

$$\forall_{\text{particulate}} = \frac{4}{3} \pi r_{\text{particulate}}^3 \quad (\text{G.5})$$

Where:

$$r_{\text{particulate}} = \text{radius of particulate (unit: cm)}$$

Since FLUENT employs diameter as the defining characteristic of a particulate, equation (G.5) will be restated with the particulate diameter instead of radius. Equation (G.6) relates these two quantities.

$$r_{\text{particulate}} = \frac{1}{2} D_{\text{particulate}} \quad (\text{G.6})$$

Where:

$$D_{\text{particulate}} = \text{diameter of particulate (unit: cm)}$$

Substitute equation (G.6) into (G.5).

$$\forall_{\text{particulate}} = \frac{4}{3} \pi \left(\frac{1}{2} D_{\text{particulate}} \right)^3$$

Simplifying the above expression yields:

$$V_{\text{particulate}} = \frac{1}{6} \pi D_{\text{particulate}}^3 \quad (\text{G.7})$$

To find the final expression for activity, substitute equations (G.2), (G.3), and (G.7) into equation (G.4).

$$A_{\text{particulate}} = \left(\frac{\ln(2)}{T_{1/2}({}^{140}\text{La})} \right) \left(\frac{N_A \rho_{{}^{140}\text{La}}}{M_M({}^{140}\text{La})} \right) \left(\frac{1}{6} \pi D_{\text{particulate}}^3 \right)$$

Simplifying the above expression yields:

$$A_{\text{particulate}} = \frac{1}{6} \pi D_{\text{particulate}}^3 \left(\frac{\ln(2)}{T_{1/2}({}^{140}\text{La})} \right) \left(\frac{N_A \rho_{{}^{140}\text{La}}}{M_M({}^{140}\text{La})} \right)$$

(G.8)

G.2 Unit Analysis of Activity Equation

To ensure equation (G.8) yields the correct unit for activity, a dimensional analysis will be performed whereby the units of each variable on the right hand side will be substituted into equation (G.8).

$$[A_{\text{particulate}}] = [D_{\text{particulate}}^3] \cdot \frac{1}{\left[T_{1/2}({}^{140}\text{La}) \right]} \cdot \frac{[N_A] [\rho_{{}^{140}\text{La}}]}{[M_M({}^{140}\text{La})]}$$

$$[A_{\text{particulate}}] = [\text{cm}^3] \cdot \frac{1}{[\text{s}]} \cdot \frac{[\text{nuclei} \cdot \text{mol}^{-1}] [\text{g} \cdot \text{cm}^{-3}]}{[\text{g} \cdot \text{mol}^{-1}]}$$

$$[A_{\text{particulate}}] = [\text{nuclei} \cdot \text{s}^{-1}] \quad (\text{G.9})$$

The unit of activity is the Becquerel. Being the SI unit of activity, a Becquerel is equivalent to one radioactive decay per second. Each nuclei in a radioactive material will undergo radioactive decay at any given time. As a result, one can create a conversion factor of 1 nuclei = 1 decay. This can then be applied to equation (G.9):

$$[A_{\text{particulate}}] = [\text{nuclei} \cdot \text{s}^{-1}] [\text{decay} \cdot \text{nuclei}^{-1}]$$

$$[A_{\text{particulate}}] = [\text{decays} \cdot \text{s}^{-1}] \quad (\text{G.10})$$

Thus, the units displayed on the right hand side of equation (G.10) are equivalent to the Becquerel and as such equation (G.8) does yield the correct unit of activity.

A Becquerel is typically a small measure of activity and as such, multiples of Becquerel are used. The Curie is an older unit of activity (used prior to the introduction of Becquerel) and it represents a larger quantity of activity. The equivalency between these two units is shown in equation (G.11).

$$1 \text{ Ci} = 3.7 \times 10^{10} \text{ Bq} \tag{G.11}$$

APPENDIX H

DESCRIPTION OF MONTE CARLO APPROXIMATIONS TO RADIATION TRANSPORT EQUATIONS

A transport equation seeks to account for each radioactive particle that enters, resides, and leaves an arbitrary volume of space at any given time. In other words, a transport equation essentially performs a radioactive *particle balance* in that it calculates the number of radioactive particles that resides in an arbitrary volume of space at any given time. The MC approach does not solve the actual transport equation, rather approximations are made to the transport equation. These approximations are a set of mathematical equations that are used in concert such that radioactive particle transport is simulated on a point-by-point basis [35]. The MC technique allows for one to capture the history of a particle as it moves through a medium. This history commences from the birth of a particle and ends with its death. A defining characteristic of the MC technique is that the mathematical approximations made to the transport equations employ random numbers (extracted from probability distributions) such that a probabilistic description of what happens to a radioactive particle at each point in its history is made.

Before a description of how a transport equation is formulated, consider Figure H.1 which illustrates how a radioactive particle interacts with a medium composed of some material. Note that this discussion applies for all radiation types.

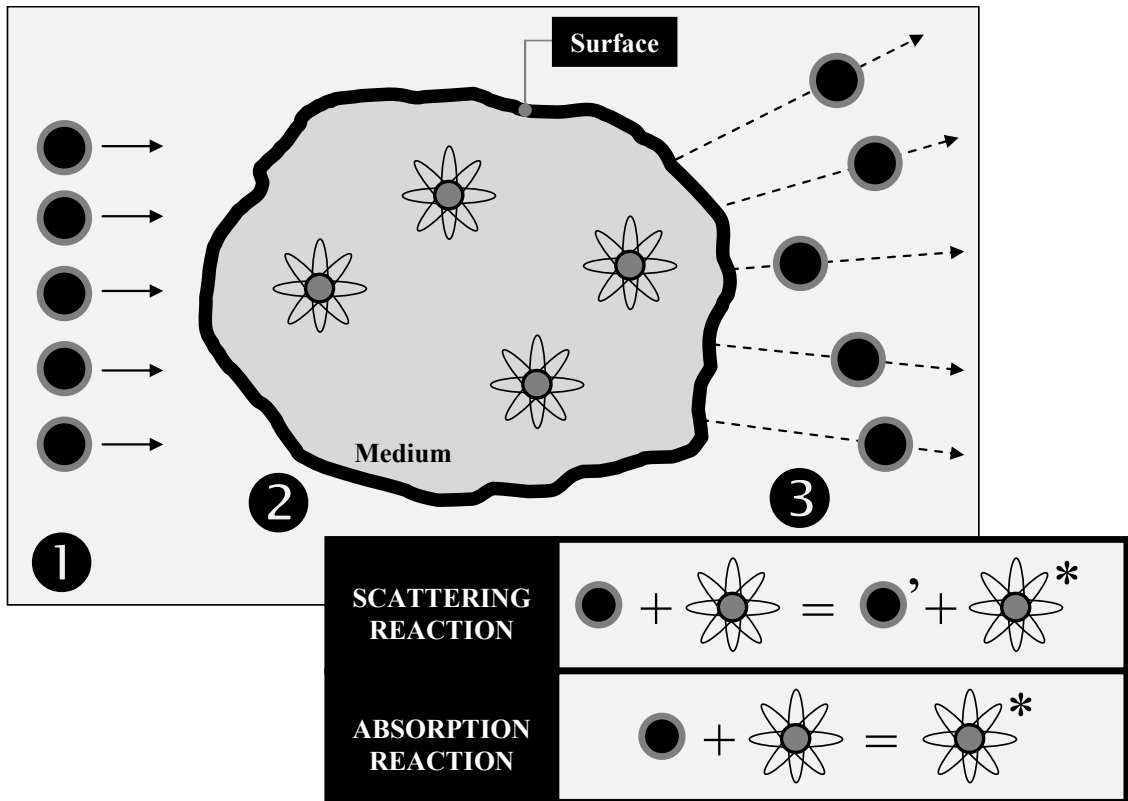


Figure H.1 – Illustration of Radiation Interaction with Matter

Figure H.1 illustrates the basic steps in the interaction of radiation with matter, and are further described in Table H.1.

Step	Description
1	Radioactive particles enter the medium.
2	<p>Bearing in mind that the medium is composed of some material, when a radioactive particle interacts with the atoms of the host material, there are three types of reactions that can occur:</p> <p>(1) <i>Scattering Reaction</i> The scattering reaction is illustrated in the upper portion of the inset in Figure H.1. Here, the radioactive particle interacts with an atom of the host material and imparts <i>some</i> of its kinetic energy to the atom. After the interaction takes place, the radioactive particle acquires a decreased kinetic energy. The radioactive particle can undergo further scattering reactions until it loses all its kinetic energy and subsequently ceases to exist or it does not interact with anymore atoms and escapes the material.</p> <p>(2) <i>Absorption Reaction</i> The absorption reaction is illustrated in the lower portion of the inset in Figure H.1. Here, the radioactive particle interacts with an atom of the host material and imparts <i>all</i> of its kinetic energy to the atom. The radioactive particle ceases to exist thereafter.</p> <p>(3) <i>No Reaction</i> The radioactive particle does not interact with the material atoms and escapes the material.</p>
3	The radioactive particle escapes the material only if it retains enough kinetic energy after undergoing multiple scattering reactions or if it does not interact with any of the material atoms. When a particle escapes the material, it must have a kinetic energy that is greater than what is known as the <i>thermal energy</i> . The thermal energy acts as a threshold in that if a radioactive particle possesses kinetic energy above the thermal energy, it is considered to be existent. Otherwise, the radioactive particle ceases to exist.

Table H.1 – Description of the Basic Steps of Radiation Interaction with Matter

It is important to mention that in the scattering and absorption reactions described in Table H.1, these reactions involve the *incident* radioactive particle imparting either some or all of its kinetic energy to an atom of the host material. The atom with this excess energy is said to be in an *excited state* and will seek to get rid of this excess energy (i.e. return to the ground state) by emitting a radioactive particle. This emitted radioactive particle is called a *secondary* radioactive particle.

Based on what was discussed in Figure H.1 and Table H.1, a basic description of the contents of a transport equation can now be provided. As stated earlier, the transport equation keeps a record of how many radioactive particles resides in an arbitrary volume of space at any given time. In reference to Figure H.1, the qualitative

interpretation of a transport equation is described in Figure H.2. Note that in Figure H.2, n denotes the density of particles within the volume of space for which the transport equation is analyzing.

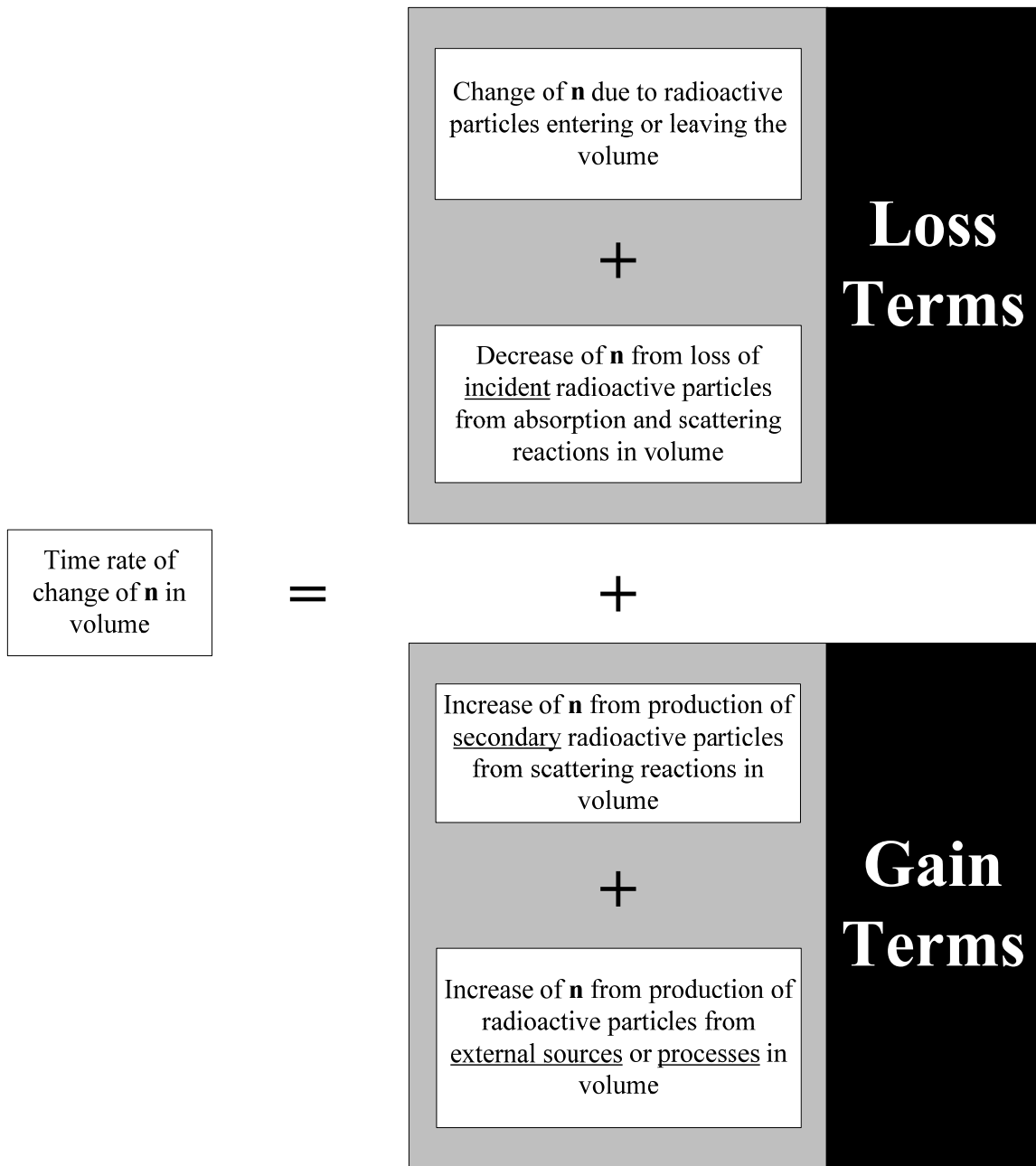


Figure H.2 – Qualitative Description of a Transport Equation

With respect to the last quantity in the “Gain Terms” shown in Figure H.2, *external sources* are those that supply radioactive particles to the volume of space being analyzed. An example of an external source, if one is analyzing the transport of neutrons for example, is a beam that produces neutrons which are then directed into the volume of space being analyzed. Moreover, *processes* are those that produce radioactive particles from nuclear processes. In the case of neutrons, an example of such a process is *fission*. Fission is the means by which thermal

power is created in a nuclear reactor (which is then converted to electric power) and so it lies at the heart of nuclear power production. In the fission process, a neutron interacts with the nuclear fuel that is placed in the nuclear reactor. The neutron interacts with the ^{235}U isotope that is contained in the fuel, which then results in the “fissioning” (i.e. fragmentation) of the ^{235}U isotope into smaller elements (known as *fission products*) plus the production of two to three neutrons. Thus, the introduction of one neutron into the fission process produces two to three neutrons.

It is important to state that due to the differences between each radiation type outlined in Table 2.11, the transport equation for each radiation type will be different. One of the reasons for this is the fact that charged particles interact differently with matter than neutral particles since the former particle type will actively interact with the electric field of the electron shells of the host material atoms. As such, the transport equations must account for such interactions. Nonetheless, what has been described about transport equations thus far is applicable to all radiation types since the discussion up to this point describes the transport equation as one that keeps track of the number of radioactive particles that reside in an arbitrary volume of space at a particular time by accounting for the general phenomena that increase or decrease the population of radioactive particles in this volume (such as absorption and scattering reactions – reactions that all radioactive particles participate in).

Now that a qualitative description of a transport equation has been discussed, a mathematical description of a transport equation will now be provided. One of the most important radiation transport equations in the field of Nuclear Engineering is the neutron transport equation. In reference to Figure H.2, this equation is shown below [47].

$$\underbrace{\frac{\partial}{\partial t} (n(\vec{r}, v, t))}_{\substack{\text{Time rate of change} \\ \text{of neutron density} \\ \text{in volume}}} = \underbrace{\underbrace{-v\nabla n(\vec{r}, v, t)}_{\substack{\text{Neutrons entering} \\ \text{or leaving volume}}} - \underbrace{v \sum_{\text{total}}(\vec{r}, v)n(\vec{r}, v, t)}_{\substack{\text{Loss of incident neutrons} \\ \text{from absorption and scattering reactions}}}}_{\text{Loss Terms}} + \underbrace{\int v' \Sigma_{\text{scatter}}(\vec{r}, v' \rightarrow v)n(\vec{r}, v', t)dv' + \nu \int v' \Sigma_{\text{fission}}(\vec{r}, v' \rightarrow v)n(\vec{r}, v', t)dv' + Q(\vec{r}, v, t)}_{\substack{\text{Creation of secondary neutrons} \\ \text{from scattering reactions} \quad \quad \quad \text{Creation of neutrons from fission} \quad \quad \quad \text{Creation of neutrons} \\ \text{from external sources}}}}_{\text{Gain Terms}} \quad \quad \quad \text{(H.1)}$$

Where:

- $n(\vec{r}, v, t)$ = density of neutrons at spatial position \vec{r} , that possess a velocity v , at time t (unit: neutrons·cm⁻³)
- \vec{r} = spatial position at which neutron population is being analyzed
- t = time (unit: s)
- v' = velocity of neutron prior to interacting with host material atom (unit: cm·s⁻¹)
- v = velocity of neutron after interacting with host material atom (unit: cm·s⁻¹)
- ν = 2-3 (number of neutrons produced from fission process)

$$\Sigma_{\text{total}}(\vec{r}, v) = \Sigma_{\text{absorption}}(\vec{r}, v) + \Sigma_{\text{scattering}}(\vec{r}, v)$$

Where:

$\Sigma_{\text{total}}(\vec{r}, v) =$ macroscopic total cross section at spatial position \vec{r} , neutron velocity v (unit: cm^{-1})

$\Sigma_{\text{absorption}}(\vec{r}, v) =$ macroscopic absorption cross section at spatial position \vec{r} , neutron velocity v (unit: cm^{-1})

$\Sigma_{\text{scatter}}(\vec{r}, v) =$ macroscopic scattering cross section at spatial position \vec{r} , neutron velocity v (unit: cm^{-1})

$\Sigma_{\text{fission}}(\vec{r}, v) =$ macroscopic fission cross section (unit: cm^{-1})

$Q(\vec{r}, v, t) =$ external neutron source strength at spatial position \vec{r} , neutron velocity v , and at time t (unit: $\text{neutrons} \cdot \text{cm}^{-3} \cdot \text{s}^{-1}$)

It is important to recognize the fact that the macroscopic cross sections stated in equation (H.1), namely the absorption, scattering, and fission cross sections (herein collectively known as the *cross section*; the total macroscopic cross section is excluded from this discussion since it is simply the sum of absorption and scattering cross sections), essentially represents the probability that a neutron will undergo a reaction for which the cross section is corresponding to. For example, the macroscopic absorption cross section represents the probability that a neutron will undergo an absorption reaction, and so on. Another property of the cross section that must be discussed is its dependence on the position in space whose neutron density is being analyzed and the neutron velocity. These dependencies are explained below:

- The cross section's dependence on spatial position is really meant to convey that the value of the cross section is a function of the material that the volume in space for which the spatial position is located in is composed of. This illustrates the fact that the value of the cross section varies from material to material. Oftentimes, nuclear systems are composed of different material types and so when quantifying the neutron population in the system via solving the neutron transport equation, knowledge of the spatial placement of materials will aid this process.
- The neutron velocity also influences the value of the cross section. The reason being is that the velocity at which the neutron approaches an atom will affect its ability to undergo an absorption, scattering, or fission reaction. To understand the concept, consider the manner in which a neutron approaches an atom. If it moves at a very high velocity, the cross section (i.e. the probability of reaction) is small since the neutron will not move slow enough to fully interact with the atom. If the neutron moves slower, however, the cross section will be higher since the neutron will be better able to focus its trajectory squarely on the atom.

Bearing in mind the mathematical description of the neutron transport equation, an explanation of how MC approximations are made to quantify neutron transport will now be discussed. To illustrate how such approximations are formulated, two-dimensional neutron transport in a slab of material will be analyzed. Central to the derivation of the MC model for two-dimensional neutron transport is the use of *billiard ball kinematics*, which is described in Figure H.3.

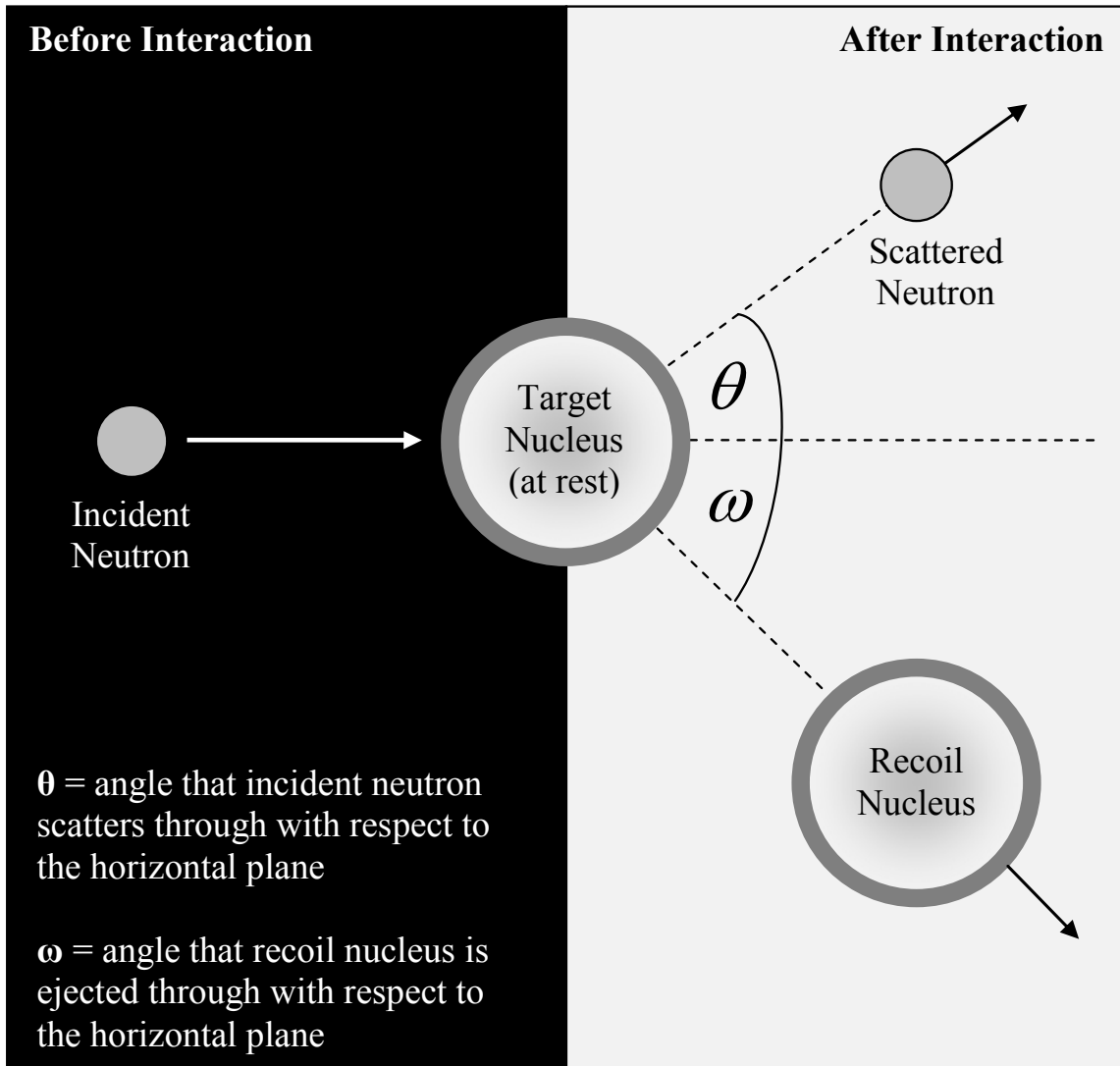


Figure H.3 – Illustration of Billiard Ball Kinematics [47]

As shown in Figure H.3, billiard ball kinematics state that neutrons interact with the nucleus of a host material atom by bouncing off the nucleus. In essence, this constitutes a scattering reaction since the neutron will impart some of its kinetic energy to the target nucleus, and “scatters” into another direction. The target nucleus will also be affected by this reaction whereby it will recoil into direction different than that of the scattered neutron.

The MC model used to describe neutron transport in a two-dimensional slab is recursive in nature. More specifically, the properties of the neutron, namely position and kinetic energy, at a particular point in its history is dependent on the value of these properties at the previous point in its history. Figure H.4 illustrates this feature of the MC model.

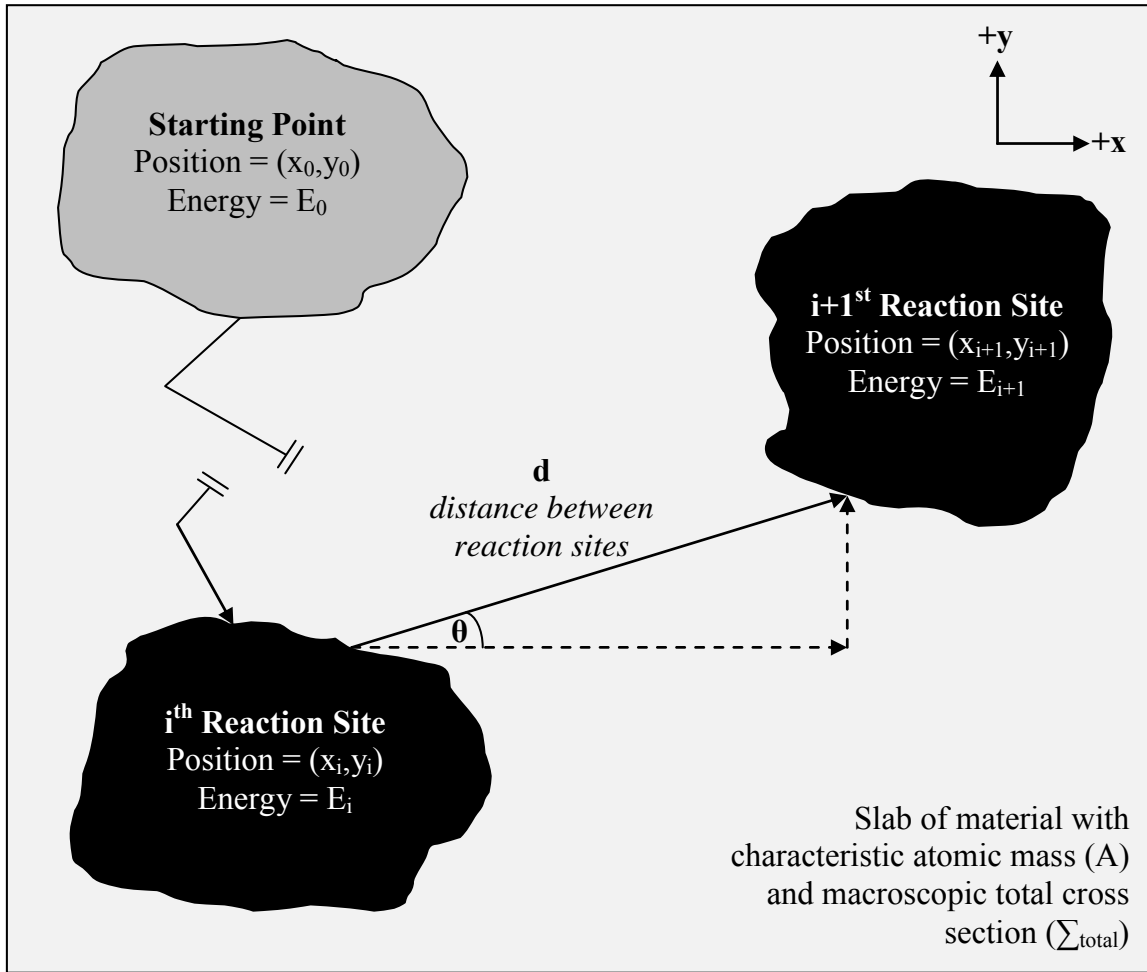


Figure H.4 – Illustration of the Recursive Nature of MC Neutron Transport Modelling

It is clear from Figure H.4 that initial conditions must be provided to the properties of each neutron that is being transported within the slab of material. The MC model that describes neutron transport in a two-dimensional slab of material will now be presented in Table H.2, in reference to Figure H.4.

Quantity	Equation	Equation Number
Neutron kinetic energy at $(i+1)^{\text{st}}$ reaction site	$E_{i+1} = E_i \left(\frac{1}{A+1} \right)^2 \left((1-2p_1) + \sqrt{(1-2p_1)^2 + A^2 - 1} \right)^2$	(H.2)
Distance between reaction sites	$d = \left(\frac{1}{\Sigma_{\text{total}}(E_i, \text{material})} \right) \ln(1-p_2)$	(H.3)
x-position of the neutron at the $(i+1)^{\text{st}}$ reaction site	$x_{i+1} = x_i + d(1-2p_1)$	(H.4)

y-position of the neutron at the $i+1^{\text{st}}$ reaction site	$y_{i+1} = y_i + \left(\sqrt{d^2 - (x_{i+1} - x_i)^2} \right) \left(\frac{p_3 - 0.5}{ p_3 - 0.5 } \right)$	(H.5)
--	--	-------

Where:

E_i = neutron kinetic energy at i^{th} reaction site (unit: MeV)

d = distance between reaction sites (unit: cm)

x_i = x-position of the neutron at the i^{th} reaction site (unit: cm)

y_i = y-position of the neutron at the i^{th} reaction site (unit: cm)

A = atomic mass of the host material (unit: atomic mass unit (amu))

Σ_{total} = macroscopic total cross section (unit: cm^{-1})

p_1, p_2, p_3 = random numbers that are uniformly distributed on the interval $[0,1)$

Table H.2 – MC Model for Neutron Transport in a Two-Dimensional Slab [50]

Note that the macroscopic total cross section shown in the denominator of equation (H.3) is a function of the neutron kinetic energy at the i^{th} reaction site. As described previously, the cross section was stated to be a function of the neutron velocity. The neutron velocity and neutron kinetic energy are directly proportional to one another and so it follows that the cross section can be dependent on either neutron velocity or neutron kinetic energy.

The equations shown in Table H.2 are used in the order shown to collectively describe the transport of neutrons in a two-dimensional slab. It is evident that the equations shown in Table H.2 employ random numbers, whose use is pivotal in quantifying neutron transport.

It has been shown in this appendix how MC techniques are employed to describe radioactive particle transport without solving the actual transport equation for the radioactive particle whose transport is under investigation.

APPENDIX I

VOLUMETRIC ACTIVITY AND BIAS PARTITION DATA

The purpose of this appendix is to present the volumetric activity and bias data for each partition and for each time step number for which the radiation field in the wind tunnel is being analyzed. Table I.1 contains the volumetric activity for each partition and for each time step number and Table I.2 contains the bias values for each partition as a function of time step number.

Table I.1 – Volumetric Activity for each Partition as a Function of Time Step Number (unit: Bq·m³)

Time Step # / Partition	1	2	3	4	5	6	7	8	9	10
1	0.00E+00									
2	4.07E+09	0.00E+00								
3	0.00E+00									
4	0.00E+00									
5	0.00E+00									
6	0.00E+00									
7	0.00E+00									
8	4.95E+10	0.00E+00								
9	0.00E+00									
10	0.00E+00	0.00E+00	0.00E+00	0.00E+00	1.46E+09	6.05E+08	1.58E+09	1.54E+09	8.60E+08	6.16E+08
11	2.86E+09	0.00E+00								
12	2.56E+10	6.78E+08	0.00E+00	4.63E+08	2.60E+08	1.85E+09	1.34E+08	4.88E+07	0.00E+00	0.00E+00
13	0.00E+00									
14	0.00E+00	0.00E+00	2.26E+10	3.91E+09	0.00E+00	0.00E+00	0.00E+00	0.00E+00	1.16E+07	0.00E+00

15	0.00E+00	2.38E+08	2.75E+09	7.80E+09	1.81E+09	3.00E+09	4.97E+08	1.23E+09	1.97E+08	0.00E+00
16	3.78E+09	0.00E+00	0.00E+00	0.00E+00	1.83E+08	4.28E+08	1.31E+09	8.53E+08	5.38E+08	3.72E+06
17	1.51E+09	0.00E+00								
18	2.08E+08	0.00E+00	0.00E+00	0.00E+00	5.79E+07	0.00E+00	0.00E+00	0.00E+00	0.00E+00	0.00E+00
19	0.00E+00									
20	0.00E+00	3.25E+09	8.80E+09	5.56E+09	0.00E+00	0.00E+00	0.00E+00	0.00E+00	0.00E+00	0.00E+00
21	0.00E+00	7.90E+09	4.63E+09	9.35E+07	4.09E+09	1.95E+09	1.71E+09	7.08E+08	1.01E+09	3.74E+05
22	9.45E+08	0.00E+00	0.00E+00	0.00E+00	2.97E+08	0.00E+00	5.07E+08	1.33E+08	1.45E+08	0.00E+00
23	0.00E+00	0.00E+00	1.82E+08	1.30E+08	0.00E+00	0.00E+00	0.00E+00	0.00E+00	0.00E+00	0.00E+00
24	0.00E+00	0.00E+00	0.00E+00	6.11E+07	8.37E+05	0.00E+00	0.00E+00	0.00E+00	0.00E+00	0.00E+00
25	0.00E+00									
26	0.00E+00	8.59E+07	3.65E+08	3.22E+07	0.00E+00	0.00E+00	6.71E+08	6.71E+08	8.48E+08	0.00E+00
27	0.00E+00	3.60E+09	1.01E+09	4.33E+07	3.18E+08	7.25E+08	1.30E+08	7.14E+08	5.72E+08	0.00E+00
28	0.00E+00									
29	0.00E+00									
30	4.07E+09	0.00E+00								
31	0.00E+00									
32	0.00E+00									
33	4.95E+10	0.00E+00								
34	0.00E+00									
35	2.86E+09	0.00E+00								
36	2.56E+10	6.78E+08	0.00E+00	4.63E+08	2.60E+08	1.85E+09	1.34E+08	4.88E+07	0.00E+00	0.00E+00
37	0.00E+00									
38	1.51E+09	0.00E+00								
39	2.08E+08	0.00E+00	0.00E+00	0.00E+00	5.79E+07	0.00E+00	0.00E+00	0.00E+00	0.00E+00	0.00E+00
40	0.00E+00									
41	0.00E+00	0.00E+00	1.82E+08	1.30E+08	0.00E+00	0.00E+00	0.00E+00	0.00E+00	0.00E+00	0.00E+00

42	0.00E+00	0.00E+00	0.00E+00	6.11E+07	8.37E+05	0.00E+00	0.00E+00	0.00E+00	0.00E+00	0.00E+00
43	0.00E+00									

Table I.2 – Bias Data for each Partition as a Function of Time Step Number

Time Step # / Partition	1	2	3	4	5	6	7	8	9	10
1	0.00E+00									
2	2.36E-02	0.00E+00								
3	0.00E+00									
4	0.00E+00									
5	0.00E+00									
6	0.00E+00									
7	0.00E+00									
8	2.87E-01	0.00E+00								
9	0.00E+00									
10	0.00E+00	0.00E+00	0.00E+00	0.00E+00	1.66E-01	5.81E-02	2.37E-01	2.59E-01	2.06E-01	9.93E-01
11	1.66E-02	0.00E+00								
12	1.49E-01	4.13E-02	0.00E+00	2.47E-02	2.96E-02	1.77E-01	2.01E-02	8.21E-03	0.00E+00	0.00E+00
13	0.00E+00									
14	0.00E+00	0.00E+00	5.58E-01	2.09E-01	0.00E+00	0.00E+00	0.00E+00	0.00E+00	2.77E-03	0.00E+00
15	0.00E+00	1.45E-02	6.78E-02	4.16E-01	2.05E-01	2.89E-01	7.45E-02	2.07E-01	4.71E-02	0.00E+00
16	2.20E-02	0.00E+00	0.00E+00	0.00E+00	2.08E-02	4.11E-02	1.96E-01	1.43E-01	1.29E-01	6.00E-03
17	8.79E-03	0.00E+00								

The bias for an active partition at a particular time step number is defined as the ratio of the volumetric activity for that partition to the sum of the volumetric activities of all active partitions. Thus, at each time step number, the summing the bias of each active partition must be result in a value of unity, which is the case with the data presented in Table I.2.

APPENDIX J
SUBMERSION DOSE AND POINT SOURCE TECHNIQUE DATA

The purpose of this appendix is to present data produced by the submersion dose and point source techniques discussed in Section 4.4.1.1 and 4.4.1.2, respectively. This appendix is divided into two parts, and the first will discuss data pertaining to the submersion dose technique while the second will contain data produced by the point source technique.

J.1 Submersion Dose Technique Data

The first topic that must be addressed is the dependency of the bias that each source shown in Figure 4.13 has on the source volume. As described in Section 4.4.1.1, the spatially averaged volumetric activity calculated via equation (4.1) (whose values are shown in Table J.3) represents the volumetric activity possessed by the single radiation source shown in Figure 4.12. This therefore implies that within the shaded region shown in the aforementioned figure, the activity per unit volume of space within this region is equivalent to the spatially averaged volumetric activity calculated via equation (4.1). Thus, the volumetric activity within each of the sources shown in Figure 4.13 is equivalent to the spatially averaged volumetric activity. With this being said, if one was to find the volumetric activity within Source 1 shown in Figure 4.13, for instance, the following equivalency can be made:

$$\frac{A_1(i)}{V_1} = \bar{A}_V(i) \tag{J.1}$$

Where:

$A_1(i)$ = activity of Source 1 for the i^{th} time step iteration (unit: Bq)

V_1 = volume of Source 1 (unit: m^3)

$\bar{A}_V(i)$ = spatially averaged volumetric activity at the i^{th} time step iteration (unit: $\text{Bq}\cdot\text{m}^{-3}$)

When analyzing equation (J.1), one can see that of the attributes of the source (that is, its activity and volume), the activity of the source must be adjusted in order to satisfy the equivalency shown in equation (J.1), as opposed to the source volume which is constant (see Table J.1 for the spatial bounds and volume for each of the sources shown in Figure 4.13). As a result, the bias of this source, as with all sources, is dependent on the source activity. Of course, one can solve for the source activity in equation (J.1) by cross-multiplying to give:

$$A_1(i) = \bar{A}_V(i)V_1 \tag{J.2}$$

To calculate the bias possessed by a source, the ratio of the source activity to the sum of the activities of all the sources shown in Figure 4.13 must be taken, and this is mathematically shown in equation (J.3).

$$\text{Bias}_j(i) = \frac{A_j(i)}{\sum_{m=1}^n A_m(i)} \quad (\text{J.3})$$

Where:

- Bias_j(i) = bias of the jth source at the ith time step iteration
- A_j(i) = activity of the jth source at the ith time step iteration (unit: Bq)
- n = number of sources (as per Figure 4.13, n=7)
- A_m(i) = activity of the mth source at the ith time step iteration (unit: Bq)

As per equation (J.2), the activity of a source is defined as the product of the volume of the source and the spatially averaged volumetric activity. In light of this, equation (J.3) can be simplified as follows:

$$\text{Bias}_j(i) = \frac{\bar{A}_v(i)\nabla_j}{\bar{A}_v(i)\nabla_1 + \bar{A}_v(i)\nabla_2 + \dots + \bar{A}_v(i)\nabla_n}$$

The above equation can be further simplified by factoring out the spatially averaged volumetric activity in the numerator and denominator.

$$\text{Bias}_j(i) = \frac{\bar{A}_v(i)\nabla_j}{\bar{A}_v(i)(\nabla_1 + \nabla_2 + \dots + \nabla_n)}$$

The above expression can now be reduced to:

$$\text{Bias}_j(i) = \frac{\nabla_j}{\nabla_1 + \nabla_2 + \dots + \nabla_n}$$

It has been mentioned earlier that the source volume remains constant for each time step iteration and as such, the source bias is not dependent on the time step iteration for which the radiation field in the wind tunnel is being analyzed. Thus, the above expression becomes:

$$\text{Bias}_j = \frac{\nabla_j}{\nabla_1 + \nabla_2 + \dots + \nabla_n}$$

Since the denominator of the above equation represents the sum of the source volumes, the above expression can be re-stated:

$$\text{Bias}_j = \frac{\nabla_j}{\sum_{m=1}^n \nabla_m} \quad (\text{J.4})$$

Thus, it has been shown that the bias possessed by each of the sources shown in Figure 4.13 is dependent on the source volume and is therefore independent of the time step iteration. The bias possessed by each of the sources shown in Figure 4.13 is displayed in Table J.2.

Source	Spatial Bounds (unit: cm)	Volume (unit: cm ³)
1	$0 \leq x \leq 20$ $0 \leq y \leq 85$ $-572 \leq z \leq -472$	1.70E+05
2	$20 \leq x \leq 120$ $0.2 \leq y \leq 85$ $-572 \leq z \leq -472$	8.48E+05
3	$120 \leq x \leq 140$ $0 \leq y \leq 85$ $-572 \leq z \leq -472$	1.70E+05
4	$0 \leq x \leq 12$ $0 \leq y \leq 85$ $-588 \leq z \leq -572$	1.63E+04
5	$128 \leq x \leq 140$ $0 \leq y \leq 85$ $-588 \leq z \leq -572$	1.63E+04
6	$12 \leq x \leq 128$ $32 \leq y \leq 85$ $-588 \leq z \leq -572$	9.84E+04
7	$0 \leq x \leq 140$ $0 \leq y \leq 85$ $-1004 \leq z \leq -588$	4.95E+06
SUM		6.27E+06

Table J.1 – Spatial Bounds and Volume Data for MCNPX Submersion Sources

It is of note that the sum of the source volumes shown at the bottom of Table J.1 represents the submersion source volume employed by equations (4.3) and (4.4). This quantity can also be thought of as the volume of the shaded region shown in Figure 4.12.

Source	Bias
1	2.71E-02
2	1.35E-01
3	2.71E-02
4	2.60E-03
5	2.60E-03
6	1.57E-02
7	7.90E-01
SUM	1.00E+00

Table J.2 – Bias Data for MCNPX Submersion Sources

As per equation (J.4), the bias of each source is defined as the ratio of the source's volume to the sum of all source volumes. Thus, the sum of all sources biases must be equal to unity, as is the case with the data shown in Table J.2.

J.2 Point Source Technique Data

Table J.3 displays several quantities. The first of which is the spatially averaged volumetric activity that is calculated at each time step iteration (this quantity is also calculated by the submersion dose technique). The second quantity is the volume of the single representative partition, while the third and fourth quantities are the distances from the centre of the single representative partition to detector locations 1 and 2 respectively. Note that each of these quantities has been calculated at each time step iteration.

Time Step Iteration	Spatially Averaged Volumetric Activity (unit: Bq·m ⁻³)	Volume of Point Source (unit: m ³)	Distance from Point Source to Detector 1 (unit: cm)	Distance from Point Source to Detector 2 (unit: cm)
1	9.46E+08	3.45E-02	8.15E+01	1.52E+02
2	9.28E+08	3.54E-01	1.31E+02	5.24E+01
3	6.08E+08	9.41E-02	4.92E+01	7.22E+01
4	4.83E+08	1.62E-01	4.50E+01	7.49E+01
5	4.52E+08	3.22E-01	8.08E+01	6.98E+01
6	4.47E+08	2.70E-01	6.87E+01	9.81E+01
7	3.50E+08	3.29E-01	9.66E+01	9.85E+01
8	3.24E+08	3.41E-01	1.05E+02	1.21E+02
9	2.24E+08	3.36E-01	1.39E+02	1.11E+02
10	1.00E+07	1.02E-01	7.68E+01	1.65E+02

Table J.3 – Point Source Technique Data

APPENDIX K
COMPUTER CODES WRITTEN FOR THESIS

The purpose of this appendix is to present computer codes that have been developed in support of this thesis. Two sets of codes have been developed, the first being MATLAB codes developed in support of the Black Box (see Section 3.2.2) and Dose calculations (see Section 3.2.4) while the second set are the MCNPX input files for the MC radiation transport simulations (see Section 3.2.3) and submersion dose simulations (see Section 4.4.1.1). Prior to these codes being presented, a brief description will be given to each individual code made.

Code	Description
MATLAB Codes	
Activity_Calculations.m	Converts the particulate spatial distribution exported by FLUENT into a spatial distribution of volumetric activity at each time step iteration.
Source_Bias.m	Calculates the bias that each active spatial partition possesses at each time step iteration.
MCNPX_Black_Box.m	Uses the biases calculated above to prepare an MCNPX input file for each time step iteration.
External_Dose.m	This code calculates the time-integrated external dose at each detector location.
Internal_Dose.m	This code calculates the time-integrated internal dose at each detector location.
DCF.m	Using the time-integrated external and internal doses, the surface activity-to-dose conversion factor is calculated at each detector location.
Point_Source_Dose_Calculation.m	The application of the point source technique to the scenario modelled in this thesis is implemented here.
Submersion_Dose_Calculation_MCNPX.m	The application of the submersion dose technique to the scenario modelled in this thesis is implemented here.
MCNPX Codes	
1	MCNPX input file for time step iteration 1. *Note that the MCNPX input file for time step iteration 1 is similar in structure to that of time step iterations 2-10. As such, the MCNPX input files for time step iterations 2-10 will not be included in this appendix.
SM	MCNPX input file for the submersion dose technique.

Table K.1 – Description of Computer Codes Developed for Thesis

```

%Name: Fawaz Ali
%MATLAB Code for MCSC Thesis
%Purpose of Code: Convert particulate spatial distribution to spatial
%distribution of volumetric activity
%=====
format long e %this will allow for the use of more significant figures
%Step (1) Read in the particulate spatial distribution data from FLUENT output files
%-----
%The following reads in the data for each aerosol stream
D1 = importdata('i0.part'); %1st rake
D2 = importdata('i1.part'); %2nd rake
D3 = importdata('i2.part'); %3rd rake
D4 = importdata('i3.part'); %4th rake
D5 = importdata('i4.part'); %5th rake
D6 = importdata('i5.part'); %6th rake
%The following calculates the number of data rows in each of the above
%files
a1 = length(D1); %computes how many rows are in the 'i0.part' data file
a2 = length(D2); %computes how many rows are in the 'i1.part' data file
a3 = length(D3); %computes how many rows are in the 'i2.part' data file
a4 = length(D4); %computes how many rows are in the 'i3.part' data file
a5 = length(D5); %computes how many rows are in the 'i4.part' data file
a6 = length(D6); %computes how many rows are in the 'i5.part' data file
%The following reads in the diameter characteristic of each rake
diam1 = D1(1,8); %diameter of 1st rake particulates
diam2 = D2(1,8); %diameter of 2nd rake particulates
diam3 = D3(1,8); %diameter of 3rd rake particulates
diam4 = D4(1,8); %diameter of 4th rake particulates
diam5 = D5(1,8); %diameter of 5th rake particulates
diam6 = D6(1,8); %diameter of 6th rake particulates
%Step (2) Declare the required information
%-----
np = 100; %this stores the number of particulates released per rake
n_regions = 28; %this stores the number of sub-regions in the domain
n_symmetry = 13; %this stores the number of sub-regions that have been
    %dissected by the symmetry plane
n_rakes = 6; %this stores the number of rakes
n_steps = 10; %this stores the number of time steps for which the radiation
    %field in the domain will be analyzed
%The following stores nuclear radiation data for La-140
T_Half = 40.220; %Half Life of La-140 (units: hours)
N_A = 6.023E23; %Avogadro's Number (units: atoms/mol)
Density = 6.19; %Density of La-140 (units: g/cc)
M_M = 138.906; %Molar Mass of La-140 (units: g/mol)
%The following is an activity conversion factor to go from Becquerels (Bq)
%to Curies (Ci)
CF = 3.7E10; % (units: Bq/Ci)
%Store the diameters stated above in a vector
diameters = zeros(n_rakes,1);
%Populate the above vector
diameters(1,1) = diam1;
diameters(2,1) = diam2;
diameters(3,1) = diam3;
diameters(4,1) = diam4;
diameters(5,1) = diam5;
diameters(6,1) = diam6;
%Store the relevant data in the particle data files in one large matrix.
%First, find the maximum length of data read in
%The following will store the lengths of the data files read in

```

```

tempDvector = zeros(n_rakes,1);
%The following populates the above vector
tempDvector(1,1) = a1;
tempDvector(2,1) = a2;
tempDvector(3,1) = a3;
tempDvector(4,1) = a4;
tempDvector(5,1) = a5;
tempDvector(6,1) = a6;
%The following finds the maximum data length read in
tempD = max(tempDvector);
%The following creates a large matrix that will store the above data
D_total = zeros(tempD,4*n_rakes);
%The following extracts the relevant data from the 1st rake data
%file
for t1 = 1:1:a1
    D_total(t1,1) = D1(t1,1);
    D_total(t1,2) = D1(t1,2);
    D_total(t1,3) = D1(t1,3);
    D_total(t1,4) = D1(t1,4);
end
%The following extracts the relevant data from the 2nd rake data
%file
for t2 = 1:1:a2
    D_total(t2,5) = D2(t2,1);
    D_total(t2,6) = D2(t2,2);
    D_total(t2,7) = D2(t2,3);
    D_total(t2,8) = D2(t2,4);
end
%The following extracts the relevant data from the 3rd rake data
%file
for t3 = 1:1:a3
    D_total(t3,9) = D3(t3,1);
    D_total(t3,10) = D3(t3,2);
    D_total(t3,11) = D3(t3,3);
    D_total(t3,12) = D3(t3,4);
end
%The following extracts the relevant data from the 4th rake data
%file
for t4 = 1:1:a4
    D_total(t4,13) = D4(t4,1);
    D_total(t4,14) = D4(t4,2);
    D_total(t4,15) = D4(t4,3);
    D_total(t4,16) = D4(t4,4);
end
%The following extracts the relevant data from the 5th rake data
%file
for t5 = 1:1:a5
    D_total(t5,17) = D5(t5,1);
    D_total(t5,18) = D5(t5,2);
    D_total(t5,19) = D5(t5,3);
    D_total(t5,20) = D5(t5,4);
end
%The following extracts the relevant data from the 6th rake data
%file
for t6 = 1:1:a6
    D_total(t6,21) = D6(t6,1);
    D_total(t6,22) = D6(t6,2);
    D_total(t6,23) = D6(t6,3);
    D_total(t6,24) = D6(t6,4);
end
%Step (3) Determine the range of heights particulates will achieve
%-----

```

```

%This matrix will hold information for particulates whose height is between 1cm
%(inclusive) and 10cm (exclusive)
temp1 = zeros(a1,2);
%This matrix will hold information for particulates whose height exceeds 10cm
%(inclusive)
temp2 = zeros(a1,2);
%These indices will be used to populate the 'temp1' and 'temp2' matrices
j1 = 0;
j2 = 0;
j3 = 0;
%The following loop will populate the 'temp1' and 'temp2' matrices
for i1 = 1:1:a1
    if (D1(i1,3)>=10^-2 && D1(i1,3)<10^-1)
        j1 = j1+1;
        temp1(j1,1) = D1(i1,1);
        temp1(j1,2) = D1(i1,3);
    elseif (D1(i1,3)>=10^-1)
        j2 = j2+1;
        temp2(j2,1) = D1(i1,1);
        temp2(j2,2) = D1(i1,3);
    else
        j3 = j3+1;
    end
end
end
%Step (4) Re-state the 'temp1' and 'temp2' matrix for efficient storage
%-----
%First, declare the indices that will be used to store the first instance
%where each matrix will contain a zero
j4 = 0;
j5 = 0;
%Now, detect the first instance where each vector contains a zero
for i2 = 1:1:a1
    if (temp1(i2,1)==0)
        j4 = i2;
        break
    end
end
for i3 = 1:1:a1
    if (temp2(i3,1)==0)
        j5 = i3;
        break
    end
end
end
%Now, re-state the matrices that will feature the new dimensions of the
%abovementioned matrices
temp1new = zeros(j4-1,2);
temp2new = zeros(j5-1,2);
%Implement a loop that will populate the 'temp1new' and 'temp2new' matrices
for i4 = 1:1:(j4-1)
    temp1new(i4,1) = temp1(i4,1);
    temp1new(i4,2) = temp1(i4,2);
end
for i5 = 1:1:(j5-1)
    temp2new(i5,1) = temp2(i5,1);
    temp2new(i5,2) = temp2(i5,2);
end
end
%Step (5) Detect the minimum and maximum height attained for each height
%range and the corresponding time step
%-----
%The following will store the minimum and maximum heights found in
%temp1new, respectively
temp1new_minheight = min(temp1new(:,2));

```

```

temp1new_maxheight = max(temp1new(:,2));
%The following will store the minimum and maximum heights found in
%temp2new, respectively
temp2new_minheight = min(temp2new(:,2));
temp2new_maxheight = max(temp2new(:,2));
%The following will store the time step at which 'temp1new_minheight' and
%'temp1new_maxheight' are achieved, respectively
j6 = 0;
j7 = 0;
%The following will store the time step at which 'temp2new_minheight' and
%'temp2new_maxheight' are achieved, respectively
j8 = 0;
j9 = 0;
%Via the following loop, find the time step at which temp1new_minheight is
%achieved
for i6 = 1:1:(j4-1)
    if (temp1new(i6,2)==temp1new_minheight)
        j6 = temp1new(i6,1);
        break
    end
end

%Via the following loop, find the time step at which temp1new_maxheight is
%achieved
for i7 = 1:1:(j4-1)
    if (temp1new(i7,2)==temp1new_maxheight)
        j7 = temp1new(i7,1);
        break
    end
end

%Via the following loop, find the time step at which temp2new_minheight is
%achieved
for i8 = 1:1:(j5-1)
    if (temp2new(i8,2)==temp2new_minheight)
        j8 = temp2new(i8,1);
        break
    end
end

%Via the following loop, find the time step at which temp2new_maxheight is
%achieved
for i9 = 1:1:(j5-1)
    if (temp2new(i9,2)==temp2new_maxheight)
        j9 = temp2new(i9,1);
        break
    end
end

%Step (6) For the time steps found in step (5), find the corresponding
%iteration number
%-----
%The first step is to detect the iteration number where the time step for
%each particulate is exactly zero
%The following vector will store these numbers
temp3zero = zeros(np,1);
%The following index will be used to populate the 'temp3zero' vector
j10 = 0;
%The following loop will implement the above task
for i10 = 1:1:a1
    if (D1(i10,1)==0)
        j10 = j10+1;
        temp3zero(j10,1) = i10;
    end
end
end

```

```

%The following indices will hold the iteration number for which
%'temp1new_minheight', 'temp1new_maxheight', 'temp2new_minheight', and
%'temp2new_maxheight' and their corresponding time steps (respectively),
%'j6', 'j7', 'j8', and 'j9' are achieved
j11 = 0;
j12 = 0;
j13 = 0;
j14 = 0;
%The following loop will find the value for 'j11'
for i11 = 1:1:a1
    if (D1(i11,1)==j6 && D1(i11,3)==temp1new_minheight)
        j11 = i11;
        break
    end
end
%The following loop will find the value for 'j12'
for i12 = 1:1:a1
    if (D1(i12,1)==j7 && D1(i12,3)==temp1new_maxheight)
        j12 = i12;
        break
    end
end
%The following loop will find the value for 'j13'
for i13 = 1:1:a1
    if (D1(i13,1)==j8 && D1(i13,3)==temp2new_minheight)
        j13 = i13;
        break
    end
end
%The following loop will find the value for 'j14'
for i14 = 1:1:a1
    if (D1(i14,1)==j9 && D1(i14,3)==temp2new_maxheight)
        j14 = i14;
        break
    end
end
%The next step is to find the iteration number with respect to when the
%particulate is FIRST being tracked (i.e. at time step = 0).
%The following loop will find this for 'j11'. Note that 'j15' will store
%the elapsed amount of iterations after the particulate tracking is initiated
j15 = 0;
for i15 = 1:1:(np-1)
    if (temp3zero(i15,1)<j11 && temp3zero(i15+1,1)>j11)
        j15 = j11 - temp3zero(i15,1);
        break
    end
end
%The following 'if' statement will consider the case when 'j11' is greater
%than the last entry in 'temp3zero'
if (j11>temp3zero(np))
    j15 = j11 - temp3zero(np);
end
%The following loop will find the elapsed time for 'j12' with respect to
%the iteration that initiated the particulate tracking. Note that 'j16' will store
%this value
j16 = 0;
for i16 = 1:1:(np-1)
    if (temp3zero(i16,1)<j12 && temp3zero(i16+1,1)>j12)
        j16 = j12 - temp3zero(i16,1);
        break
    end
end
end

```

```

%The following 'if' statement will consider the case when 'j12' is greater
%than the last entry in 'temp3zero'
if (j12>temp3zero(np))
    j16 = j12 - temp3zero(np);
end
%The following loop will find the elapsed time for 'j13' with respect to
%the iteration that initiated the particulate tracking. Note that 'j17' will store
%this value
j17 = 0;
for i17 = 1:1:(np-1)
    if (temp3zero(i17,1)<j13 && temp3zero(i17+1,1)>j13)
        j17 = j13 - temp3zero(i17,1);
        break
    end
end
%The following 'if' statement will consider the case when 'j13' is greater
%than the last entry in 'temp3zero'
if (j13>temp3zero(np))
    j17 = j13 - temp3zero(np);
end
%The following loop will find the elapsed time for 'j14' with respect to
%the iteration that initiated the particulate tracking. Note that 'j18' will store
%this value
j18 = 0;
for i18 = 1:1:(np-1)
    if (temp3zero(i18,1)<j14 && temp3zero(i18+1,1)>j14)
        j18 = j14 - temp3zero(i18,1);
        break
    end
end
%The following 'if' statement will consider the case when 'j14' is greater
%than the last entry in 'temp3zero'
if (j14>temp3zero(np))
    j18 = j14 - temp3zero(np);
end
%Step (7) Locate in each data file, the row number where tracking for each
%particulate commences
%-----
%The following matrix will store the abovementioned data
tempDzeros = zeros(np,n_rakes);
%The following indices will be used to populate the above matrix
k1 = 1; %this index is used to extract time values from the D_total matrix
%The following loop will populate the above vector
for k3 = 1:1:n_rakes
    k5 = 0;
    for k4 = 1:1:tempDvector(k3,1)
        if (D_total(k4,k1)==0)
            k5 = k5 + 1;
            tempDzeros(k5,k3) = k4;
        end
    end
    k1 = k1 + 4;
end
%Step (8) Find the time steps that are intermediary between those already
%found
%-----
%FIRST, find the iteration number where the time steps equals or exceeds 1s
for i19 = 1:1:a1
    if(D1(i19,1)>=1)
        j19 = i19;
        break;
    end
end

```

```

end
%Now, find the corresponding number of time steps (i.e. iterations) taken
%with respect to when the particulate is first being tracked

for i20 = 1:1:np
    if (i20>=1 && i20<=(np-1))
        if (j19>tempDzeros(i20,1) && j19<tempDzeros(i20+1,1))
            j15_1 = j19 - tempDzeros(i20,1);
        end
    else
        if (j19>tempDzeros(np,1))
            j15_1 = j19 - tempDzeros(np,1);
        end
    end
end
end
%SECOND, find the iteration number where the time steps equals or exceeds
%2s
for i21 = 1:1:a1
    if(D1(i21,1)>=2)
        j21 = i21;
        break;
    end
end
end
%Now, find the corresponding number of time steps (i.e. iterations) taken
%with respect to when the particulate is first being tracked
for i22 = 1:1:np
    if (i22>=1 && i22<=(np-1))
        if (j21>tempDzeros(i22,1) && j21<tempDzeros(i22+1,1))
            j15_2 = j21 - tempDzeros(i22,1);
        end
    else
        if (j21>tempDzeros(np,1))
            j15_2 = j21 - tempDzeros(np,1);
        end
    end
end
end
%THIRD, find the iteration number where the time steps equals or exceeds
%3s
for i23 = 1:1:a1
    if(D1(i23,1)>=3)
        j23 = i23;
        break;
    end
end
end
%Now, find the corresponding number of time steps (i.e. iterations) taken
%with respect to when the particulate is first being tracked
for i24 = 1:1:np
    if (i24>=1 && i24<=(np-1))
        if (j23>tempDzeros(i24,1) && j23<tempDzeros(i24+1,1))
            j15_3 = j23 - tempDzeros(i24,1);
        end
    else
        if (j23>tempDzeros(np,1))
            j15_3 = j23 - tempDzeros(np,1);
        end
    end
end
end
%FOURTH, find the iteration number where the time steps equals or exceeds
%5s
for i25 = 1:1:a1
    if(D1(i25,1)>=5)
        j25 = i25;
    end
end

```

```

        break;
    end
end
%Now, find the corresponding number of time steps (i.e. iterations) taken
%with respect to when the particulate is first being tracked
for i26 = 1:1:np
    if (i26>=1 && i26<=(np-1))
        if (j25>tempDzeros(i26,1) && j25<tempDzeros(i26+1,1))
            j17_1 = j25 - tempDzeros(i26,1);
        end
    else
        if (j25>tempDzeros(np,1))
            j17_1 = j25 - tempDzeros(np,1);
        end
    end
end
end
%FIFTH, find the iteration number where the time steps equals or exceeds
%6s
for i27 = 1:1:a1
    if(D1(i27,1)>=6)
        j27 = i27;
        break;
    end
end
%Now, find the corresponding number of time steps (i.e. iterations) taken
%with respect to when the particulate is first being tracked
for i28 = 1:1:np
    if (i28>=1 && i28<=(np-1))
        if (j27>tempDzeros(i28,1) && j27<tempDzeros(i28+1,1))
            j17_2 = j27 - tempDzeros(i28,1);
        end
    else
        if (j27>tempDzeros(np,1))
            j17_2 = j27 - tempDzeros(np,1);
        end
    end
end
end
%SIXTH, find the iteration number where the time steps equals or exceeds
%7s
for i29 = 1:1:a1
    if(D1(i29,1)>=7)
        j29 = i29;
        break;
    end
end
%Now, find the corresponding number of time steps (i.e. iterations) taken
%with respect to when the particulate is first being tracked
for i30 = 1:1:np
    if (i30>=1 && i30<=(np-1))
        if (j29>tempDzeros(i30,1) && j29<tempDzeros(i30+1,1))
            j17_3 = j29 - tempDzeros(i30,1);
        end
    else
        if (j29>tempDzeros(np,1))
            j17_3 = j29 - tempDzeros(np,1);
        end
    end
end
end
%Step (9) For the particulate tracking steps found, find the corresponding time
%values
%-----
%The following will store the values of the tracking steps

```

```

aerosol_steps = zeros(n_steps,1);
%The following will store the corresponding time values of the tracking
%steps
time_aerosol_steps = zeros(n_steps,1);
%The following will store the number of particulates that exit the domain prior
%to the tracking step taking place as a function of the particulate diameter
countexit = zeros(n_steps,n_rakes);
%The following populates the 'aerosol_steps' vector
aerosol_steps(1,1) = j15;
aerosol_steps(2,1) = j15_1;
aerosol_steps(3,1) = j15_2;
aerosol_steps(4,1) = j15_3;
aerosol_steps(5,1) = j16;
aerosol_steps(6,1) = j17;
aerosol_steps(7,1) = j17_1 + 2000;
aerosol_steps(8,1) = j17_2 + 2500;
aerosol_steps(9,1) = j17_3 + 3000;
aerosol_steps(10,1) = j18;
%The following loop will find the corresponding time step for each of the
%tracking steps performed
for k6 = 1:1:n_steps
    k9 = 1; %this is used to point to the relevant column in the 'D_total' matrix
    for k7 = 1:1:n_rakes
        for k8 = 1:1:np
            if (k8>=1 && k8<=(np-1))
                if ((tempDzeros(k8,k7)+aerosol_steps(k6,1)) < tempDvector(k7,1))
                    time_aerosol_steps(k6,1) = time_aerosol_steps(k6,1) +
D_total(tempDzeros(k8,k7)+aerosol_steps(k6,1),k9);
                else
                    countexit(k6,k7) = countexit(k6,k7) + 1;
                end
            else
                if ((tempDzeros(np,k7)+aerosol_steps(k6,1)) < tempDvector(k7,1))
                    time_aerosol_steps(k6,1) = time_aerosol_steps(k6,1) +
D_total(tempDzeros(k8,k7)+aerosol_steps(k6,1),k9);
                else
                    countexit(k6,k7) = countexit(k6,k7) + 1;
                end
            end
        end
        k9 = k9 + 4; %Updates the 'k9' index
    end
end
%The following loop calculates the corresponding time value for each tracking step
for k10 = 1:1:n_steps
    time_aerosol_steps(k10,1) = time_aerosol_steps(k10,1)/(np*n_rakes - sum(countexit(k10,:)));
end

%Step (10) Bin the number of particulates found in each sub-region and for each
%time step
%-----
%Before any calculations proceed, it is important to store the boundaries
%of each sub-region. These boundaries will be stored in the matrix
%declared below
bounds = zeros(n_regions,6);
%The following will populate the above matrix
bounds = [0, 0.20, 0, 0.01, -5.72, -4.72; 0, 0.20, 0.01, 0.32, -5.72, ...
-4.72; 0, 0.20, 0.32, 0.85, -5.72, -4.72; 0.20, 0.70, 0.002, 0.01, ...
-5.72, -4.72; 0.20, 0.70, 0.01, 0.32, -5.72, -4.72; 0.20, 0.70, 0.32, ...
0.85, -5.72, -4.72; 0, 0.12, 0, 0.01, -5.88, -5.72; 0, 0.12, 0.01, ...
0.32, -5.88, -5.72; 0, 0.12, 0.32, 0.85, -5.88, -5.72; 0.12, 0.70, ...
0.32, 0.85, -5.88, -5.72; 0, 0.12, 0, 0.01, -6.88, -5.88; 0, 0.12, ...

```

```

0.01, 0.32, -6.88, -5.88; 0, 0.12, 0.32, 0.85, -6.88, -5.88; 0.12, ...
0.70, 0, 0.01, -6.88, -5.88; 0.12, 0.70, 0.01, 0.32, -6.88, -5.88; ...
0.12, 0.70, 0.32, 0.85, -6.88, -5.88; 0, 0.12, 0, 0.01, -7.88, ...
-6.88; 0, 0.12, 0.01, 0.32, -7.88, -6.88; 0, 0.12, 0.32, 0.85, ...
-7.88, -6.88; 0.12, 0.70, 0, 0.01, -7.88, -6.88; 0.12, 0.70, ...
0.01, 0.32, -7.88, -6.88; 0.12, 0.70, 0.32, 0.85, -7.88, -6.88; ...
0, 0.12, 0, 0.01, -10.04, -7.88; 0, 0.12, 0.01, 0.32, -10.04, ...
-7.88; 0, 0.12, 0.32, 0.85, -10.04, -7.88; 0.12, 0.70, 0, 0.01, ...
-10.04, -7.88; 0.12, 0.70, 0.01, 0.32, -10.04, -7.88; 0.12, 0.70, ...
0.32, 0.85, -10.04, -7.88];
%Create a matrix that will store the quantities stated above
count = zeros(n_rakes*n_regions,n_steps);
%The following loop will carry out the abovementioned task
for k10 = 1:1:n_steps %Set the time step value
    k14 = 2; %State the column pointer for the x position
    k15 = 3; %State the column pointer for the y position
    k16 = 4; %State the column pointer for the z position
    for k11 = 1:1:n_rakes
        for k12 = 1:1:np
            temp = aerosol_steps(k10,1) + tempDzeros(k12,k11);
            for k13 = 1:1:n_regions
                if (k12>=1 && k12<=(np-1))
                    if (temp < tempDzeros(k12+1,k11))
                        if (D_total(temp,k14)>=bounds(k13,1) && D_total(temp,k14)<=bounds(k13,2) &&
D_total(temp,k15)>=bounds(k13,3) && D_total(temp,k15)<=bounds(k13,4) && D_total(temp,k16)>=bounds(k13,5)
&& D_total(temp,k16)<=bounds(k13,6))
                            count(k13 + (k11-1)*n_regions,k10) = count(k13 + (k11-1)*n_regions,k10) + 1;
                            break;
                        end
                    end
                else
                    if ((temp > tempDzeros(np,k11)) && (temp < tempDvector(k11,1)))
                        if (D_total(temp,k14)>=bounds(k13,1) && D_total(temp,k14)<=bounds(k13,2) &&
D_total(temp,k15)>=bounds(k13,3) && D_total(temp,k15)<=bounds(k13,4) && D_total(temp,k16)>=bounds(k13,5)
&& D_total(temp,k16)<=bounds(k13,6))
                            count(k13 + (k11-1)*n_regions,k10) = count(k13 + (k11-1)*n_regions,k10) + 1;
                            break;
                        end
                    end
                end
            end
        end
    end
    k14 = k14 + 4; %Update the column pointer for the x position
    k15 = k15 + 4; %Update the column pointer for the y position
    k16 = k16 + 4; %Update the column pointer for the z position
end
end
%Normalize the contents of the 'count' matrix to the total number of
%particulates initially in the domain. To do this, first calculate the total
%number of particulates in the system
np_total = 2*np*n_rakes;
%Now, divide each entry in the 'count' matrix by the above quantity
count_scaled = count./np_total;
%Also, scale the contents of the 'countexit' matrix by the number of
%particulates of a given diameter initially placed in the domain. For
%example, the contents in the first column is related to data from the
%first rake (where 1um particulates are released). Thus, one would scale this
%data set by total number of 1um particulates initially placed in the domain,
%which, in this case is 100 (stored in the 'np' variable). So, scale each
%quantity in the 'countexit' matrix by 'np'. This method of scaling is
%more meaningful since one is expressing the fraction/percentage of
%particulates of a particular diameter that have exited the domain prior to a

```

```

%particular time step taking place.
countexit_scaled = countexit./np;
%Step (11) Calculate the Activity in each sub-region and for each time step
%-----
%The following matrix will store the above
Activity_1_Bq = zeros(n_regions,n_steps);
%The following loop will calculate the Activity (in Becquerels) for each
%sub-region and for each time step
for k17 = 1:1:n_steps
    for k18 = 1:1:n_regions
        for k19 = 1:1:n_rakes
            Activity_1_Bq(k18,k17) = Activity_1_Bq(k18,k17) + count(k18 + (k19-
1)*n_regions,k17)*(1/6)*(pi)*(diameters(k19,1)^3)*(100^3)*(log(2))*N_A*Density/(T_Half*3600*M_M);
        end
    end
end
end
%Convert the Acitivity values calculated above to Curies. The following
%matrix will store these values
Activity_1_Ci = Activity_1_Bq./CF;
%Step (12) Calculate the Volumetric Activity in each sub-region and for
%each time step
%-----
%First, calculate the volume (units: m^3) of each sub-region. The first
%step is to declare a vector that will store these values
Volume = zeros(n_regions,1);
%The following loop will calculate the volume of each sub-region
for k20 = 1:1:n_regions
    Volume(k20,1) = (bounds(k20,2) - bounds(k20,1))*(bounds(k20,4) - bounds(k20,3))*(bounds(k20,6) -
bounds(k20,5));
end
%The following matrices will holds the volumetric activity in units of
%Bq/m^3 and Ci/m^3, respectively
Activity_1_Bq_V = zeros(n_regions,n_steps); %units:Bq/m^3
Activity_1_Ci_V = zeros(n_regions,n_steps); %units:Ci/m^3
%The following loop will now populate the above matrices
for k21 = 1:1:n_steps
    for k22 = 1:1:n_regions
        Activity_1_Bq_V(k22,k21) = Activity_1_Bq(k22,k21)/Volume(k22,1);
        Activity_1_Ci_V(k22,k21) = Activity_1_Ci(k22,k21)/Volume(k22,1);
    end
end
end
%Step (13) Account for symmetry in the calculated data
%-----
%In this step, the aim is to re-state the data calculated already (for
%example, Activity) such that symmetry will be accounted for. Before any
%further steps are taken, calculate the TOTAL number of sub-regions in the
%domain
%The following calculates the TOTAL number of sub-regions in the domain
n_regions_total = (2*n_regions) - n_symmetry;

%Since the contents of the 'Volume' vector are not dependent on the time
%step, re-state this vector to account for symmetry. The following vector
%will hold this
Volume_Total = zeros(n_regions_total,1);
%Populate the 'Volume_Total' vector from the 1st index to the 'n_regions'
%index
Volume_Total(1:n_regions,1) = Volume(1:n_regions,1);
%The following loop will populate the above vector
for k23 = 1:1:n_regions
    %The following will calculate the volume for the symmetrical
    %sub-regions

```

```

if ((k23>=4 && k23<=6) || (k23==10) || (k23>=14 && k23<=16) || (k23>=20 && k23<=22) || (k23>=26 &&
k23<=28))
    Volume_Total(k23,1) = 2*Volume(k23,1);
    %The following will calculate the volume for sub-regions 1-3 and the
    %corresponding symmetrical sub-regions
    elseif (k23>=1 && k23<=3)
        Volume_Total(k23+n_regions,1) = Volume(k23,1);
    %The following will calculate the volume for sub-regions 7-9 and the
    %corresponding symmetrical sub-regions
    elseif (k23>=7 && k23<=9)
        Volume_Total(k23+(n_regions-3),1) = Volume(k23,1);
    %The following will calculate the volume for sub-regions 11-13 and the
    %corresponding symmetrical sub-regions
    elseif (k23>=11 && k23<=13)
        Volume_Total(k23+(n_regions-4),1) = Volume(k23,1);
    %The following will calculate the volume for sub-regions 17-19 and the
    %corresponding symmetrical sub-regions
    elseif (k23>=17 && k23<=19)
        Volume_Total(k23+(n_regions-7),1) = Volume(k23,1);
    %The following will calculate the volume for sub-regions 23-25 and the
    %corresponding symmetrical sub-regions
    else
        Volume_Total(k23+(n_regions-10),1) = Volume(k23,1);
    end
end
end
%For the Activity data, re-state the data to account for symmetry
Activity_Bq_Total = zeros(n_regions_total,n_steps); %Stores the Activity in Bq
Activity_Ci_Total = zeros(n_regions_total,n_steps); %Stores the Activity in Ci
Activity_Bq_V_Total = zeros(n_regions_total,n_steps); %Stores the Volumetric Activity in Bq/m^3
Activity_Ci_V_Total = zeros(n_regions_total,n_steps); %Stores the Volumetric Activity in Ci/m^3

%Populate the above matrices from the 1st index to the 'n_regions'
%index for each time step
Activity_Bq_Total(1:n_regions,1:n_steps) = Activity_1_Bq(1:n_regions,1:n_steps);
Activity_Ci_Total(1:n_regions,1:n_steps) = Activity_1_Ci(1:n_regions,1:n_steps);
Activity_Bq_V_Total(1:n_regions,1:n_steps) = Activity_1_Bq_V(1:n_regions,1:n_steps);
Activity_Ci_V_Total(1:n_regions,1:n_steps) = Activity_1_Ci_V(1:n_regions,1:n_steps);
%The following loop will populate the above matrices
for k24 = 1:1:n_steps
    for k25 = 1:1:n_regions
        %The following will calculate the Activity and Volumetric Activity for
        %the symmetrical sub-regions
        if ((k25>=4 && k25<=6) || (k25==10) || (k25>=14 && k25<=16) || (k25>=20 && k25<=22) || (k25>=26 &&
k25<=28))
            Activity_Bq_Total(k25,k24) = 2*Activity_1_Bq(k25,k24);
            Activity_Ci_Total(k25,k24) = 2*Activity_1_Ci(k25,k24);
            Activity_Bq_V_Total(k25,k24) = Activity_1_Bq_V(k25,k24);
            Activity_Ci_V_Total(k25,k24) = Activity_1_Ci_V(k25,k24);
        %The following will calculate the Activity and Volumetric Activity for
        %sub-regions 1-3 and the corresponding symmetrical sub-regions
        elseif (k25>=1 && k25<=3)
            Activity_Bq_Total(k25+n_regions,k24) = Activity_1_Bq(k25,k24);
            Activity_Ci_Total(k25+n_regions,k24) = Activity_1_Ci(k25,k24);
            Activity_Bq_V_Total(k25+n_regions,k24) = Activity_1_Bq_V(k25,k24);
            Activity_Ci_V_Total(k25+n_regions,k24) = Activity_1_Ci_V(k25,k24);
        %The following will calculate the Activity and Volumetric Activity for
        %sub-regions 7-9 and the corresponding symmetrical sub-regions
        elseif (k25>=7 && k25<=9)
            Activity_Bq_Total(k25+(n_regions-3),k24) = Activity_1_Bq(k25,k24);
            Activity_Ci_Total(k25+(n_regions-3),k24) = Activity_1_Ci(k25,k24);
            Activity_Bq_V_Total(k25+(n_regions-3),k24) = Activity_1_Bq_V(k25,k24);
            Activity_Ci_V_Total(k25+(n_regions-3),k24) = Activity_1_Ci_V(k25,k24);
        end
    end
end

```

```

%The following will calculate the Activity and Volumetric Activity for
%sub-regions 11-13 and the corresponding symmetrical sub-regions
elseif (k25>=11 && k25<=13)
    Activity_Bq_Total(k25+(n_regions-4),k24) = Activity_1_Bq(k25,k24);
    Activity_Ci_Total(k25+(n_regions-4),k24) = Activity_1_Ci(k25,k24);
    Activity_Bq_V_Total(k25+(n_regions-4),k24) = Activity_1_Bq_V(k25,k24);
    Activity_Ci_V_Total(k25+(n_regions-4),k24) = Activity_1_Ci_V(k25,k24);
%The following will calculate the Activity and Volumetric Activity for
%sub-regions 17-19 and the corresponding symmetrical sub-regions
elseif (k25>=17 && k25<=19)
    Activity_Bq_Total(k25+(n_regions-7),k24) = Activity_1_Bq(k25,k24);
    Activity_Ci_Total(k25+(n_regions-7),k24) = Activity_1_Ci(k25,k24);
    Activity_Bq_V_Total(k25+(n_regions-7),k24) = Activity_1_Bq_V(k25,k24);
    Activity_Ci_V_Total(k25+(n_regions-7),k24) = Activity_1_Ci_V(k25,k24);
%The following will calculate the Activity and Volumetric Activity for
%sub-regions 23-25 and the corresponding symmetrical sub-regions
else
    Activity_Bq_Total(k25+(n_regions-10),k24) = Activity_1_Bq(k25,k24);
    Activity_Ci_Total(k25+(n_regions-10),k24) = Activity_1_Ci(k25,k24);
    Activity_Bq_V_Total(k25+(n_regions-10),k24) = Activity_1_Bq_V(k25,k24);
    Activity_Ci_V_Total(k25+(n_regions-10),k24) = Activity_1_Ci_V(k25,k24);
end
end
end
%For the normalized particulate counts, re-state this data to account for
%symmetry
%The following matrix will hold this data
count_scaled_Total = zeros(n_rakes*n_regions_total,n_steps);
% %Populate the 'count_scaled_Total' matrix using entries from the
%'count_scaled' matrix
%First, calculate the difference between the TOTAL number of sub-regions
%and the ORIGINAL number of sub-regions
n_difference = n_regions_total - n_regions;
%The following loop will populate the 'count_scaled_Total' matrix
for m1 = 1:1:n_steps
    for m2 = 1:1:n_rakes
        for m3 = 1:1:n_regions
            count_scaled_Total(m3 + ((m2-1)*n_regions) + (n_difference*(m2-1)),m1) = count_scaled(m3 + (m2-
1)*n_regions,m1);
        end
    end
end
%The following loop will account for symmetry in the 'count_scaled_Total'
%matrix
for k26 = 1:1:n_steps
    for k27 = 1:1:n_rakes
        for k28 = 1:1:n_regions
            %The following will calculate the number of particulates for
            %the symmetrical sub-regions
            if ((k28>=4 && k28<=6) || (k28==10) || (k28>=14 && k28<=16) || (k28>=20 && k28<=22) || (k28>=26 &&
k28<=28))
                count_scaled_Total(k28 + ((k27-1)*n_regions) + n_difference*(k27-1),k26) = 2*count_scaled_Total(k28+
((k27-1)*n_regions) + n_difference*(k27-1),k26);
            %The following will calculate the number of particulates for
            %sub-regions 1-3 and the corresponding symmetrical sub-regions
            elseif (k28>=1 && k28<=3)
                count_scaled_Total(k28 + ((k27-1)*n_regions) + n_regions + n_difference*(k27-1),k26) =
count_scaled_Total(k28 + ((k27-1)*n_regions) + n_difference*(k27-1),k26);
            %The following will calculate the number of particulates for
            %sub-regions 7-9 and the corresponding symmetrical sub-regions
            elseif (k28>=7 && k28<=9)

```

```

        count_scaled_Total(k28 + ((k27-1)*n_regions) + (n_regions-3) + n_difference*(k27-1),k26) =
count_scaled_Total(k28 + ((k27-1)*n_regions) + n_difference*(k27-1),k26);
    %The following will calculate the number of particulates for
    %sub-regions 11-13 and the corresponding symmetrical sub-regions
    elseif (k28>=11 && k28<=13)
        count_scaled_Total(k28 + ((k27-1)*n_regions) + (n_regions-4) + n_difference*(k27-1),k26) =
count_scaled_Total(k28 + ((k27-1)*n_regions)+n_difference*(k27-1),k26);
    %The following will calculate the number of particulates for
    %sub-regions 17-19 and the corresponding symmetrical sub-regions
    elseif (k28>=17 && k28<=19)
        count_scaled_Total(k28 + ((k27-1)*n_regions) + (n_regions-7) + n_difference*(k27-1),k26) =
count_scaled_Total(k28 + ((k27-1)*n_regions)+n_difference*(k27-1),k26);
    %The following will calculate the number of particulates for
    %sub-regions 23-25 and the corresponding symmetrical sub-regions
    else
        count_scaled_Total(k28 + ((k27-1)*n_regions) + (n_regions-10) + n_difference*(k27-1),k26) =
count_scaled_Total(k28 + ((k27-1)*n_regions)+n_difference*(k27-1),k26);
    end
end
end
end
%Step (14) Create plots to illustrate how particulate populations change over
%time for each sub-region
%-----
%The first task is to convert all of the time values to strings
time1 = num2str(time_aerosol_steps(1,1)); %1st Time Step
time2 = num2str(time_aerosol_steps(2,1)); %2nd Time Step
time3 = num2str(time_aerosol_steps(3,1)); %3rd Time Step
time4 = num2str(time_aerosol_steps(4,1)); %4th Time Step
time5 = num2str(time_aerosol_steps(5,1)); %5th Time Step
time6 = num2str(time_aerosol_steps(6,1)); %6th Time Step
time7 = num2str(time_aerosol_steps(7,1)); %7th Time Step
time8 = num2str(time_aerosol_steps(8,1)); %8th Time Step
time9 = num2str(time_aerosol_steps(9,1)); %9th Time Step
time10 = num2str(time_aerosol_steps(10,1)); %10th Time Step
%The following stores the diameters of the particulates without the 10e-6
%portion
diameters_simple = [1,2,3,4,5,6];
%STEP (14.1) Create a plot for sub-regions 1-3
for n1 = 1:1:3
    figure (1) %Stores the plot in Figure 1
    subplot(3,1,n1) %Creates a 3x1 subplot
    tempstr1 = num2str(n1); %Convert the sub-region number to string format
    tempvec1 = zeros(n_rakes,n_steps); %For the particular sub-region, the number of particulates are binned as a
function of both diameter and time step
    %The following loop populates the above matrix
    for p1 = 1:1:n_steps
        for q1 = 1:1:n_rakes
            tempvec1(q1,p1) = count_scaled_Total(n1 + (q1-1)*n_regions_total,p1);
        end
    end
end
%The following calculates the maximum particulate count
temp1 = max(max(tempvec1));
%When plotting, it is intended to scale the y axis from 0 to the
%maximum particulate count for the sub-region. If this count is zero, then
%make the upper y-limit to 1
if (temp1==0)
    temp1 = 1;
end
%Plot the required data
plot(diameters_simple,tempvec1(:,1),'-',diameters_simple,tempvec1(:,2),'-o',diameters_simple,tempvec1(:,3),'-
x',diameters_simple,tempvec1(:,4),'-+',diameters_simple,tempvec1(:,5),'-*',diameters_simple,tempvec1(:,6),'-

```

```

s',diameters_simple,tempvec1(:,7),'-d',diameters_simple,tempvec1(:,8),'-v',diameters_simple,tempvec1(:,9),'-
^',diameters_simple,tempvec1(:,10),'-p'), xlabel('Particle Diameter (um)'), ylabel('Number of Particles (scaled)'),
title(['Number of particles binned according to diameter for partition: ',tempstr1])
    legend(['time (s) = ',time1],[ 'time (s) = ',time2],[ 'time (s) = ',time3],[ 'time (s) = ',time4],[ 'time (s) = ',time5],[ 'time (s)
= ',time6],[ 'time (s) = ',time7],[ 'time (s) = ',time8],[ 'time (s) = ',time9],[ 'time (s) = ',time10])
    axis([1 n_rakes 0 temp1]) %Re-state the axes bounds
    hold on;
end
%STEP (14.2) Create a plot for symmetrical sub-regions 29-31
for n2 = 1:1:3
    figure (2) %Stores the plot in Figure 2
    subplot(3,1,n2) %Creates a 3x1 subplot
    tempstr2 = num2str(n2+n_regions); %Convert the sub-region number to string format
    tempvec2 = zeros(n_rakes,n_steps); %For the particular sub-region, the number of particulates are binned as a
function of both diameter and time step
    %The following loop populates the above matrix
    for p2 = 1:1:n_steps
        for q2 = 1:1:n_rakes
            tempvec2(q2,p2) = count_scaled_Total(n2 + n_regions + (q2-1)*n_regions_total,p2);
        end
    end
    %The following calculates the maximum particulate count
    temp2 = max(max(tempvec2));
    %When plotting, it is intended to scale the y axis from 0 to the
    %maximum particulate count for the sub-region. If this count is zero, then
    %make the upper y-limit to 1
    if (temp2==0)
        temp2 = 1;
    end
    %Plot the required data
    plot(diameters_simple,tempvec2(:,1),'-',diameters_simple,tempvec2(:,2),'-o',diameters_simple,tempvec2(:,3),'-
x',diameters_simple,tempvec2(:,4),'-+',diameters_simple,tempvec2(:,5),'-*',diameters_simple,tempvec2(:,6),'-
s',diameters_simple,tempvec2(:,7),'-d',diameters_simple,tempvec2(:,8),'-v',diameters_simple,tempvec2(:,9),'-
^',diameters_simple,tempvec2(:,10),'-p'), xlabel('Particle Diameter (um)'), ylabel('Number of Particles (scaled)'),
title(['Number of particles binned according to diameter for partition: ',tempstr2])
    legend(['time (s) = ',time1],[ 'time (s) = ',time2],[ 'time (s) = ',time3],[ 'time (s) = ',time4],[ 'time (s) = ',time5],[ 'time (s)
= ',time6],[ 'time (s) = ',time7],[ 'time (s) = ',time8],[ 'time (s) = ',time9],[ 'time (s) = ',time10])
    axis([1 n_rakes 0 temp2]) %Re-state the axes bounds
    hold on
end
%STEP (14.3) Create a plot for sub-regions 7-9
for n3 = 7:1:9
    figure (3) %Stores the plot in Figure 3
    subplot(3,1,(n3-6)) %Creates a 3x1 subplot
    tempstr3 = num2str(n3); %Convert the sub-region number to string format
    tempvec3 = zeros(n_rakes,n_steps); %For the particular sub-region, the number of particulates are binned as a
function of both diameter and time step
    %The following loop populates the above matrix
    for p3 = 1:1:n_steps
        for q3 = 1:1:n_rakes
            tempvec3(q3,p3) = count_scaled_Total(n3 + (q3-1)*n_regions_total,p3);
        end
    end
    %The following calculates the maximum particulate count
    temp3 = max(max(tempvec3));
    %When plotting, it is intended to scale the y axis from 0 to the
    %maximum particulate count for the sub-region. If this count is zero, then
    %make the upper y-limit to 1
    if (temp3==0)
        temp3 = 1;
    end
    %Plot the required data

```

```

    plot(diameters_simple,tempvec3(:,1),'-',diameters_simple,tempvec3(:,2),'-o',diameters_simple,tempvec3(:,3),'-
x',diameters_simple,tempvec3(:,4),'-+',diameters_simple,tempvec3(:,5),'-*',diameters_simple,tempvec3(:,6),'-
s',diameters_simple,tempvec3(:,7),'-d',diameters_simple,tempvec3(:,8),'-v',diameters_simple,tempvec3(:,9),'-
^',diameters_simple,tempvec3(:,10),'-p'), xlabel('Particle Diameter (um)'), ylabel('Number of Particles (scaled)'),
title(['Number of particles binned according to diameter for partition: ',tempstr3])
    legend(['time (s) = ',time1],[ 'time (s) = ',time2],[ 'time (s) = ',time3],[ 'time (s) = ',time4],[ 'time (s) = ',time5],[ 'time (s)
= ',time6],[ 'time (s) = ',time7],[ 'time (s) = ',time8],[ 'time (s) = ',time9],[ 'time (s) = ',time10])
    axis([1 n_rakes 0 temp3]) %Re-state the axes bounds
    hold on;
end
end
%STEP (14.4) Create a plot for symmetrical sub-regions 32-34
for n4 = 7:1:9
    figure (4) %Stores the plot in Figure 4
    subplot(3,1,(n4-6)) %Creates a 3x1 subplot
    tempstr4 = num2str(n4+(n_regions-3)); %Convert the sub-region number to string format
    tempvec4 = zeros(n_rakes,n_steps); %For the particular sub-region, the number of aerosols are binned as a function
of both diameter and time step
    %The following loop populates the above matrix
    for p4 = 1:1:n_steps
        for q4 = 1:1:n_rakes
            tempvec4(q4,p4) = count_scaled_Total(n4 + (n_regions-3) + (q4-1)*n_regions_total,p4);
        end
    end
    %The following calculates the maximum particulate count
    temp4 = max(max(tempvec4));
    %When plotting, it is intended to scale the y axis from 0 to the
    %maximum particulate count for the sub-region. If this count is zero, then
    %make the upper y-limit to 1
    if (temp4==0)
        temp4 = 1;
    end
    %Plot the required data
    plot(diameters_simple,tempvec4(:,1),'-',diameters_simple,tempvec4(:,2),'-o',diameters_simple,tempvec4(:,3),'-
x',diameters_simple,tempvec4(:,4),'-+',diameters_simple,tempvec4(:,5),'-*',diameters_simple,tempvec4(:,6),'-
s',diameters_simple,tempvec4(:,7),'-d',diameters_simple,tempvec4(:,8),'-v',diameters_simple,tempvec4(:,9),'-
^',diameters_simple,tempvec4(:,10),'-p'), xlabel('Particle Diameter (um)'), ylabel('Number of Particles (scaled)'),
title(['Number of particles binned according to diameter for partition: ',tempstr4])
    legend(['time (s) = ',time1],[ 'time (s) = ',time2],[ 'time (s) = ',time3],[ 'time (s) = ',time4],[ 'time (s) = ',time5],[ 'time (s)
= ',time6],[ 'time (s) = ',time7],[ 'time (s) = ',time8],[ 'time (s) = ',time9],[ 'time (s) = ',time10])
    axis([1 n_rakes 0 temp4]) %Re-state the axes bounds
    hold on
end
end
%STEP (14.5) Create a plot for sub-regions 11-13
for n5 = 11:1:13
    figure (5) %Stores the plot in Figure 5
    subplot(3,1,(n5-10)) %Creates a 3x1 subplot
    tempstr5 = num2str(n5); %Convert the sub-region number to string format
    tempvec5 = zeros(n_rakes,n_steps); %For the particular sub-region, the number of particulates are binned as a
function of both diameter and time step
    %The following loop populates the above matrix
    for p5 = 1:1:n_steps
        for q5 = 1:1:n_rakes
            tempvec5(q5,p5) = count_scaled_Total(n5 + (q5-1)*n_regions_total,p5);
        end
    end
    %The following calculates the maximum particulate count
    temp5 = max(max(tempvec5));
    %When plotting, it is intended to scale the y axis from 0 to the
    %maximum particulate count for the sub-region. If this count is zero, then
    %make the upper y-limit to 1
    if (temp5==0)
        temp5 = 1;
    end
end

```

```

end
%Plot the required data
plot(diameters_simple,tempvec5(:,1),'-',diameters_simple,tempvec5(:,2),'-o',diameters_simple,tempvec5(:,3),'-
x',diameters_simple,tempvec5(:,4),'-+',diameters_simple,tempvec5(:,5),'-*',diameters_simple,tempvec5(:,6),'-
s',diameters_simple,tempvec5(:,7),'-d',diameters_simple,tempvec5(:,8),'-v',diameters_simple,tempvec5(:,9),'-
^',diameters_simple,tempvec5(:,10),'-p'), xlabel('Particle Diameter (um)'), ylabel('Number of Particles (scaled)'),
title(['Number of particles binned according to diameter for partition: ',tempstr5])
legend(['time (s) = ',time1],['time (s) = ',time2],['time (s) = ',time3],['time (s) = ',time4],['time (s) = ',time5],['time (s)
= ',time6],['time (s) = ',time7],['time (s) = ',time8],['time (s) = ',time9],['time (s) = ',time10])
axis([1 n_rakes 0 temp5]) %Re-state the axes bounds
hold on;
end
%STEP (14.6) Create a plot for symmetrical sub-regions 35-37
for n6 = 11:1:13
figure (6) %Stores the plot in Figure 6
subplot(3,1,(n6-10)) %Creates a 3x1 subplot
tempstr6 = num2str(n6+(n_regions-4)); %Convert the sub-region number to string format
tempvec6 = zeros(n_rakes,n_steps); %For the particular sub-region, the number of particulates are binned as a
function of both diameter and time step
%The following loop populates the above matrix
for p6 = 1:1:n_steps
for q6 = 1:1:n_rakes
tempvec6(q6,p6) = count_scaled_Total(n6 + (n_regions-4) + (q6-1)*n_regions_total,p6);
end
end
%The following calculates the maximum particulate count
temp6 = max(max(tempvec6));
%When plotting, it is intended to scale the y axis from 0 to the
%maximum particulate count for the sub-region. If this count is zero, then
%make the upper y-limit to 1
if (temp6==0)
temp6 = 1;
end
%Plot the required data
plot(diameters_simple,tempvec6(:,1),'-',diameters_simple,tempvec6(:,2),'-o',diameters_simple,tempvec6(:,3),'-
x',diameters_simple,tempvec6(:,4),'-+',diameters_simple,tempvec6(:,5),'-*',diameters_simple,tempvec6(:,6),'-
s',diameters_simple,tempvec6(:,7),'-d',diameters_simple,tempvec6(:,8),'-v',diameters_simple,tempvec6(:,9),'-
^',diameters_simple,tempvec6(:,10),'-p'), xlabel('Particle Diameter (um)'), ylabel('Number of Particles (scaled)'),
title(['Number of particles binned according to diameter for partition: ',tempstr6])
legend(['time (s) = ',time1],['time (s) = ',time2],['time (s) = ',time3],['time (s) = ',time4],['time (s) = ',time5],['time (s)
= ',time6],['time (s) = ',time7],['time (s) = ',time8],['time (s) = ',time9],['time (s) = ',time10])
axis([1 n_rakes 0 temp6]) %Re-state the axes bounds
hold on
end
end
%STEP (14.7) Create a plot for sub-regions 17-19
for n7 = 17:1:19
figure (7) %Stores the plot in Figure 7
subplot(3,1,(n7-16)) %Creates a 3x1 subplot
tempstr7 = num2str(n7); %Convert the sub-region number to string format
tempvec7 = zeros(n_rakes,n_steps); %For the particular sub-region, the number of particulates are binned as a
function of both diameter and time step
%The following loop populates the above matrix
for p7 = 1:1:n_steps
for q7 = 1:1:n_rakes
tempvec7(q7,p7) = count_scaled_Total(n7 + (q7-1)*n_regions_total,p7);
end
end
%The following calculates the maximum particulate count
temp7 = max(max(tempvec7));
%When plotting, it is intended to scale the y axis from 0 to the
%maximum particulate count for the sub-region. If this count is zero, then
%make the upper y-limit to 1

```

```

if (temp7==0)
    temp7 = 1;
end
%Plot the required data
plot(diameters_simple,tempvec7(:,1),'-',diameters_simple,tempvec7(:,2),'-o',diameters_simple,tempvec7(:,3),'-
x',diameters_simple,tempvec7(:,4),'-+',diameters_simple,tempvec7(:,5),'-*',diameters_simple,tempvec7(:,6),'-
s',diameters_simple,tempvec7(:,7),'-d',diameters_simple,tempvec7(:,8),'-v',diameters_simple,tempvec7(:,9),'-
^',diameters_simple,tempvec7(:,10),'-p'), xlabel('Particle Diameter (um)'), ylabel('Number of Particles (scaled)'),
title(['Number of particles binned according to diameter for partition: ',tempstr7])
legend(['time (s) = ',time1],[ 'time (s) = ',time2],[ 'time (s) = ',time3],[ 'time (s) = ',time4],[ 'time (s) = ',time5],[ 'time (s)
= ',time6],[ 'time (s) = ',time7],[ 'time (s) = ',time8],[ 'time (s) = ',time9],[ 'time (s) = ',time10])
axis([1 n_rakes 0 temp7]) %Re-state the axes bounds
hold on;
end
%STEP (14.8) Create a plot for symmetrical sub-regions 38-40
for n8 = 17:1:19
    figure (8) %Stores the plot in Figure 8
    subplot(3,1,(n8-16)) %Creates a 3x1 subplot
    tempstr8 = num2str(n8+(n_regions-7)); %Convert the sub-region number to string format
    tempvec8 = zeros(n_rakes,n_steps); %For the particular sub-region, the number of particulates are binned as a
function of both diameter and time step
    %The following loop populates the above matrix
    for p8 = 1:1:n_steps
        for q8 = 1:1:n_rakes
            tempvec8(q8,p8) = count_scaled_Total(n8 + (n_regions-7) + (q8-1)*n_regions_total,p8);
        end
    end
    %The following calculates the maximum particulate count
    temp8 = max(max(tempvec8));
    %When plotting, it is intended to scale the y axis from 0 to the
    %maximum particulate count for the sub-region. If this count is zero, then
    %make the upper y-limit to 1
    if (temp8==0)
        temp8 = 1;
    end
    %Plot the required data
    plot(diameters_simple,tempvec8(:,1),'-',diameters_simple,tempvec8(:,2),'-o',diameters_simple,tempvec8(:,3),'-
x',diameters_simple,tempvec8(:,4),'-+',diameters_simple,tempvec8(:,5),'-*',diameters_simple,tempvec8(:,6),'-
s',diameters_simple,tempvec8(:,7),'-d',diameters_simple,tempvec8(:,8),'-v',diameters_simple,tempvec8(:,9),'-
^',diameters_simple,tempvec8(:,10),'-p'), xlabel('Particle Diameter (um)'), ylabel('Number of Particles (scaled)'),
title(['Number of particles binned according to diameter for partition: ',tempstr8])
    legend(['time (s) = ',time1],[ 'time (s) = ',time2],[ 'time (s) = ',time3],[ 'time (s) = ',time4],[ 'time (s) = ',time5],[ 'time (s)
= ',time6],[ 'time (s) = ',time7],[ 'time (s) = ',time8],[ 'time (s) = ',time9],[ 'time (s) = ',time10])
    axis([1 n_rakes 0 temp8]) %Re-state the axes bounds
    hold on
end
%STEP (14.9) Create a plot for sub-regions 23-25
for n9 = 23:1:25
    figure (9) %Stores the plot in Figure 9
    subplot(3,1,(n9-22)) %Creates a 3x1 subplot
    tempstr9 = num2str(n9); %Convert the sub-region number to string format
    tempvec9 = zeros(n_rakes,n_steps); %For the particular sub-region, the number of particulates are binned as a
function of both diameter and time step
    %The following loop populates the above matrix
    for p9 = 1:1:n_steps
        for q9 = 1:1:n_rakes
            tempvec9(q9,p9) = count_scaled_Total(n9 + (q9-1)*n_regions_total,p9);
        end
    end
    %The following calculates the maximum particulate count
    temp9 = max(max(tempvec9));
    %When plotting, it is intended to scale the y axis from 0 to the

```

```

%maximum particulate count for the sub-region. If this count is zero, then
%make the upper y-limit to 1
if (temp9==0)
    temp9 = 1;
end
%Plot the required data
plot(diameters_simple,tempvec9(:,1),'-',diameters_simple,tempvec9(:,2),'-o',diameters_simple,tempvec9(:,3),'-
x',diameters_simple,tempvec9(:,4),'-+',diameters_simple,tempvec9(:,5),'-*',diameters_simple,tempvec9(:,6),'-
s',diameters_simple,tempvec9(:,7),'-d',diameters_simple,tempvec9(:,8),'-v',diameters_simple,tempvec9(:,9),'-
^',diameters_simple,tempvec9(:,10),'-p'), xlabel('Particle Diameter (um)'), ylabel('Number of Particles (scaled)'),
title(['Number of particles binned according to diameter for partition: ',tempstr9])
legend(['time (s) = ',time1],[ 'time (s) = ',time2],[ 'time (s) = ',time3],[ 'time (s) = ',time4],[ 'time (s) = ',time5],[ 'time (s)
= ',time6],[ 'time (s) = ',time7],[ 'time (s) = ',time8],[ 'time (s) = ',time9],[ 'time (s) = ',time10])
axis([1 n_rakes 0 temp9]) %Re-state the axes bounds
hold on;
end
end
%STEP (14.10) Create a plot for symmetrical sub-regions 41-43
for n10 = 23:1:25
    figure (10) %Stores the plot in Figure 10
    subplot(3,1,(n10-22)) %Creates a 3x1 subplot
    tempstr10 = num2str(n10+(n_regions-10)); %Convert the sub-region number to string format
    tempvec10 = zeros(n_rakes,n_steps); %For the particular sub-region, the number of particulates are binned as a
function of both diameter and time step
    %The following loop populates the above matrix
    for p10 = 1:1:n_steps
        for q10 = 1:1:n_rakes
            tempvec10(q10,p10) = count_scaled_Total(n10 + (n_regions-10) + (q10-1)*n_regions_total,p10);
        end
    end
    %The following calculates the maximum particulate count
    temp10 = max(max(tempvec10));
    %When plotting, it is intended to scale the y axis from 0 to the
    %maximum particulate count for the sub-region. If this count is zero, then
    %make the upper y-limit to 1
    if (temp10==0)
        temp10 = 1;
    end
    %Plot the required data
    plot(diameters_simple,tempvec10(:,1),'-',diameters_simple,tempvec10(:,2),'-o',diameters_simple,tempvec10(:,3),'-
x',diameters_simple,tempvec10(:,4),'-+',diameters_simple,tempvec10(:,5),'-*',diameters_simple,tempvec10(:,6),'-
s',diameters_simple,tempvec10(:,7),'-d',diameters_simple,tempvec10(:,8),'-v',diameters_simple,tempvec10(:,9),'-
^',diameters_simple,tempvec10(:,10),'-p'), xlabel('Particle Diameter (um)'), ylabel('Number of Particles (scaled)'),
title(['Number of particles binned according to diameter for partition: ',tempstr10])
    legend(['time (s) = ',time1],[ 'time (s) = ',time2],[ 'time (s) = ',time3],[ 'time (s) = ',time4],[ 'time (s) = ',time5],[ 'time (s)
= ',time6],[ 'time (s) = ',time7],[ 'time (s) = ',time8],[ 'time (s) = ',time9],[ 'time (s) = ',time10])
    axis([1 n_rakes 0 temp10]) %Re-state the axes bounds
    hold on
end
end
%STEP (14.11) Create a plot for symmetrical sub-regions 4-6
for n11 = 4:1:6
    figure (11) %Stores the plot in Figure 11
    subplot(3,1,(n11-3)) %Creates a 3x1 subplot
    tempstr11 = num2str(n11); %Convert the sub-region number to string format
    tempvec11 = zeros(n_rakes,n_steps); %For the particular sub-region, the number of particulates are binned as a
function of both diameter and time step
    %The following loop populates the above matrix
    for p11 = 1:1:n_steps
        for q11 = 1:1:n_rakes
            tempvec11(q11,p11) = count_scaled_Total(n11 + (q11-1)*n_regions_total,p11);
        end
    end
    %The following calculates the maximum particulate count

```

```

temp11 = max(max(tempvec11));
%When plotting, it is intended to scale the y axis from 0 to the
%maximum aerosol count for the sub-region. If this count is zero, then
%make the upper y-limit to 1
if (temp11==0)
    temp11 = 1;
end
%Plot the required data
plot(diameters_simple,tempvec11(:,1),'-',diameters_simple,tempvec11(:,2),'-o',diameters_simple,tempvec11(:,3),'-
x',diameters_simple,tempvec11(:,4),'-+',diameters_simple,tempvec11(:,5),'-*',diameters_simple,tempvec11(:,6),'-
s',diameters_simple,tempvec11(:,7),'-d',diameters_simple,tempvec11(:,8),'-v',diameters_simple,tempvec11(:,9),'-
^',diameters_simple,tempvec11(:,10),'-p'), xlabel('Particle Diameter (um)'), ylabel('Number of Particles (scaled)'),
title(['Number of particles binned according to diameter for partition: ',tempstr11])
legend(['time (s) = ',time1],[ 'time (s) = ',time2],[ 'time (s) = ',time3],[ 'time (s) = ',time4],[ 'time (s) = ',time5],[ 'time (s)
= ',time6],[ 'time (s) = ',time7],[ 'time (s) = ',time8],[ 'time (s) = ',time9],[ 'time (s) = ',time10])
axis([1 n_rakes 0 temp11]) %Re-state the axes bounds
hold on;
end
%STEP (14.12) Create a plot for symmetrical sub-region 10
n12 = 10; %Sub-Region Number
figure (12) %Stores the plot in Figure 12
tempstr12 = num2str(n12); %Convert the sub-region number to string format
tempvec12 = zeros(n_rakes,n_steps); %For the particular sub-region, the number of particulates are binned as a
function of both diameter and time step
%The following loop populates the above matrix
for p12 = 1:1:n_steps
    for q12 = 1:1:n_rakes
        tempvec12(q12,p12) = count_scaled_Total(n12 + (q12-1)*n_regions_total,p12);
    end
end
%The following calculates the maximum particulate count
temp12 = max(max(tempvec12));
%When plotting, it is intended to scale the y axis from 0 to the
%maximum particulate count for the sub-region. If this count is zero, then
%make the upper y-limit to 1
if (temp12==0)
    temp12 = 1;
end
%Plot the required data
plot(diameters_simple,tempvec12(:,1),'-',diameters_simple,tempvec12(:,2),'-o',diameters_simple,tempvec12(:,3),'-
x',diameters_simple,tempvec12(:,4),'-+',diameters_simple,tempvec12(:,5),'-*',diameters_simple,tempvec12(:,6),'-
s',diameters_simple,tempvec12(:,7),'-d',diameters_simple,tempvec12(:,8),'-v',diameters_simple,tempvec12(:,9),'-
^',diameters_simple,tempvec12(:,10),'-p'), xlabel('Particle Diameter (um)'), ylabel('Number of Particles (scaled)'),
title(['Number of particles binned according to diameter for partition: ',tempstr12])
legend(['time (s) = ',time1],[ 'time (s) = ',time2],[ 'time (s) = ',time3],[ 'time (s) = ',time4],[ 'time (s) = ',time5],[ 'time (s)
= ',time6],[ 'time (s) = ',time7],[ 'time (s) = ',time8],[ 'time (s) = ',time9],[ 'time (s) = ',time10])
axis([1 n_rakes 0 temp12]) %Re-state the axes bounds
%STEP (14.13) Create a plot for symmetrical sub-regions 14-16
for n13 = 14:1:16
    figure (13) %Stores the plot in Figure 13
    subplot(3,1,(n13-13)) %Creates a 3x1 subplot
    tempstr13 = num2str(n13); %Convert the sub-region number to string format
    tempvec13 = zeros(n_rakes,n_steps); %For the particular sub-region, the number of particulates are binned as a
function of both diameter and time step
%The following loop populates the above matrix
for p13 = 1:1:n_steps
    for q13 = 1:1:n_rakes
        tempvec13(q13,p13) = count_scaled_Total(n13 + (q13-1)*n_regions_total,p13);
    end
end
%The following calculates the maximum particulate count
temp13 = max(max(tempvec13));

```

```

%When plotting, it is intended to scale the y axis from 0 to the
%maximum particulate count for the sub-region. If this count is zero, then
%make the upper y-limit to 1
if (temp13==0)
    temp13 = 1;
end
%Plot the required data
plot(diameters_simple,tempvec13(:,1),'-',diameters_simple,tempvec13(:,2),'-o',diameters_simple,tempvec13(:,3),'-
x',diameters_simple,tempvec13(:,4),'-+',diameters_simple,tempvec13(:,5),'-*',diameters_simple,tempvec13(:,6),'-
s',diameters_simple,tempvec13(:,7),'-d',diameters_simple,tempvec13(:,8),'-v',diameters_simple,tempvec13(:,9),'-
^',diameters_simple,tempvec13(:,10),'-p'), xlabel('Particle Diameter (um)'), ylabel('Number of Particles (scaled)'),
title(['Number of particles binned according to diameter for partition: ',tempstr13])
    legend(['time (s) = ',time1],[ 'time (s) = ',time2],[ 'time (s) = ',time3],[ 'time (s) = ',time4],[ 'time (s) = ',time5],[ 'time (s)
= ',time6],[ 'time (s) = ',time7],[ 'time (s) = ',time8],[ 'time (s) = ',time9],[ 'time (s) = ',time10])
    axis([1 n_rakes 0 temp13]) %Re-state the axes bounds
    hold on;
end

%STEP (14.14) Create a plot for symmetrical sub-regions 20-22
for n14 = 20:1:22
    figure (14) %Stores the plot in Figure 14
    subplot(3,1,(n14-19)) %Creates a 3x1 subplot
    tempstr14 = num2str(n14); %Convert the sub-region number to string format
    tempvec14 = zeros(n_rakes,n_steps); %For the particular sub-region, the number of particulates are binned as a
function of both diameter and time step
    %The following loop populates the above matrix
    for p14 = 1:1:n_steps
        for q14 = 1:1:n_rakes
            tempvec14(q14,p14) = count_scaled_Total(n14 + (q14-1)*n_regions_total,p14);
        end
    end
    %The following calculates the maximum particulate count
    temp14 = max(max(tempvec14));
    %When plotting, it is intended to scale the y axis from 0 to the
    %maximum particulate count for the sub-region. If this count is zero, then
    %make the upper y-limit to 1
    if (temp14==0)
        temp14 = 1;
    end
    %Plot the required data
    plot(diameters_simple,tempvec14(:,1),'-',diameters_simple,tempvec14(:,2),'-o',diameters_simple,tempvec14(:,3),'-
x',diameters_simple,tempvec14(:,4),'-+',diameters_simple,tempvec14(:,5),'-*',diameters_simple,tempvec14(:,6),'-
s',diameters_simple,tempvec14(:,7),'-d',diameters_simple,tempvec14(:,8),'-v',diameters_simple,tempvec14(:,9),'-
^',diameters_simple,tempvec14(:,10),'-p'), xlabel('Particle Diameter (um)'), ylabel('Number of Particles (scaled)'),
title(['Number of particles binned according to diameter for partition: ',tempstr14])
    legend(['time (s) = ',time1],[ 'time (s) = ',time2],[ 'time (s) = ',time3],[ 'time (s) = ',time4],[ 'time (s) = ',time5],[ 'time (s)
= ',time6],[ 'time (s) = ',time7],[ 'time (s) = ',time8],[ 'time (s) = ',time9],[ 'time (s) = ',time10])
    axis([1 n_rakes 0 temp14]) %Re-state the axes bounds
    hold on;
end

%STEP (14.15) Create a plot for symmetrical sub-regions 26-28
for n15 = 26:1:28
    figure (15) %Stores the plot in Figure 15
    subplot(3,1,(n15-25)) %Creates a 3x1 subplot
    tempstr15 = num2str(n15); %Convert the sub-region number to string format
    tempvec15 = zeros(n_rakes,n_steps); %For the particular sub-region, the number of particulates are binned as a
function of both diameter and time step
    %The following loop populates the above matrix
    for p15 = 1:1:n_steps
        for q15 = 1:1:n_rakes
            tempvec15(q15,p15) = count_scaled_Total(n15 + (q15-1)*n_regions_total,p15);
        end
    end

```

```

end
%The following calculates the maximum particulate count
temp15 = max(max(tempvec15));
%When plotting, it is intended to scale the y axis from 0 to the
%maximum particulate count for the sub-region. If this count is zero, then
%make the upper y-limit to 1
if (temp15==0)
    temp15 = 1;
end
%Plot the required data
plot(diameters_simple,tempvec15(:,1),'-.',diameters_simple,tempvec15(:,2),'-o',diameters_simple,tempvec15(:,3),'-
x',diameters_simple,tempvec15(:,4),'-+',diameters_simple,tempvec15(:,5),'-*',diameters_simple,tempvec15(:,6),'-
s',diameters_simple,tempvec15(:,7),'-d',diameters_simple,tempvec15(:,8),'-v',diameters_simple,tempvec15(:,9),'-
^',diameters_simple,tempvec15(:,10),'-p'), xlabel('Particle Diameter (um)'), ylabel('Number of Particles (scaled)'),
title(['Number of particles binned according to diameter for partition: ',tempstr15])
legend(['time (s) = ',time1],[ 'time (s) = ',time2],[ 'time (s) = ',time3],[ 'time (s) = ',time4],[ 'time (s) = ',time5],[ 'time (s) = ',time6],[ 'time (s) = ',time7],[ 'time (s) = ',time8],[ 'time (s) = ',time9],[ 'time (s) = ',time10])
axis([1 n_rakes 0 temp15]) %Re-state the axes bounds
hold on;
end
%Step (15) Export relevant data for later use in building the MCNPX Black
%Box
%-----
%STEP (15.1) Export data containing the Volume of each sub-region
fid = fopen('VolumeData.txt','wt')
for u1 = 1:1:n_regions_total
    fprintf(fid,'%d',u1)
    fprintf(fid,'\t')
    fprintf(fid,'%e',Volume_Total(u1,1))
    fprintf(fid,'\n')
end
fclose(fid);
%STEP (15.2) Export data containing the Activity (in Bq) in each sub-region
fid = fopen('ActivityBq.txt','wt')
for u2 = 1:1:n_regions_total
    fprintf(fid,'%d',u2)
    fprintf(fid,'\t')
    for u3 = 1:1:n_steps
        fprintf(fid,'%e',Activity_Bq_Total(u2,u3))
        fprintf(fid,'\t')
    end
    fprintf(fid,'\n')
end
fclose(fid);
%STEP (15.3) Export data containing the Activity (in Ci) in each sub-region
fid = fopen('ActivityCi.txt','wt')
for u4 = 1:1:n_regions_total
    fprintf(fid,'%d',u4)
    fprintf(fid,'\t')
    for u5 = 1:1:n_steps
        fprintf(fid,'%e',Activity_Ci_Total(u4,u5))
        fprintf(fid,'\t')
    end
    fprintf(fid,'\n')
end
fclose(fid);
%STEP (15.4) Export data containing the Volumetric Activity (in Bq/m^3) in
%each sub-region
fid = fopen('ActivityBqV.txt','wt')
for u6 = 1:1:n_regions_total
    fprintf(fid,'%d',u6)
    fprintf(fid,'\t')

```

```

for u7 = 1:1:n_steps
    fprintf(fid,'%e',Activity_Bq_V_Total(u6,u7))
    fprintf(fid,'\t')
end
fprintf(fid,'\n')
end
fclose(fid);
%STEP (15.5) Export data containing the Volumetric Activity (in Ci/m^3) in
%each sub-region
fid = fopen('ActivityCiV.txt','wt')
for u8 = 1:1:n_regions_total
    fprintf(fid,'%d',u8)
    fprintf(fid,'\t')
    for u9 = 1:1:n_steps
        fprintf(fid,'%e',Activity_Ci_V_Total(u8,u9))
        fprintf(fid,'\t')
    end
    fprintf(fid,'\n')
end
end

fclose(fid);
%STEP (15.6) Export Time Values for each corresponding Tracking Step
fid = fopen('Time.txt','wt')
for u10 = 1:1:n_steps
    fprintf(fid,'%d',time_aerosol_steps(u10,1))
    fprintf(fid,'\n')
end
fclose(fid);

```

Source_Bias.m

Calculates the bias that each active spatial partition possesses at each time step iteration

```

%Name: Fawaz Ali
%MATLAB Code for MCSC Thesis
%Purpose of Code: Calculate the bias that each partition possesses for
%each time step iteration
%=====
format long e %this will allow for the use of more significant figures
%Step (1) Declare the required information
%-----
n_regions = 28; %this stores the number of sub-regions in the domain
n_symmetry = 13; %this stores the number of sub-regions that have been
    %dissected by the symmetry plane
n_rakes = 6; %this stores the number of rakes
n_steps = 10; %this stores the number of time steps for which the radiation
    %field in the domain will be analyzed
%The following calculates the TOTAL number of sub-regions in the domain
n_regions_total = (2*n_regions) - n_symmetry;
%Step (2) Import the required data
%-----
%Since the Volumetric Activity is only needed, the data stored in
%'ActivityBqV.txt' will be imported
A_V = importdata('ActivityBqV.txt');
%Step (3) Declare the required matrices/vectors
%-----
%The following vector will store the sum of the volumetric activities for
%each time step
sum_A_V = zeros(n_steps,1);
%The following matrix will store the bias that each sub-region possesses
%for each time step
Bias_A_V = zeros(n_regions_total,n_steps);

```

```

%Step (4) Perform the required calculations
%-----
%STEP (4.1) Calculate the sum of the volumetric activity for each time step
for i1 = 1:1:n_steps
    for i2 = 1:1:n_regions_total
        sum_A_V(i1,1) = sum_A_V(i1,1) + A_V(i2,i1+1);
    end
end
%STEP (4.2) Calculate the bias that each sub-region possesses
%for each time step
for i3 = 1:1:n_steps
    for i4 = 1:1:n_regions_total
        Bias_A_V(i4,i3) = A_V(i4,i3+1)/sum_A_V(i3,1);
    end
end
%Step (5) Export the Bias Data
%-----
fid = fopen('SourceBias.txt','wt')
for i5 = 1:1:n_regions_total
    fprintf(fid,'%d',i5)
    fprintf(fid,'\t')
    for i6 = 1:1:n_steps
        fprintf(fid,'%e',Bias_A_V(i5,i6))
        fprintf(fid,'\t')
    end
    fprintf(fid,'\n')
end
fclose(fid);

```

MCNPX_Black_Box.m

Creates an MCNPX input file for each time step iteration

```

%Name: Fawaz Ali
%MATLAB Code for MCSC Thesis
%Purpose of Code: Create an MCNPX input file for each time step iteration
%=====
format long e %this will allow for the use of more significant figures
%Step (1) Declare the required information
%-----
n_regions = 28; %this stores the number of sub-regions in the domain
n_symmetry = 13; %this stores the number of sub-regions that have been
    %dissected by the symmetry plane
n_rakes = 6; %this stores the number of rakes
n_steps = 10; %this stores the number of time steps for which the radiation
    %field in the domain will be analyzed
%The following calculates the TOTAL number of sub-regions in the domain
n_regions_total = (2*n_regions) - n_symmetry;
%Step (2) Import the required data
%-----
%Since the Volumetric Activity is only needed, the data stored in
%'ActivityBqV.txt' will be imported
A_V = importdata('ActivityBqV.txt');
%The bias that each sub-region possesses for each time step will also need
%to be imported
BiasMatrix = importdata('SourceBias.txt');
%The geometric bounds of each sub-region will also be needed
BoundsMatrix = importdata('Bounds.txt');
%The Gamma Energy Spectrum for La-140 will also be needed
Gamma_ES = importdata('Gamma_Energy_Spectrum.txt');
%Step (3) Create MCNPX Input file for each time step
%-----

```

```

for i1 = 1:1:n_steps
    temp = num2str(i1); %Convert the time step number to a string
    fid = fopen(temp,'wt'); %Create and open a file that will store the MCNPX input commands for the particular time
step
    %STEP (3.1) Insert the first block of the MCNPX code (CELL CARDS)
    fprintf(fid,'%s','CFD-MCNPX Integration')
    fprintf(fid,'\n')
    fprintf(fid,'%s','C Cell Cards')
    fprintf(fid,'\n')
    fprintf(fid,'%s','10 1 -0.65 -1                imp:p=1    $Plate')
    fprintf(fid,'\n')
    fprintf(fid,'%s','20 1 -0.65 -2                imp:p=1    $Bluff body')
    fprintf(fid,'\n')
    fprintf(fid,'%s','30 2 -0.001236 -3 -4 -5 #(-1) #(-2)    imp:p=1    $Wind Tunnel with Plate and Bluff Body')
    fprintf(fid,'\n')
    fprintf(fid,'%s','40 0 3:4:5 #(-1) #(-2)                imp:p=0    $Outside of Wind Tunnel with Plate and Bluff Body')
    fprintf(fid,'\n')
    fprintf(fid,'\n')
    %STEP (3.2) Insert the second block of the MCNPX code (SURFACE CARDS)
    fprintf(fid,'%s','C Surface Cards')
    fprintf(fid,'\n')
    fprintf(fid,'%s','1 RPP 20 120 0 0.2 -572 -472 $Plate')
    fprintf(fid,'\n')
    fprintf(fid,'%s','2 RPP 12 128 0 32 -588 -572 $Bluff Body')
    fprintf(fid,'\n')
    fprintf(fid,'%s','3 RPP 0 140 0 143 -1004 0    $Wind Tunnel')
    fprintf(fid,'\n')
    fprintf(fid,'%s','4 1 py 0                $Plane for Indent 1')
    fprintf(fid,'\n')
    fprintf(fid,'%s','5 2 py 0                $Plane for Indent 2')
    fprintf(fid,'\n')
    fprintf(fid,'\n')
    fprintf(fid,'%s','*tr1  0 85 0 -60.362 29.638 90 -150.362 -60.362 90 90 90 0 1 $Transformation for Indent 1')
    fprintf(fid,'\n')
    fprintf(fid,'%s','*tr2 140 85 0  60.362 150.362 90 -29.638  60.362 90 90 90 0 1 $Transformation for Indent 2')
    fprintf(fid,'\n')
    fprintf(fid,'%s','C')
    fprintf(fid,'\n')
    %STEP (3.3) Insert the third block of the MCNPX code (DATA CARDS)
    fprintf(fid,'%s','C Data Cards')
    fprintf(fid,'\n')
    fprintf(fid,'%s','mode p')
    fprintf(fid,'\n')
    %The following will insert the SDEF card
    fprintf(fid,'%s','SDEF X=D1 Y=fx=D91 Z=fx=D92 ERG=D90')
    fprintf(fid,'\n')
    %The following will implement the Gamma Energy Spectrum for La-140.
    %The contents below will insert the discrete Gamma energies
    fprintf(fid,'%s','SI90 L ')
    fprintf(fid,'%d',Gamma_ES(1,2))
    fprintf(fid,'%s',' $')
    fprintf(fid,'\n')
    for i2 = 1:1:(length(Gamma_ES)-1)
        fprintf(fid,'%s',' ')
        fprintf(fid,'%d',Gamma_ES(i2+1,2))
        fprintf(fid,'%s',' $')
        fprintf(fid,'\n')
    end
    end
    %The following will insert the probabilities of the above Gamma
    %energies
    fprintf(fid,'%s','SP90 D ')
    fprintf(fid,'%d',Gamma_ES(1,1))

```

```

fprintf(fid,'%s',' $')
fprintf(fid,'\n')
for i3 = 1:(length(Gamma_ES)-1)
    fprintf(fid,'%s',' ')
    fprintf(fid,'%d',Gamma_ES(i3+1,1))
    fprintf(fid,'%s',' $')
    fprintf(fid,'\n')
end
%STEP (3.3.1) Detect how many and which sub-regions have non-zero
%activity/volumetric activity
%The following loop will detect how many sub-regions have a non-zero
%volumetric activity
countnonzero = 0;
for i4 = 1:n_regions_total
    if (A_V(i4,i1+1)~=0)
        countnonzero = countnonzero + 1;
    end
end
%The following loop will record which particular sub-regions have
%non-zero volumetric activity
countindices = zeros(countnonzero,1);
i6 = 0;
for i5 = 1:n_regions_total
    if (A_V(i5,i1+1)~=0)
        i6 = i6 + 1;
        countindices(i6,1) = i5;
    end
end
%The following loop will state the SI card for the different sources
%that will be inserted in the position of the active sub-regions
fprintf(fid,'%s','SI1 S ')
for i7 = 2:(countnonzero+1)
    fprintf(fid,'%d',i7)
    fprintf(fid,'%s',' ')
end
fprintf(fid,'\n')
%The following will state the bias that each sub-region possesses
fprintf(fid,'%s','SP1 ')
fprintf(fid,'%d',BiasMatrix(countindices(1,1),i1+1))
fprintf(fid,'%s',' $')
fprintf(fid,'\n')
for i8 = 2:countnonzero
    fprintf(fid,'%s',' ')
    fprintf(fid,'%d',BiasMatrix(countindices(i8,1),i1+1))
    fprintf(fid,'%s',' $')
    fprintf(fid,'\n')
end
%The following will now state the x-coordinate bounds of each active
%sub-region
for i9 = 2:(countnonzero+1)
    fprintf(fid,'%s','SI')
    fprintf(fid,'%d',i9)
    fprintf(fid,'%s',' ')
    fprintf(fid,'%d',BoundsMatrix(countindices(i9-1,1),1))
    fprintf(fid,'%s',' ')
    fprintf(fid,'%d',BoundsMatrix(countindices(i9-1,1),2))
    fprintf(fid,'\n')
    fprintf(fid,'%s','SP')
    fprintf(fid,'%d',i9)
    fprintf(fid,'%s',' ')
    fprintf(fid,'%s','0 1')
    fprintf(fid,'\n')
end

```

```

end
%The following will state the DS card for each active sub-region
fprintf(fid,'%s','DS91 S ')
for i10 = (i7+1):1:(countnonzero+i7)
    fprintf(fid,'%d',i10)
    fprintf(fid,'%s',' ')
end
fprintf(fid,'\n')
%The following will now state the y-coordinate bounds of each active
%sub-region
i12 = 0;
for i11 = (i7+1):1:(countnonzero+i7)
    i12 = i12 + 1;
    fprintf(fid,'%s','SI')
    fprintf(fid,'%d',i11)
    fprintf(fid,'%s',' ')
    fprintf(fid,'%d',BoundsMatrix(countindices(i12,1),3))
    fprintf(fid,'%s',' ')
    fprintf(fid,'%d',BoundsMatrix(countindices(i12,1),4))
    fprintf(fid,'\n')
    fprintf(fid,'%s','SP')
    fprintf(fid,'%d',i11)
    fprintf(fid,'%s',' ')
    fprintf(fid,'%s','0 1')
    fprintf(fid,'\n')
end
%The following will state the DS card for each active sub-region
fprintf(fid,'%s','DS92 S ')
for i13 = (i11+1):1:(countnonzero+i11)
    fprintf(fid,'%d',i13)
    fprintf(fid,'%s',' ')
end
fprintf(fid,'\n')
%The following will now state the z-coordinate bounds of each active
%sub-region
i14 = 0;
for i15 = (i11+1):1:(countnonzero+i11)
    i14 = i14 + 1;
    fprintf(fid,'%s','SI')
    fprintf(fid,'%d',i15)
    fprintf(fid,'%s',' ')
    fprintf(fid,'%d',BoundsMatrix(countindices(i14,1),5))
    fprintf(fid,'%s',' ')
    fprintf(fid,'%d',BoundsMatrix(countindices(i14,1),6))
    fprintf(fid,'\n')
    fprintf(fid,'%s','SP')
    fprintf(fid,'%d',i15)
    fprintf(fid,'%s',' ')
    fprintf(fid,'%s','0 1')
    fprintf(fid,'\n')
end
%The following will now state the outstanding information required for
%the appropriate completion of the MCNPX input deck
fprintf(fid,'%s','nps 1000000') %number of source particles
fprintf(fid,'\n')
fprintf(fid,'%s','m1 1001.50c -6.2 6000.50c -44.5 8016.50c -49.3') %Material Information for Plywood
fprintf(fid,'\n')
fprintf(fid,'%s','m2 1001.50c -1.18 7014.50c -77.08 8016.50c -21.28 18000.35c -0.46') %Material Information for
Air
fprintf(fid,'\n')
fprintf(fid,'%s','F5:p 70 8 -638 1') %Declaration of Photon Tally Detctor Location #1
fprintf(fid,'\n')

```

```

fprintf(fid,'%s','F15:p 70 8 -738 1') %Declaration of Photon Tally Detctor Location #2
fprintf(fid,'\n')
fprintf(fid,'%s','DF5 iu=2 fac=1 ic=31') %Conversion of Detector 1 reading to Dose
fprintf(fid,'\n')
fprintf(fid,'%s','DF15 iu=2 fac=1 ic=31') %Conversion of Detector 2 reading to Dose

fclose(fid); %Close the file
end

```

External_Dose.m

Calculates the time-integrated external dose at each detector location

```

%Name: Fawaz Ali
%MATLAB Code for MCSC Thesis
%Purpose of Code: Create a MATLAB code that calculates (a) the EXTERNAL
%DOSE RATE at each detector and for each time step iteration and (b) the
%time-integrated external dose
%=====
format long e %this will allow for the use of more significant figures
%Step (1) State the required information
%-----
n_regions = 28; %this stores the number of sub-regions in the domain
n_symmetry = 13; %this stores the number of sub-regions that have been
    %dissected by the symmetry plane
n_rakes = 6; %this stores the number of rakes
n_steps = 10; %this stores the number of time steps for which the radiation
    %field in the domain will be analyzed
%The following calculates the TOTAL number of sub-regions in the domain
n_regions_total = (2*n_regions) - n_symmetry;
%Step (2) Import the required data
%-----
%The Volumetric Activity (units: Bq/m^3) for each sub-region and for each
%time step will be required
A_V = importdata('ActivityBqV.txt');
%The Gamma Energy Spectrum for La-140 will also be needed. More
%specifically, the Gamma yeild will also be required
Gamma_ES = importdata('Gamma_Energy_Spectrum.txt');
%The volume of each sub-region will be required
Volume = importdata('VolumeData.txt');
%The time value for each aerosol tracking step will be required
TimeValues = importdata('Time.txt');
%The following converts the above time values to hours
TimeValuesNew = TimeValues./3600;
%Step (3) State the required MCNPX Tally Data
%-----
Tally_1 = zeros(n_steps,1); %this will store the tally data at point (70,8,-638)
Tally_2 = zeros(n_steps,1); %this will store the tally data at point (70,8,-738)

%The following will populate 'Tally_1'
Tally_1(1,1) = 1.9409E-13;
Tally_1(2,1) = 1.5039E-13;
Tally_1(3,1) = 9.8870E-13;
Tally_1(4,1) = 1.0268E-12;
Tally_1(5,1) = 4.5490E-13;
Tally_1(6,1) = 6.0577E-13;
Tally_1(7,1) = 2.9369E-13;
Tally_1(8,1) = 4.5918E-13;
Tally_1(9,1) = 2.1279E-13;
Tally_1(10,1) = 1.9893E-13;
%The following will populate 'Tally_2'
Tally_2(1,1) = 7.0341E-14;

```

```

Tally_2(2,1) = 1.0816E-12;
Tally_2(3,1) = 6.0047E-13;
Tally_2(4,1) = 5.4730E-13;
Tally_2(5,1) = 8.0207E-13;
Tally_2(6,1) = 3.8671E-13;
Tally_2(7,1) = 4.8957E-13;
Tally_2(8,1) = 2.7513E-13;
Tally_2(9,1) = 4.5273E-13;
Tally_2(10,1) = 4.7782E-14;
%Step (4) Calculate te Gamma Yield for La-140
%-----
GammaYield = 0; %This will store the Gamma Yield
%The following loop will calculate the abovementioned quantity
for i1 = 1:1:length(Gamma_ES);
    GammaYield = GammaYield + Gamma_ES(i1,1);
end
%Step (5) Calculate the DOSE RATE (units: Sv/hr) for each time step
%-----
DoseRate = zeros(n_steps,2); %The following matrix will store the dose rate at each time step for each dose point
for i2 = 1:1:n_steps
    %STEP (5.1) Find how many sub-regions are active
    countnonezero = 0;
    for i3 = 1:1:n_regions_total
        if (A_V(i3,i2+1) ~= 0)
            countnonezero = countnonezero + 1;
        end
    end
    %STEP (5.2) For each active sub-region, store the sub-region number
    countindices = zeros(countnonezero,1);
    j1 = 0;
    for i4 = 1:1:n_regions_total
        if (A_V(i4,i2+1) ~= 0)
            j1 = j1 + 1;
            countindices(j1,1) = i4;
        end
    end
    %STEP (5.3) Calculate the TOTAL Volumetric Activity from each active
    %sub-region
    VolumetricActivitySum = 0;
    for i5 = 1:1:countnonezero
        VolumetricActivitySum = VolumetricActivitySum + A_V(countindices(i5,1),i2+1);
    end
    %STEP (5.4) Calculate the TOTAL Volume from each active sub-region
    VolumeSum = 0;
    for i6 = 1:1:countnonezero
        VolumeSum = VolumeSum + Volume(countindices(i6,1),2);
    end
    %STEP (5.5) Calculate the DOSE RATE at each time step and for each dose
    %point
    DoseRate(i2,1) = Tally_1(i2,1)*VolumetricActivitySum*VolumeSum*GammaYield; %Calculations for dose point 1
    DoseRate(i2,2) = Tally_2(i2,1)*VolumetricActivitySum*VolumeSum*GammaYield; %Calculations for dose point 2
end
%Step (6) Calculate the CUMULATIVE EXTERNAL DOSE (units: Sv)
%-----
CumulativeDose1 = 0; %stores the cumulative external dose delivered at point 1
CumulativeDose2 = 0; %stores the cumulative external dose delivered at point 2
%The following will be used to compute the above two quantities
temp1 = 0;
temp2 = 0;
%STEP (6.1) Calculate the cumulative external dose delivered to point 1
%(coordinates = (70,8,-638))
for i7 = 1:1:(n_steps-1)

```

```

    delta_t = TimeValuesNew(i7+1,1) - TimeValuesNew(i7,1); %Calculate the change in time between adjacent data
    points
    delta_D_rate = abs(DoseRate(i7+1,1) - DoseRate(i7,1)); %Calculate the change in dose rate between adjacent data
    points
    %Determine which data point, of the two adjacent data points, has the smallest dose rate
    if (DoseRate(i7+1,1) <= DoseRate(i7,1))
        temp1 = DoseRate(i7+1,1);
    else
        temp1 = DoseRate(i7,1);
    end
    %The following calculates the cumulative external dose
    CumulativeDose1 = CumulativeDose1 + (0.5*delta_t*delta_D_rate) + (delta_t*temp1);
end
%STEP (6.2) Calculate the cumulative external dose delivered to point 2
%(coordinates = (70,8,-738))
for i8 = 1:1:(n_steps-1)
    delta_t = TimeValuesNew(i8+1,1) - TimeValuesNew(i8,1); %Calculate the change in time between adjacent data
    points
    delta_D_rate = abs(DoseRate(i8+1,2) - DoseRate(i8,2)); %Calculate the change in dose rate between adjacent data
    points
    %Determine which data point, of the two adjacent data points, has the
    %smallest dose rate
    if (DoseRate(i8+1,2) <= DoseRate(i8,2))
        temp2 = DoseRate(i8+1,2);
    else
        temp2 = DoseRate(i8,2);
    end
    %The following calculates the cumulative external dose
    CumulativeDose2 = CumulativeDose2 + (0.5*delta_t*delta_D_rate) + (delta_t*temp2);
end
%STEP (6.3) Convert the cumulative external doses to uSv
CumulativeDose1uSv = CumulativeDose1/1E-6;
CumulativeDose2uSv = CumulativeDose2/1E-6;
%Step (7) Output the External Dose to 'ExternalDose.txt'
%-----
fid = fopen('ExternalDose.txt','wt') ; %Opens the File
fprintf(fid,'%e',CumulativeDose1); %States the External Dose at (70,8,-638)
fprintf(fid,'\n')
fprintf(fid,'%e',CumulativeDose2); %States the External Dose at (70,8,-738)
fclose(fid); %Close the File

```

Internal_Dose.m

Calculates the time-integrated internal dose at each detector location

```

%Name: Fawaz Ali
%MATLAB Code for MCSC Thesis
%Purpose of Code: Create a MATLAB code that calculates (a) the INTERNAL
%DOSE RATE at each detector and for each time step and (b) the
%time-integrated internal dose
%=====
format long e %this will allow for the use of more significant figures
%Step (1) State the required information
%-----
n_region_1 = 15; %this is the sub-region number that dose point 1 (coordinates = (70,8,-638)) is placed in
n_region_2 = 21; %this is the sub-region number that dose point 2 (coordinates = (70,8,-738)) is placed in
n_steps = 10; %this stores the number of time steps for which the radiation
    %field in the domain will be analyzed
BR = 1.2; %This is the breathing rate for an adult
DCF = 1.10E-09; %This is the dose conversion factor (DCF) for La-140
%Step (2) Important the required data
%-----

```

```

%The Volumetric Activity (units: Bq/m^3) for each sub-region and for each
%time step will be required
A_V = importdata('ActivityBqV.txt');
%The time value for each aerosol tracking step will be required
TimeValues = importdata('Time.txt');
%The following converts the above time values to hours
TimeValuesNew = TimeValues./3600;
%Step (3) Calculate the INTERNAL DOSE RATE (units: Sv/hr) at each dose
%point for each time step
%-----
%The following will store the dose rate for each dose point and at each
%time step
DoseRate = zeros(n_steps,2);
%The following loop will calculate the abovementioned quantity for dose
%point 1
for i1 = 1:1:n_steps
    DoseRate(i1,1) = A_V(n_region_1,i1+1)*BR*DCF;
end
%The following loop will calculate the abovementioned quantity for dose
%point 2
for i2 = 1:1:n_steps
    DoseRate(i2,2) = A_V(n_region_2,i2+1)*BR*DCF;
end
%Step (4) Calculate the CUMULATIVE INTERNAL DOSE (units: Sv) at each dose
%point
%-----
%The following will store the internal cumulative dose for each dose point,
%respectively
CumulativeInternalDose1 = 0;
CumulativeInternalDose2 = 0;
%The following will be used to compute the above quantities
temp1 = 0;
temp2 = 0;
%STEP (4.1) Calculate the cumulative internal dose delivered to point 1
%(coordinates = (70,8,-638))
for i3 = 1:1:(n_steps-1)
    delta_t1 = TimeValuesNew(i3+1,1) - TimeValuesNew(i3,1); %Calculate the change in time between adjacent data
points
    delta_D_rate1 = abs(DoseRate(i3+1,1) - DoseRate(i3,1)); %Calculate the change in dose rate between adjacent data
points
    %Determine which data point, of the two adjacent data points, has the
    %smallest dose rate
    if (DoseRate(i3+1,1) <= DoseRate(i3,1))
        temp1 = DoseRate(i3+1,1);
    else
        temp1 = DoseRate(i3,1);
    end
    %The following calculates the cumulative internal dose
    CumulativeInternalDose1 = CumulativeInternalDose1 + (0.5*delta_t1*delta_D_rate1) + (delta_t1*temp1);
end
%STEP (4.2) Calculate the cumulative internal dose delivered to point 2
%(coordinates = (70,8,-738))
for i4 = 1:1:(n_steps-1)
    delta_t2 = TimeValuesNew(i4+1,1) - TimeValuesNew(i4,1); %Calculate the change in time between adjacent data
points
    delta_D_rate2 = abs(DoseRate(i4+1,2) - DoseRate(i4,2)); %Calculate the change in dose rate between adjacent data
points
    %Determine which data point, of the two adjacent data points, has the
    %smallest dose rate
    if (DoseRate(i4+1,2) <= DoseRate(i4,2))
        temp2 = DoseRate(i4+1,2);
    else

```

```

temp2 = DoseRate(i4,2);
end
%The following calculates the cumulative internal dose
CumulativeInternalDose2 = CumulativeInternalDose2 + (0.5*delta_t2*delta_D_rate2) + (delta_t2*temp2);
end
%STEP (4.3) Convert the cumulative internal doses to mSv
CumulativeInternalDose1mSv = CumulativeInternalDose1/1E-3;
CumulativeInternalDose2mSv = CumulativeInternalDose2/1E-3;
%Step (5) Output the Internal Dose to 'InternalDose.txt'
%-----
fid = fopen('InternalDose.txt','wt') ; %Opens the File
fprintf(fid,'%e',CumulativeInternalDose1); %States the Internal Dose at (70,8,-638)
fprintf(fid,'\n')
fprintf(fid,'%e',CumulativeInternalDose2); %States the Internal Dose at (70,8,-738)
fclose(fid); %Close the File

```

DCF.m

Calculates the surface activity-to-dose conversion factor at each detector location

```

%Name: Fawaz Ali
%MATLAB Code for MCSC Thesis
%Purpose of Code: Calculate the surface activity-to-dose conversion factor
%at each detector location
%=====
format long e %this will allow for the use of more significant figures
%Step (1) Declare the required information
%-----
n_rakes = 6; %this stores the number of rakes
np = 100; %this stores the number of particulates released per rake
npoints = 2; %this stores the number of dose points
%The following stores nuclear radiation data for La-140
T_Half = 40.220; %Half Life of La-140 (units: hours)
N_A = 6.023E23; %Avogadro's Number (units: atoms/mol)
Density = 6.19; %Density of La-140 (units: g/cc)
M_M = 138.906; %Molar Mass of La-140 (units: g/mol)
%The following stores the diameter of the particulates from each rake
diameters = zeros(n_rakes,1);
%The following will populate the above vector
diameters(1,1) = 1E-6;
diameters(2,1) = 2E-6;
diameters(3,1) = 3E-6;
diameters(4,1) = 4E-6;
diameters(5,1) = 5E-6;
diameters(6,1) = 6E-6;
%Step (2) Calculate the Activity on the Plate
%-----
ActivityPlate = 0; %The following will store the activity on the plate
%The following loop will calculate the activity of each rake
for i1 = 1:1:n_rakes
    ActivityPlate = ActivityPlate +
(np*(1/6)*(pi)*(diameters(i1,1)^3)*(100^3)*(log(2))*N_A*Density/(T_Half*3600*M_M));
end
%Step (3) Calculate the Surface Activity on the Plate
%-----
%The following will store this quantity
SurfaceActivity = 0;
%The following store the area of the plate (units:m^2)
AreaPlate = 1;
%The following will calculate the Surface Activity on the Plate
SurfaceActivity = ActivityPlate/AreaPlate;
%The following will re-calculate the surface activity by including the

```

```

%%presence of symmetry
SurfaceActivity = 2*SurfaceActivity;
%Step (4) Import the External and Internal Dose Quantities
%-----
ExternalDose = importdata('ExternalDose.txt');
InternalDose = importdata('InternalDose.txt');
%The following will store the Dose Conversion Factor for the External Dose
%data
DCF_External = zeros(npoints,1);
%The following loop will populate the above vector
for i2 = 1:1:npoints
    DCF_External(i2,1) = ExternalDose(i2,1)/SurfaceActivity;
end
%The following will store the Dose Conversion Factor for the Internal Dose
%data
DCF_Internal = zeros(npoints,1);
%The following loop will populate the above vector
for i3 = 1:1:npoints
    DCF_Internal(i3,1) = InternalDose(i3,1)/SurfaceActivity;
end

```

Point_Source_Dose_Calculation.m

Calculates the time-integrated point source dose at each detector location

```

%Name: Fawaz Ali
%MATLAB Code for MCSC Thesis
%Purpose of Code: To calculate the time-integrated external dose via the
%point source analytical technique, at each detector location
%=====
format long e %this will allow for the use of more significant figures
%Step (1) State the required information
%-----
n_steps = 10; %this stores the number of time steps for which the radiation
    %field in the domain will be analyzed
n_regions = 28; %this stores the number of sub-regions in the domain
n_symmetry = 13; %this stores the number of sub-regions that have been
    %dissected by the symmetry plane
%The following calculates the TOTAL number of sub-regions in the domain
n_regions_total = (2*n_regions) - n_symmetry;
%The following is the conversion factor to convert gamma fluence to
%gamma dose (units: Sv-cm^2/gamma)
CF = 5.2E-12;
%Step (2) Import the required data
%-----
%The Volumetric Activity (units: Bq/m^3) for each sub-region and for each
%time step will be required
Activity_V = importdata('ActivityBqV.txt');
%The volume of each sub-region will be required
Volume = importdata('VolumeData.txt');
%The time value for each aerosol tracking step will be required
TimeValues = importdata('Time.txt');
%The following will import the spatial bounds of each partition
BoundsPartition = importdata('Bounds.txt');
%Step (3) Calculate 'd_bar'
%-----
%Step (3.1) Calculate the centroid of each partition
%The following will store the x, y, and z coordinate of each partition's
%centroid, respectively
x = zeros(n_regions_total,1);
y = zeros(n_regions_total,1);
z = zeros(n_regions_total,1);

```

```

%The following loop will populate the above vectors
for i1 = 1:1:n_regions_total
    x(i1,1) = 0.5*(BoundsPartition(i1,1) + BoundsPartition(i1,2));
    y(i1,1) = 0.5*(BoundsPartition(i1,3) + BoundsPartition(i1,4));
    z(i1,1) = 0.5*(BoundsPartition(i1,5) + BoundsPartition(i1,6));
end
%Step (3.2) Compute the distance between detector location 1 and 2 and each
%partition's centroid
%The following stores the (x,y,z) coordinates of detector 1
x_d1 = 70;
y_d1 = 8;
z_d1 = -638;
%The following stores the (x,y,z) coordinates of detector 2
x_d2 = 70;
y_d2 = 8;
z_d2 = -738;
%The following vectors will store the distance (in x, y, and z dimensions)
%from detector 1 and 2 to each partition, respectively
distance_d1 = zeros(n_regions_total,3);
distance_d2 = zeros(n_regions_total,3);
%The following loop populates the above vectors
for i2 = 1:1:n_regions_total
    distance_d1(i2,1) = x_d1 - x(i2,1);
    distance_d1(i2,2) = y_d1 - y(i2,1);
    distance_d1(i2,3) = z_d1 - z(i2,1);
    distance_d2(i2,1) = x_d2 - x(i2,1);
    distance_d2(i2,2) = y_d2 - y(i2,1);
    distance_d2(i2,3) = z_d2 - z(i2,1);
end
%The following will compute the magnitude of the distance between detector
%1 and 2 to each partition, respectively
distance_d1_magnitude = zeros(n_regions_total,1);
distance_d2_magnitude = zeros(n_regions_total,1);
%The following loop populates the above vectors
for i3 = 1:1:n_regions_total
    distance_d1_magnitude(i3,1) = sqrt((distance_d1(i3,1)^2) + (distance_d1(i3,2)^2) + (distance_d1(i3,3)^2));
    distance_d2_magnitude(i3,1) = sqrt((distance_d2(i3,1)^2) + (distance_d2(i3,2)^2) + (distance_d2(i3,3)^2));
end
%The following vectors will store the sum of the products of the distance
%of a detector to a partition and the partition's volumetric activity, for
%each respective detector
d_bar_d1_num = zeros(n_steps,1);
d_bar_d2_num = zeros(n_steps,1);
%The following loop populates the above vectors
for i4 = 1:1:n_steps
    for i5 = 1:1:n_regions_total
        d_bar_d1_num(i4,1) = d_bar_d1_num(i4,1) + (distance_d1_magnitude(i5,1)*Activity_V(i5,i4+1));
        d_bar_d2_num(i4,1) = d_bar_d2_num(i4,1) + (distance_d2_magnitude(i5,1)*Activity_V(i5,i4+1));
    end
end
%The following will store the total volumetric activity in the wind tunnel
%at each time step
d_bar_den = zeros(n_steps,1);
%The following loop will populate the above vector
for i6 = 1:1:n_steps
    for i7 = 1:1:n_regions_total
        d_bar_den(i6,1) = d_bar_den(i6,1) + Activity_V(i7,i6+1);
    end
end
%The following vectors will hold the volumetric activity weighted average
%distance from each detector location to the centre of the sphere
d_bar_d1 = zeros(n_steps,1);

```

```

d_bar_d2 = zeros(n_steps,1);
%The following loop populates the above vectors
for i8 = 1:1:n_steps
    d_bar_d1(i8,1) = d_bar_d1_num(i8,1)/d_bar_den(i8,1);
    d_bar_d2(i8,1) = d_bar_d2_num(i8,1)/d_bar_den(i8,1);
end
%Step (4) Calculate 'A_v_bar'
%-----
%Step (4.1) Calculate the total volume of the partitions
%The following will store the abovementioned quantity
VolumeTotal = 0;
%The following loop will populate the above quantity
for i9 = 1:1:n_regions_total
    VolumeTotal = VolumeTotal + Volume(i9,2);
end
%Step (4.2) Calculate the sum of the products of the partition's volume and
%the volumetric activity of that partition, for each time step
%The following vector will store the above quantity
Activity_bar_num = zeros(n_steps,1);
%The following will populate the above vector
for i10 = 1:1:n_steps
    for i11 = 1:1:n_regions_total
        Activity_bar_num(i10,1) = Activity_bar_num(i10,1) + (Activity_V(i11,i10+1)*Volume(i11,2));
    end
end
%Step (4.3) Calculate the volume weighted average volumetric activity for
%each time step
%The following vector will store the above quantity
Activity_bar = zeros(n_steps,1);
%The following will populate the above vector
for i12 = 1:1:n_steps
    Activity_bar(i12,1) = Activity_bar_num(i12,1)/VolumeTotal;
end
%Step (5) Calculate the Gamma Flux at each time step and at each detector
%-----
%Step (5.1) Calculate the Gamma Flux normalized to the effective volume
%The following vectors will store the gamma flux at each detector
Flux1 = zeros(n_steps,1);
Flux2 = zeros(n_steps,1);
%The following will populate the above vectors
for i13 = 1:1:n_steps
    Flux1(i13,1) = Activity_bar(i13,1)/(4*pi*(d_bar_d1(i13,1)^2));
    Flux2(i13,1) = Activity_bar(i13,1)/(4*pi*(d_bar_d2(i13,1)^2));
end
%Step (5.2) Calculate the Gamma Flux by multiplying the Gamma Flux,
%normalized to the effective volume, by the effective volume
%First, calculate the effective volume at each time step. The following
%vector will hold this quantity
V_eff = zeros(n_steps,1);
%The following vector will store the numerator of the effective volume
%equation, which will be the product of the Volumetric Activity of the ith
%partition and the volume of the ith partition
V_eff_num = zeros(n_steps,1);
%The following loop will populate the above vector
for i14 = 1:1:n_steps
    for i15 = 1:1:n_regions_total
        V_eff_num(i14,1) = V_eff_num(i14,1) + (Activity_V(i15,i14+1)*Volume(i15,2));
    end
end
%The following vector will store the sum of the Volumetric Activity over
%all partitions, at each time step
A_V_total = zeros(n_steps,1);

```

```

%The following loop will populate the above vector
for i16 = 1:1:n_steps
    for i17 = 1:1:n_regions_total
        A_V_total(i16,1) = A_V_total(i16,1) + Activity_V(i17,i16+1);
    end
end
%The following loop will calculate the effective volume at each time step
for i18 = 1:1:n_steps
    V_eff(i18,1) = V_eff_num(i18,1)/A_V_total(i18,1);
end
%The following loop will calculate the Gamma Flux at each time step
for i19 = 1:1:n_steps
    Flux1(i19,1) = Flux1(i19,1)*V_eff(i19,1);
    Flux2(i19,1) = Flux2(i19,1)*V_eff(i19,1);
end
%Step (6) Calculate the external dose rate at each detector
%-----
%The following will store the external dose rate at each detector location,
%respectively
DoseRate1 = zeros(n_steps,1);
DoseRate2 = zeros(n_steps,1);
%The following will populate the above vectors
for i20 = 1:1:n_steps
    DoseRate1(i20,1) = Flux1(i20,1)*CF;
    DoseRate2(i20,1) = Flux2(i20,1)*CF;
end
%Step (7) Calculate the time-integrated external dose at each detector
%-----
%The following will store the time-integrated external dose each detector,
%respectively
CumDose1 = 0;
CumDose2 = 0;
%The following will assist in calculating the above quantities
temp1 = 0;
temp2 = 0;
%The following will calculate the time-integrated external dose at detector
%1
for i21 = 1:1:(n_steps-1)
    delta_t1 = TimeValues(i21+1,1) - TimeValues(i21,1);
    delta_D1 = abs(DoseRate1(i21+1,1) - DoseRate1(i21,1));
    if (DoseRate1(i21,1) <= DoseRate1(i21+1,1))
        temp1 = DoseRate1(i21,1);
    else
        temp1 = DoseRate1(i21+1,1);
    end
    CumDose1 = CumDose1 + (0.5*delta_D1*delta_t1) + (temp1*delta_t1);
end
%The following will calculate the time-integrated external dose at detector
%2
for i22 = 1:1:(n_steps-1)
    delta_t2 = TimeValues(i22+1,1) - TimeValues(i22,1);
    delta_D2 = abs(DoseRate2(i22+1,1) - DoseRate2(i22,1));
    if (DoseRate2(i22,1) <= DoseRate2(i22+1,1))
        temp2 = DoseRate2(i22,1);
    else
        temp2 = DoseRate2(i22+1,1);
    end
    CumDose2 = CumDose2 + (0.5*delta_D2*delta_t2) + (temp2*delta_t2);
end

%Step (8) Convert the time-integrated external doses to uSv
%-----

```

```
CumDose1uSv = CumDose1/1E-6;  
CumDose2uSv = CumDose2/1E-6;
```

Submersion_Dose_Calculation_MCNPX.m

Calculates the submersion dose at each detector location

```
%Name: Fawaz Ali  
%MATLAB Code for MCSC Thesis  
%Purpose of Code: To calculate the time-integrated external dose via the  
%submersion source technique, at each detector location  
%=====
```

format long e %this will allow for the use of more significant figures
%Step (1) State the required information
%-----

```
n_steps = 10; %this stores the number of time steps for which the radiation  
%field in the domain will be analyzed  
%Step (2) Import the required data  
%-----
```

%The spatially averaged volumetric activity (units: Bq/m³) will be
%required
A_V_Weighted = importdata('SpatiallyAveraged_A_V.txt');
%The Gamma Energy Spectrum for La-140 will also be needed. More
%specifically, the Gamma yeild will be required
Gamma_ES = importdata('Gamma_Energy_Spectrum.txt');
%The volume of each partition is required. More specifically, the total
%volume of the region of the wind tunnel that is being partitioned is
%required
Volume = importdata('VolumeData.txt');
%The following stores the external normalized dose rate at each detector
%location, respectively
Tally_1 = 1.8530E-13;
Tally_2 = 1.9075E-13;
%The time value for each aerosol tracking step will be required
TimeValues = importdata('Time.txt');
%The following converts the above time values to hours
TimeValuesNew = TimeValues./3600;
%Step (3) Calculate the required quantities
%-----

%The following calculates the Gamma Yield
GammaYield = 0;
for i1 = 1:length(Gamma_ES)
GammaYield = GammaYield + Gamma_ES(i1,1);
end
%The following calculates the total volume of the region of the wind tunnel
%that has been partitioned
VolumeTotal = 0;
for i2 = 1:length(Volume)
VolumeTotal = VolumeTotal + Volume(i2,2);
end
%Step (4) Calculate the external dose rate at each time step
%-----

%The following stores the external dose rates at each detector location,
%respectively
DoseRate_1 = zeros(n_steps,1);
DoseRate_2 = zeros(n_steps,1);
%The following calculates the dose rate at the first detector location
for i3 = 1:n_steps
DoseRate_1(i3,1) = Tally_1*GammaYield*A_V_Weighted(i3,1)*VolumeTotal;
end
%The following calculates the dose rate at the second detector location
for i4 = 1:n_steps

```

DoseRate_2(i4,1) = Tally_2*GammaYield*A_V_Weighted(i4,1)*VolumeTotal;
end
%Step (5) Calculate the time-integrated external dose at each detector
%location
%-----
%The following will assist in computing the above quantities
temp1 = 0;
temp2 = 0;
%The following will store the time-integrated external dose rate at each
%detector location, respectively
CumSub1 = 0;
CumSub2 = 0;
%The following loop computes the time-integrated external at the
%first detector location
for i5 = 1:1:(n_steps-1)
    delta_DR_1 = abs(DoseRate_1(i5+1,1) - DoseRate_1(i5,1));
    delta_t1 = TimeValuesNew(i5+1,1) - TimeValuesNew(i5,1);
    if (DoseRate_1(i5,1) <= DoseRate_1(i5+1,1))
        temp1 = DoseRate_1(i5,1);
    else
        temp1 = DoseRate_1(i5+1,1);
    end
    CumSub1 = CumSub1 + (0.5*delta_DR_1*delta_t1) + (temp1*delta_t1);
end
%The following loop computes the time-integrated external dose at the
%second detector location
for i6 = 1:1:(n_steps-1)
    delta_DR_2 = abs(DoseRate_2(i6+1,1) - DoseRate_2(i6,1));
    delta_t2 = TimeValuesNew(i6+1,1) - TimeValuesNew(i6,1);
    if (DoseRate_2(i6,1) <= DoseRate_2(i6+1,1))
        temp2 = DoseRate_2(i6,1);
    else
        temp2 = DoseRate_2(i6+1,1);
    end
    CumSub2 = CumSub2 + (0.5*delta_DR_2*delta_t2) + (temp2*delta_t2);
end
%Step (6) Convert the time-integrated external doses to uSv
%-----
CumSub1uSv = CumSub1/1E-6;
CumSub2uSv = CumSub2/1E-6;

```

1

MCNPX input file for time step iteration 1

CFD-MCNPX Integration

C Cell Cards

```

10 1 -0.65 -1          imp:p=1   $Plate
20 1 -0.65 -2          imp:p=1   $Bluff body
30 2 -0.001236 -3 -4 -5 #(-1) #(-2)  imp:p=1   $Wind Tunnel with Plate and Bluff Body
40 0 3:4:5 #(-1) #(-2)  imp:p=0   $Outside of Wind Tunnel with Plate and Bluff Body

```

C Surface Cards

```

1 RPP 20 120 0 0.2 -572 -472 $Plate
2 RPP 12 128 0 32 -588 -572 $Bluff Body
3 RPP 0 140 0 143 -1004 0 $Wind Tunnel
4 1 py 0          $Plane for Indent 1
5 2 py 0          $Plane for Indent 2

```

```

*tr1  0 85 0 -60.362 29.638 90 -150.362 -60.362 90 90 0 1 $Transformation for Indent 1
*tr2  140 85 0 60.362 150.362 90 -29.638 60.362 90 90 0 1 $Transformation for Indent 2
C

```

C Data Cards

mode p

SDEF X=D1 Y=fx=D91 Z=fx=D92 ERG=D90

SI90 L 2.547100e+000 \$

1.735500e-001 \$
1.094200e-001 \$
4.840000e-003 \$
3.930000e-002 \$
1.208000e+000 \$
2.419700e-001 \$
3.427900e-002 \$
2.665500e-001 \$
9.509000e-001 \$
1.311200e-001 \$
2.348800e+000 \$
3.472000e-002 \$
9.196300e-001 \$
4.325300e-001 \$
2.521700e+000 \$
7.517900e-001 \$
8.678200e-001 \$
9.252400e-001 \$
3.287700e-001 \$
8.158500e-001 \$
4.870300e-001 \$
1.596500e+000 \$

SP90 D 1.041000e-003 \$

1.241000e-003 \$
1.910000e-003 \$
2.549000e-003 \$
3.223000e-003 \$
4.163000e-003 \$
4.297000e-003 \$
4.718000e-003 \$
4.870000e-003 \$
5.347000e-003 \$
5.538000e-003 \$
8.508000e-003 \$
8.656000e-003 \$
2.883800e-002 \$
2.941100e-002 \$
3.456700e-002 \$
4.402100e-002 \$
5.633900e-002 \$
7.085400e-002 \$
2.053000e-001 \$
2.349100e-001 \$
4.554900e-001 \$
9.549000e-001 \$

SII S 2 3 4 5 6 7 8 9 10 11 12 13 14 15

SP1 2.362665e-002 \$

2.871295e-001 \$
1.660166e-002 \$
1.489214e-001 \$
2.195849e-002 \$
8.789113e-003 \$
1.207585e-003 \$
5.489623e-003 \$
2.362665e-002 \$
2.871295e-001 \$
1.660166e-002 \$
1.489214e-001 \$

8.789113e-003 \$
1.207585e-003 \$
SI2 0 20
SP2 0 1
SI3 0 12
SP3 0 1
SI4 0 12
SP4 0 1
SI5 0 12
SP5 0 1
SI6 12 128
SP6 0 1
SI7 0 12
SP7 0 1
SI8 0 12
SP8 0 1
SI9 12 128
SP9 0 1
SI10 120 140
SP10 0 1
SI11 128 140
SP11 0 1
SI12 128 140
SP12 0 1
SI13 128 140
SP13 0 1
SI14 128 140
SP14 0 1
SI15 128 140
SP15 0 1
DS91 S 16 17 18 19 20 21 22 23 24 25 26 27 28 29
SI16 1 32
SP16 0 1
SI17 1 32
SP17 0 1
SI18 0 1
SP18 0 1
SI19 1 32
SP19 0 1
SI20 32 85
SP20 0 1
SI21 0 1
SP21 0 1
SI22 1 32
SP22 0 1
SI23 32 85
SP23 0 1
SI24 1 32
SP24 0 1
SI25 1 32
SP25 0 1
SI26 0 1
SP26 0 1
SI27 1 32
SP27 0 1
SI28 0 1
SP28 0 1
SI29 1 32
SP29 0 1
DS92 S 30 31 32 33 34 35 36 37 38 39 40 41 42 43
SI30 -572 -472
SP30 0 1

SI31 -588 -572
 SP31 0 1
 SI32 -688 -588
 SP32 0 1
 SI33 -688 -588
 SP33 0 1
 SI34 -688 -588
 SP34 0 1
 SI35 -788 -688
 SP35 0 1
 SI36 -788 -688
 SP36 0 1
 SI37 -788 -688
 SP37 0 1
 SI38 -572 -472
 SP38 0 1
 SI39 -588 -572
 SP39 0 1
 SI40 -688 -588
 SP40 0 1
 SI41 -688 -588
 SP41 0 1
 SI42 -788 -688
 SP42 0 1
 SI43 -788 -688
 SP43 0 1
 nps 1000000
 m1 1001.50c -6.2 6000.50c -44.5 8016.50c -49.3
 m2 1001.50c -1.18 7014.50c -77.08 8016.50c -21.28 18000.35c -0.46
 F5:p 70 8 -638 1
 F15:p 70 8 -738 1
 DF5 iu=2 fac=1 ic=31
 DF15 iu=2 fac=1 ic=31

SM

MCNPX input file for submersion dose calculation

Submersion Dose Calculation

C Cell Cards

10 1 -0.65 -1 imp:p=1 \$Plate
 20 1 -0.65 -2 imp:p=1 \$Bluff body
 30 2 -0.001236 -3 -4 -5 #(-1) #(-2) imp:p=1 \$Wind Tunnel with Plate and Bluff Body
 40 0 3:4:5 #(-1) #(-2) imp:p=0 \$Outside of Wind Tunnel with Plate and Bluff Body

C Surface Cards

1 RPP 20 120 0 0.2 -572 -472 \$Plate
 2 RPP 12 128 0 32 -588 -572 \$Bluff Body
 3 RPP 0 140 0 143 -1004 0 \$Wind Tunnel
 4 1 py 0 \$Plane for Indent 1
 5 2 py 0 \$Plane for Indent 2

*tr1 0 85 0 -60.362 29.638 90 -150.362 -60.362 90 90 90 0 1 \$Transformation for Indent 1
 *tr2 140 85 0 60.362 150.362 90 -29.638 60.362 90 90 90 0 1 \$Transformation for Indent 2

C

C Data Cards

mode p
 SDEF X=D1 Y=fx=D91 Z=fx=D92 ERG=D90
 SI90 L 2.547100e+000 \$
 1.735500e-001 \$
 1.094200e-001 \$
 4.840000e-003 \$

3.930000e-002 \$
 1.208000e+000 \$
 2.419700e-001 \$
 3.427900e-002 \$
 2.665500e-001 \$
 9.509000e-001 \$
 1.311200e-001 \$
 2.348800e+000 \$
 3.472000e-002 \$
 9.196300e-001 \$
 4.325300e-001 \$
 2.521700e+000 \$
 7.517900e-001 \$
 8.678200e-001 \$
 9.252400e-001 \$
 3.287700e-001 \$
 8.158500e-001 \$
 4.870300e-001 \$
 1.596500e+000 \$
 SP90 D 1.041000e-003 \$
 1.241000e-003 \$
 1.910000e-003 \$
 2.549000e-003 \$
 3.223000e-003 \$
 4.163000e-003 \$
 4.297000e-003 \$
 4.718000e-003 \$
 4.870000e-003 \$
 5.347000e-003 \$
 5.538000e-003 \$
 8.508000e-003 \$
 8.656000e-003 \$
 2.883800e-002 \$
 2.941100e-002 \$
 3.456700e-002 \$
 4.402100e-002 \$
 5.633900e-002 \$
 7.085400e-002 \$
 2.053000e-001 \$
 2.349100e-001 \$
 4.554900e-001 \$
 9.549000e-001 \$
 SII S 2 3 4 5 6 7 8
 SP1 0.027115798 \$
 0.13525998 \$
 0.027115798 \$
 0.002603117 \$
 0.002603117 \$
 0.015690158 \$
 0.789612034 \$
 SI2 0 20
 SP2 0 1
 SI3 20 120
 SP3 0 1
 SI4 120 140
 SP4 0 1
 SI5 0 12
 SP5 0 1
 SI6 128 140
 SP6 0 1
 SI7 12 128
 SP7 0 1

SI8 0 140
SP8 0 1
DS91 S 9 10 11 12 13 14 15
SI9 0 85
SP9 0 1
SI10 0.2 85
SP10 0 1
SI11 0 85
SP11 0 1
SI12 0 85
SP12 0 1
SI13 0 85
SP13 0 1
SI14 32 85
SP14 0 1
SI15 0 85
SP15 0 1
DS92 S 16 17 18 19 20 21 22
SI16 -572 -472
SP16 0 1
SI17 -572 -472
SP17 0 1
SI18 -572 -472
SP18 0 1
SI19 -588 -572
SP19 0 1
SI20 -588 -572
SP20 0 1
SI21 -588 -572
SP21 0 1
SI22 -1004 -588
SP22 0 1
nps 1000000
m1 1001.50c -6.2 6000.50c -44.5 8016.50c -49.3
m2 1001.50c -1.18 7014.50c -77.08 8016.50c -21.28 18000.35c -0.46
F5:p 70 8 -638 1
F15:p 70 8 -738 1
DF5 iu=2 fac=1 ic=31
DF15 iu=2 fac=1 ic=31

REFERENCES

- [1] Hill, J.D. (2007). *Resuspension Programme: Experimental Trials held at WIS Munster 19th-23rd March 2007*. Technical Memorandum. Harwell Didcot, Oxfordshire, United Kingdom: Serco Group plc.
- [2] Nicholson, K. W. (1988). Review Article: A Review of Particle Resuspension. *Atmospheric Environment*, 22 (12), 2639-2651.
- [3] Waller, E., Perera, S., Satgunanathan, R., Erhardt, L.S., & Cousins, T. (2007). *Phenomenology of Resuspension: Radioactive Particles and Aerosols – Implications to Radiological Dispersal Device (RDD) Events*. Technical Memorandum. Ottawa, Ontario, Canada: Defence Research and Development Canada
- [4] Shinn, J.H., Homan, D.N., & Hofmann, C.B. (1986). *A summary of Plutonium aerosol studies: Resuspension at the Nevada Test Site (Report No. UCRL-90746)*. Livermore, California, United States of America: Lawrence Livermore National Laboratory.
- [5] Shinn, J.H. (2003). *Studies of Plutonium aerosol resuspension at the time of the Maralinga cleanup (Report No. UCRL-ID-155063)*. Livermore, California, United States of America: Lawrence Livermore National Laboratory.
- [6] Langer, G. (1991). *Resuspension of soil particles from Rocky Flats containing Plutonium particulates (Report No. GHS-0070-91)*. Golden, Colorado, United States of America: EG&G Rocky Flats, Inc.
- [7] Wagenpfeil, F., Paretzke, H.G., Peres, J.M., & Tschiersch, J. (1998). Resuspension of coarse particles in the region of Chernobyl. *Atmospheric Environment*, 33(1999), 3313-3323.
- [8] Hinds, W. (1999). *Aerosol Technology: Properties, Behavior, and Measurement of Airborne Particles* (2nd ed.). Toronto, Ontario, Canada: Wiley-Interscience.
- [9] Nigro, N., Filippini, G., & Franck, G. (2005). Flow around a sharp-edged surface-mounted cube by Large Eddy Simulation. *VIII Argentine Congress on Computational Mechanics* (pp. 1299-1318). Buenos Aires, Argentina: Mecánica Computacional.
- [10] Krajnović, S., & Davidson, L. (2000). Flow around a three-dimensional bluff body.

9th International Symposium on Flow Visualisation (pp. 177-1 – 177-10). United Kingdom: International Symposium on Flow Visualisation.

- [11] Harwell. (2008). *CFD modelling in support of re-suspension trials*. Technical Memorandum. Harwell Didcot, Oxfordshire, United Kingdom: Serco Group plc.
- [12] Hill, J.D., Flemming, M.A., Locke, J., & Vettese, F. (2007, November). *Resuspension of Hazardous Particulate Materials by Vehicle Movements*. Presented at the International CBRN Defence Symposium 2007, Shrivenham, United Kingdom.
- [13] Luxat, J.C. (2008, November). *Multiphysics software and the challenge to validating physical models*. Presented at the 23rd Canadian Nuclear Society Symposium on Simulation Methods in Nuclear Engineering, Ottawa, Ontario, Canada.
- [14] Fehri, M.F., Chambon, R., & Teyssedou, A. (2008, June). *A transient neutronic-thermalhydraulic coupled modelling approach*. Presented at the 29th Annual Conference of the Canadian Nuclear Society - 32nd Canadian Nuclear Society/Canadian Nuclear Association Student Conference, Toronto, Ontario, Canada.
- [15] Szymandera, J., Blake, L., Phan, B.G., & Nainer, O. (2008, November). *PhysicsShell: A Solution to Multi-Code Linking*. Presented at the 23rd Canadian Nuclear Society Symposium on Simulation Methods in Nuclear Engineering, Ottawa, Ontario, Canada.
- [16] Popescu, A.I., Wu, E., Yousef, W.W., Pascoe, J., Parlatan, Y., & Kwee, M. (2006, June). *Development of TUF-ELOCA – A software tool for integrated single-channel thermal-hydraulic and fuel element analyses*. Presented at the 27th Annual Conference of the Canadian Nuclear Society – 30th Canadian Nuclear Society/Canadian Nuclear Association Student Conference, Toronto, Ontario, Canada.
- [17] Hu, J., & Uddin, R. (2008, June). *Coupled Neutronics and Thermal-Hydraulics Simulations Using Monte Carlo and CFD*. Presented at the 2008 International Congress on Advances in Nuclear Power Plants, Anaheim, California, United States of America.
- [18] Seker, V., Thomas, J.W., & Downar, T.J. (2007, June). *Reactor Physics*

Simulations with Coupled Monte Carlo Calculation and Computational Fluid Dynamics. Presented at the 2007 International Conference on Emerging Nuclear Energy Systems, Istanbul, Turkey.

- [19] Waller, E. (2008, April 30). *Discussion of radiation field determination from radioactive particulate resuspension*. Personal Communication.
- [20] Defense Threat Reduction Agency. (n.d.). *Hazard Prediction and Assessment Capability (HPAC)*. Retrieved December 2, 2009, from <http://www.dtra.mil/rd/programs/acec/hpac.cfm>
- [21] Defense Threat Reduction Agency. (n.d.). *Consequence Assessment Tool Set (CATS)*. Retrieved December 2, 2009, from <http://www.dtra.mil/rd/programs/acec/cats.cfm>
- [22] Lawrence Livermore National Laboratory. (n.d.). *HOTSPOT – Health Physics Codes for the PC*. Retrieved December 2, 2009, from <https://www-gs.llnl.gov/hotspot/index.htm>
- [23] Numerical Applications, Inc. (2009). *GOTHIC Applications*. Retrieved December 2, 2009, from http://www.numerical.com/gothic/gothic_main.htm
- [24] Doria, F. J. (2001). *CANDU Safety #19: Safety Analysis Tools*. Retrieved from <http://canteach.candu.org/library/19990120.pdf>
- [25] Munson, B.R., Young, D.F., & Okiishi, T.H. (2002). *Fundamentals of Fluid Mechanics* (4th ed.). United States of America: John Wiley & Sons, Inc.
- [26] Versteeg, H.K., & Malalasekera, W. (2007). *An Introduction to Computational Fluid Dynamics: The Finite Volume Method* (2nd ed.). Glasgow, Scotland: Pearson Education Limited.
- [27] FLUENT User Services Center. (2005). *Modeling Turbulent Flows: Introductory FLUENT Notes*. Canonsburg, Pennsylvania, United States of America: ANSYS, Inc. Retrieved from <https://www.ing.unimo.it/campusone/VisualizzazioneIngegneria/StreamFile.asp?File=../MaterialeDidattico/Matdidattico7257/06-FLUENT-turbulence.pdf>
- [28] Kaftori, D., Hetsroni, G., & Banerjee, S. (1995). Particle behavior in the turbulent boundary layer. I. Motion, deposition, and entrainment. *Physics of Fluids*, 7(5), 1095-1106.

- [29] Braaten, D.A., Paw U, K.T., & Shaw, R.H. (1990). Particle Resuspension in a Turbulent Boundary Layer – Observed and Modeled. *Journal of Aerosol Science*, 21(5), 613-628.
- [30] Biasi, L., de los Reyes, A., Reeks, M.W., & de Santi, G.F. (2001). Use of a simple model for the interpretation of experimental data on particle resuspension in turbulent flows. *Journal of Aerosol Science*, 32(2001), 1175-1200.
- [31] Kim, Y., Gidwani, A., Sippola, M., & Sohn, C.W. (2008). *Source Term Model for Fine Particle Resuspension from Indoor Surfaces (Report No. ERDC/CERL TR-08-4)*. Washington, District of Columbia, United States of America: U.S. Army Corps of Engineers – Engineer Research and Development Center.
- [32] Hill, J. (2008). *Resuspension Research Programme*. Technical Memorandum. Harwell Didcot, Oxfordshire, United Kingdom: Serco Group plc.
- [33] PHARMAHUB. (2008). *Discussion on Hamaker Constant*. Retrieved December 2, 2009, from <http://pharmahub.org/resources/206>
- [34] Cember, H. (1996). *Introduction to Health Physics* (3rd ed.). United States of America: McGraw-Hill.
- [35] James, M.R., McKinney, G.W., & Waters, L.S. (2008). *MCNPX Intermediate Workshop*. Los Alamos, New Mexico, United States of America: Los Alamos National Laboratory.
- [36] Hacker, C. (2005). *Radiation Decay: Version 3.6*. Brisbane, Australia: Griffith University – Electronics and Signal Processing Group.
- [37] ANSYS Inc. (2006). *GAMBIT 2.3 Modeling Guide – Chapter 3: Meshing the Model*. Canonsburg, Pennsylvania, United States of America
- [38] ANSYS Inc. (2006). *FLUENT 6.3 Getting Started Guide – Chapter 2: Introduction to FLUENT*. Canonsburg, Pennsylvania, United States of America
- [39] ANSYS, Inc. (2006). *FLUENT 6.3 User's Guide – Chapter 8: Physical Properties*. Canonsburg, Pennsylvania, United States of America.
- [40] ANSYS, Inc. (2006). *FLUENT 6.3 User's Guide – Chapter 7: Boundary*

Conditions. Canonsburg, Pennsylvania, United States of America.

- [41] ANSYS, Inc. (2006). *FLUENT 6.3 User's Guide – Chapter 11: Modeling Turbulence*. Canonsburg, Pennsylvania, United States of America.
- [42] Lavezzo, V., Campolo, M., & Soldati, A. (2007, June). *Role of a-periodic large scale flow structures in particle resuspension in stirred tanks*. Presented at the 8th International Conference on Chemical and Process Engineering and 10th Conference on Process Integration, Modelling and Optimisation for Energy Saving and Pollution Reduction, Ischia Island, Gulf of Naples, Italy.
- [43] ANSYS, Inc. (2006). *FLUENT 6.3 User's Guide – Chapter 22: Modeling Discrete Phase*. Canonsburg, Pennsylvania, United States of America.
- [44] Oak Ridge National Laboratory. (2007). *Rad Toolbox: Version 2.0.0*. Oak Ridge, Tennessee, United States of America: Oak Ridge National Laboratory.
- [45] ANSYS, Inc. (2006). *FLUENT 6.3 User's Guide – Chapter 26: Using the Solver*. Canonsburg, Pennsylvania, United States of America.
- [46] *ICRP Publication 74: Conversion Coefficients for use in Radiological Protection against External Radiation*. (1997). United Kingdom: Elsevier Science Ltd.
- [47] Lamarsh, J.R., & Baratta, A.J. (2001). *Introduction to Nuclear Engineering* (3rd ed.). United States of America: Prentice-Hall, Inc.
- [48] Waller, E. (2009, March 20). *Ballistic Research Laboratory Material Codes*. Personal Communication.
- [49] Cooper, J.R., Randle, K., & Sokhi, R.S. (2003). *Radioactive Releases in the Environment: Impact and Assessment*. United Kingdom: John Wiley & Sons, Ltd.
- [50] Waller, E. (2008, March 4). *Monte Carlo Approximations to the Neutron Transport Equation*. Personal Communication.